

Université catholique de Louvain  
(UCLouvain)  
Institute of Condensed Matter and Nanosciences  
(IMCN)

**Fine-tuning photochromic properties of *N*-  
Salicylideneaniline derivatives using cocrystal  
engineering**

Dissertation  
submitted in fulfillment  
of the requirements for the degree of  
Doctor of Science

**Gabriel M. M. F. E. Mercier**

Louvain-la-Neuve

2022



## **Jury members**

Pr. Benoît Champagne

Unamur

Pr. Yaroslav Filinchuk

UCLouvain

Dr. Koen Robeyns

UCLouvain

Pr. Johan Wouters

Unamur

Pr. Sophie Demoustier

**President of jury**

UCLouvain

Pr. Tom Leyssens

**Supervisor**

UCLouvain



## Acknowledgements

Doing a Ph. D. thesis is not only about getting a degree but also is a major step in a life. A step which not only allows you to get a sizeable amount of knowledge in a field, but also allows to encounter many persons, situations, places, universities and research groups. It is not only about sciences but also about finding who you are and a personal evolution.

I think a Ph. D. is not only a personal success but also greatly depends of the peoples around you: family, friends, colleagues, supervisor and students. Finishing a Ph. D. thesis is not easy and I know many peoples who couldn't or hadn't the possibility to finish it. Thus, I think all the peoples I met over the past 7 years and more have contributed in a way or another to help me going through and finishing this thesis. I would like to give a special thanks to the persons below:

**Pr. Tom Leysens**, which accepted me in his lab, gave me the freedom to choose my own new project, taught me so many things about crystals and physical chemistry but also always looked after the well-being of all of the members of his team. Thank you for being not only a great teacher but also a great person.

**Pr. Benoît Champagne and Pr. Johan Wouters** as members of the ARC ConTrast project, which helped me and discussed with me many times throughout this thesis. Thank you for your kindness and help over the years.

**Pr. Yaroslav Filinchuk, Pr. Olivier Riant and Dr. Koen Robeyns** as members of my thesis committee, for their advices, useful discussions and their teaching when I was one of their students.

**Pr. Michel Devillers and Pr. Istvan Marko (†)** for their brilliant teaching when I was a 1<sup>st</sup> year bachelor student in biology. They made me envy to be a chemist instead.

I would like to thanks all my colleagues and co-workers, from the ARC ConTrast project, from the lab, from the other labs I have been working with, all over the years (if I forgot anybody please pardon me): **Thomas Vergote, Géraldine Springuel, Fanny George, Natalia Tumanova, Ricky Payen, Bram Harmsen, Voraksmy Ban, Yurii Dovgaliuk, Nikolay Tumanov, Fabrice Morelle** ("souviens-toi"), **Lixing Song, Xiao Li, Carolina Picasso, Damir Safin**

("It smell chemistry"), **Vanessa Seiler, Jean-Baptiste de Maere d'aertrycke, Michaël Guillot, Xavier Buol, Claire Clérin, Sarah Huynen, Raphaël Da Silva, Martin Appelmans, Adel Moulai, Timothy Steenhaut, Véronique Louppe, Joséphine de Meester, Camila Caro Garrido, Volodia Gounaris, Mathieu Vanderdonckt ("le touriste"), Chloé Matheys, Carole Body ("elle a plein de pattes !"), Li Ting, Guillaume Wéry, Lisa Gubbels, Gilles Marghem, Fuli Zhou, Fucheng Leng, Iago Maye, Robin Crits, Aurore Becquevort, Claire Umutoni, Gabrielle Barozzino Consiglio, François Billard, François Devred;** my classmates: **Simon Cerfontaine, Marine Devos, Nicolas Diercxens, Laurent Gillard, Florence Josse, Nadzeya Kryvutsa, Anaëlle L'hoost, Sébastien Leloux, Pierre Libioule, Audric Nagy, Jean-Boris Nshimyumuremyi ("Spock five!"), Coralie Renders, Mathieu Soetens and Kyril Wittouck;** And finally my colleagues which I didn't cited yet from "Ecole de Chimie de l'UCLouvain" (for which I worked as a teaching assistant from 2014 to 2021): **Antoine Raillet, Tommy Haynes, Corentin Rasson, Jérôme Savary, Axel Morelle, Géraldine Chanteux, Vincent Delmez, Catherine Liégeois, Agnès Gnagnarella, Laurent Collard, Samuel Carlier, Marine Lefèvre, Martin Gillard, Corentin Pochet, Edouard Vandendorpel, Anne Vermaut, Nadine Spelier,** and a special thanks to **Pascale Smitz** for the nice collaboration all over the years.

I won't be who I am without all the friends I met over the years: **José, Adrien, Lucas, Renaud, François, Elric, Bernard, Yves,** and all the other Go players I ever met from **Belgium, France, Germany, Canada, Korea, ...** and the members of **LLN Jujutsu club** and of **Karaté Shitokai LLN club:** I improved as a human being as much as I improved my skills thanks to you all.

Finally, I'd like to thanks my mother **Oksana,** my father **Philippe (+),** my brother **Sébastien,** the parrot **Cowin,** all my family, and most important of all, **Séverine** with whom I share my life, my joys and fears, my doubts and success. She helps me every day to be a better man since more than 8 years now.

## List of Publications

Gabriel M. Mercier, Koen Robeyns and Tom Leysens; “Altering the Photochromic Properties of *N*-Salicylideneanilines Using a Co-Crystal Engineering Approach”; *Cryst. Growth Des.*, **2016**, 16, 3198–3205, DOI: 10.1021/acs.cgd.6b00108.

Freddy Zutterman, Orian Louant, Gabriel Mercier, Tom Leysens and Benoît Champagne; “Predicting Keto–Enol Equilibrium from Combining UV/Visible Absorption Spectroscopy with Quantum Chemical Calculations of Vibronic Structures for Many Excited States. A Case Study on Salicylideneanilines”; *J. Phys. Chem. A*, **2018**, 122, 24, 5370–5374, DOI: 10.1021/acs.jpca.8b03389.

Gabriel M. Mercier, Koen Robeyns, Nikolay Tumanov, Benoit Champagne, Johan Wouters and Tom Leysens; “New Insights into Photochromic Properties of *N*-Salicylideneaniline Derivatives Using a Cocrystal Engineering Approach”; *Cryst. Growth Des.*, **2019**, 19, 5544–5556, DOI: 10.1021/acs.cgd.9b00363.



## Abstract

*N*-Salicylideneaniline (also called anil) is a compound which exhibits photochromism (reversible color change induced by light) in the solid-state. Such a feature is quite rare and requires in-deep studies to fully understand it, especially because it can be quite useful in many industrial applications such as secured inks (for banknotes for instance), screens or even optical data storage.

Within this thesis, *N*-Salicylideneaniline and many of its derivatives (the “anils”) were studied in the scope of crystal engineering in order to establish a structure-property relationship and to improve its properties. More specifically, cocrystals were researched and studied using small organic molecules (such as carboxylic acids, amides, amines, benzene halides) as cofomers. This resulted in the identification of about 100 cocrystals through the use of X-ray powder diffraction (XRPD), single crystal X-ray diffraction (SC-XRD), diffuse reflectance spectroscopy (DRS), thermal analysis such as thermogravimetric analysis (TGA) and differential scanning calorimetry (DSC) along with a few other methods such as Raman spectroscopy. The amount of collected data allowed to show a correlation between the number of intermolecular interactions involving the “moving moiety” of the anils and the presence of photochromism. We also present here a new approach of the Diffuse Reflectance Spectroscopy data treatment, which allows a better classification of the photochromic properties and also allowed the discovery of “weakly” photochromic compounds. These results encourage a revision of the old-empirical “dihedral angle rule” especially because a link between the intensity of photochromism and the torsion angle has been observed in this work.

In the last part, we focused on cocrystals containing 2 different anils (instead of one anil and one cofomer) and this allowed to observe the existence of a complex multi-phases binary diagram in the case of *N*-Salicylideneaniline/ *N*-Salicylidene-4-fluoroaniline solid-solution. Also, intermediate photochromic intensity values and kinetical parameters could be observed for the first time compared to parent anils alone, achieving a step towards control and fine-tuning of photochromic properties of anils.

Ph. D. Thesis dissertation in Chemistry,  
**Ottignies-Louvain-la-Neuve, 04 Novembre 2021**



## Résumé

Le *N*-Salicylideneaniline (aussi appelé anil) est un composé présentant une propriété particulière à l'état solide : le photochromisme (soit un changement de couleur réversible induit par la lumière). Cette propriété n'est pas courante et mérite une attention particulière du fait de ses nombreuses applications possibles telles que les encres inviolables (pour les billets de banques par exemple), les écrans ou même encore le stockage optique d'information.

Au cours de cette thèse, nous avons étudié le photochromisme au sein de nombreux dérivés du *N*-Salicylideneaniline (« les anils ») et sous l'angle de l'ingénierie du cristal, afin d'essayer d'établir des liens entre la structure du matériau et ses propriétés et de pouvoir améliorer celles-ci. Plus précisément, nous avons recherché des cocristaux contenant un anil et un coformer (ici une petite molécule organique du type acide carboxylique, amide, amine ou encore benzène-halide). Cette recherche a abouti à l'identification et la caractérisation d'une centaine de cocristaux via diverses méthodes telles que la diffraction des rayons X sur poudre (XRPD), la diffraction des rayons X sur monocristal (SC-XRD), la spectroscopie de réflectance diffuse (DRS), les analyses thermiques telles que l'analyse thermogravimétrique (TGA) et la calorimétrie différentielle à balayage (DSC) ainsi que d'autres méthodes complémentaires telles que la spectroscopie Raman par exemple. La quantité de données ainsi obtenue nous a permis d'établir un lien entre le nombre d'interactions intermoléculaires impliquant la partie mobile de la molécule et la présence ou non du photochromisme.

Nous présentons également une nouvelle approche dans le traitement des données issues de la DRS qui a permis une meilleure classification des composés et la découverte des composés « faiblement » photochromiques. Ces résultats encouragent une révision de l'ancienne loi empirique concernant l'angle dièdre, d'autant plus qu'un lien entre intensité du photochromisme et l'angle de torsion a pu être observé dans le cadre de cette thèse.

Dans la dernière partie, nous avons étudiés les cocristaux contenant deux anils (au lieu d'un anil et d'un coformer) et cela a mené à la découverte d'un cas particulier pour le système *N*-Salicylideneaniline/ *N*-Salicylidene-4-fluoraniline qui présente un diagramme binaire complexe avec plusieurs phases du type solution-solide. De plus, ce système permet d'obtenir pour la première fois des valeurs intermédiaires de l'intensité du photochromisme

et des paramètres cinétiques par rapport aux deux anils isolés, ce qui représente une avancée vers le contrôle et l'optimisation du photochromisme des anils en général.

Dissertation doctorale en Chimie,  
**Ottignies-Louvain-la-Neuve, 04 Novembre 2021**

## Table of contents

<b>Jury members</b>	iii
<b>Acknowledgements</b>	v
<b>List of Publications</b>	vii
<b>Abstract</b>	ix
<b>Résumé</b>	xi
<b>Table of contents</b>	xiii
<b>Chapter 1. Introduction</b>	1
<b>I.1. State of the art and general aim of this work</b>	3
<b>I.2. Light and colors</b>	7
I.2.a. The nature of light	7
I.2.b. Discovery of Infrared and other forms of light	8
I.2.c. The origin of colors	10
<b>I.3. Chromism and Photochromism</b>	13
I.3.a. Photochromism in anils	13
I.3.b. Other photochromic materials	15
<b>I.4. Crystal engineering</b>	21
I.4.a. Hydrogen bonds	24
I.4.b. Halogen bonds	25
I.4.c. Other important intermolecular interactions	27
I.4.d. Hirshfeld surfaces	28
<b>I.5. Solid-solutions</b>	31
<b>I.6. Methods for solid-state analysis</b>	35

1.6.a. Thermal analysis	35
1.6.b. Thermogravimetric analysis (TGA)	36
1.6.c. Differential Scanning Calorimetry (DSC)	37
1.6.d. X-rays diffraction techniques: SC-XRD and XRPD	39
1.6.e.1. Diffuse Reflectance Spectroscopy: theoretical aspects	45
1.6.e.2. Diffuse Reflectance Spectroscopy: practical aspects	47
1.6.f. IR and Raman spectroscopy	48
1.6.g. Terahertz spectroscopy (THz)	51
<b>1.7. References</b>	<b>53</b>
<b>Preface of Chapter 2</b>	<b>63</b>
<b>Chapter 2. Altering the Photochromic Properties of <i>N</i>-Salicylideneanilines using a Co-Crystal Engineering Approach</b>	<b>65</b>
<b>Abstract</b>	<b>66</b>
<b>Introduction</b>	<b>67</b>
<b>Experimental section</b>	<b>70</b>
<b>Results</b>	<b>75</b>
<b>Co-crystals of 4-fluoro-<i>N</i>-Salicylideneaniline</b>	<b>78</b>
<b>Co-crystal between <i>N</i>-Salicylideneaniline (A) and citraconic acid (C10)</b>	<b>79</b>
<b>Conclusion</b>	<b>86</b>
<b>References</b>	<b>88</b>
<b>Preface of Chapter 3</b>	<b>93</b>
<b>Chapter 3. New Insights into Photochromic Properties of <i>N</i>-Salicylideneaniline Derivatives Using a CoCrystal Engineering Approach</b>	<b>95</b>
<b>Abstract</b>	<b>96</b>

<b>Introduction</b>	97
<b>Experimental section</b>	99
<b>Results</b>	103
Cocrystal screening	103
Photo- and non-photochromic behavior	107
Linking photochromism to structural characteristics	110
Kinetic measurements	119
<b>Conclusion</b>	121
<b>References</b>	123
<b>Preface of Chapter 4</b>	131
<b>Chapter 4. Anil cross crystallization</b>	133
<b>Introduction</b>	135
<b>Materials and methods</b>	136
<b>Results</b>	137
Screening results	137
Photochromic studies	138
System <b>A+M</b>	141
System <b>E+N</b>	143
System <b>G+H</b>	147
<b>Conclusion</b>	149
<b>References</b>	149
<b>Preface of Chapter 5</b>	151
<b>Chapter 5. <i>N</i>-Salicylideneaniline solid-solutions between structurally related anils: a complex multitude of phases and evidences of an organic ternary-solid-solution</b>	153

<b>Abstract</b>	154
<b>Introduction</b>	155
<b>Experimental section</b>	158
<b>Results</b>	161
Solid-solution formation	161
Structural studies	162
XRPD results	165
Thermal analysis	167
Photochromic properties of <b>A/B</b> system	169
<b>Discussion</b>	172
<b>Conclusion</b>	175
<b>References</b>	176
<b>Chapter 6. Conclusion and perspectives</b>	179
<b>Conclusion</b>	181
<b>Perspectives</b>	187
<b>Supporting Information</b>	191
<b>Chapter 4 Supporting Information</b>	195
<b>Chapter 5 Supporting Information</b>	217

# **Chapter 1**

## **Introduction**



### **I.1. State of the art and general aim of this work**

In a world constantly evolving and facing new crises on a regular basis, there is a need for new technologies in order to adapt, discover and tackle these. The development of new technologies naturally arises from a deep understanding of the laws of physics and chemistry. Thus, fundamental research is required in order to provide such knowledge.

The present project subscribes to the fundamental research as its main aim is to reach new insights and understanding of a physicochemical property which may ultimately lead to new applications both for research and everyday life: photochromism.

Chromism in chemistry usually refers to the ability of a material to undergo a reversible color change, thus photochromic compounds exhibit a reversible color change induced by UV-Visible light. Other types of chromism exist such as thermochromism (induced by heat), solvatochromism (induced by the presence of a solvent) piezochromism (induced by pressure) etc [1]. Photochromism was discovered in the second half of the 19<sup>th</sup> century and can be exhibited by both inorganic and organic compounds, in solution or liquid state, in the amorphous solid-state and even in the crystalline solid-state [2] [3] [4]. Since, compounds exhibiting this property have been widely researched as industrial applications are numerous and range from secured photochromic inks for banknotes, official stamps, etc. [5] to photochromic glasses and lenses for everyday life [2] or new optical devices as well as potential applications in optical data storage [6].

Photochromism is a very wide subject and the present thesis has been made in the context of an ARC ("Action de la Recherche Concertée") constituted of different research groups working on different areas and families of compounds which can present it: *N*-Salicylideneaniline derivatives (also called anils) discussed within this work but also *N*-Salicylidene-3-aminopyridine [7] and spiropyrans [8]. Theoretical and modelization studies were also performed within the ARC project with the aim to advance on structure prediction [9] but also to predict chromical properties with the keto-enol equilibrium prediction [10]. In this last contribution, the theoretical approach was combined with experimental results (absorption spectra) of some anils studied within this thesis. These last researches won't be discussed further in the text but they illustrate the external added-value of the present work.

At the beginning of this thesis project, the choice has been made to study this property in the crystalline state as this later presents many advantages such as facility to process [11], increased stability and resistance to fatigue [12]. Sensitivity to light is not high for most compounds in their crystalline form, however, it is not the case for *N*-Salicylideneaniline derivatives among which some present photochromism, thermochromism or both in the solid-state [13]. As these compounds have the advantage to be easy to synthesize and easily crystallize, they perfectly matched the requirements of this project. Still, many anils do exhibit photochromism in solution but not in the solid-state [13] [14]. As a result, many approaches have been performed over the years in order to switch on photochromism in the solid-state, such as: adding bulky groups on the anils [15], including anils in metal-organic frameworks [16], inserting anils in cyclodextrines [17] or in zeolites [18].

All these results have proven that the molecular environment can have a crucial impact over the photochromism of anils. As a result, in this work we aimed to alter and switch on photochromical properties of anils by directly changing their structural environment. Thus, the first goal of this project was to prove that modifying the crystalline environment of a molecule through cocrystallization affects or even enables its photochromic properties. The effect of the crystalline environment was already highlighted by the fact that various polymorphs present different degrees of photochromism. However here we also aim at proving we can improve or even switch on this property in compounds which do not present it otherwise.

In order to do this, the first task was to create a database of anils and to crystallize them in many different structural environments through cocrystallization. The first part of the project was therefore focused on the synthesis and cocrystal research of two well-known anils, one that is photochromic only and the other one which is thermochromic only. Many cocomers were tested and a few cocrystal systems have been identified among which one showed a strong variation of photochromic property of the target compound. These results were published in *Crystal Growth and Design* and constitute chapter 2 of the present thesis.

After the encouraging results obtained in the first part, we set the goal to gain a deeper understanding of the cocrystallization effect on the photochromic property. Thus, the anil dataset was extended with 13 new

anils. All anils contained a common core, allowing them to present photochromism but differ in functional groups which should change their propensity to cocrystallize in accordance with crystal engineering principles presented in Section I.4. of the introduction. Their synthesis was optimized and the anils used for cocrystal screening. The coformers were selected using those which successfully cocrystallized during the first part of the project as well as some others known to easily cocrystallize, resulting in a total of 21 compounds among which 12 are carboxylic acids, 6 are amides and 3 are halogenated benzenes (with fluorine and iodine). The complete cocrystal screening led to the identification of about 100 cocrystal systems among which more than 20 were structurally determined. Combined with the crystalline structure of the parent anils a statistical insight could be drawn relating structure properties to the photochromic ones and allowing identifying a better descriptor than the empirical “dihedral-angle rule”. These results were published in *Crystal Growth and Design* and constitute chapter 3 of the present thesis.

Based on our findings, we showed how cocrystallization can have a strong impact on photochromism. The downside of cocrystallization in a stoichiometric manner, is that it can only serve to switch the property on or off, or to modulate photochromism from one value to another. It does not, however, allow to finetune photochromism, as this would require adding various amounts of coformer into the crystalline lattice. This can however be done when dealing with a solid solution. A final part of this thesis therefore looks into this aspect as, theoretically, in a solid-solution we can change the ratio of the two components. As a result, we could estimate how the photochromic property changes with respect to the ratio of component. The use of solid-solution could be powerful as it should allow to fine-tune properties in a controlled way. This last would allow achieving full control of the anils and may lead to the design of ideal systems for specific applications and furthermore they could be extendable to other systems as well. These results are presented in chapter 5 and are also expected to be published shortly. We can now summarize the goals pursued in this project:

- Verify whether cocrystallization affects photochromism of anils (chap. 2);
- Search for suitable coformers and cocrystal propensity (chap. 2 and 3);
- Discover new insights about the structure-reactivity relationship (chap. 3);
- Design ideal systems (chap. 4 and 5).



## I.2 Light and colors

### I.2.a. The nature of light

Light is the beginning of everything. Life itself may have begun because photochemical reactions occurred between CO<sub>2</sub>, CH<sub>4</sub>, N<sub>2</sub> and O<sub>2</sub> in the early atmosphere and oceans 4 billion years ago [19]. Light is defined as “the brightness that comes from the sun, fire, etc. and from electrical devices, and that allows things to be seen” according to the Cambridge dictionary [20]. This everyday life definition however doesn’t explain what the nature of that “brightness” is and what its properties are.

From a physical point of view, light is defined as “an electromagnetic radiation within the portion of the electromagnetic spectrum that can be perceived by the human eye [21] which usually correspond to a wavelength comprised between 400 and 700 nanometers. Above 700 nm are the infrared radiations and below 400 nm are the ultraviolet ones [22] [23]”. By the *International Lighting Vocabulary*, the definition of *light* is: "Any radiation capable of causing a visual sensation directly."

The nature of light, an electromagnetic wave, was first stated by Michael Faraday in 1845 and theoretically demonstrated by J. C. Maxwell in 1865 which in turn was verified experimentally in 1887 by H. Hertz and led to the development of new technologies such as radio, television and all forms of radio-communication [24]. Beside this wave behavior, it is also important to note that light can also behave like a particle: using the quantification of energy introduced by M. Planck in 1900, A. Einstein demonstrated in 1905 that particles of light with quantified energy could explain the results of the photoelectric effect experiments. These particles of light are nowadays called “photons” and the energy of photons ( $E_{ph}$ ) is given by Einstein formula:  $E_{ph} = h \frac{c}{\lambda}$  (with  $h$  the Planck constant). This surprising dual behavior for light (wave and particle) was later generalized by L. De Broglie for all particles and is now known as the wave-particle duality [25].

The electromagnetic spectrum is very large varying from frequencies as low as 100 Hz for radio-waves to 10<sup>28</sup> Hz for gamma-rays and there are no theoretical limits to the available frequencies [24]. Knowing that for an electromagnetic wave the frequency ( $\nu$ ) is linked to the wavelength ( $\lambda$ ) through  $\nu = \frac{c}{\lambda}$  where  $c$  is the speed of light (2.9979x10<sup>8</sup> m/s) this leads to

observed wavelengths comprised between  $3 \times 10^{-20}$  m to  $3 \times 10^6$  m. Knowing that the radius of a hydrogen atom is typically 0,529 Å which is equal to  $0,529 \times 10^{-10}$  m (and that the radius of a proton is about  $8,5 \times 10^{-16}$  m) it means an electromagnetic wavelength can be smaller than the smallest atom or larger than a continent. Within this large spectrum, visible light is comprised between approx.  $4 \times 10^{14}$  and  $7.5 \times 10^{14}$  Hz.

### **I.2.b Discovery of Infra-Red and others forms of light**

Infra-red light was discovered in 1800 by the British astronomer William Herschel and is the first part of the electromagnetic spectrum which is invisible to human eye ever to be discovered [26]. Herschel discovered it while doing an experiment in order to measure the amount of heat vehiculated by red and blue light: sun light was diffracted by a prism and thermometers were placed under the outcoming red and blue lights while the control thermometer was (fortunately) placed into the shadow next to the red light, where no visible light could be observed. As a result, the temperature measured under red light was higher than under blue light as expected by Herschel, but surprisingly the control thermometer measured a higher temperature in the shadow than under red light. Doing the experiment many times with many thermometers (as presented in Figure 1) finally proved the existence of an invisible type of light below red-light which was in turn called "Infra-Red".

After the discovery of I.R., other forms of light were discovered over time such as:

- 1801: discovery of UV-rays by Johann Wilhelm Ritter,
- 1867: prediction of other forms of light by James Clerk Maxwell,
- 1888: discovery of Radio Waves/ Microwaves by Heinrich Hertz,
- 1895: discovery of X-rays by Wilhelm Conrad Roentgen.

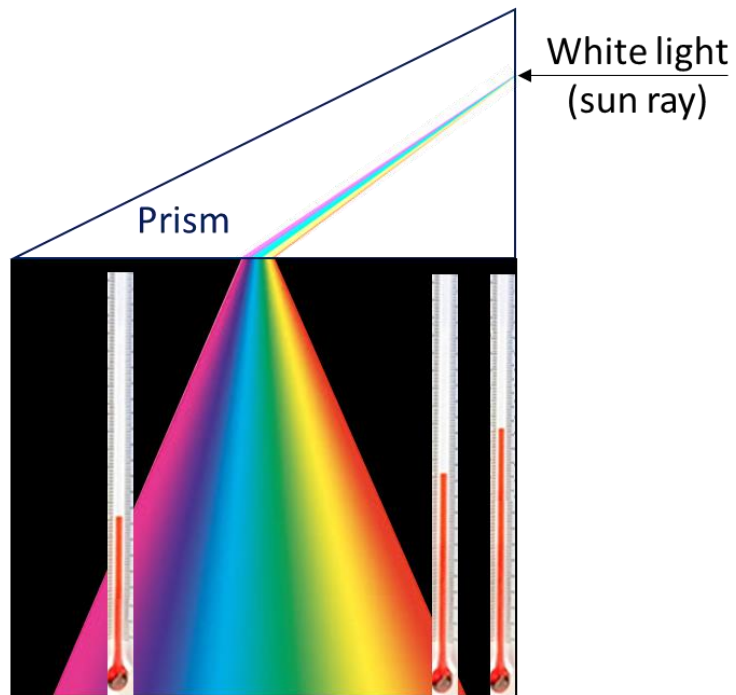


Figure 1: the Herschel experiment: a sun ray was focalized on a prism and two thermometers were placed under the outcoming blue and red lights while the control thermometer was placed into the shadow next to the red light. This last thermometer showed a larger increase in temperature, hence proving the existence of an invisible light on the red side.

### I.2.c. The origin of colors

Any object that we see has its own color. The origin of that color may be easy to understand when we are facing a bright object (candle, lamp, sun...): as light is an electromagnetic wave, any object emitting light appears with the color it emits. However, most of the objects we face in everyday life are not light sources or do not emit any visible light but still appear colored. The reason of this phenomenon is due to the interaction of matter with light: when an object is put under a ray of visible light it might absorb some of the wavelengths composing the ray and reflect the others. Thus, its color corresponds to the complementary color to the ones absorbed as shown in Figure 2 [27]: for instance, if an object can absorb blue light, it will be perceived as orange under white light. By extension, the color of a chemical compound comes from two effects: the wavelength composition of the light which illuminates it and the wavelengths which are absorbed by the compound. An example of this is given with the absorption spectra of anil **A** (shown in Figure 2): the enol forms before irradiation (yellow curve) can absorb UV and violet light and thus appear yellow as shown in the picture. The *trans*-keto form (after UV irradiation – red curve) absorbs also the green light and thus appears red as shown on Figure 2. It's important to note that we are not describing objects/compounds which can re-emit light here (i.e., the phenomenon known as fluorescence).

From the above discussion, we can notice that any object or chemical compound is able to absorb light. It is important to understand how such phenomena can occur and how light and matter can interact.

First, we need to notice that not all wavelengths can be absorbed by a compound, otherwise there would be no color anymore: everything would appear black. There is thus a condition which states that a wavelength can be absorbed if it corresponds to an energetic transition into the compounds studied [27] [28]. This was discovered and explained in the early 20<sup>th</sup> century with the works of M. Planck, A. Einstein and N. Bohr [28]. Using Einstein formula ( $E_{ph} = h \frac{c}{\lambda}$ ) for wavelengths equal to 400 to 700 nm, the calculated values of the energy are similar to electronic transitions. As a result, UV and visible light can change the energetic level of electrons as illustrated in Figure 3, IR and micro-waves radiation might respectively change the vibrational and rotational levels of molecules, gamma rays can change the energetic level of atom nuclei, etc. and these properties further lead to the development of spectroscopic methods [27] [28].

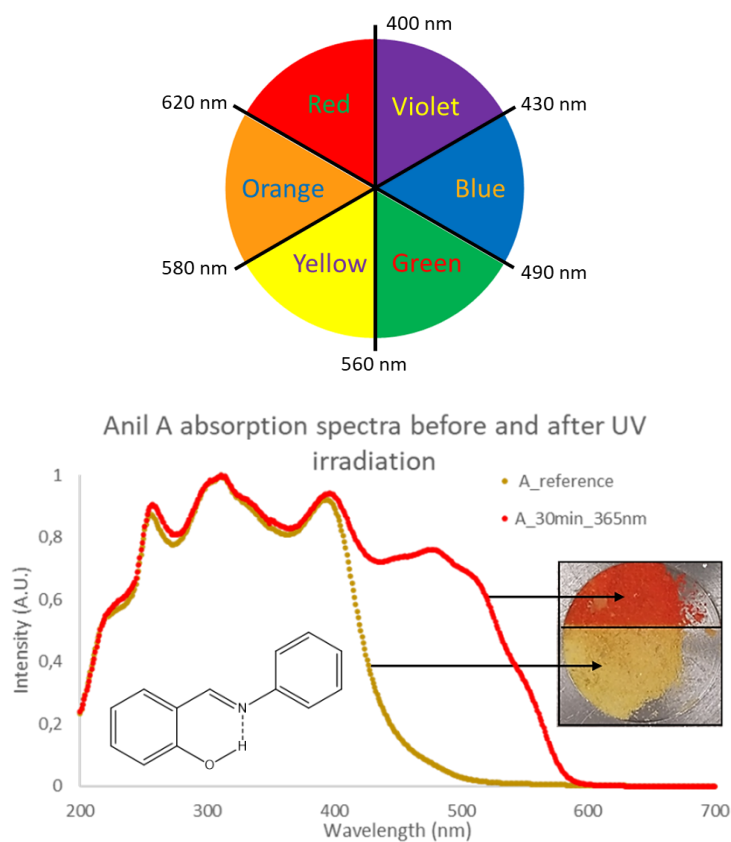


Figure 2: (top) complementary color disk (adapted from [27]) - the observed color of a compound is the one opposed to the color it absorbs (numbers represent the value of limit wavelengths in nm); (bottom) the absorption spectra of anil **A** (structure shown below the curves) before irradiation (yellow curve) and after UV-irradiation (red curve) and the corresponding picture of irradiated and non-irradiated powders.

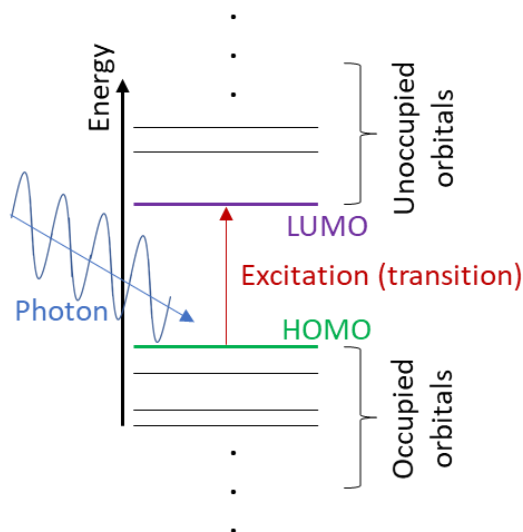


Figure 3: simplified general representation of electronic transitions in the case of atoms/simple molecules (adapted from [27]). A transition can occur between an occupied orbital (here the HOMO – Highest Occupied Molecular Orbital) and an unoccupied orbital (here the LUMO – Lowest Unoccupied Molecular Orbital) if the energy of incident photon corresponds to the energy difference between the two orbitals [27] [28].

As UV and visible light absorption leads to electronic transitions in the atom/molecule, it is these electronic transitions which account for the colors we perceive. It's interesting to notice we include UV radiations but not IR for instance in this discussion. This stems from a simple fact: as the compound absorbs energy, the changes generated through this absorption can only occur at an energy lower or equal to the incident light and thus at higher wavelengths according to Einstein formula. As a result, the absorption of UV light can generate a change in the visible region of the electromagnetic spectrum while the absorption of higher wavelength radiations (such as IR, Micro-wave, ...) will generate change(s) above the visible region and thus won't affect the color of the compounds, unless it generates chemical reaction (for instance the degradation of chocolate by micro-wave heating which easily occurs while preparing dessert). For a similar reason, x-rays and gamma rays are not taken into account as they are too energetic and generate ionization/nuclear degradation and further reactions. In that case, the resulting color is not linked to the studied compound but to the newly formed one.

### **I.3. Chromism and Photochromism**

As colors can be related to electronic energy levels of compounds, changing the electron distribution in a compound (e.g., through molecular rearrangement or chemical reaction) can change its color. The species involved in such a photochemical reaction may have different absorption spectra (different colors). In that case, and if the photochemical reaction is reversible, we get a photochromic system. Photochromism is a reversible color change of a system triggered by light [29]. It was discovered at the end of 19<sup>th</sup> century and the label “photochromism” is used since 1950 [30]. Photochromic compounds can be useful in many industrial applications such as intelligent screens [31], secured inks (for banknotes, stamps and official papers) [32] [33], photochromic lenses for optical devices or glasses [34] [2] [35] and ultimately for optical data storage [36] [37].

Besides light, other stimuli can also be used to induce reversible color changes such as heat (thermochromism), solvation (solvatochromism), pressure (piezochromism) etc. [1]. A wide variety of mechanisms/reactions might lead to a color change. This is also true for photochromism itself as it can occur in many different states: in solution, in the liquid state, in the amorphous and crystalline solid-state state [3] [4]. This last one is of great interest as the local environment of the molecule of interest is constant which is important in order to study the structure-activity relationship of the material. The most common mechanisms that can lead to photochromism in the solid (and crystalline) state are the keto-enol equilibrium (which can be observed in anils), the cis-trans isomerization (present in stilbenes and anils), the ring opening – ring closure (in spiroopyrans) and inter- or intra-molecular proton transfer [1] [38]. This above list of mechanisms (and compounds that can exhibit them) is non-exhaustive but already gives a good overview. The mechanism involved in anils is detailed below along with some of the other mechanisms and compounds in order to highlight some general trends.

#### **I.3.a. Photochromism in anils**

Anils or *N*-Salicylideneaniline derivatives are substituted aromatic compounds which belong to the group of Schiff bases because they contain an azomethine moiety (a carbon-nitrogen double bond). Furthermore, they also contain an alcohol moiety which is located in the ortho position of the azomethine bridge (Figure 4 – left). This hydroxy moiety can undergo a

thermal keto-enol equilibrium as presented in Figure 4 and both states (keto and enol) are usually present at room temperature [39]. Some of the derivatives (including *N*-Salicylideneaniline itself) can switch (either from the enol or *cis*-keto form) to a *trans*-keto form as presented in Figure 4 [40]. This phenomenon can occur in the crystalline state where it mostly takes place on the surface of the crystal (even though some part of the bulk can also react) and the general conversion is also quite low – a conversion of only about 5% has been reported in the case of the anils [41].

*N*-Salicylideneaniline exhibits two main absorption bands at room temperature: an intense one around 340 nm and a weaker one around 440 nm. This last band is not present when the compound is dissolved in hydrocarbon solvents at room temperature but is comparable to the *cis*-keto form band when dissolved in methanol [42]. When the temperature decreases, the intensity of the first band increases while it decreases for the second one. The presence of an isosbestic point at 375nm clearly indicates there is a thermal equilibrium between the enol and *cis*-keto forms in the solid state [42]. After irradiation at 365 or 436 nm at room temperature, another band appears at around 570-600 nm and the compounds color switches to red. Once this color is reached, it slowly reverts to its original color (through thermal equilibrium) if left into the dark, or it can also be re-switched directly if irradiated at 560 nm [42].

The lowest energy state of the process is the *trans*-enol form (usually labeled “enol”) and is colorless (and thus appears white) while the *cis*-keto form usually exhibits a deep yellow to orange coloration and the *trans*-keto form is red. Due to these equilibria, some anils derivatives can exhibit thermochromism, photochromism or both properties.

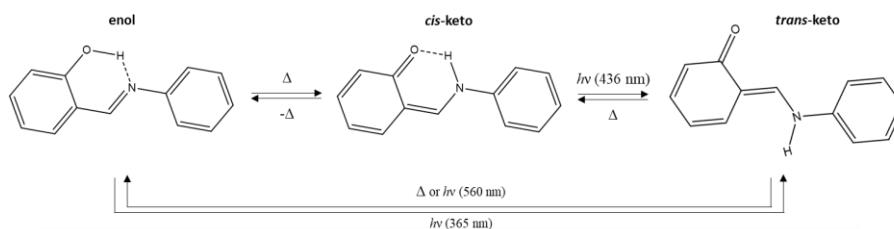


Figure 4: summary of photo- and thermo-induced transitions in *N*-Salicylideneaniline (adapted from [40]).

In a simplified overview, the mechanism is that UV irradiation of the enol form leads to an excited enol\* form which can then tautomerize to the excited *cis*-keto\* form. This last either relaxes to the enol form in a radiative way or undergoes a photo-isomerization to produce the excited *trans*-keto\* form. This latter relaxes in non-radiative way to the *trans*-keto form. This *trans*-keto form is metastable and thermally decays towards the *cis*-keto or enol forms as presented in Figure 5. [40].

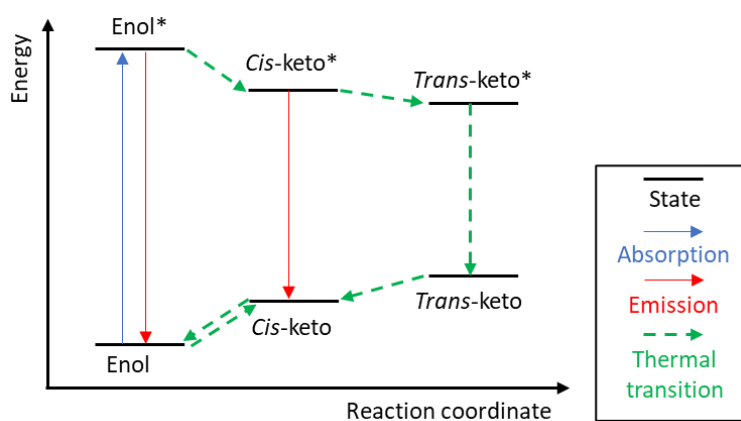


Figure 5: general mechanism of photo- and thermo-induced transitions in anils (adapted from [40]).

The above presented mechanism is, however, too simple and doesn't draw an exact view of the process as a more complex mechanism based on quantum simulations and ultrafast time resolved experiments (both in gas phase and in solution) has been reported in literature [43] [44]. It is accepted that light irradiation of the enol form leads to an excited enol form (enol\*) which can undergo an excited state intramolecular proton transfer (ESIPT) yielding a fluorescent excited state (*cis*-keto\*) [44]. This state can further lead to both the *cis*-keto ground state by radiative decay or the *trans*-keto form through non-radiative decay [43]. The enol\* can in parallel also deactivate through a rotational isomerization reaction, leading to *twisted*-enol isomer [43] [44] as presented in Figure 6.

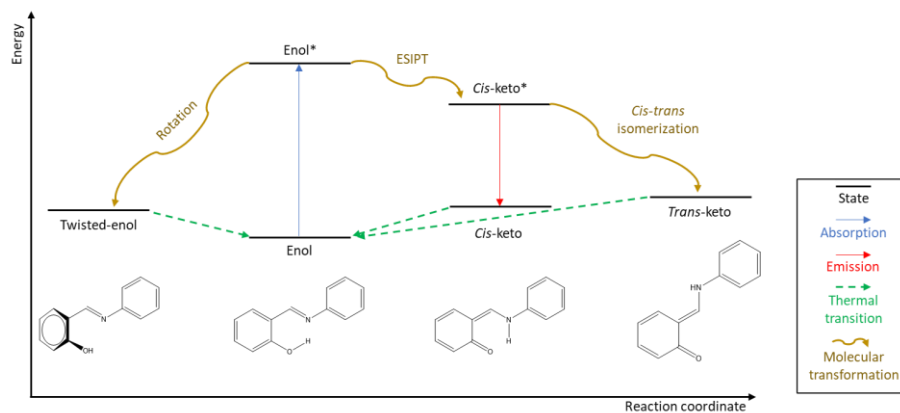


Figure 6: reported mechanism for photo-induced transformations of *N*-Salicylideneaniline and corresponding molecular products (adapted from [43] and [44]).

Photochromism and thermochromism were thought to be mutually exclusive properties in the case of anils, however recent studies based on Diffuse Reflectance Spectroscopy (the measure of UV-visible absorption spectrum of a compound in the solid state) at various temperatures and after excitation found some photochromic anils to also be thermochromic [42]. New insights about this fact have been found during this work and are presented in chapter 3 of the present thesis.

### 1.3.b. Other photochromic materials

Anils are not the only compounds that can undergo a reversible cis-trans isomerization. As a matter of fact, any alkene which has different substituents on each side may be photo-isomerisable following the general scheme presented in Figure 7. As this isomerization is reversible (either photo- or thermally-induced) it might lead to photochromism if the isomers exhibit different absorption bands in the visible region of the spectrum. As a result, many alkene derivatives are able to undergo such photo-isomerization. Known examples of this are stilbene and its derivatives and in a similar fashion azobenzene and its derivatives, as presented in Figure 8.

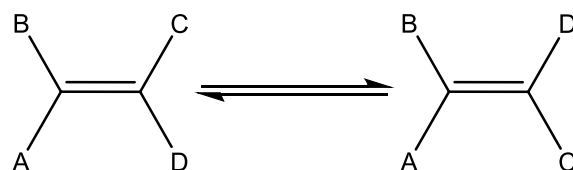


Figure 7: general alkene scheme. If substituents are such that  $A \neq B$  and  $C \neq D$  then the two isomers have different chemical and physical properties and such a system may be photochromic.

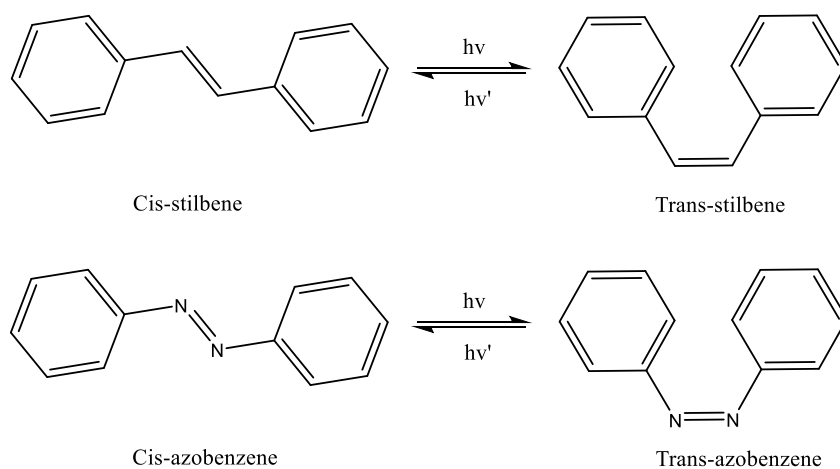


Figure 8: (top) photo-isomerization of stilbene; (bottom) photo-isomerization of azobenzene.

As already discussed, the above presented cis-trans isomerization of a double bond is not the only mechanism that can lead to photochromism. For instance, the ring-opening/ ring-closure, which occurs in spirocyan derivatives and fulgides (as presented in Figure 9), is another known mechanism [45].

Beside the above presented mechanisms, any mechanism which leads to an equilibrium between two (or more) species might lead to photochromism if at least one of the transitions can be triggered by light and if at least one of the species involved presents an absorption band in the UV-visible region of the electromagnetic spectrum.

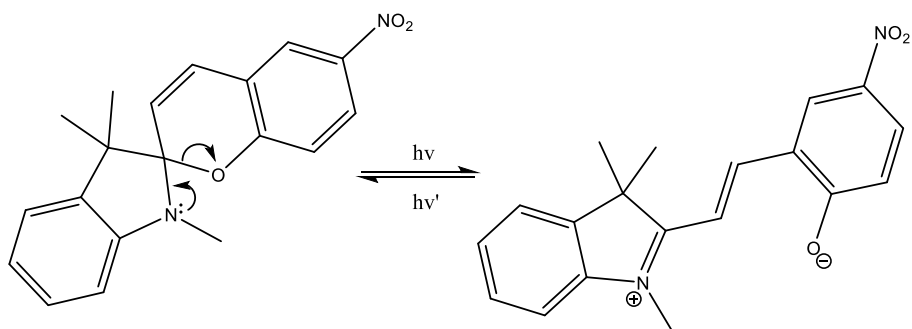
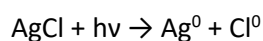


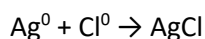
Figure 9: mechanism of the ring opening (triggered by light) of spiropyran derivatives. The ring closure mechanism is the corresponding backwards mechanism [45].

For instance, the photolytic decomposition of silver halide salts followed by the formation of silver colloids leads to a strong darkening of the salts. Because of its reversibility, it is a typical photochromic system and it is used in industrial applications such as photochromic glasses [2] and lenses [35]. Even though the mechanism differs from what is observed in the anils, it is also simpler and deserves to be presented here to fully illustrate the interest of photochromic systems.

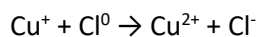
In the crystalline structure, halide ions can absorb UV-light and emit an electron which in turn can be transferred to a silver cation to form a silver atom following the reaction:



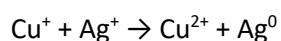
However, the thermal back reaction:



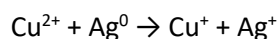
is extremely fast, which is a problem because the total reaction does not last enough to produce a darkening of the glass. As the darkening is still observed, another mechanism takes place: if neutral atoms are quickly moved apart, they can stay longer in this state. Inside the lattice it is extremely unlikely that atoms move fast enough, but due to the presence of impurities such as  $\text{Cu}^+$ , another reaction can take place (instead of the thermal back reaction):



This is equivalent to moving the neutral chlorine atom away from the silver atom. The global reaction thus occurring within the salt is:



The silver atom can now move on the surface or within the crystalline defects and aggregates with other silver atoms, hence producing a locally high concentration of neutral silver atoms (colloid) and a darkening effect as presented in Figure 10 [2] [35]. In order to produce a fading of the darkened color,  $\text{Cu}^{2+}$  cations need to move very close to silver atoms to allow the opposite reaction:



However, due to their double positive charges, copper cations cannot move very fast within the crystal lattice, hence explaining why the darkening effect is faster than the fading effect, resulting in a global and observable color change of the crystallite (and of the material containing this crystallite). It is worth to note that silver halide crystallites should be small enough to not diffract visible light and leave the lenses/glass transparent [2].

The above presented mechanism does not relate directly to what has been done within this thesis. However, it enlightens many important aspects of the photochromic systems: color change induced by UV-visible light, the reversibility of the process and how fast this reversibility occurs – which is a critical point for further applications. For this reason, photochromic studies are often accompanied by kinetic studies of the thermal back reaction. Kinetic aspects for photochromic anils (and anils cocrystals) were thus studied in chapters 3 and 5 of the present thesis.

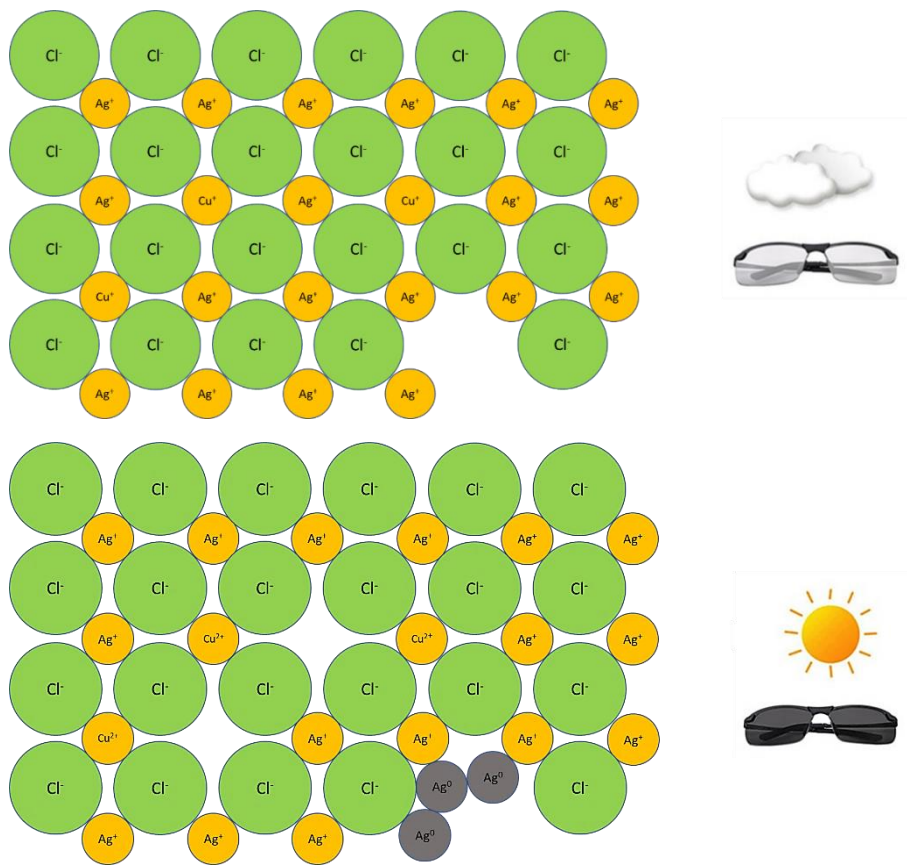


Figure 10: (top) A realistic crystallite of silver chloride with some impurities ( $\text{Cu}^+$ ) and defects; (bottom) the same crystallite after UV irradiation: a locally high concentration of neutral silver atoms may occurs generating a darkening of the material, leaving some vacancies and  $\text{Cu}^{2+}$  in cation sites [2].

#### **I.4. Crystal engineering**

Polymorphs of a photochromic anil are not necessarily photochromic themselves [46], hence the nature of the solid state strongly impacts photochromism, which is why we decided to use crystal engineering principles to alter the photochromic property of a target anil.

Historically crystals were known as natural solids with a well-defined geometric appearance [47] and the general definition in chemistry describes them as highly ordered microscopic arrangements of the solid constituents (atoms, ions or molecules) which may also present a well-defined geometric appearance [48]. A recent crystallographic definition relates the definition of a crystal to the observation of a discrete X-ray diffraction pattern and thus the periodic arrangement of constituents is no longer a requirement to define a solid as crystalline. This last definition is very large and includes many recently discovered forms such as quasi-crystals, aperiodic crystals, etc. [49].

Crystal engineering is defined as “the understanding of intermolecular interactions in the context of crystal packing and the utilization of such understanding in the design of new solids with desired physical and chemical properties” [50]. The purpose is to design new crystal structures while using molecule(s) of interest as building blocks. In the context of the present thesis our purpose is to synthesize new photochromic cocrystals using anils as building blocks combining them with a second component in the crystal lattice.

Even though supramolecular interactions are not very strong compared to covalent bonds (this is detailed in the next section) they play a key role to form a stable structure thanks to the fact that they are very numerous. This is known as the “Gulliver effect” [51].

One major issue encountered in crystal engineering is the relatively low predictability of a crystal structure based on molecular structures and properties despite an important increase in IT resources and performances. This is especially true when some features such as molecular flexibility are encountered [52]. An illustration of this issue is the case of acetic acid which is found in solution as a dimer but as an infinite catemer in its crystal structure [51]. The most likely explanation is that the dimer can form very

quickly due to a strong double H-bond feature but is unable to grow further (because only very weak interactions are available between dimers) while the monomer unit of the catemer is maybe less stabilized but has strong H-bond interactions available, which provide a pathway for crystal growth as presented in Figure 11 [51].

The above presented case of acetic acid illustrates that the strongest available intermolecular interactions do not systematically lead to crystal growth. Such counter-intuitive results imply a series of difficulties when performing crystal structure predictions based on a functional group approach [50]. In order to face this challenge, the definition of new representative kinetic units called supramolecular synthons (a few examples are given in Figure 12) has become increasingly popular. Supramolecular synthons are “structural units within supermolecules, which can be formed and/or assembled by known or conceivable synthon operations involving intermolecular interaction” [53]. The interpretation of this concept in the field of crystal construction is the following: “a synthon is a probabilistic event” which means the more probable a synthon is, the more often it will be present in a crystal of molecule containing the requisite functional groups [50]. Synthons are representative of the entire crystal structure in the ideal case but as discontinuity can always occur in the building process (due to competition between different synthons) this statement is not universal [51].

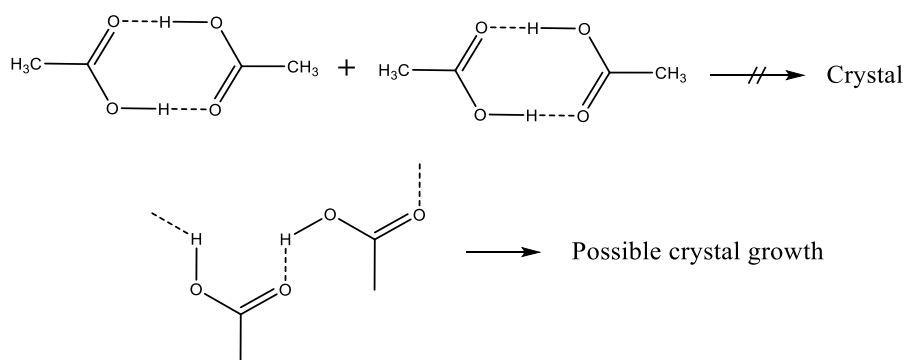


Figure 11: (top) supramolecular interaction between dimers are not strong enough to lead to crystal. (bottom) one dimensional growth is allowed due to available H-bonds [50].

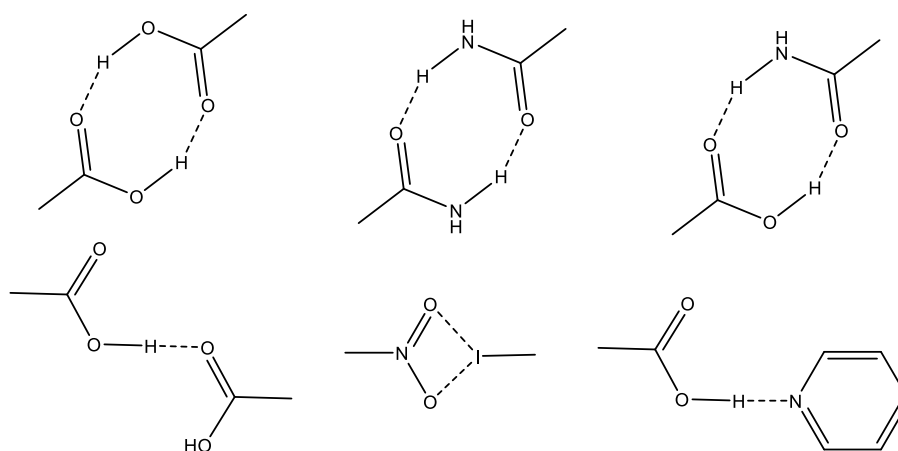


Figure 12: Some common supramolecular synthons [50] [51] [53].

Starting from a viewpoint, where crystals are constructed of synthons, one needs to determine which synthons may form or not. This means that a careful analysis of all possible intermolecular interactions is required. However, as presented above, the idea of fully describing synthons with a set of specific interactions is not fully accurate [50]. Association between molecules should be described in the limit of n-body interaction to be more accurate and then merged into the domain of “close-packing”: close-packing principle states that “molecules pack in a crystal so that any reference molecule is surrounded by a maximum number of close neighbors” and come from the model describing all crystals as the result of the most efficient utilization of space of his molecules [51].

Crystallization is a kinetic phenomenon so crystal structures are built with strong and/or directionally specific interactions with a tendency for the most directional interaction to form first. Directionality is the second important property of an intermolecular interaction and is very important in crystal design strategy as it can be exploited to create a specific molecular orientation [51].

Directional interactions are usually the most long-ranged and this implies they are the first interactions which are able to form in solution which means it’s a kinetical driving force [50]. The knowledge of these simple principles leads to the strategy of describing crystals as networks where molecules are nodes and interactions are nodes’ connections. Because the

formation and the breakage of both covalent and supramolecular bonds are governed by kinetics, it's possible to use an approach equivalent to (inorganic) retrosynthesis for crystals [50].

In order to provide a basis for future works, it's important to realize an as exhaustive as possible list of supramolecular interactions, to determine their strength and to look at the "robustness" of synthons. A robust synthon is "one which appears in a large number of cases wherein a particular set of molecular functionalities is present" [50]. To define this concept more precisely, if molecules have a set of functionalities ( $M_1, M_2, M_3, \dots, M_n$ ), then the synthon  $M_i$ - $M_j$  is robust if it appears in all molecules, irrespective to their other functionalities. In other words, the presence of  $M_i$  and  $M_j$  ensures the presence of the synthon  $M_i$ - $M_j$  [50].

#### **1.4.a. Hydrogen bonds**

The first supramolecular interactions to be considered are hydrogen bonds because they are both strong (ranging from 1 to 4 kcal.mol<sup>-1</sup> for the weak ones and from 4 to 20 kcal.mol<sup>-1</sup> for the strong ones - and they could be even stronger) and directional. As a result, they are highly relevant to understand the packing of crystal structures [50]. The interaction between a hydrogen bond donor (labelled X-H) and a hydrogen bond acceptor (labelled Y-Z) is usually noted X-H...Y-Z. A hydrogen bond tends to lower the distance between element X and Y: the length of the hydrogen bond is usually lower than the sum of the van der Waals radii of involved atoms. For instance, the distance between oxygen and nitrogen in the hydrogen bond of an amide (N-H...O=C) is around 2.7-2.8 Å while the sum of their van der Waals radii is 3.1 Å [50]. There is also a special type of moderately strong hydrogen bonds occurring between two (or more) hydrogen atoms with one of them having a hydridic character and thus act as a proton acceptor [54]. Evidences of such specific interactions were advanced by Brown et al. in the case of amine-boranes [55] and they were later called dihydrogen bonds by Crabtree and al. [56]. These dihydrogen bonds usually range from 3 to 7 kcal.mol<sup>-1</sup> and thus can have a high impact on the crystalline structure and the properties of the compound [54]. However, the hydridic character of the hydrogen atom is usually found in boranes and metal-organic compounds, which are not used within this thesis and thus dihydrogen bonds won't be discussed further here as they are out of the scope of the present work.

In order to build a cocrystal structure, the cofomers used need to have a geometrical complementarity with the parent molecule [57]. As a result, directionality is a criterion of importance for supramolecular interactions and so are the angular properties of hydrogen bonds. Hydrogen bonds usually tend to be linear for the strong ones while the weak ones (C-H...O, O-H... $\pi$ ) have a higher tendency to bend. Very weak ones such as C-H... $\pi$  can have non-specific properties both with regard to length and to angle properties [50].

Because organic molecules often have many functional groups, other types of hydrogen bonding like *bifurcated hydrogen bonds* (three centered interaction) and *multifurcated hydrogen bonds* (multi-centered interaction) do exist and they are even common in organic crystals [50].

#### **1.4.b. Halogen bonds**

The second most important supramolecular interactions are the halogen bonds which are able to form relatively strong non-covalent bonds and with high directionality [58]. The ability of covalently bond halogen atoms to attract negatively charged sites is due to an anisotropic charge density distribution [59]. For instance, an Iodine atom covalently bound to carbon is polarized positively in its polar region (the furthest away from the carbon) and negatively in its equatorial region and this way, is able to make electrostatic contacts as shown in Figure 13 [50].

Typical energy values for this kind of interaction are ranging from 1 to 20 kcal.mol<sup>-1</sup>. Halogen bonds can be symmetrical (contact between two halogen atoms) or un-symmetrical (one halogen and a different type of atom). Geometry and orientation encountered in halogen bonds are more variable, because here a single atom has two different regions that are able to interact. As a result, a halogen bond can be linear or present an angle of around 90° [50]. Other geometries are possible according to circumstances and some examples are given in Figure 13.

According to literature, halogen bonds like I...N, I...O and Br...O are well known (since the 1960s at least) with the work of Odd Hassel on polarized interaction Br <sup>$\delta^+$</sup> ...O <sup>$\delta^-$</sup>  in a dioxane-bromine complex (Figure 14). The geometry of halogen bonds in dioxane-bromine complexes is neither linear

nor with a 90° angle because polarization of Br in Br<sub>2</sub> differs from C-Br polarization [50].

Studies about halogen bonds tend to focus much more on heavier halogens (iodine, bromine and chlorine) because fluorine is usually considered as a poor halogen bond donor due to its non-polarizability. However, it has been suggested that this non-polarizability can be modified by the presence of other functional groups on the molecule and thus fluorine bonds can also be used in crystal growth and design [59]. This last result is of high interest as some fluorinated anils were selected within this thesis along with a few fluorinated cofomers as presented in Figure 15.

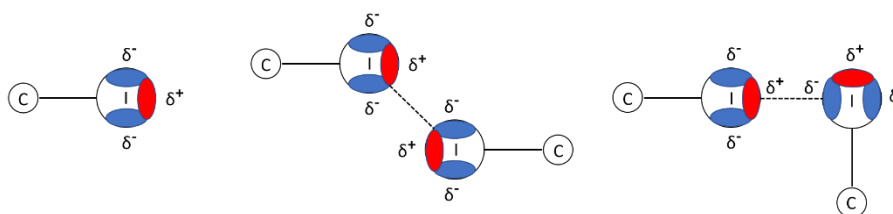


Figure 13: (left) density charge distribution over an iodine atom covalently bonded to a carbon atom, with positively charged region highlighted in red and negatively charged region highlighted in blue; (middle and right) two possible geometries of halogen bonds arising from the anisotropic charge density: type I and II depending of the bond angles (in type I both bond angles are similar while in type II one angle is near linear and the second close to 90°). Adapted from [50].

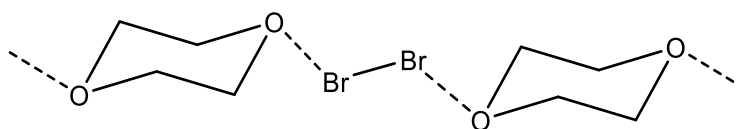


Figure 14: dioxane-bromine complex with halogen bonds [50].

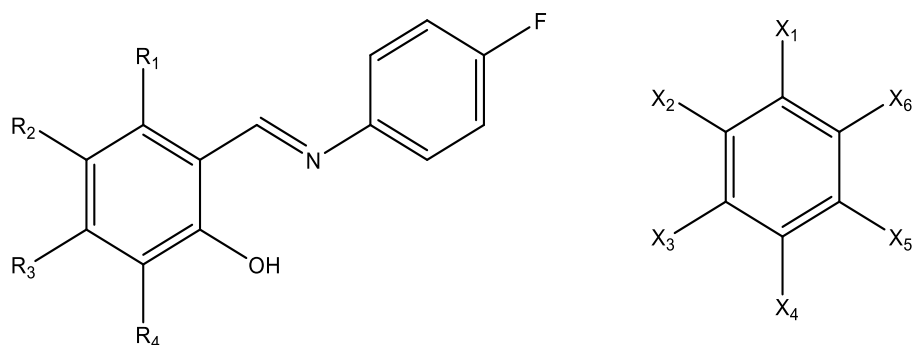


Figure 15: (left) common skeleton to fluorinated anils selected within this thesis (with  $R_1$  to  $R_4$  being functional groups); (right) skeleton common to benzene halides used as cofomers within this thesis (with  $X_1$  to  $X_6$  being either fluorine or iodine atoms).

#### I.4.c. Other important intermolecular interactions

Polarization can also occur in atoms like sulfur and leads to the formation of short directional contacts such as:  $S^{\delta+} \cdots N^{\delta-}$ ,  $S^{\delta+} \cdots S^{\delta-}$  and  $S^{\delta+} \cdots Cl^{\delta-}$ . Intermolecular contacts of other chalcogen atoms (such as Se [60] and Te [61]), pnicogens [62] as well as metalloids (like Bi) are also reported [61].

Metals have also been examined as design element for crystal engineering but their primary interaction (coordination of negatively charged ligands) does not strictly belong to supramolecular interactions. However, halogen atoms linked to metal atoms can act as powerful hydrogen bond acceptors [50].

Because they have different effects on the crystal packing, interactions between ions can be separated into two different categories: small inorganic ions and large organic ions. Large polarizable organic ions are similar to neutral molecules whereas small inorganic ions can show a considerable effect in directing crystal packing (ions like ammonium or carboxylate, sulfonate, etc., are often used because of their strong charge-assisted interaction) [50].

To summarize the above discussion: supramolecular interaction energies range from 1 to 20 kcal.mol<sup>-1</sup> and can be considered as the glue that links molecules together to form a crystal structure which is the (often best) compromise between these interactions. Among them, hydrogen bonds are the most significant anisotropic interactions which thus are the easiest to use in order to modify the crystalline structure [50].

As a result, most of the coformers used in the work of the present thesis are able to form strong hydrogen bonds as presented in chapter 2. Later, coformers able to provide halogen bonds were also added as presented in chapter 3.

#### **I.4.d. Hirshfeld surfaces**

Above we discussed the nature and strength of intermolecular interactions and how they can impact the growth of a crystal. Once the crystal is formed, there are many more intermolecular interactions than the crystallization driving ones, and the weakest of them can now play a major role through a “Gulliver effect” over the packing and final properties of the material [50].

From this statement, there is a need to quantify the entirety of the interactions which affect the molecule in the crystal instead of focusing on a few which are assumed to be of importance. This issue can be tackled with the use of Hirshfeld surfaces [63]. A Hirshfeld surface is an isosurface which surrounds the molecule of interest and delineates the space occupied by the molecule within the crystal [64]. More precisely, it is defined as  $0.5w(\mathbf{r})$  where  $w(\mathbf{r})$  is the “weight function” i.e., the function corresponding to the sum of spherical electron densities of atoms in the molecule of interest divided by the same sum for atoms in the crystal. Corresponding equations write [63]:

$$w(\mathbf{r}) = \frac{\rho_{promolecule}(\mathbf{r})}{\rho_{procrystal}(\mathbf{r})} = \frac{\sum_{A \in molecule} \rho_A(\mathbf{r})}{\sum_{A \in crystal} \rho_A(\mathbf{r})}$$

The consequence of this equation is that within the Hirshfeld surface the electron density of the molecule dominates the electron density from the crystal. Going away from the molecule (increasing  $\mathbf{r}$ ) reduces progressively

its contribution and progressively increases the contribution of outside atoms (crystal) until it comes arbitrarily close to 0 [63].

Beside this, another approach allows taking into account the relative size of the atoms by considering a normalized contact distance ( $d_{norm}$ ) such as:

$$d_{norm} = \frac{d_i - r_i^{vdW}}{r_i^{vdW}} + \frac{d_e - r_e^{vdW}}{r_e^{vdW}}$$

With  $r^{vdW}$  the Van der Waals radius of the corresponding atom [63].

From this equation we see that an intermolecular contact shorter than the Van der Waals radius of the corresponding atom will lead to a negative  $d_{norm}$  while contacts longer than Van der Waals radius will give a positive value. Negative, null and positive  $d_{norm}$  values respectively colored in red, white and blue can be added to Hirshfeld surface and allows a quick visual analysis of the short contacts. A typical example is given in Figure 16 with anil **N** (studied further in chapter 3). The generation of the Hirshfeld surface allows to quickly discover the strong short contacts and which moieties of the molecule are involved, thanks to the visual observation of red spots on the surface. As a result, the structural analysis of crystallized structures is facilitated: for instance, we can directly observe (from Figure 16) strong short contacts involving the fluorine atom, one of the oxygen atoms and one of the hydrogen atoms. These pieces of information will allow to establish easier links between the solid-state structure and the observed properties of the studied compounds. Such analyses were performed during the present work and are presented in chapter 3.

On the Hirshfeld surface, two distances can be defined: the internal distance  $d_i$  (corresponding to the distance between the surface and closest atom of the molecule) and the external distance  $d_e$  (corresponding to the distance between the surface and closest atom of the crystal). Knowing these distances for each point of the surface allows to study the intermolecular interactions. Furthermore, a plot of  $d_i$  versus  $d_e$  gives a two-dimensional summary of the intermolecular interactions of the molecule and can be seen as a fingerprint of it [63]. The fingerprint of anil **N** is given in Figure 17-left. These fingerprints allow to study further specific aspects of the intermolecular interactions. For instance, we observed strong short contacts involving the fluorine atom in Figure 16 and using fingerprint analysis we can

deduce it is mostly F...H interactions (Figure 17-right) while in another analysis we observe no F...F interactions and very few F...C interactions. As a result, fingerprint analysis of the Hirshfeld surface allows a deeper comprehension of the studied interactions. These fingerprint analyses were also used within this work and a few of them are presented in chapter 3.

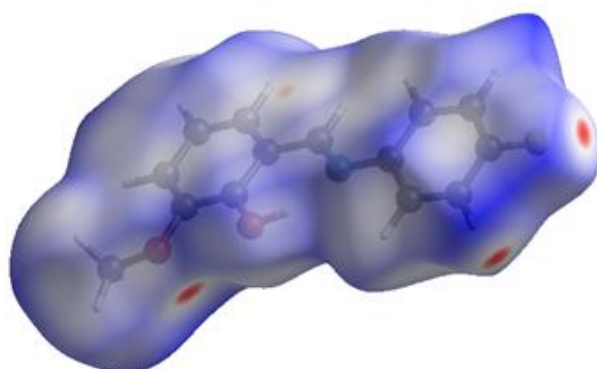


Figure 16: Hirshfeld surface of anil **N** (anil **N** in chapter 3 – shown inside the surface) mapped with  $d_{\text{norm}}$  property. Close short contacts appear red.

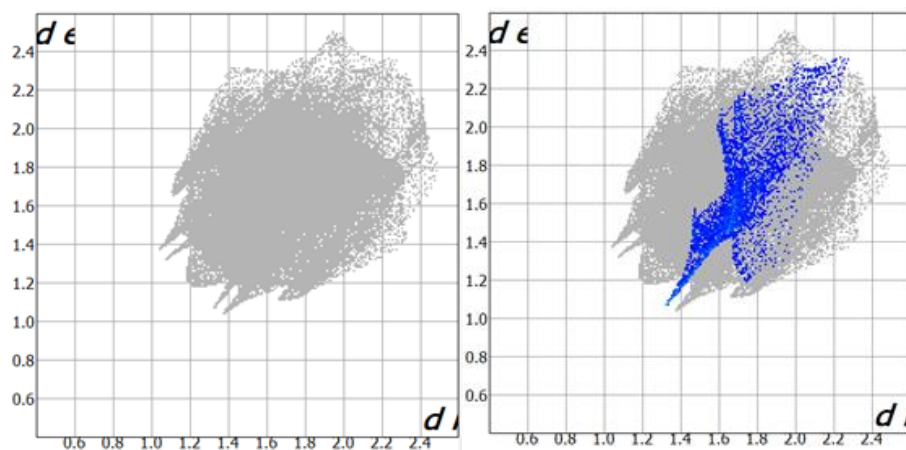


Figure 17: (left) Intermolecular interactions fingerprint for anil **N** (grey points); (right) Intermolecular interactions fingerprint for anil **N** with enlightened F...H interactions (blue points).

### **I.5. Solid-solutions**

Among multi-component crystals there is a specific category where crystal components have a range of composition but form a unique crystalline structure. In these specific crystals, any crystal component can be replaced by another one without changing the structure. Such systems are called “solid-solution”. According to IUPAC dictionary, a solid-solution is “a solid in which components are compatible and form a unique phase” [65]. Solid-solutions are also labelled “mixed crystals” and were first described by Roozeboom in 1899 [66].

Solid-solutions are very common for inorganic materials such as alloys and they usually crystallize in a structure close to the major constituent [67]. In organic materials, solid-solutions can occur when the constituents of a multi-component system are geometrically similar. As a result, there are many examples including enantiomers or molecules with one atom substituted by another such as carbon by nitrogen in aromatic compounds or chlorine by bromine, hydrogen by fluorine etc. [50] [68].

Solid-solutions can exhibit specific properties regarding their nature compared to their pure constituents alone. Because the structure is slightly modified through the varying ratio of constituents, structurally dependent properties can be impacted and fine-tuned through formation of solid-solutions [69].

Before going further, it is important to notice there are different possible types of solid-solutions which thus may have a significant impact on the studied properties. At first Roozeboom described three types according to their binary diagrams as presented in Figure 18 [66]. Type II and III are similar to the binary diagrams exhibited by the azeotropic mixtures. Type I represent the ideal case where components are perfectly compatible and no specific interaction is present. In type II and III however, the interactions between the two compounds are respectively slightly stronger and slightly weaker than within pure components leading to respectively an upwards and a downwards deviation of the melting curves. Also, in both cases there is a temperature area where a mixture of solid and liquid phase is observed (in between the curves). If strong interactions arise (stronger than Van der Waals interactions), the system may more likely form a new phase with a definite stoichiometry (a cocrystal) instead of a solid-solution. The bottom curves correspond to the solidus ones (below the solidus line the entire

material is solid) and the upper curves are the liquidus ones (above the liquidus line there is only a liquid phase present).

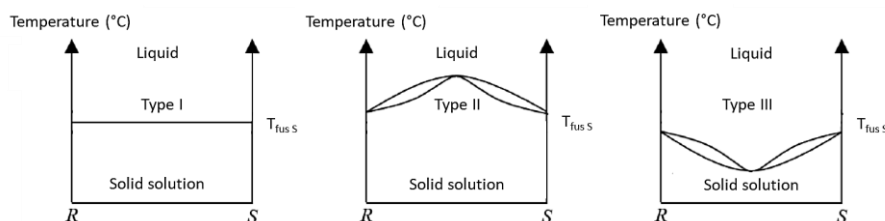


Figure 18: the different types of solid-solution in the case of an enantiomeric system (adapted from [66]). Left: ideal case with no specific interaction; middle: stabilizing interactions arise between the two components; right: destabilizing interactions arise between the two components. The solid solution phase is present under the liquidus/solidus line/curves.

Beside the complete solid-solution exists also partial solid-solutions i.e., a solid-solution for which the miscibility domain does not cover all possible ratios but only a certain range. In that case, the diagram presents a eutectic line instead of a single point (an eutectic is defined as a homogeneous mixture which melts at a lower temperature than its separated components [70]). A few examples of this have been reported in literature [71] and, for instance, a typical symmetrical binary diagram for such system is presented in Figure 19. These diagrams are constructed through precise DSC measurements of the eutectics and liquidus points for many different molar ratios of the constituents. When the limit of solid-solution domain is not directly observable due to lack or poor experimental data, it can still be calculated using Tammann's method: the eutectic enthalpy is plotted versus the molar ratio and the intersection of the linear regression with the x-axis gives the limit molar ratio [72]. This method has been used in chapter 5 in order to construct the binary diagram of anils **A** and **B** solid-solution system and is further described in section 1.6.c. of the present chapter.

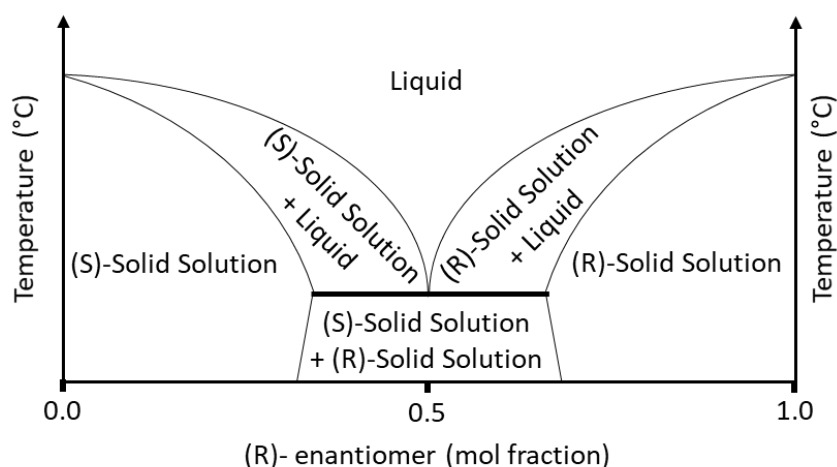


Figure 19: a partial solid-solution system exhibiting a typical symmetrical binary diagram – a feature which may appear in enantiomeric systems (adapted from [71]).

However, most of the systems mentioned above with their respective diagrams, including the original description of a solid-solution by Roozeboom, concern symmetrical systems (e.g., racemates) while solid-solutions can also occur with other type of compounds, usually ones with a similar geometry but with one atom changed between the molecules of the system as mentioned above. For such system the equivalent non-symmetrical diagrams also exist, especially if there is a large difference between the melting temperature of the parent compounds.

The above presented systems are among the simplest ones in terms of their behavior and corresponding binary diagrams, and other more complex situations can arise such as the so-called “secondary solid-solution system” where a new phase is formed for specific molar ratios of the compounds typically in the middle of the diagram which forms a solid-solution in a given range (as extremal solid-solutions do on the extremes of the diagram). A typical diagram of such system is presented in Figure 20 [73].

The interest of the last system is the apparition of a completely new phase which is not structurally related to the pure components and which also exists for a specific range of molar ratios. Within this range, the properties of this new phase can be fine-tuned.

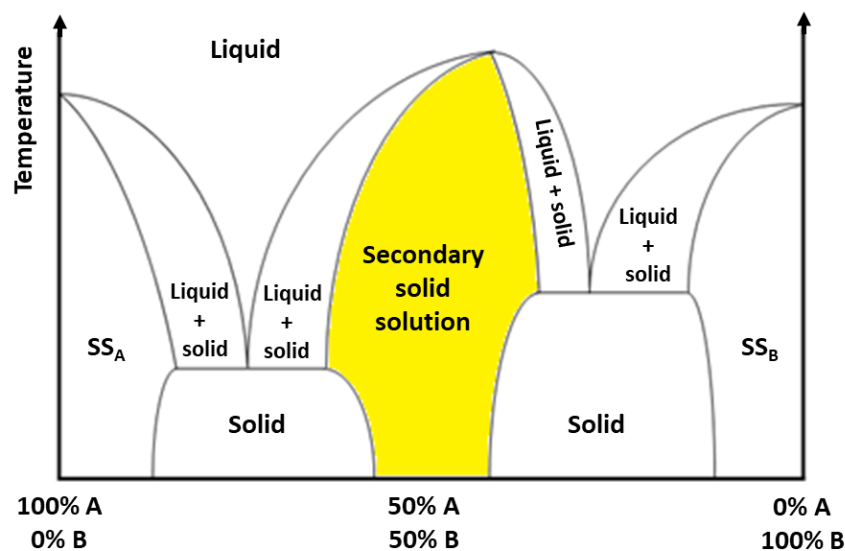


Figure 20: a typical binary diagram for a secondary solid-solution system. The new solid-solution is colored in yellow.  $SS_A$  and  $SS_B$  are the normal extremal solid-solutions (adapted from [73]).

Furthermore, in partial and secondary solid-solution systems, it is possible that one of the parent compounds does exhibit a property of interest and not the other meaning at least one of the extremal solid-solutions of such a system should be tunable through variation of the molar ratio.

As a result, the formation of a solid-solution could provide a way to improve photochemical properties of anils and this approach has already been partially explored by Cohen et al. in 1968 [74] and more recently by Uekusa et al. in 2018 [67]. However, both these studies mainly focused on finding photochromic solid-solutions and they both presented only one specific ratio of constituent for which photochromism could be visually observed. Thus, they lacked in-deep analysis of this property as no information about the evolution of photochromic intensity was reported along with structural evolution of the system. Thus, we decided to focus on such a system to study further the impact of solid-solution systems in the case of anils and the results are presented in chapter 5.

## **I.6. Methods for solid-state analysis**

In order to study the properties of a compound it is a necessity to use adapted methods to get proper qualitative and quantitative information. As this thesis focuses on the solid-state (and more specifically on the crystalline state) the present section will cover all relevant solid-state analytical tools used within this project: Thermo Gravimetric Analysis (TGA); Differential Scanning Calorimetry (DSC); Single-Crystal X-Ray Diffraction (SC-XRD); X-Ray Powder Diffraction (XRPD); Diffuse Reflectance Spectroscopy (DRS). This section will also quickly cover other interesting methods which are (or could be) of interest in this field such as Infra-Red spectroscopy (IR) and Raman spectroscopy and TeraHertz Spectroscopy (THz). For the sake of the clarity, techniques are gathered into three sections: thermal analysis (TGA and DSC); diffraction techniques (SC-XRD and XRPD) and spectroscopic methods (DSC, IR, Raman, THz).

Of course, many other techniques can/could be used in order to get other complementary information such as (non-exhaustive list): Solid-State Nuclear Magnetic Resonance (SS-NMR) or Fluorimetry, but the project here did not require them and thus they are not discussed further in the present thesis.

### **I.6.a. Thermal analysis**

Thermal analysis (TA) is a set of investigation tools which allow to measure some physical properties and composition through the changes which occur when the sample is heated or cooled. Popular thermal analysis methods are [75]:

- Differential Scanning Calorimetry (DSC) which is based on the measure of heat flux difference with a reference;
- Differential Thermal Analysis (DTA) which is based on the measure of a temperature difference with a reference;
- Dynamic Mechanical Analysis (DMA) which is based on the measure of oscillating force at given temperature(s);
- Thermogravimetric Analysis (TGA) which is based on the measure of the mass loss;
- Thermal Volatilization Analysis (TVA) which is based on the measure of the volatilization rate.

Among these techniques, TGA and DSC were used in the present thesis and are briefly described below.

### **1.6.b. Thermogravimetric analysis (TGA)**

Thermogravimetric analysis (TGA) is a thermal analysis method which allows to quantify the change in mass weight which occurs when a sample is submitted to a controlled temperature variation and under a controlled atmosphere [76]. The results are often presented in a thermogram which is a plot of the sample weight over temperature and/or time of heating. Furthermore, the derivative of the resulting curve allows to identify the temperature(s) for which the weigh change is the highest, hence giving further insights about the thermal stability and occurring reaction(s) and composition such as water/moisture content [76], volatile compounds such as residual solvents, low-molecular mass additive, generation of low-mass product etc. [77].

Usually, the TGA set-up is constituted of a thermobalance (allowing to measure mass while heating and/or over time) placed in a furnace with controlled atmosphere [77]. Factors which affect the measurements are the buoyancy forces due to the atmosphere density changes with temperature above the thermobalance or when changing the composition of the atmosphere for a specific reason/experiment. These effects can be controlled doing a baseline/blank measurement [77]. Along with this, atmosphere convection movements may alter the measurements and thus controlling its flow is required [77]. Another problem encountered is the unequal expansion of thermobalance constituents with increasing temperature which can affect the measured mass. However, some specific set-ups allow to reduce it [77].

Within this thesis, TGA was mainly used to identify main transition temperatures and especially the degradation temperature in order to know in which temperature range Differential Scanning Calorimetry should be performed. It also allows to identify the nature of peaks observed with DSC: a peak with no mass loss corresponds to a phase transition for instance, while a partial mass loss is linked to a partial degradation or de-solvation (depending of the sample nature and composition) while a total mass loss correspond to a total degradation or vaporization of the sample.

### 1.6.c. Differential Scanning Calorimetry (DSC)

Differential Scanning Calorimetry (DSC) is a very popular thermal analysis method based on the measurement of heat flow difference between a sample and a reference while submitted to a controlled temperature change [78]. This technique allows to determine heat capacity, melting and crystallization temperature, glass transition temperature, heat of fusion and some other thermal parameters [78].

Heat flow can occur within three different mechanisms: conduction, convection and thermal radiation. However, there is no way to measure it directly. As a result, DSC is based on an indirect method which is the use of the temperature difference between the sample and reference when they are both submitted to a temperature change: reference and sample holders are placed on temperature sensor inside a furnace. Depending on the specific heat of the sample and transitions occurring, the temperatures measured by the sensors below the sample and reference will differ [78]. The usual corresponding set-up is presented in Figure 21.

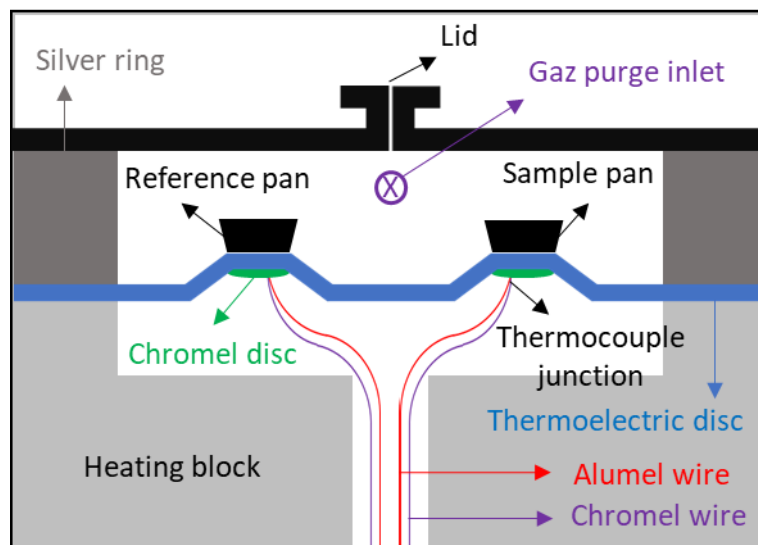


Figure 21: Cross section of a classical DSC set-up (based on [78]).

Among the factors which may impact the measurements is the establishment of a thermal gradient inside the sample (anisotropic

distribution of temperature within the sample). This effect depends on many parameters among which the size of the sample and the heat conductivity of the sample holder. The size of the sample can be easily reduced while sample holder with high thermal conductivity can be chosen in order to reduce this effect. Other effects such as thermal lag (due to thermal resistance of components) can be controlled with the use of symmetrical sample holders and corrected by software [78].

DSC was used along with TGA to evaluate the thermal stability of compounds and systems studied in all chapters but it also allowed to draw the binary diagram of a solid-solution system (anils **A** and **B** in chapter 5), which presented an unexpected multiple-phase behavior. The drawing of that diagram was thus a necessity in order to match photochromical properties with the corresponding phase. The main information researched in that case is the presence and evolution of eutectic peaks, which allows to determine the limits between the phases. Furthermore, the Tammann's approach can be used to calculate precisely the limit molar ratios. This approach consists in plotting the eutectic enthalpies versus the molar compositions [72] and is detailed and illustrated in Figure 22. Eutectic enthalpies are calculated by performing the integration of the eutectic peaks. This integration can be calculated directly with the DSC software used.

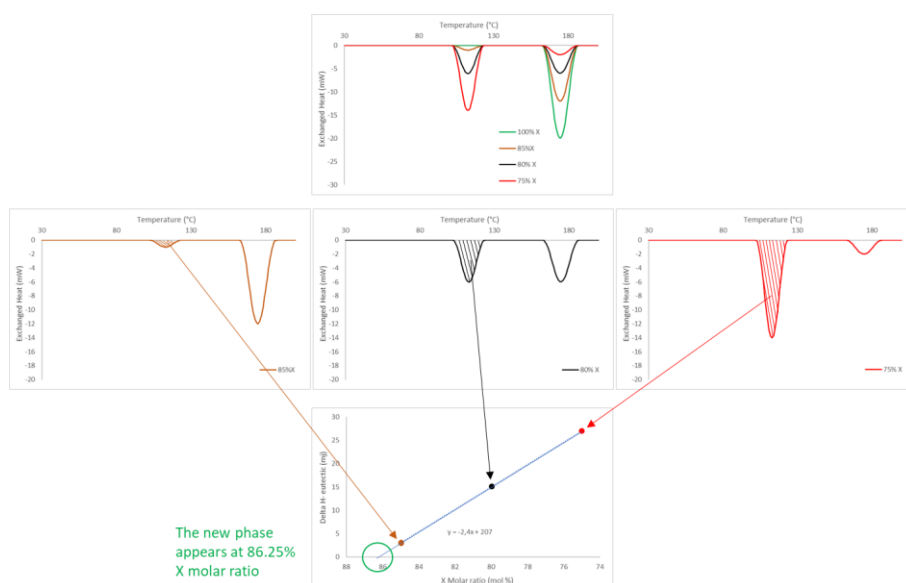


Figure 22: (top) DSC screening for a theoretical two compound (labeled X and Y) system: with decreasing X molar ratio a eutectic peak appears and grows at around 110 °C while the peak of the pure X phase (green curve) decreases at 175 °C; (middle) Individual DSC screening showing the integration on the eutectic peaks; (bottom) Tammann's graph giving the limit molar ratio (here 86.25%) at which the second phase appears.

#### 1.6.d. X-rays diffraction techniques: SC-XRD and XRPD

Among the techniques used to characterize solid-state compounds, X-ray diffraction (XRD) is extremely powerful when facing crystalline structures as it allows obtaining the exact position of atoms and molecules within the crystal. Its development came from the discovery by von Laue in 1912 that crystals can diffract X-Rays and that the diffraction pattern depends of the crystalline structure [79].

X-ray powder diffraction (XRPD) is useful as it is a non-destructive analysis which allow both qualitative and quantitative structural analysis: a comparison with a database allows quick identification of phases (if already known) and also allows to detect/monitor new phases appearing during a process. It allows to study the crystallinity of a phase or monitor a crystallization process. Beside this, it can give quantitative structural information (crystal cell parameters for instance) or even allows finding the

exact structure if the measurement is of high quality (synchrotron measurement for instance) [79] [80] [81].

X-Rays are electromagnetic waves with wavelengths comprised between 10 and 0.001 nm [47]. They are produced when a charged particle with high kinetic energy is rapidly decelerated. Electrons are widely used for this purpose due to the easiness to generate an electrical discharge between high voltage (tens of thousands of volts) plates: during that process electrons are accelerated from the cathode towards the anode by the electrical field and already reach-up to one third of the speed of light for a 30 kV electrical field. At the moment the electrons collide with the anode they lose their kinetic energy mostly as heat but around 1 percent of it is converted into X-Rays [79].

When X-rays penetrate a sample, they can be scattered by the electrons around the nucleus of atoms, which compose the sample [47]. This scattering occurs even without direct absorption and for any kind of electromagnetic waves and is used in other spectroscopic methods such as Raman spectroscopy discussed further on. Crystals are quite specific as they consist (in most of the case) as a three-dimensional periodic arrangement of their constituent atoms, each of them being able to scatter X-ray [82]. If the crystal is exposed to strictly parallel incident X-Ray beams, each atom will scatter them in the same way as other identical atoms as illustrated in Figure 23 for a 2-dimensional periodic arrangement (atoms separated by vectors **a** and **b**) of one unique element atoms [82].

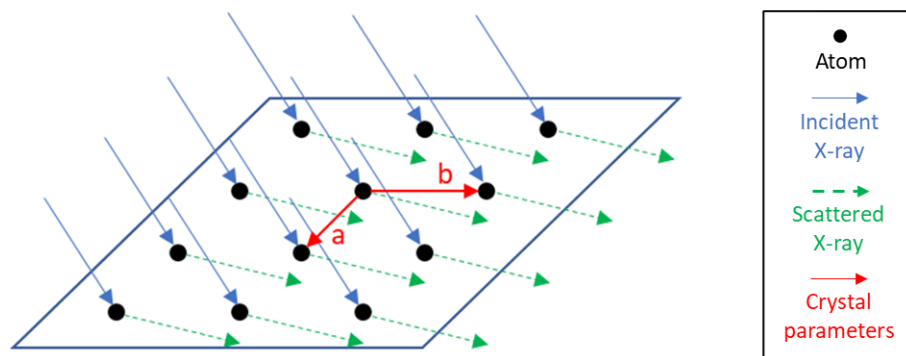


Figure 23: a two-dimensional crystal composed of one kind of atoms hit by parallel X-ray beams. Every atom scatters X-Ray according to its nature and incident angle of the X-ray which are constant in this specific example (adapted from [82]).

The above example shows a crystal might scatter X-Rays but does not explain how a diffraction pattern can be obtained. When von Laue proposed that crystals might diffract X-Rays, he reasoned by analogy with optical diffraction of visible light by a grating for which the repeat distance corresponds to a few multiples of the wavelength: a crystal for which the distance between identical units is of the order of ten Angstroms (around one nanometer) could act as a grating for wavelengths around a few Angstroms (tenths of nanometers) which in turn corresponds to X-rays (which cover ten to 1 thousandths of nanometer) [82].

This hypothesis was proven experimentally by Friedrich and Knipping with X-ray diffraction pictures and later, in 1913, the positions of diffraction spots was explained mathematically by W. L. Bragg: the crystal consisting of equi-spaced plans (containing the scatterers) which act as partial reflectors for X-rays. When a parallel strain of X-rays hits a surface, all reflected rays will have the same phase. However, when reflected rays come from different surfaces, they will have the same phase only if the extra distance travelled by the rays corresponds to an integer multiple of the wavelength  $\lambda$  as illustrated in Figure 24. The corresponding relationship is known as Bragg's law and gives:

$$2d\sin\theta = n \cdot \lambda$$

Where  $\theta$  is the incident angle,  $d$  is the interplanar distance and  $n$  is an integer.

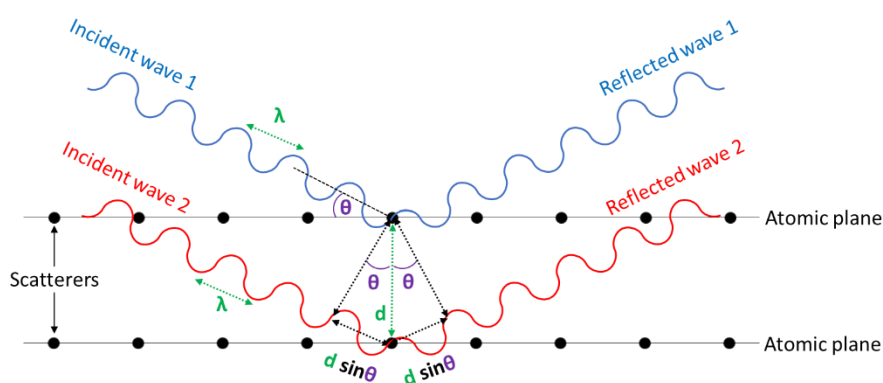


Figure 24: phase of incident and reflected X-rays in accordance with Bragg Law (adapted from [83]).

Having the same phase will allow constructive interferences while different phases will lead to destructive interferences and no diffraction spot [82].

It is demonstrated that there is no significant diffracted intensity by a three-dimensional periodic arrangement (characterized by vectors **a**, **b** and **c**) unless the following system of equations (known as Laue equations) can be verified:

$$\begin{aligned} \mathbf{a} \cdot \mathbf{s} &= h & a(\cos\varphi_a - \cos\varphi_{a,0}) &= h\lambda \\ \mathbf{b} \cdot \mathbf{s} &= k & \text{which can also be written: } b(\cos\varphi_b - \cos\varphi_{b,0}) &= k\lambda \\ \mathbf{c} \cdot \mathbf{s} &= l & c(\cos\varphi_c - \cos\varphi_{c,0}) &= l\lambda \end{aligned}$$

With **s** being the scattered vector; h, k, l being integer values; a, b, c the respective norms of vector **a**, **b**, **c**;  $\varphi_{i,0}$  the incident angle with vector **i**;  $\varphi_i$  the scattered angle with vector **i** and  $\lambda$  the wavelength of X-rays [82].

This system is central in crystallography as it links crystal parameters (a, b, c) with incident and scattered angles of X-rays of known wavelengths. It is closely related to Bragg's law (the two systems are mathematically equivalent) and solving this system allows to calculate crystal parameters once the diffraction pattern of the crystal as well as experimental parameters such as  $\theta$  and  $\lambda$  are known [82]. However, this is complicated and won't be discussed further here as it is out of the scope of the present thesis. The main point here is to know that crystals can diffract X-rays and that the diffraction pattern is typical of the crystal. Recording the X-ray diffraction patterns of a crystal thus may allow obtaining its structural parameters.

Beside the exact structure resolution of the crystal, there is another application of X-ray diffraction by crystals which is easier to perform: the powder diffraction of X-ray. A powder is constituted of a multitude of very small crystals which are oriented in all possible directions (in the case of an ideal powder).

As a result, if a single crystal gives a discrete diffraction pattern, a powder which correspond to all possible orientations of this crystal will give diffraction patterns constituted of continuous rings as presented in Figure 25 [79]. As a real powder sample is not ideal but may contains rather coarse crystals it is useful to rotate the powder during the measurement to get an average signal instead of a "spotty" one [79].

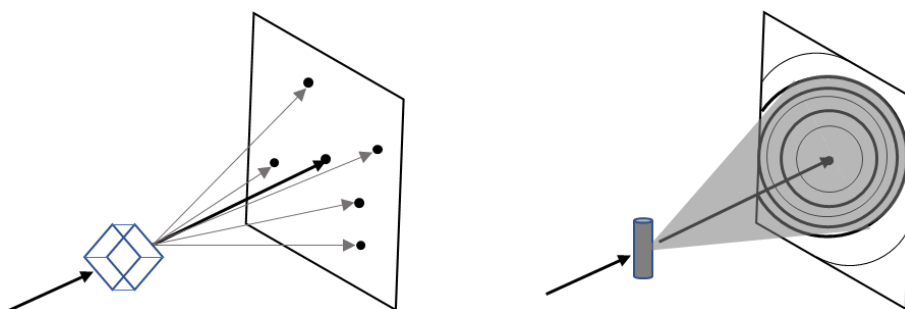


Figure 25: (left) diffraction pattern of a single-crystal - black arrows showing incident X-ray and grey arrows showing diffracted X-rays; (right) diffraction pattern of an ideal powder (inside a capillary) - black arrows showing incident X-ray and grey cone illustrating one of the diffraction cones (adapted from [79]).

The intensity of X-Ray scattering by a charged particle is given by the Thompson equation:

$$I = I_0 \frac{e^4}{r^2 m^2 c^2} \sin^2 \alpha$$

Where:  $I$  is the measured intensity,  $I_0$  the incoming intensity,  $e$  is the charge of the particle,  $m$  is the mass of the particle,  $r$  is the distance between the incoming X-ray wave and the particle,  $c$  is the velocity of light and  $\alpha$  is the angle between the incident X-ray and the generated motion of the particle [79].

We can deduce from the Thompson equation that diffracted spot intensity depends on the position and nature of atoms (and more specifically their number of electrons) inside the crystal unit cell. As a result, the diffraction pattern is unique for a specific crystalline structure compound and so is its powder pattern [79].

Modern X-ray powder diffraction set-up use an X-ray counter which also move around the rotating sample. This allows to measure the intensity of diffracted X-ray along a cut of the rings plane shown in Figure 25. This gives a pattern which is typical of the sample and thus, XRPD may be used to identify the formation of new phases as shown in Figure 26.

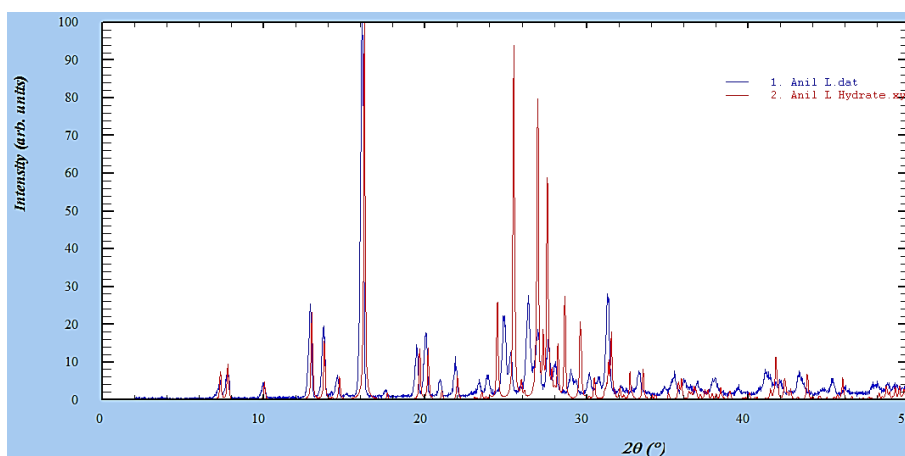


Figure 26: A X-ray powder pattern showing the intensity of diffracted X-ray (normalized at 100 for highest peak) plotted versus the rotating angle of the X-ray counter for an anil (anil **L** in chapter 3 and 4) after synthesis (blue pattern) and after crystallization (red pattern): as the two patterns strongly differs above 25°, a new phase is expected. This phase was later identified as a hydrate with SC-XRD.

Both XRPD and SC-XRD techniques were used during the present thesis and allowed to quickly find new phases (and cocrystals) after cocrystal screening (as presented in the chapters 2 to 5) for XRPD and to get precise structural information from SC-XRD. Beside this, the combination of these two techniques allowed in-deep structural studies among which the impact of supramolecular interactions on the photochromic property as presented in chapter 3.

### 1.6.e.1. Diffuse Reflectance Spectroscopy: theoretical aspects

DRS or Diffuse Reflectance Spectroscopy is a spectroscopic method used in the UV-visible, near-infrared and mid-infrared domain. It allows to get molecular information for opaque solid-samples for which usual transmission (UV-vis) spectroscopy is impossible to perform [84]. As a result, this technique has many applications such as characterizing the color of the soils for geographic/geologic studies [85], studying paints and glass properties for further applications, etc. [86]. This technique is also highly relevant in the case of the present thesis to analyze optical and spectroscopic properties of anils in the solid (crystalline) state.

This technique is based on the measurement of the light which is reflected by the surface of a sample. This reflection is due to two distinct phenomena as illustrated in Figure 27: the specular reflection (reflection by smooth surfaces like mirrors) which occurs at a precise angle depending of the incident angle and the diffuse reflection (due to textured surface like powders) which is independent of the incident angle and takes into account refraction and diffraction phenomena by the small crystals constituting the powder [84].

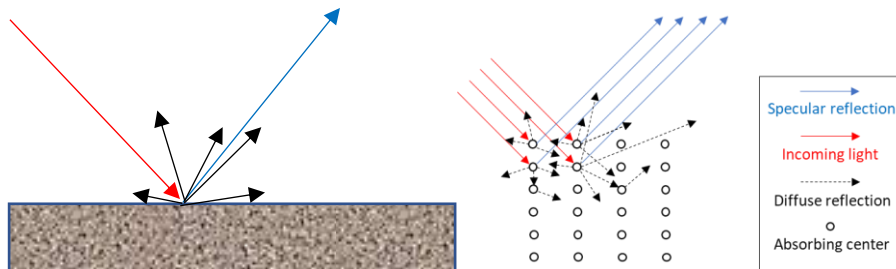


Figure 27: Left: An incident light (red arrow) hits a solid surface and produces specular reflection at a precise angle (blue arrow) and scattered light at various angles (black arrows); Right: detailed overview of an illuminated discrete surface and resulting specular reflection and diffuse reflection (adapted from [87]).

Beside surface characteristics, if the studied sample is of spectroscopic interest, it will also absorb specific wavelengths depending on its nature [84]. Thus, measuring intensity of scattered light (through the use of hemispherical mirror) for varying incident wavelengths will provide the

absorption spectrum of the compound if the sample is composed of infinitely fine powder [86].

The main theory used to describe the phenomena involved in diffuse reflectance has been developed by Kubelka and Munk. It is based on analogies with classical transmission spectroscopy with for instance de definition of the total remittance ( $R_{\infty}$ ) as the ratio  $J/I_0$  where  $J$  is the intensity of reflected light and  $I_0$  the intensity of incident light – similarly to the definition of the total transmittance  $T= I/I_0$  where  $I$  is the intensity of transmitted light [84].

As the absolute total remittance (also called diffuse reflectance) is not easy to measure, the relative total remittance (relative diffuse reflectance) is preferred and is defined as:

$$R'_{\infty} = \frac{R_{\infty, sample}}{R_{\infty, standard}}$$

Where  $R_{\infty, standard}$  is the reflectance of a non-absorbing standard [84].

Kubelka and Munk developed their equation similarly to Beer's law in transmission spectroscopy, in order to have an equation which links the concentration and reflectance characteristics of a sample. This equation writes:

$$F(R'_{\infty}) = \frac{(1 - R'_{\infty})^2}{2R'_{\infty}} = \frac{k}{s}$$

Where  $R'_{\infty}$  is the relative diffuse reflectance (referred to a non-absorbing standard) of an infinitely thick and opaque layer,  $k$  is the molar extinction coefficient as defined by Lambert's law and  $s$  is the scattering coefficient (assumed to be independent of the wavelength) [86].

In this equation, both  $k$  and  $s$  are constants but  $k$  is also a function of the concentration of the analyte which is fixed in the solid state [84]. As a result, a plot of  $F(R_{\infty})$  versus  $k$  should give a straight line [86] and this result has been developed further in the chapter 3 of the present thesis in order to yield a more quantitative approach of the anil photochromism.

As presented above, this technique allows to get spectroscopic information for samples which are not suitable for classical transmission spectroscopy. However, it has some major drawback as it is highly dependent

of experimental parameters such as the grain-size of the powder and air humidity [86]. Ideally the powder should be infinitely thin but practically this is never achieved and thus some extra precaution has to be taken to have reliable and reproducible results. Experimental aspects are discussed below as well as the experimental protocol used through the whole thesis.

#### **1.6.e.2. Diffuse Reflectance Spectroscopy: practical aspects**

DRS is the most important analytical technique used within this work and thus deserve extra explanations about the experimental aspects, especially because a precise protocol has been developed and used during the whole present thesis.

The device used is a regular UV-Vis spectrophotometer (specified in each chapter) but with a solid-state set-up allowing to perform measurements over powder samples. This set-up consists in a mirror system permitting to send the incident UV-Vis beam towards the surface of the (powder) sample and to collect the diffused reflection beam thanks to a hemi-spherical mirror located above the sample holder as presented in Figure 28. To correct the signal due to specular reflection, a baseline signal is measured with a perfectly flat white surface such as PTFE prior to analysis.

The sample holder is a piece of steel (which allows a good thermal conductivity in case a thermostatic set-up is available) with a small hole of about 2 mm diameter and depth in which the solid sample can be loaded. As explained in the theoretical aspects above, the grain-size of the powder should be as small as possible, requiring grinding of the sample before loading it in the sample holder. Furthermore, as the surface needs to be as regular as possible, the powder sample is squeezed with a glass blade before measurement in order to present the most regular surface as possible.

Because of these experimental constraints, the choice has been made to operate using the following protocol when studying photochromic properties of a sample: the first step consists in preparing the sample as explained above (grinding it, loading it and squeezing it into the sample holder); the second step consists in 3 measurements of the absorption spectrum of the sample but each time removing and replacing it into the spectrophotometer (in order to average variations due to small position changes of the sample holder); the third step consists in directly irradiating the sample within the sample holder with the selected wavelength (details

specified in related chapters) by a UV-Vis source in a black box; and finally the fourth step which consists in measuring the absorption spectrum 3 times. This protocol allows to make the comparison after/before irradiation of the sample while controlling the most relevant experimental parameters and ensure the changes measured/observed are mainly due to photo-induced reactions.

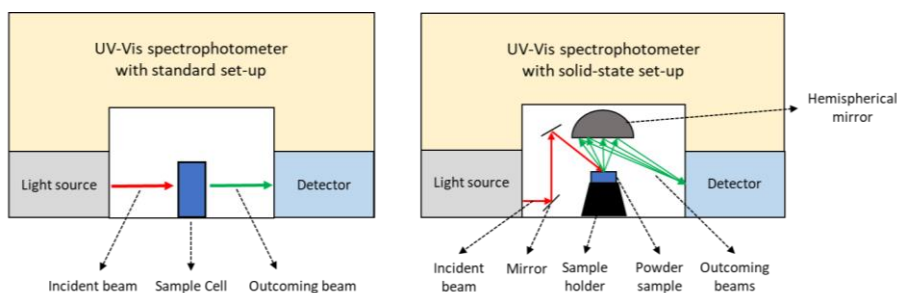


Figure 28: (left) simplified representation of UV-Vis spectrophotometer with standard set-up for absorption spectroscopy; (right) simplified representation of UV-Vis spectrophotometer with solid-state set-up for diffuse reflectance spectroscopy.

### 1.6.f. IR and Raman spectroscopy

Infra-red spectroscopy is a method similar to UV-Visible spectroscopy but using infra-red light: an incident I.R. light is sent through the analyzed sample and the intensity of outcoming light is measured. The difference between incident and outcoming light corresponds to absorbed light. Recording the absorbed intensity for different wavelengths can give further insights into the nature of the sample.

More specifically, I.R. light corresponds to wavelengths in between  $7 \times 10^{-8}$  m and  $10^{-3}$  m while most of the molecular vibrations of interest (such as C-C; C-O; C-H; C-N; ...) occur in a much narrower range comprised between  $2.5 \times 10^{-6}$  m and  $1.5 \times 10^{-5}$  m, which in turn corresponds to a range comprised between respectively  $4000 \text{ cm}^{-1}$  and  $667 \text{ cm}^{-1}$  (using spectroscopic unit  $\bar{\nu}$  expressed in  $\text{cm}^{-1}$  and  $E_{ph} = h\nu = h\frac{c}{\lambda} = hc\bar{\nu}$ ) [88]. Thus an I.R. ray can be absorbed when an oscillating dipole moment (generated by molecular vibration) corresponds to the electrical vector of the incident beam [88]. An

example of this can be illustrated with the case of the CO<sub>2</sub> molecule which is apolar due to its symmetry (Figure 29). However, CO<sub>2</sub> also has 4 vibration modes among which 3 of them exhibit a dipolar moment change as presented in Figure 29. As a result, CO<sub>2</sub> can absorb I.R. light explaining why it is a well-known greenhouse gas.

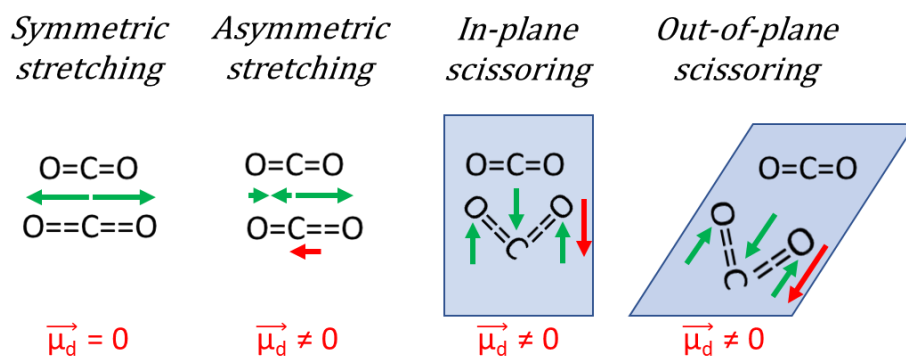


Figure 29: CO<sub>2</sub> vibration modes with corresponding movement of atoms (green arrows) and resulting dipolar moment (red arrows).

The comparison of recorded I.R. absorption intensity of a complex compound with experimental tables allows to identify the main functional groups present on the molecule and may help to identify an unknown structure. An example of the main absorption bands for organic compound is given in Figure 30. The interest of such methods in the scope of this thesis is that I.R. spectroscopy can easily be performed in the solid-state. Thus, once the spectrum of a pure solid anil is known, one can identify phase changes such as polymorphism and cocrystallization because in both cases the intermolecular interactions will differ, leading to changes in the vibrations of impacted functionalities (synthons) and different patterns on the I.R. spectrum. This is possible only in the solid-state as in solution molecules of interest are separated from each other and interact mostly with solvent molecules.

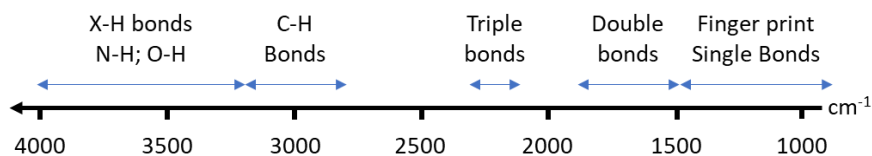


Figure 30: A few common organic bonds and their corresponding absorption area in I.R. (adapted from [89]).

A complementary technique to I.R. spectroscopy is Raman Spectroscopy which often allows to get similar information despite different physical effects and theory govern this spectroscopy. The effect studied here is the inelastic scattering of photons by the materials studied: the interaction of the incident photon leads to a transition towards virtual energy states which have very short life-time. This transition is due to the interaction of the electrical field of the incident photon which can induce a polarization of the electron cloud (but is not a transition between electronic state of the molecules). Once in the virtual energy state, the molecule quickly goes back to a lower energy state while emitting a photon which might be shifted in energy compared to incident light as a different vibrational final state might be reached. This energy difference gives insight into the nature of the transition and the vibrational states. The main principles behind Raman and I.R. spectroscopies are illustrated in Figure 31 [90].

To resume the main difference between the two techniques: I.R. spectroscopy allows to observe vibrational changes leading to an overall change of the electric dipole moment while Raman spectroscopy allows to observe vibrational changes leading to a change of the polarizability during the vibration [91].

As a result, in unsymmetrical molecules all fundamental vibrations will lead to a change of the electrical dipole moment but also to the polarizability and thus the two methods can be used to analyze the molecule. For molecules with a center of symmetry, there is a Mutual Exclusion rule which states that any fundamental transition which is active in I.R. is unactive in Raman and vice-versa and as a result, the two methods are complementary [91].

The Raman effect is very weak as only around 0.1% of the incident light is scattered and most of this scattering is due to Rayleigh diffusion. As a result, Raman Scattering accounts for  $10^{-7}$  of the incident light intensity only. However, the use of high intensity monochromatic light emitters such as lasers makes it a suitable technique [91].

As both methods can be used in the solid-state and as all molecules studied within this work are unsymmetrical, we can use either I.R. or Raman to identify the appearance of new phases through the vibrational changes they induce by comparing the spectra of references and new samples. For instance, Raman technique has been used at the beginning of the present thesis but was not used further as XRPD and DRS both allowed to retrieve

similar information but also other important information about properties and structure. Thus, the choice was made to focus on these techniques instead.

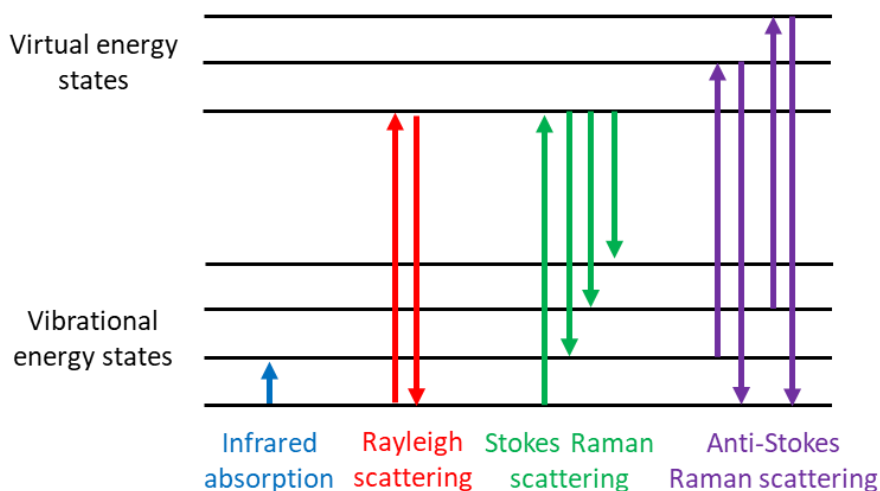


Figure 31: transitions in I.R. and Raman spectroscopy (adapted from [90]).

### I.6.g. Terahertz spectroscopy (THz)

Terahertz spectroscopy usually refers to the spectroscopy technique which specifically focus on the portion of electromagnetic spectrum comprised between  $10^{11}$  and  $10^{13}$  Hz [92] which in turn correspond respectively to 3 and 0.03 mm wavelengths. These last ones correspond to micro-waves and mid-infrared respectively and this part of the electromagnetic spectrum covers most hydrogen-bonding motions (such as stretching and bending) and low-frequencies vibrating bonds along such as Van der Waals interaction [93] with molecular rotations and crystalline phonon vibrations [92]. As a result, terahertz spectroscopy is a technique of interest in order to study hydrogen bonding which is one of the most important features in the case of organic multi-component crystals (as presented in section I.4.a. of the present chapter). This technique is further used to characterize small organic crystals and their solid-state transitions [94].

Terahertz spectroscopy is divided into three techniques depending on sample and experimental constraints: transmission which is used for

weakly absorbing samples, reflection and attenuated total reflection (also abbreviated ATR) which are used for strongly absorbing or scattering samples [92]. This last one (ATR), presents major advantages as it is suitable for powders, liquids, thin film samples etc. without further preparation of the sample [92].

As for other spectroscopic method, terahertz spectroscopy measures the difference between an incoming and outgoing electromagnetic wave passed through the sample. In the ATR-THz set-up, the sample is placed and pressed on an “ATR-crystal” – a crystal with high refractive index and transparent to THz such as germanium, silicon, gallium arsenide and sapphire [95] – and the incoming THz beam is totally internally reflected when it encounter the interface between the ATR-crystal and the sample [93]. At the crystal-sample interface, an evanescent wave (an oscillation electric of magnetic field which does not propagate as an electromagnetic field [96] is produced which penetrates (and is thus able to interact with) the sample within a certain distance (called penetration depth – usually 10 to 140  $\mu\text{m}$ ) before producing the outgoing THz wave which is measured as illustrated in Figure 32 [93].

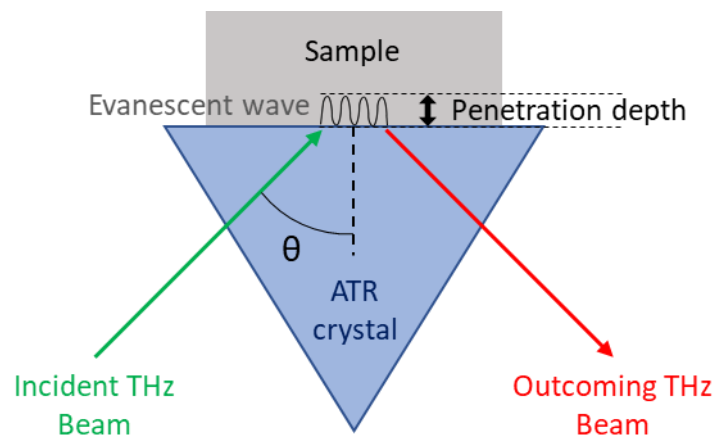


Figure 32: Principle of the ATR-THz spectroscopy technique: an incident THz beam encounter the crystal-sample interface with an angle  $\theta$ , produce an evanescent wave which penetrate the sample before producing the outgoing (reflected) THz beam (adapted from [93]).

Total internal reflection is produced only if the ATR-crystal refractive index ( $n_1$ ) is higher than the sample refractive index ( $n_2$ ) and the penetration depth which depends of the wavelength is given by the following equation:

$$d_p = \frac{\lambda_1}{2\pi\sqrt{\sin^2\theta - n_{21}^2}}$$

Where  $\lambda_1$  is the wavelength in the denser medium;  $n_{21} = \frac{n_2}{n_1}$  is the ratio of refractive index with  $n_1$  the refractive index of the denser medium and  $\theta$  is the incident angle [93].

In the scope of the present thesis, ATR-THz technique could produce results of interest as the photo-responsive anils used could be irradiated by UV-laser (in order to produce the photochromic transition) during the THz measurement which would allow to monitor the transformation. Furthermore, this would allow to study the role of hydrogen bonds and other weak intermolecular bonds over the photochromic transition and should be considered as an interesting perspective in order to gain new insights into this phenomenon.

## I.7. References

- [1] P. Bamfield and M. Hutchings, *Chromic Phenomena: Technological Applications of Colour Chemistry: Edition 3*, Cambridge: Royal Society of Chemistry, 2018.
- [2] R. J. Araujo, "Photochromic Glasses," in *Encyclopedia of Physical Science and Technology*, Elsevier Science Ltd., 2003, pp. 49-56.
- [3] J. Frietsche, "Photochromism of tetracene," *Comptes Rendus. Acad. Sci. Paris*, vol. 69, p. 1035, 1867.
- [4] T. Meer, "E Über Dinitroverbindungen der Fettreihe," *Justus Liebigs Ann. Chem.*, vol. 181, pp. 1-22, 1876.
- [5] M. Maurer, M. Huegin, T. Raimann, L. Feiler, B. Inderbitzin and A. Fuchs, "Preparation of a photochromic ink," *PCT Int. Appl. WO*, vol. 2010079098 A1, 2010.
- [6] B. L. Feringa, W. F. Jager and B. Delange, "Organic materials for reversible optical data storage," *Tetrahedron*, vol. 49, pp. 8267-8310, 1993.

- [7] A. Carletta, X. Buol, T. Leyssens, B. Champagne and J. Wouters, "Polymorphic and Isomorphic Cocrystals of a *N*-Salicylidene-3-aminopyridine with Dicarboxylic Acids: Tuning of Solid-State Photo- and Thermochromism," *The Journal of Physical Chemistry*, vol. 120, pp. 10001-10008, 2016.
- [8] V. K. Seiler, N. Tumanov, K. Robeyns, J. Wouters, B. Champagne and T. Leyssens, "A Structural Analysis of Spiropyran and Spirooxazine Compounds and Their Polymorphs," *Crystals*, vol. 7, no. 3, pp. 84-96, 2017.
- [9] J. Quertinmont, A. Carletta, N. Tumanov, T. Leyssens, J. Wouters and B. Champagne, "Assessing density functional theory approaches for predicting the structure and relative energy of salicylideneaniline molecular switches in the solid state," *Journal of Physical Chemistry C*, vol. 121, pp. 6898-6908, 2017.
- [10] F. Zutterman, O. Louant, G. Mercier, T. Leyssens and B. Champagne, "Predicting keto–enol equilibrium from combining UV/visible absorption spectroscopy with quantum with Quantum Chemical Calculations of Vibronic Structures for Many Excited States. A Case Study on Salicylideneanilines," *Journal of Physical Chemistry A*, vol. 122, no. 24, pp. 5370-5374, 2018.
- [11] B. Kaitner and M. Zbacnik, "Solvent-free Mechanochemistry of Two Thermochromic Schiff Bases," *Acta Chim. Slov.*, vol. 59, pp. 670-679, 2012.
- [12] E. Hadjoudis, S. D. Chatziefthimiou and I. M. Mavridis, "Photochromic and thermochromic anils," *Molecular Engineering*, no. 5, pp. 301-337, 1995.
- [13] M. D. Cohen and G. M. J. Schmidt, "Photochromy and Thermochromy of Anils," *The Journal of Physical Chemistry*, no. 66, pp. 2442-2446, 1962.
- [14] E. Hadjoudis, "Photochromic and Thermochromic Anils," *Molecular Engineering*, no. 5, pp. 301-337, 1995.

- [15] K. Amimoto and T. Kawato, "Photochromism of organic compounds in the crystal state," *Journal of Photochemistry and Photobiology C: Photochemistry Reviews*, vol. 6, pp. 207-226, 2005.
- [16] T. Haneda, M. Kawano, T. Kojima and M. Fujita, "Thermo-to-Photo-Switching of the Chromic Behavior of Salicylideneanilines by Inclusion in a Porous Coordination Network," *Angew. Chem., Int. Ed.*, no. 46, p. 6643-6645, 2007.
- [17] E. Hadjoudis, K. Yannakopoulou, S. D. Chatziefthimiou, A. Paulidou and I. M. Mavridis, "Supramolecular control of photochromism in a B-cyclodextrin/Schiff base system," *Journal of Photochemistry and Photobiology A: Chemistry*, vol. 217, pp. 293-298, 2011.
- [18] I. Casades, M. Álvaro, H. García and M. N. Pillai, "Photochemistry of anils in NaY zeolite," *Eur. J. Org. Chem*, no. 13, pp. 2074-2079, 2002.
- [19] R. Gurdeep, Photochemistry, S. K. Rastogi, Ed., Meerut: Krishna Prakashan Media, 2008.
- [20] <https://dictionary.cambridge.org/fr/dictionnaire/anglais/light>, Cambridge University Press, 2021.
- [21] International Lighting Vocabulary, vol. 17.4, 1987.
- [22] G. K. Pal and P. Pal, Textbook of Practical Physiology, Chennai: Orient Blackswan, 2001.
- [23] P. Buser and M. Imbert, Vision, Cambridge: The MIT Press, 1992.
- [24] H. Benson, University Physics, John Wiley & Sons, Inc., 1996.
- [25] P. Atkins and J. D. Paula, Chimie-Physique, Bruxelles: De Boeck, 2008.
- [26] N. deGrasse Tyson, Cosmos: A Spacetime Odyssey, 2014.
- [27] P. W. Atkins, L. Jones and L. Laverman, Principes de Chimie, DeBoeck, 2017.
- [28] D. A. McQuarrie and J. D. Simons, Physical Chemistry: A Molecular Approach, University Science Books, 1997.

- [29] G. H. Brown, "Photochromism," in *Wiley-Interscience*, New-York, 1971.
- [30] E. Keinan, in *Internet Archive: The Wayback Machine*, <http://www.weizmann.ac.il/ICS/booklet/17/pdf/abstracts.pdf>, 2007.
- [31] W. Zhu, Photochromic protective film and preparation method thereof, Faming Zhuanli Shenqing Patent CN 105129225 A, 2015.
- [32] M. Maurer, M. Huegin, T. Raimann, L. Feiler, B. Inderbitzin and A. Fuchs, Preparation of a photochromic ink, PCT Int. Appl. WO 2010079098 A1, 2010.
- [33] D. Zhang, Photochromic anti-counterfeiting ink, Faming Zhuanli Shenqing, Patent CN 106147399 A, 2016.
- [34] G. C. Yoo, Photochromic contact lens and manufacture method thereof, Repub. Korean Kongkae Taeho Kongbo, Patent KR 2018137234 A, 2018.
- [35] H. J. Hoffmann, "The Use of Silver Salts for Photochromic Glasses," in *Photochromism: Molecules and Systems*, Elsevier Science, 2003, pp. 822-854.
- [36] B. L. Feringa, W. F. Jager and B. Delange, "Organic materials for reversible optical data storage," *Tetrahedron*, no. 49, pp. 8267-8310, 1993.
- [37] S. Kawata and Y. Kawata, "Three-Dimensional Optical Data Storage Using Photochromic Materials," *Chem. Rev.*, no. 100, pp. 1777-1788, 2000.
- [38] M. A. Aegerter and M. Mennig, Eds., "Photochromic Coatings," in *Sol-Gel Technologies for Glass Producers and Users*, Boston, Springer, 2004.
- [39] F. Robert, "Engineering *N*-salicylidene aniline derivatives: from solid-state molecular switches to multifunctional organic-inorganic architectures," Université Catholique de Louvain, 2010.

- [40] F. Robert, A. D. Naik, F. Hidara, B. Tinant, R. Robiette, J. Wouters and Y. Garcia, "Engineering Solid-State Molecular Switches: *N*-Salicylidene *N*-Heterocycle Derivatives," *Eur. J. Org. Chem.*, pp. 621-637, 2010.
- [41] M. Sliwa, S. Létard, I. Malfant, M. Nierlich, P. G. Lacroix, T. Asahi, H. Masuhara, P. Yu and K. Nakatani, "Design, Synthesis, Structural and Nonlinear Optical Properties of Photochromic Crystals: Toward Reversible Molecular Switches," *Chem. Mater.*, vol. 17, pp. 4727-4735, 2005.
- [42] T. Fujiwara, J. Harada and K. Ogawa, "Solid-State Thermochromism Studied by Variable-Temperature Diffuse Reflectance Spectroscopy: A New Perspective on the Chromism of Salicylideneanilines," *J. Phys. Chem. B*, no. 108, pp. 4035-4038, 2004.
- [43] M. Sliwa, N. Mouton, C. Ruckebusch, L. Poisson, A. Idrissi, S. Aloïse, L. Potier, J. Dubois, O. Poizat and G. Buntinx, "Investigation of ultrafast photoinduced processes for salicylidene aniline in solution and gas phase: toward a general photo-dynamical scheme," *Photochemical & Photobiological Sciences*, pp. 661-669, 2010.
- [44] M. Sliwa, P. Naumov, H.-J. Choi, Q.-T. Nguyen, B. Debus, S. Delbaere and C. Ruckebusch, "Effects of a Self-Assembled Molecular Capsule on the Ultrafast Photodynamics of a Photochromic Salicylideneaniline Guest," *ChemPhysChem*, vol. 12, pp. 1669-1672, 2011.
- [45] R. Klajn, "Spiropyran-based dynamic materials," *Chem. Soc. Rev.*, no. 43, pp. 148-186, 2014.
- [46] E. Hadjoudis, "Photochromic and Thermochromic anils," *Molecular Engineering*, no. 5, pp. 301-337, 1995.
- [47] Y. Waseda, E. Matsubara and K. Shinoda, *X-Ray Diffraction Crystallography*, Springer, 2011.
- [48] S. Lower, "The nature of crystalline solids," in *Matter under the microscope*, <http://www.chem1.com/acad/webtext/states/states.html#SEC4>, 2017.

- [49] "International Union of Crystallography: Report of the Executive Committee for 1991," *Acta Cryst. A*, pp. 922-946, 1992.
- [50] G. R. Desiraju, J. J. Vittal and A. Ramanan, *Crystal Engineering A Textbook*, Singapore: World Scientific Publishing Co. Pte. Ltd., 2011.
- [51] G. R. Desiraju, "Crystal Engineering: From Molecule to Crystal," *J. Am. Chem. Soc.*, pp. 9952-9967, 2013.
- [52] (. authors), "Report on the sixth blind test of organic crystal structure prediction methods," *Acta Cryst. B*, pp. 439-459, 2016.
- [53] G. R. Desiraju, "Supramolecular Synthon in Crystal Engineering - A New Organic Synthesis," *Angew. Chem. Int. Ed.*, pp. 2311-2327, 1995.
- [54] R. Custelcean and J. E. Jackson, "Dihydrogen Bonding: Structures, Energetics and Dynamics," *Chem. Rev.*, vol. 101, no. 7, pp. 1963-1980, 2001.
- [55] M. P. Brown and R. W. Heseltine, "Co-ordinated BH<sub>3</sub> as a Proton Acceptor Group in Hydrogen Bonding," *Chemical Communication*, vol. 23, pp. 1551-1552, 1968.
- [56] R. H. Crabtree, P. E. M. Siegbahn, O. Eisenstein, A. L. Rheingold and T. F. Koetzle, "A New Intermolecular Interaction: Unconventional Hydrogen Bonds with Element-Hydride Bonds as Proton Acceptor," *Acc. Chem. Res.*, vol. 29, no. 7, pp. 348-354, 1996.
- [57] A. Krawczuk and M. Gryl, "Qualitative and quantitative crystal engineering of multi-functionnal co-crystals," in *Multi-Component Crystals*, Berlin, De Gruyter, 2018, pp. 60-102.
- [58] A. Crihfield, J. Hartwell, D. Phelps, R. B. Walsh, J. L. Harris, J. F. Payne, W. T. Pennington and T. W. Hanks, "Crystal Engineering through Halogen Bonding. 2. Complexes of Diacetylene-Linked Heterocycles with Organic Iodides," *Cryst. Growth and Des.*, vol. 3, no. 3, pp. 313-320, 2003.
- [59] A. Varadwaj, H. M. Marques and P. R. Varadwaj, "Nature of Halogen-Centered Intermolecular Interactions in Crystal Growth and Design: Fluorine-Centered Interactions in Dimers in Crystalline

- Hexafluoropropylene as a Prototype," *J. Comput. chem.*, vol. 40, pp. 1836-1860, 2019.
- [60] M. Fourmigué and A. Dhaka, "Chalcogen bonding in crystalline diselenides and selenocyanates: From molecules of pharmaceutical interest to conducting materials," *Coordination Chemistry review*, vol. 403, pp. 1-17, 2020.
- [61] P. Scilabra, G. Terraneo and G. Resnati, "The Chalcogen Bond in Crystalline Solids: A World Parallel to Halogen Bond," *Acc. Chem. Res.*, vol. 52, pp. 1313-1324, 2019.
- [62] S. J. Grabowski, "Pnicogen and tetrel bonds—tetrahedral Lewis acid centres," *Struc. Chem.*, vol. 30, pp. 1141-1152, 2019.
- [63] J. J. McKinnon, D. Jayatilaka and M. A. Spackman, "Towards quantitative analysis of intermolecular interaction with Hirshfeld surfaces," *ChemComm*, pp. 3814-3816, 2007.
- [64] L. J. Barbour, "Experimental and Computational Methods in Supramolecular Chemistry," in *Comprehensive Supramolecular Chemistry II*, Elsevier, 2017.
- [65] A. D. McNaught and A. Wilkinson, IUPAC. Compendium of Chemical Terminology, Oxford: Blackwell Scientific Publications, 1997.
- [66] C. Brandel, S. Petit, Y. Cartigny and G. Coquerel, "Structural Aspects of Solid Solutions of Enantiomers," *Current Pharmaceutical Design*, no. 22, pp. 1-29, 2016.
- [67] K. Johmoto and H. Uekusa, "Control of photochromism by manipulation of molecular conformation," in *Multi-Component Crystals: Synthesis, Concepts, Function*, E. R. T. Tiekink and J. Zukerman-Schpector, Eds., De Gruyter, 2018, pp. 103-11.
- [68] S. L. Sunil, S. K. Nayak, V. R. Hathwar, D. Chopra and T. N. G. Row, "Role of Fluorine in Weak Interactions in Co-crystals," in *Pharmaceutical Salts and Co-crystals*, L. Quéré and J. Wouters, Eds., Cambridge, Royal Society of Chemistry, 2012, pp. 29-39.

- [69] M. Lusi, "Engineering Crystal Properties through Solid Solutions," *Cryst. Growth and D.*, no. 18, pp. 3704-3712, 2018.
- [70] F. Guthrie, "on Eutexia," *The London, Edinburgh, and Dublin Philosophical Magazine and Journal of Science*, vol. 17, no. 108, pp. 462-482, 1884.
- [71] N. V. Taratin, H. Lorenz, E. N. Kotelnikova, A. E. Glikin, A. Galland, V. Dupray, G. Coquerel and A. Seidel-Morgenstern, "Mixed Crystals in Chiral Organic Systems: A Case Study on (R)- and (S)-Ethanolammonium 3-Chloromandelate," *Cryst. Growth Des.*, no. 12, pp. 5882-5888, 2012.
- [72] A. Mbodji, G. Gbabode, M. Sanselme, Y. Cartigny, N. Couvrat, M. Leeman, V. Dupray, R. M. Kellogg and G. Coquerel, "Evidence of Conglomerate with Partial Solid Solutions in Ethylammonium Chlocyphos," *Cryst. Growth Des.*, no. 20, pp. 2562-2569, 2020.
- [73] R. Valls and R. Frèze, "Diagrammes de phase complexes," in [http://public.iutenligne.net/chimie/valls/chimie-du-solide/partielle\\_commenter.htm](http://public.iutenligne.net/chimie/valls/chimie-du-solide/partielle_commenter.htm), 2021.
- [74] M. D. Cohen, "Topochemistry. Part XXVIII. The system: 4-chloro-*N*-salicylideneaniline—4-bromo-*N*-salicylideneaniline," *Journal of Chemical Society B: Physical Organic*, pp. 373-376, 1968.
- [75] I. Blanco and V. Siracusa, "The Use of Thermal Techniques in the Characterization of Bio-Sourced Polymers," *materials*, no. 14, pp. 1686-1706, 2021.
- [76] M. J. Diaz, M. Ruiz-Montoya, A. Palma and M.-V. de-Paz, "Thermogravimetry Applicability in Compost and Composting Research: a Review," *applied sciences*, no. 11, pp. 1692-1707, 2021.
- [77] R. B. Prime, H. E. Bair, S. Vyazovkin, P. K. Gallagher and A. Riga, "Thermogravimetric analysis (TGA)," in *Thermal Analysis of Polymers: Fundamentals and Applications*, J. D. Menczel and R. B. Prime, Eds., New Jersey, John Wiley & Sons, Inc., 2009.
- [78] J. D. Menczel, L. Judovits, R. B. Prime, H. E. Bair, M. Reading and S. Swier, "Differential Scanning Calorimetry (DSC)," in *Thermal Analysis*

- of Polymers: Fundamentals and Applications*, J. D. Menczel and R. B. Prime, Eds., New Jersey, Wiley & Sons, Inc., 2009.
- [79] B. D. Cullity, *Elements of X-Ray diffraction*, Addison-Wesley Publishing Compagny Inc., 1956.
- [80] C. N. Barnakov, G. P. Khlokhlova, A. N. Popova, S. A. Sozinoz and Z. R. Ismagilov, "X-Ray Diffraction Technique: Structure Determination of Carnonaceous Materials (Review)," *Khimiya v Interesakh Ustoichivogo Razvitiya*, pp. 569-576, 2016.
- [81] C. Tedesco and M. Brunelli, *Comprehensive Supramolecular Chemistry II*, Amsterdam: Elsevier B. V., 2017.
- [82] M. M. Woolfson, *An Introduction to X-Ray Crystallography*, Cambridge University Press, 1997.
- [83] <https://www.britannica.com/science/Bragg-law>, Encyclopedia Britannica, 1998.
- [84] J. P. Blitz, "Diffuse Reflectance Spectroscopy," in *Modern Techniques in Applied Molecular Spectroscopy*, John Wiley & sons, Inc., 1998, pp. 185-219.
- [85] J. Torrent and V. Barron, "Diffuse reflectance Spectroscopy," in *Method of Soil Analysis. Part 5. Mineralogical Methods.*, 2008, pp. 367-385.
- [86] G. Kortum, W. Braun and G. Herzog, "Principles and Techniques of Diffuse-Reflectance Spectroscopy," *Angewandte Chemie*, vol. 2, no. 7, pp. 333-341, 1963.
- [87] V. Marks and K. G. M. M. Alberit, *Clinical Biochemistry Nearer the Patient*, Churchill-Livingstone, 1985.
- [88] D. H. Williams and I. Fleming, *spectroscopic method in organic chemistry*, P. Sykes, Ed., London: McGraw-Hill Publishing Company Ltd., 1966.
- [89] G. Socrates, *Infrared and Raman Characteristic Group Frequencies: Tables and Charts*, Chichester: John Wiley & Sons, 2001.

- [90] "Raman Spectroscopy," in *DoITPoMS Teaching and Learning Package* – , University of Cambridge, <https://www.doitpoms.ac.uk/tlplib/raman/comparison.php>, 2004.
- [91] B. Straughan and S. Walker, *Spectroscopy volume two*, London: Chapman and Hall Ltd., 1976.
- [92] Y. Huang, R. Singh, L. Xie and Y. Ying, "Attenuated Total Reflection for Terahertz Modulation, Sensing, Spectroscopy and Imaging Applications: A Review," *Applied Sciences*, no. 10, pp. 4688-4706, 2020.
- [93] J. Obradovic, D. A. Newnham and P. H. Taday, "Attenuated Total Reflection Explores the Terahertz Region," *American Laboratory*, 2007.
- [94] P. Bawuah and J. A. Zeitler, "Advances in terahertz time-domain spectroscopy of pharmaceutical solids: a review," *Trends in Analytical Chemistry*, vol. 139, 2021.
- [95] A. Siemieon, "The Magic of Optics-An Overview of recent Advanced Terahertz Diffractive Optical Elements," *Sensors*, no. 21, pp. 100-122, 2021.
- [96] O. Takayama, A. A. Bogdanov and A. V. Lavrienko, "Photonic surface waves on metamaterial interfaces," *Journal of Physics: Condensed Matter*, vol. 29, no. 46, p. 463001, 2017.

## Preface of Chapter 2

The chapter 2, which is entitled “Altering the Photochromic Properties of *N*-Salicylideneanilines Using a Co-Crystal Engineering Approach” has been published in *Crystal Growth and Design* and the text is presented as such. As a result, the words “cocrystal” and “*N*-Salicylideneaniline” (used as such in all other chapters) are here written “co-crystal” and “*N*-salicylideneaniline”.



## Chapter 2

# Altering the Photochromic Properties of *N*-Salicylideneanilines Using a Co-Crystal Engineering Approach\*

*Gabriel M. Mercier*<sup>†</sup>, *Koen Robeyns*<sup>†</sup>, *Tom Leyssens*<sup>†</sup>

<sup>†</sup> Institute of Condensed Matter and Nanosciences, Université catholique de Louvain, 1348 Louvain-la-Neuve, Belgium

\* Published in *Crystal Growth & Design* **2016** 16 (6), 3198-3205  
DOI: 10.1021/acs.cgd.6b00108

## **Abstract**

In this work photochromic properties of *N*-salicylideneanilines were modified using a crystal engineering approach. Co-crystallization allowed to modify the structural arrangement and electronic properties of the target compounds altering its photochromic behavior without having to change the nature of the molecule. A co-crystal of *N*-salicylideneaniline and citraconic acid characterized by a zwitterionic anil character and showing inverted photochromic behavior when compared to the parent anil is reported here for the first time.

## Introduction

Within the race to novel technologies, chromotropic materials have gained an increasing amount of attention over the last few decades, from industrial as well as academic point of view [1]. Photochromism is likely the most sought chromotropic property, and is defined as a light induced reversible color change of a material. Most often photochromism is associated to a compound, which can occur in two specific forms absorbing at different wavelengths [2].

Among photochromic materials, *N*-salicylideneaniline (anils) derivatives have been widely studied since 1939 [3] as they present multiple advantages: they are relatively straightforward to synthesize [4,5], easy to handle and use in the solid state, and resistant to fatigue [6,7,8]. *N*-salicylideneanilines belong to the group of Schiff bases as they contain an azomethine (imine) bond [9]. The ortho-hydroxyl (phenol) group can undergo a keto-enol equilibrium through a temperature induced proton transfer to the nitrogen of the azomethine bond [4,10-12] (Figure 1). At room temperature in general both the enol and *cis*-keto forms are present in equilibrium. In some cases, upon UV-visible irradiation, both undergo transition to a third form, the *trans*-keto form [4-12] as presented in Figure 1.

The enol form (usually the most stable form) is usually colorless whereas the *cis*-keto form, which becomes more populated at high temperature, exhibits more often a deep yellow to orange coloration. Finally, the *trans*-keto form obtained after light irradiation is usually deep red-colored [3,4]. As mentioned, color changes can either be thermally or photo-induced, allowing to classify anil compounds as thermochromic and/or photochromic. Figure 2 shows the overall mechanisms believed to occur upon photo-irradiation [6,14-16]. In the simplest scheme, excitation of the enol form, will lead to an excited enol state, which either returns to the ground state by fluorescence, or which undergoes non-radiative transition to an excited *cis*-keto state. This latter can undergo a radiative relaxation to the ground *cis*-keto state, or undergo a non-radiative transition to an excited *trans*-keto state. Non-radiative relaxation of this latter is believed to lead to the red-colored ground state *trans*-keto species. Recent theoretical and

ultra-fast laser spectroscopy studies have shown this scheme to be over simplified, with a more complex situation involving multiple transient species being more likely [17,18].

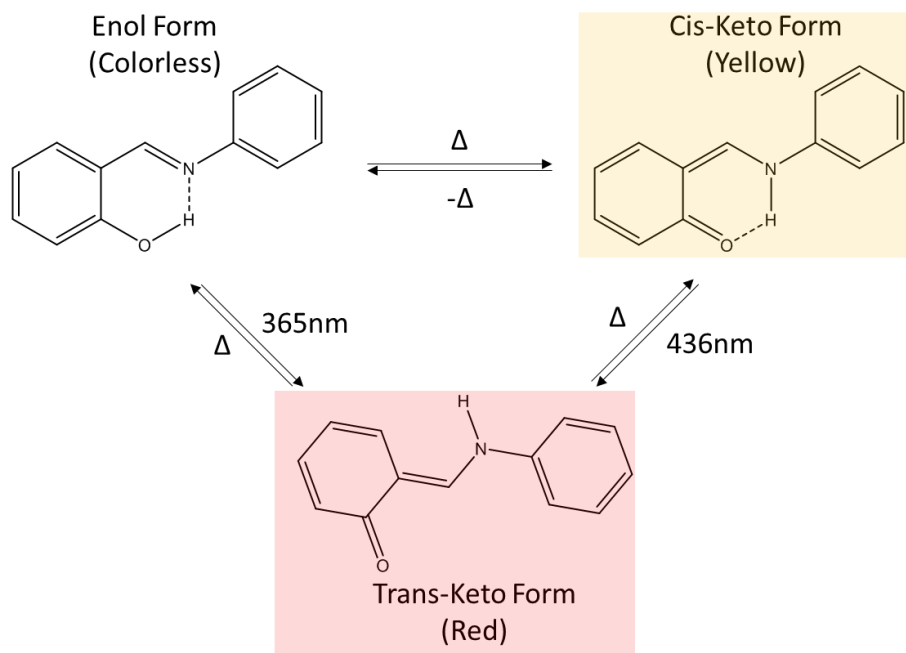


Figure 1: Photo and thermo-induced transitions in *N*-salicylideneaniline [13].

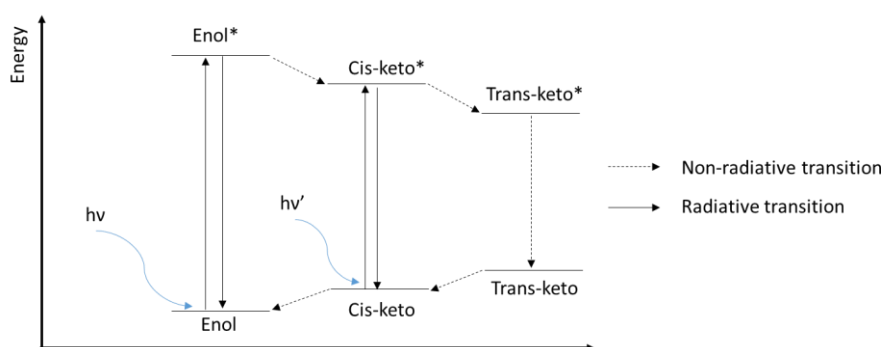


Figure 2: Simplified scheme of transition pathways for anils upon light irradiation.

From a structural point of view, photochromic anils usually present a non-planar shape with a dihedral angle between aromatic rings  $\phi > 25^\circ$  [12,16,19,20]. When the molecule is planar the anil tends to be only thermochromic. Recent work, however, suggest that planarity or non-planarity of the anil molecules is not the determining factor for thermochromic or photochromic behavior of those compounds [21]. The thermo and/or photochromic character of the anil strongly depends on the overall structural environment, explaining why different polymorphs of the same compound can exhibit different thermo/photochromic properties [4].

Although sought for, only a limited number of anils show photochromism at the solid state. In general, identification of novel photochromic anils focuses on the synthesis of new compounds by inserting or combining different functional groups. Alternatively, the photochromic compound can be inserted in a different environment such as polymers and rigid glasses [19] or porous materials [22] and zeolite [23]. In a final approach, a crystal engineering approach, the crystal environment of the compound can be impacted. By adding a metal component, metal organic frameworks (MOFs) can be obtained [13,24]. In a recent contribution, a novel methodology was used, consisting in co-crystallizing the molecule of interest with another organic molecule. This approach allows combining properties of different materials rendering them for instance more stable or less reactive to external factors. More specifically, co-crystallization allows the creation of novel crystalline forms, even for those compounds for which no salts or solvates can be formed [25,26].

In the case of *N*-salicylideneanilines, co-crystallization could allow to increase the space available in the crystal structure required for the “pedal motion” involved in the photochromic mechanism [20]. Doing so non-photochromic materials have been shown to be transformable into photochromic ones [27]. In their contribution, Johmoto *et al.* studied acid-base co-crystallization [27], with a proton transfer occurring between the co-former and the anil of interest, hereby obtaining two charged species. Another recent research succeeded in obtaining a photochromic co-crystal coming from a non-photochromic anil [28]. Hutchins *et al.* used a phenolic derivative which was hydrogen bonded with 4,4-Bipyridin [28]. We used a similar approach but aimed not only to avoid acid-base co-crystallization, but

also to impact the photochromically active site directly by changing its hydrogen bonding pattern. To do so, we focused on two model compounds (see experimental section) that do not contain any basic or acidic group other than the ones at the photochromically active site.

By allowing hydrogen bonding to the photochromic site of the anil, the goal of this study was to directly impact the photochromic behavior of these reference compound.

## **Experimental Section**

### **Starting Materials.**

Carboxylic acids used as co-formers, solvents and starting materials for synthesis were all purchased and used as such. Product codes are given in the brackets. From Accros Organic: 1-hydroxy-2-naphtoic acid (149231000); 2,5-dihydroxybenzoic acid (165200500); 4-hydroxybenzoic acid (120995000); Acetylsalicylic acid (158185000); Citric acid (110450010); Fumaric acid (119750010); Maleic acid (125230010); Mandelic acid R (101691137); Oxalic acid (186432500); Succinic acid (158745000); Tartaric acid D (137871000); 4-fluoro-aniline (119290250). From Sigma Aldrich: 2,3-dihydroxybenzoic acid (206-135-5); 2,4-dihydroxybenzoic acid (101527441); 3,4-dihydroxybenzoic acid (100986520); 3,5-dihydroxybenzoic acid (202-730-7); Salicylaldehyde (101669521). From Alfa Aesar: 2,2-dimethylsuccinic acid (209-899-6). From U.C.B. s.a.: Salicylic acid (4388); Aniline (1163-4944). From Janssen Chimica: Acetic acid (14.893.52). From TCI: Citraconic acid (207-858-7). From VWR Chemicals: Acetonitrile (200-835-2); Diethyl ether (200-467-2); Ethanol (200-578-6); Ethyl acetate (205-500-4). From Fisher Chemicals: Acetone (200-662-2).

### **Synthesis.**

Compound **A** (*N*-salicylideneaniline) was prepared by hand grinding (ten minutes) of salicylaldehyde (10 mmol) with aniline (10 mmol) in presence of a catalytic amount of acetic acid (0.2 mmol) and dried for 48 h at

45 °C and used as such (yield: 98%, purity: 99%)<sup>1</sup>. Compound **B** (4-fluoro-Salicylideneaniline) was prepared by grinding (5 minutes) of salicylaldehyde (10 mmol) with 4-fluoro-aniline (10 mmol) and dried for 48 h at 45°C and used as such (yield: 98%, purity: 99%).

### **Mechanochemical co-crystal screen.**

The experimental co-crystal screening procedure was performed as follows: in a first stage, solvent-drop grinding (10 µl of acetonitrile) was performed using an equimolar ( $10^{-3}$  mol) mixture of starting materials. Samples were ground in a RETSCH Mixer Mill MM 400 for 90 min with a beating frequency of 30 Hz. The resulting powders were characterized using X-ray Powder Diffraction. Upon co-crystal identification, attempts were made to obtain a single crystal of suitable size and quality for single crystal X-ray diffraction measurement. As a chemical reaction can occur during solvent-drop grinding, <sup>1</sup>H-NMR was used to eliminate samples where degradation/reaction occurred.

### **Single Crystal formation attempts.**

Single crystals of **A-C10** were grown by MeCN vapor diffusion in a furnace at 45 °C for 1 week after grinding. Standard slow solvent evaporation at room temperature was tried for each positive hit with acetone, acetonitrile, diethylether, ethanol, ethylacetate but did not yield successful results. MeCN vapor diffusion at 45 °C was tested for **B** co-crystals but did not yield single crystals suitable for analysis.

### **X-ray Powder Diffraction (XRPD).**

X-ray diffraction measurements were performed on a Siemens D5000 diffractometer equipped with a Cu X-ray source operating at 40 kV and 40 mA and a secondary monochromator allowing to select the K $\alpha$  radiation of Cu ( $\lambda=1.5418$  Å). A  $2\theta$  scanning range from 2° to 50° at a scan rate of 0.6° min<sup>-1</sup> was applied. Simulated patterns of the known starting

---

<sup>1</sup> The photochromically active polymorph of this compound was obtained using this procedure.

compounds were calculated from their single crystal structures with Mercury 3.1 and plotted with WinPLOTR (version: September 2015). For each reported mixture the diffraction pattern (in blue) is superimposed onto simulated patterns of its components (in red for the corresponding anil and green for the co-former). All data are normalized at 100 for the highest peak. We assume formation of new phases when at least 2 new peaks appear and at least 2 reference peaks are missing.

### **Single crystal X-Ray diffraction.**

The structure of **A-C10** was solved from single-crystal synchrotron X-ray diffraction data, which were collected on the Swiss-Norwegian Beam Line BM01A at the European Synchrotron Radiation Facility (ESRF) (Grenoble, France), using a PILATUS 2M hybrid pixel detector at a wavelength of 0.82103 Å. Prior to the data collection the sample was flash-cooled to 100(2) K using an Oxford Cryostream 700 system. The data were converted with the SNBL toolbox software [29] for integration with the CrysAlisPro software [30].

Structure was integrated with the CrysAlisPro software and the implemented multi-scan absorption correction procedure was applied. The structure was solved by direct methods, SHELXS-97 [30] and was refined by full-matrix least squares on  $|F|^2$  using SHELXL-2014 [31]. Non-hydrogen atoms were refined anisotropically and hydrogen atoms were either placed on calculated positions in riding mode with temperature factors fixed at 1.2 times  $U_{eq}$  of the parent atoms and 1.5 times  $U_{eq}$  for methyl groups, or located in the Fourier difference maps when involved in H-bonds.

### **NMR analysis.**

$^1\text{H}$  NMR spectra were recorded on Bruker-300 MHz.  $^1\text{H}$  NMR chemical shifts are reported relative to  $\text{CD}_3\text{CN}$  (1.94 ppm).

Compound **A**:  $\delta$  (ppm): 13.26 (s, 1H); 8.82 (s, 1H); 7.56-7.31 (m, 7H); 7.03-6.98 (dt, 2H,  $J_1=7.8\text{Hz}$ ,  $J_2=1.2\text{Hz}$ ).

### **Diffuse Reflectance Spectroscopy measurements.**

DRS spectra were obtained on a Varian Cary 5E spectrometer using PTFE as a reference. Spectra were measured on pure solid. Diffuse Reflectance spectra were normalized (value at  $\lambda=395$  nm set at 1). Signal assignment was supported by reported band range for *N*-salicylideneaniline derivatives [15]. Light irradiations were carried out with a LOT-ORIEL 200 W high-pressure mercury arc lamp combined with selected band pass filter. Kubelka-Munk spectra were taken before and after irradiation (irradiation time is described in the text).

### **CSD statistical analysis.**

Reference bond lengths of interest were obtained by statistical analysis of the data available in the CSD: we searched all reported organic structure (with R factor  $\leq 0.05$ ) containing at least two bonds corresponding to critical bonds of the two forms (enol and keto: Figure 3) studied. A search was performed in order to specifically describe bond lengths in the case of anil derivatives and to be more accurate than average values already reported by Frank H. Allen *et al.* [32]. Reference structures used to approximate enol-imine and conjugated-ketone form are presented in Figure 4. Doing so, reference bond lengths were obtained (noted as bond 2, 3, 4 and 5 in Figure 3) in various environments regardless of temperature. Results of average bond lengths are reported in table 1 with standard deviation and number of CSD hits. As shown by this table, there is a clear-cut difference between enol-imine and ketone bond lengths, with a slightly narrower distribution in the case of the enol-imine form. Bond lengths obtained for Conjugated Ketone 1 are different from bond lengths of Conjugated Ketone 2 and Amine 1 (Figure 4). We considered Conjugated Ketone 1 already partially displaced toward Enol-Imine 1 and furthermore there are only a few hits (126) meaning results on this form are less accurate. We therefore used both forms, Conjugated-Ketone 2 and Amine 1 (for bond 5), to better describe the conjugated ketone character. To describe the enol-imine character we selected bond length values of Enol-Imine 1 as it is the closest to the anil **A** structure and they are in good agreement with the results observed in Phenol 1 and Imine 1.

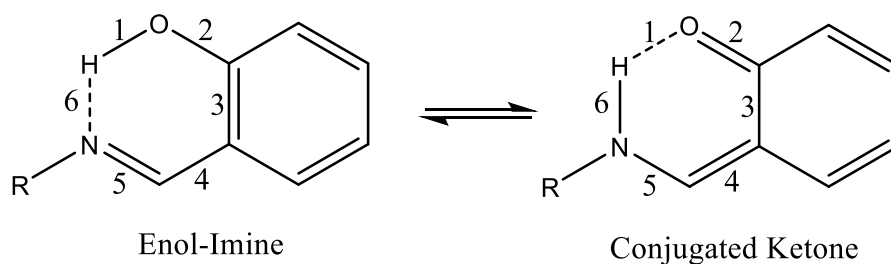


Figure 3: Common structure of all anils considered. Important bonds are noted from 1 to 6.

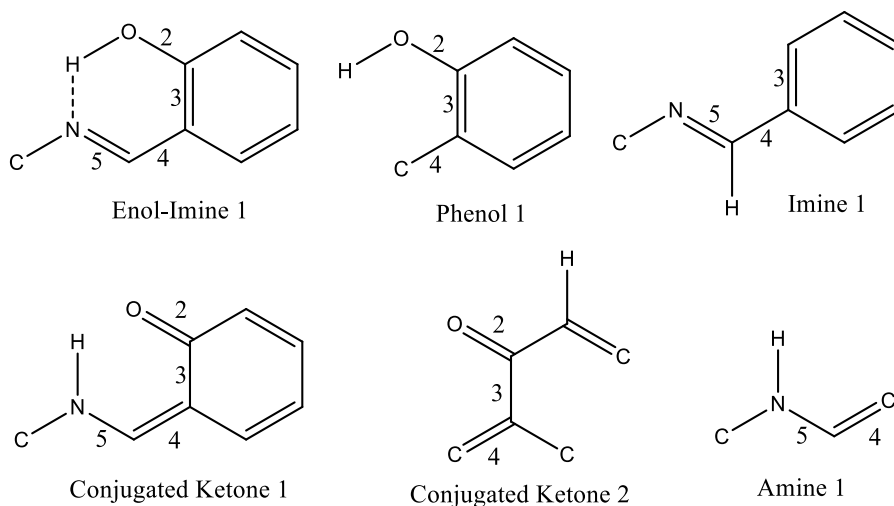


Figure 4: Structures with bond lengths researched through CSD to approach enol-imine form (Enol-Imine 1, Phenol 1, Imine 1) and ketone form (Conjugated Ketone 1, 2 and Amine 1) bond lengths. Non described bonds/atoms were not defined during the search.

Table 1: bond lengths and standard deviations for each pattern researched with its number of hits in the CSD

Pattern	Bond 2, $\sigma$ (Å)	Bond 3, $\sigma$ (Å)	Bond 4, $\sigma$ (Å)	Bond 5, $\sigma$ (Å)
Enol-Imine 1 Hits = 2652	1.344, 0.022	1.406, 0.017	1.450, 0.021	1.286, 0.021
Phenol 1 Hits = 10000	1.364, 0.020	1.399, 0.017	1.499, 0.310	/
Imine 1 Hits = 10000	/	/	1.443, 0.023	1.283, 0.021
Conj. Ketone 1 Hits = 126	1.291, 0.015	1.431, 0.013	1.414, 0.014	1.303, 0.015
Conj. Ketone 2 Hits = 881	1.249, 0.034	1.463, 0.032	1.375, 0.040	/
Amine 1 Hits = 10000	/	/	1.356, 0.026	1.358, 0.027

## Results

**Co-crystal screening.** Two very basic, well-described model anil derivatives were chosen as well as 18 common carboxylic acid co-former candidates (Figure 5). A first anil is *N*-salicylideneaniline (**A**, reported with crystal structures REFCOD SALCAN to SALCAN04 in the CSD [34,35,36]) known to show strong photochromism; the second one is 4-fluoro-*N*-salicylideneaniline (**B**, reported as CAVQAR in the CSD [37]) known to show only thermochromism in the solid-state. Both compounds have been extensively studied [4,38,39]. With the principal functionality available on classical anils being the hydroxyl function, carboxylic acids have been tested in order to form a hydrogen bridge as this type of hydrogen bonding is strong and regularly encountered in co-crystals [25,26]. A typical synthon occurring between an alcohol and carboxylic acid group is the synthon  $D_2^2(4)$  (according to Etter Nomenclature [33]) shown in Figure 6. Another common synthon is  $R_2^2(6)$  (which would extend to  $R_2^2(10)$  in the case of anils) but wasn't observed here.

Co-crystals were identified using a mechanochemical approach (see experimental details). All possible combinations of 1:1 molar ratio between the co-formers and the anils were tested. A change in XRPD pattern (Figure 7) is expected to be related to either a change in polymorphic nature of one of the compounds, degradation (=reaction) or co-crystal formation. When degradation occurred (usually dissociation of anil in amine and aldehyde), the result was discarded.

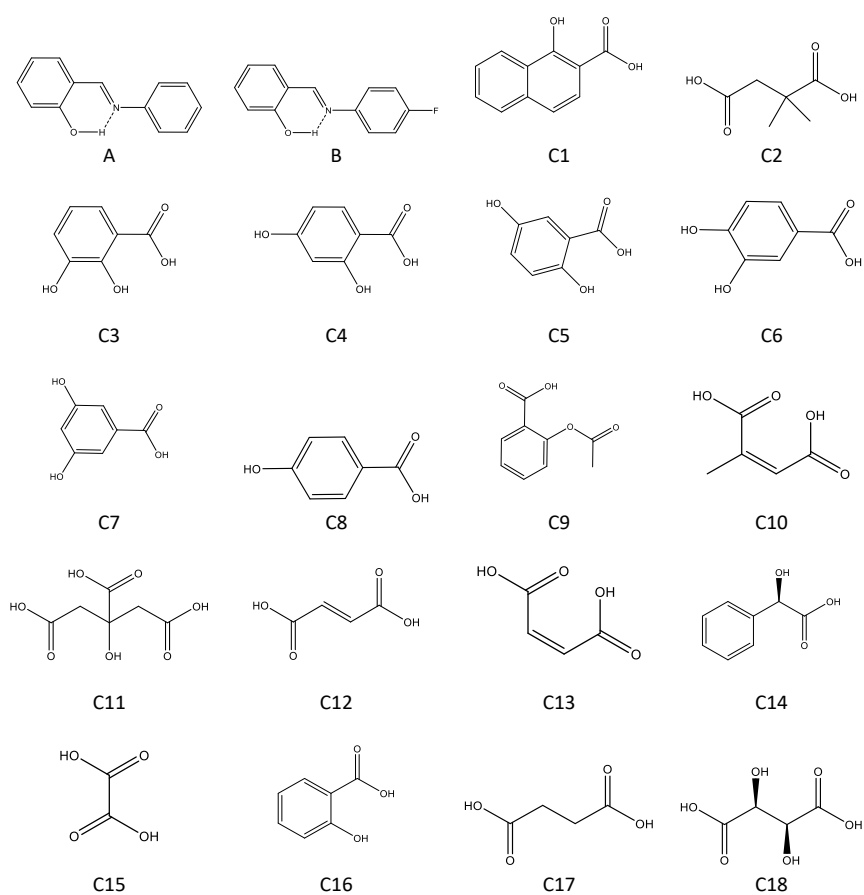


Figure 5: Compounds studied (IUPAC name in Table 1).

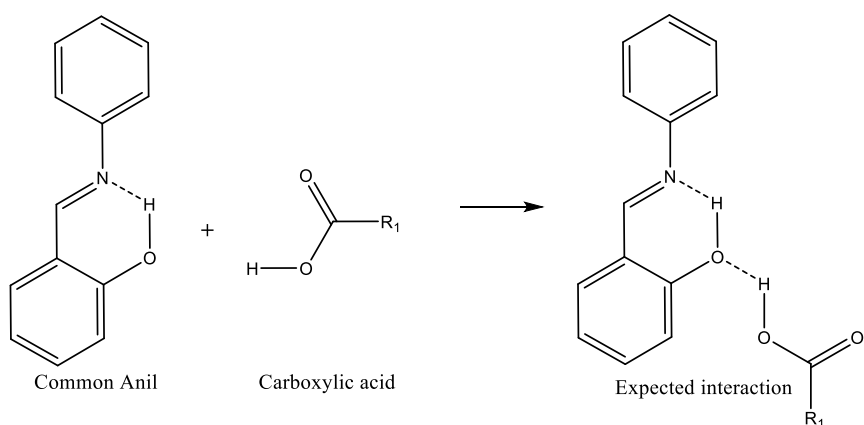


Figure 6: Expected  $D_2^2(4)$  supramolecular interaction [33] between *N*-salicylideneaniline and a carboxylic acid (R1 stands for alkyl group).

As shown in table 2, a positive hit was obtained when working with *N*-salicylideneaniline (entry **A**) and citraconic acid (Entry **C10**). Figure 7 shows that the XRPD patterns of the ground material is different from any of the known polymorphic forms of **A**, as well as from the XRPD pattern of citraconic acid. NMR analysis confirmed no degradation occurred, leaving co-crystal formation as the likely outcome, as confirmed by single crystal analysis. This result shows how co-crystallization can effectively occur even when a limited amount of functional groups is present on the target compound. For compound **B**, a total of 4 positive results were identified, using 2,4-dihydroxybenzoic acid, 3,4-dihydroxybenzoic acid, maleic acid, or oxalic acid as a co-former.

Table 2: XRPD and H-NMR comparison results between ground compounds and reference. X implies a perfect superposition of XRPD data, XX implies reaction/degradation of products and v means a structural change without degradation of starting materials (co-crystal or polymorph) <sup>2</sup>

Ground with:	A ( <i>N</i> -salicylideneaniline)	B (4-fluoro- <i>N</i> -salicylideneaniline)
<b>C1</b> (1-hydroxy-2-naphtoic acid)	X	X
<b>C2</b> (2,2-dimethylsuccinic acid)	X	X
<b>C3</b> (2,3-dihydroxybenzoic acid)	X	X
<b>C4</b> (2,4-dihydroxybenzoic acid)	XX	V
<b>C5</b> (2,5-dihydroxybenzoic acid)	X	X
<b>C6</b> (3,4-dihydroxybenzoic acid)	XX	V
<b>C7</b> (3,5-dihydroxybenzoic acid)	X	X
<b>C8</b> (4 hydroxybenzoic acid)	X	X
<b>C9</b> (acetylsalicylic acid)	X	X
<b>C10</b> (citraconic acid)	V	XX
<b>C11</b> (citric acid)	X	X
<b>C12</b> (fumaric acid)	X	X
<b>C13</b> (maleic acid)	XX	V
<b>C14</b> (mandelic acid R)	X	X
<b>C15</b> (oxalic acid)	XX	V
<b>C16</b> (salicylic acid)	X	X
<b>C17</b> (succinic acid)	X	X
<b>C18</b> (tartaric acid D)	X	X

### Co-crystals of 4-fluoro-*N*-salicylideneaniline

Although 4 novel co-crystals of 4-fluoro-*N*-salicylideneaniline are suspected based on the data in Table 2, no single crystals of these have been obtained so far. One reason could be the sensitivity of anil to hydrolysis catalyzed by acids (co-formers). As solvent used are all slightly hygroscopic process like slow evaporation could lead to the degradation of anil and

<sup>2</sup> Screening was limited to grinding methods, so the possibility exists that some co-crystals might have been overlooked.

recombination of amine with the co-former to make a salt. Such a process should then be performed under water-free atmosphere to avoid this.

Furthermore, DRS analyses on the ground co-crystal powders did not show significant differences with respect to the reference compound, nor did irradiation at different wavelengths for prolonged periods. These co-crystals, are thus, like the reference parent compound, expected to be thermochromic, with no significant difference between the keto-enol equilibrium found in the parent compound as compared to that within the co-crystals.

#### **Co-crystal between *N*-salicylideneaniline (A) and citraconic acid (C10)**

A single crystal was successfully grown and structural analysis shows both compounds to co-crystallize in the  $P2_1/c$  space group (structural details are presented in table 3), with the expected  $D_2^2(4)$  synthon (which is a combination at the binary level of S(6) and D patterns) forming between the carboxylic acid group and the phenolate function (Figure 8). To the best of our knowledge, we are the first to report on a direct impact of co-crystallization on the functional groups that are involved in the thermochromic and photochromic nature of the anils by impacting the hydrogen bonding pattern. The co-crystal is not a salt as the carboxylic proton was clearly visible in the density maps and the carbon-oxygen bond lengths in the carboxylic group are significantly different, identifying them as a C=O double bond (1.223(2) Å) and a single C-O bond (1.298(2) Å), opposed to the salt form where equal bond distances are expected.

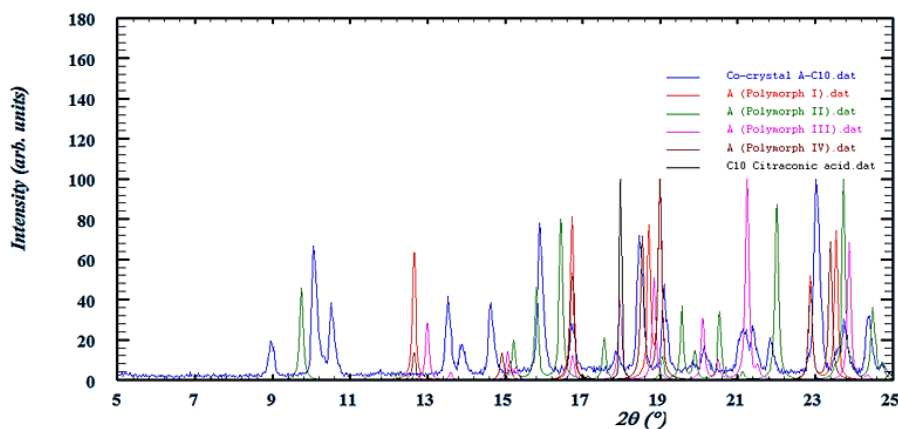


Figure 7: XRPD pattern of **A-C10** powder versus references: the ground mixture (blue spectra) is clearly different from all references of **A** (four polymorphs) and **C10** (black).

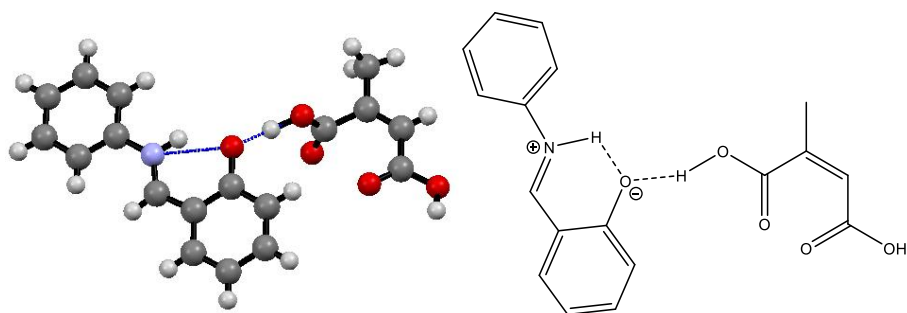


Figure 8 left: ORTEP projection of crystal structure of co-crystal between anil **A** and co-former **C10**. Dashed blue line represent the  $D_2^2(4)$  synthon with two hydrogen atoms shared between the three electronegative atoms. Right: schematic representation of the structure showing the zwitterionic character of anil moiety.

To study the impact of co-crystallization on the keto-enol equilibrium, we compare the main bond lengths involved in the **A-C10** co-crystal with those of the free anil (**A**), as well as with a statistical analysis as specified in the experimental details of similar derivatives available in the CSD (Figure 5). Results are given in table 3.

Table 3: Expected values with their standards deviations<sup>3</sup> for bond lengths 2 to 5 of Enol-Imine and Keto-form (regardless to the temperature) based on CSD statistical analysis and comparison with **A-C10** co-crystal (bond lengths measured and their standard deviations) and **A** (SALCAN01).

	Bond 2, $\sigma$ (Å)	Bond 3, $\sigma$ (Å)	Bond 4, $\sigma$ (Å)	Bond 5, $\sigma$ (Å)
Enol-Imine	1.344, 0.022	1.406, 0.017	1.45, 0.021	1.286, 0.021
Conj. Ketone	1.249, 0.034	1.463, 0.032	1.375, 0.04	1.358, 0.027
<b>A</b> (120K)	1.352, 0.003	1.419, 0.003	1.455, 0.003	1.280, 0.003
<b>A-C10</b> (100K)	1.316, 0.002	1.424, 0.003	1.407, 0.003	1.309, 0.002

Table 3 clearly shows **A** to exist in an enol/*cis*-keto equilibrium which is strongly displaced towards the enol form. An important structural variation is observed when **A** co-crystallizes with **C10** (crystal data and structure refinement are given in table 4), as bond lengths indicate the equilibrium is shifted in favor of the keto form. As data were collected at 120 K for **A** and 100 K for **A-C10** we expect only a neglectable temperature effect on the bond lengths. Bonds 2 and 4 are shorter within the co-crystal, whereas the length of bond 5 increases.

Even though these bond lengths indicate a displacement towards the keto form, at this stage, the use of the term 'keto'-form does seem inappropriate. The 'keto'-form can actually be represented under two resonance structures, either using a charge neutral keto representation or through a zwitterionic representation. This latter seems much more pertinent in the current case: the hydrogen of the enol is clearly transferred to the nitrogen atom as shown by the Xray density maps. Even though, this clear transfer of the hydrogen atom, bond 2 (1.316 Å) is intermediate between a pure C=O double bond (1.249 Å) and a C-OH single bond (1.344 Å) as shown in table 3. Furthermore, the C-C bond 3 (1.424 Å) is almost not

---

<sup>3</sup> The errors of the CSD search are one order of magnitude higher compared to the error on a single structure, as they are derived from an ensemble of structure.

affected whereas a clear increase up to 1.46 Å would be observed (according to table 3) if one would expect a more keto character. Finally, the C-N bond 5 length (1.309 Å) is closer to that of a C=N (1.286 Å) double bond, than that of a C-N single bond (1.358 Å). These combined observations suggest to consider the 'keto'-form rather as a 'zwitterionic form' in this case, and the keto-enol equilibrium should rather be presented as the "enol-zwitterionic" equilibrium shown in Figure 9. This zwitterionic form was already reported for anils inserted into zeolites however in that case no photochromism was observed [23].

The displacement from the enol form towards the zwitterionic form upon co-crystallization is likely induced by the hydrogen donating effect of the co-former (synthon  $D_2^2(4)$ ). The directionalized interaction of the co-former hydrogen towards the alcohol function, could allow for a better hydrogen transfer of this latter to the imine function, and stabilizes the negative charge on the oxygen atom, create by doing so. This displacement also induces a change in optical properties as illustrated in Figure 10 showing the color change between the original compound and the co-crystals, at room temperature and at 50 °C. At room temperature co-crystal **A-C10** has a more intense yellow color compared to the reference **A** which can be explained by an increased amount of *zwitterionic* form. When heated up to 50 °C anil **A** starts to melt and is characterized by a more intense brown color whereas **A-C10** remains solid, exhibiting a more intense yellow color (melting occurs at 80 °C). When cooled to -80 °C anil **A** turns to pale yellow whereas no change is observed for **A-C10**.

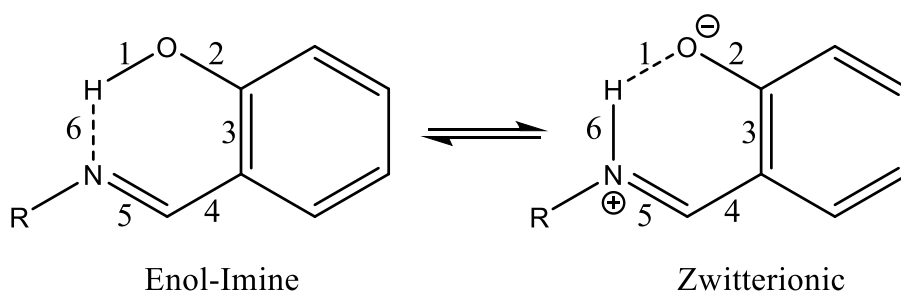


Figure 9: New equilibrium pattern based on structural analysis

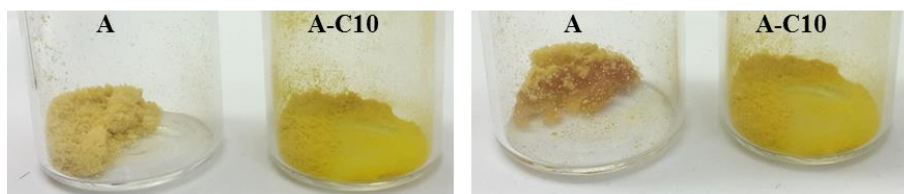


Figure 10: Comparison between **A** and **A-C10** at room temperature (left) and upon heating at 50 °C (right).

To study the effect of co-crystallization on the photochromic properties of the parent anil, Kubelka-Munk spectra of the anil **A** and co-crystal **A-C10** were measured under standard conditions (room temperature and pressure) as shown in Figure 11. Data are normalized to 1 for the peak at 395 nm. Spectra of the two compounds clearly differ. No such difference is found when comparing the spectrum of reference **A** (polymorph alpha 2) with that of a physical mixture (see supporting information) between **A** and **C10**. Both the parent anil **A** as well as the co-crystal **A-C10** show a strong absorption band at 375 nm, attributed to the absorption of the enol form [4]. The strongest difference for the co-crystal comes from the very strong absorption band centered on 488 nm which is typically attributed to the keto form (or the zwitterionic form in our case) of the product. This form appears to be strongly populated which is in line with the structural analysis, pointing towards an increased amount of zwitterionic form in the equilibrium. The weak absorption at 450 nm clearly shows why the parent anil, was labeled non-thermochromic.

When zooming into the 525-700 nm range both forms present a small shoulder centered on 600 nm, attributed to the *trans*-keto form.

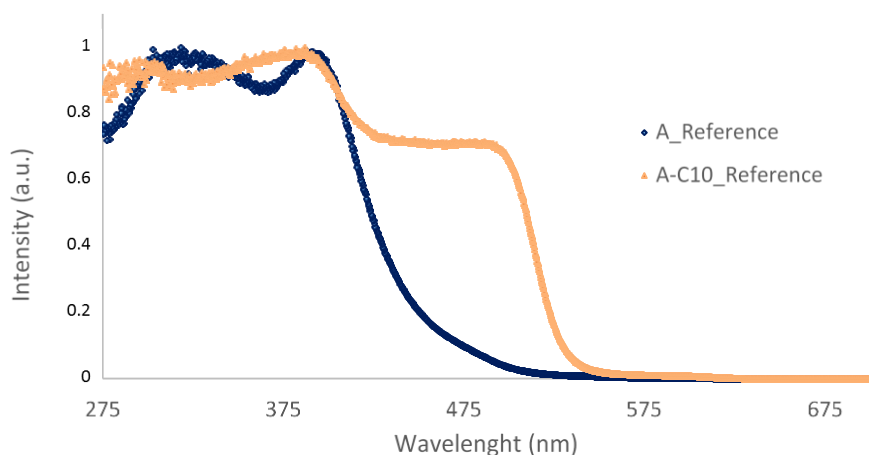


Figure 11: Kubelka-Munk spectra of anil **A** and co-crystal **A-C10** at room temperature.

The photochromic effect of both forms was studied by comparing variation of the absorption spectra upon prolonged irradiation (30 minutes to 1 hour). Irradiation of **A** at 365 nm leads to an increase in *cis*-keto and *trans*-keto form, whereas an irradiation at 436 nm leads to a depopulation of the already small amount of *cis*-keto form in favor of the *trans*-keto form, in agreement with the earlier work by Fujiwara *et al.* [15]. However, in the case of **A-C10** a surprisingly different behavior is observed. Irradiation at 365 nm, leads to both a strong depletion of the *cis*-zwitterionic form (centered at 450 nm) and *trans*-keto (600 nm) forms relatively to the enol form (centered at 380 nm). Subsequent irradiation at 546 nm (+/- 20 minutes) restores the original situation contrary to what is observed for the parent anil (Figure 12). Another difference observed is irradiation at 436 nm which has no observable effect on the zwitterion/enol equilibrium in this case. These results might indicate that the *trans*-keto form is also impacted by co-crystallization, and might also show a strong zwitterionic character, although this remains to be proven.

After prolonged irradiation, the initial equilibrium can be restored thermally (without irradiation), but at room temperature, one requires about 8 hours to return to original levels.

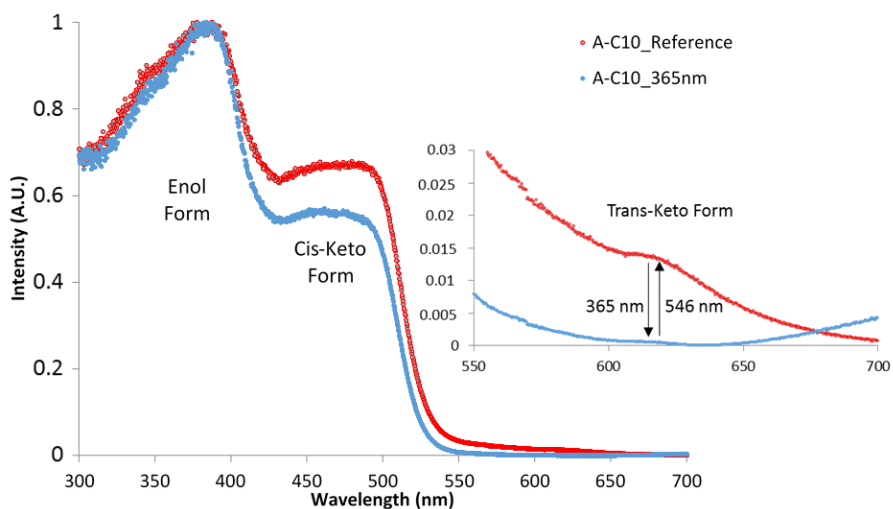


Figure 12: Kubelka-Munk spectra of **A-C10** after irradiation at 365 nm (blue) for 20 minutes and reference (red).

From the results above, it is clear that co-crystallization strongly affects the photochromic behavior of anils, likely due to the impact on the hydrogen bonding pattern which is affected. To fully understand the underlying mechanism, one would have to review the scheme as presented in Figure 2. A future full investigation using, e.g., femtosecond spectroscopy could be interesting to elucidate this behavior.

Our results clearly show that tackling the structure of anils through co-crystallization and more specifically through alteration of the hydrogen bonding pattern directly involved in the keto (zwitterion)/enol equilibrium, offers new possibilities for varying the photochromic behavior of anils, and might lead to promising results on future candidates.

Table 4: Crystal data and structure refinement for co-crystal **A-C10**

Co-crystal <b>A-C10</b>	
Empirical formula	C <sub>18</sub> H <sub>17</sub> NO <sub>5</sub>
M	327.32
T [K]	100(2)
Crystal system	Monoclinic
Space group	<i>P</i> 2 <sub>1</sub> / <i>c</i> (no.14)
<i>a</i> [Å]	10.7434(4)
<i>b</i> [Å]	8.3025(2)
<i>c</i> [Å]	19.0548(7)
$\beta$ [°]	113.813(3)
<i>V</i> [Å <sup>3</sup> ]	1554.94(10)
<i>Z</i>	4
$\rho_{calcd}$ [Mg m <sup>-3</sup> ]	1.398
F(000)	688
$\mu$ [mm <sup>-1</sup> ]	0.142
Crystal size [mm]	0.15x0.10x0.10
$\vartheta_{max}$ [°]	31.2129
Reflection collected/unique	7945/2471
<i>R</i> <sub>int</sub>	0.0393
<i>R</i> <sub>1</sub> [ <i>I</i> >2 $\sigma$ ( <i>I</i> )]	0.0401
<i>wR</i> <sub>2</sub>	0.0926
Largest diff. Peak/hole [e Å <sup>-3</sup> ]	0.152/-0.223

## Conclusion

We have crystallized a co-crystal of *N*-salicylideneaniline and citraconic acid which shows new and unexpected photochromic behavior. A careful structural analysis reveals co-crystallization affected bond lengths and electronic structure of the photochromic center in such a manner to suggest viewing the classical keto-enol equilibrium rather as an enol-zwitterionic equilibrium. This effect is due to the co-formers we chose for synthon creation in order to build the co-crystal. By altering the hydrogen bonding pattern of the alcohol functionality, we are able to impact the

photochromic mechanism directly. To do so, we added a hydrogen donor to the alcohol group, creating a push-and-pull effect on the hydrogen involved in the enol-zwitterionic equilibrium. For the parent *N*-salicylideneaniline, co-crystallization not only led to a substantial change in the classical view of the keto/enol equilibrium, which is in our case described as an enol-zwitterionic equilibrium, but furthermore to some unexpected photochromic behavior, which up to now remains unexplained by the classical scheme. These findings open new ways to fine-tune photochromism of *N*-salicylideneaniline derivatives: one can not only increase the space available in the crystal structure through co-crystallization (allowing cis-trans isomerization), but one can also directly impact the electronic behavior of the centers involved in the photochromic and thermochromic behavior.

#### **Supporting Information.**

Structures described in this contribution have been deposited at the Cambridge Crystallographic Data Centre and allocated the deposition numbers CCDC 1448718 for **A-C10**. Supporting information also contains TGA, DSC, XRPD and DRS patterns of discussed compounds. This material is available free of charge via the Internet at:

<https://pubs.acs.org/doi/10.1021/acs.cgd.6b00108>.

#### **Corresponding Author**

Email: [tom.leyssens@uclouvain.be](mailto:tom.leyssens@uclouvain.be).

#### **Acknowledgments.**

The authors would like to thank the UCL for financial support (Gabriel Mercier is a UCL teaching assistant). This work was published thanks to funding of "Actions de Recherche Concertées (ARC) de la Direction générale de l'Enseignement non obligatoire et de la Recherche scientifique – Direction de la Recherche scientifique – Communauté française de Belgique. The authors would like to thank Johan Wouters (UNamur) for his review of the article.

## References

- [1] E. Hadjoudis, S. D. Chatziefthimiou, I. M. Mavridis, *Current Organic Chemistry*, **2009**, 13, 269-286.
- [2] G. H. Brown, *Photochromism*, Wiley-Interscience, New York **1971**.
- [3] V. de Gaouck, R. J. W. Le Fevre, *J. Chem. Soc.* **1939**, 1457.
- [4] E. Hadjoudis, *Molecular Engineering*, **1995**, 5, 301.
- [5] B. Kaitner, M. Zbačnik, *Acta Chim. Slov.* **2012**, 59, 670.
- [6] Robert, F., **2010**, *Engineering N-salicylidene aniline derivatives: from solid-state molecular switches to multifunctional organic-inorganic architectures*. PhD thesis, Université Catholique de Louvain, Belgique.
- [7] M. Sliwa, S. Létard, I. Malfant, M. Nierlich, P. G. Lacroix, T. Asahi, H. Masuhara, P. Yu, K. Nakatani, *Chem. Mater.* **2005**, 17, 4727.
- [8] K. Amimoto, T. Kawato, *Journal of Photochemistry and Photobiology*, **2005**, 6, 207–226.
- [9] B. C. Jain, P. Mirchandani, B. H. Iyer, P. C. Guha, *Science and Culture*, **1946**, 11, 567-8.
- [10] M. D. Cohen, G. M. J. Schmidt, S. Flavian, *Journal of the Chemical Society*, **1964**, June, 2041-2051.
- [11] W. F. Richey, R. S. Becker, *Journal of Chemical Physics*, **1968**, 49, 5, 2092-2101.
- [12] F. Milia, E. Hadjoudis, J. Seliger, *Journal of Molecular Structure*, **1988**, 177, 191-197.

- [13] F. Robert, A. D. Naik, F. Hidara, B. Tinant, R. Robiette, J. Wouters, Y. Garcia, *European Journal of Organic Chemistry*, **2010**, 621–637.
- [14] F. Robert, P.-L. Jacquemin, B. Tinant, Y. Garcia, *CrystEngComm*, **2012**, 14, 4396-4406.
- [15] T. Fujiwara, J. Harada, K. Ogawa, *J. Phys. Chem.*, **2004**, 108, 4035-4038.
- [16] S. D. Chatziefthimiou, Y. G. Lazarou, E. Hadjoudis, T. Dziembowska, I. M. Mavridis, *J. Phys. Chem.*, **2006**, 110, 23701-23709.
- [17] M. Sliwa, P. Naumov, H.-J. Choi, Q.-T. Nguyen, B. Debus, S. Delbaere, C. Ruckebusch, *ChemPhysChem*, **2011**, 12, 1669–1672.
- [18] T. Sekikawa, O. Schalk, G. Wu, A. E. Bogulavskiy, A. Stolow, *J. Phys. Chem.*, **2013**, 117, 2971-2979.
- [19] E. Hadjoudis, V. Verganlakis, C. Trapalis, G. Kordas, *Molecular Engineering*, **1999**, 8, 459-469.
- [20] F. Robert, A. D. Naik, B. Tinant, R. Robiette, Y. Garcia, *Chem. Eur. J.*, **2009**, 4327-4342.
- [21] M. S. Rawat, S. Mal, P. Singh, *Open Chemistry Journal*, **2015**, 2, 7-19.
- [22] T. Haneda, M. Kawano, T. Kojima, M. Fujita, *Angewandte Chemie International Edition*, **2007**, 46, 6643–6645.
- [23] I. Casades, M. Álvaro, H. García, M. N. Pillai, *Eur. J. Org. Chem.*, **2002**, 2074-2079.

- [24] F. Robert, A. D. Naik, B. Tinant, Y. Garcia, *Inorganica Chimica Acta*, **2012**, 380, 104-113.
- [25] G. R. Desiraju, *J. Am. Chem. Soc.*, **2013**, 135, 9952–9967.
- [26] G. R. Desiraju, J. J. Vittal, A. Ramanan, *Crystal Engineering: A textbook*, World Scientific Publishing Co. Pte. Ltd., IISc Press, **2011**.
- [27] K. Johmoto, A. Sekine, H. Uekusa, *Cryst. Growth Des.*, **2012**, 12, 4779-4786.
- [28] K. M. Hutchins, S. Dutta, B. P. Loren, L. R. MacGillivray, *Chemistry of Materials*, **2014**, 26 (10), 3042-3044.
- [29] V. Dyadkin, SNBL Tool Box, version 0.5, Swiss Norwegian Beam Line at ESRF, Grenoble, France, **2013**.
- [30] CrysAlys PRO, Agilent Technologies UK Ltd., Oxford, UK, **2013**.
- [31] G. M. Sheldrick, *Acta Crys. A*, **2008**, 64, 112.
- [32] F. H. Allen, O. Kennard, D. G. Watson, *J. CHEM. SOC., Perkin Trans. II*, **1987**, 12, 1-19.
- [33] M. C. Etter, J. C. MacDonald, *Acta Crys.*, **1990**, B46, 262-266.
- [34] R. Destro, A. Gavezzotti, M. Simoneta , *Acta Crys. B*, **1978**, 34, 2867.
- [35] F. Arod, M. Gardon, P. Pattison, G. Chapuis, *Acta Cryst. C*, **2005**, 61, 317.
- [36] F. Arod, P. Pattison, K. J. Schenk, G. Chapuis, *Cryst. Growth Des.*, **2007**, 7, 1679.

- [37] J. Burgess, J. Fawcett, D. R. Russell, S. R. Gilani, V. Palma, *Acta Crys.*, **1999**, C55, 1707-1710.
- [38] A. Senier, F. G. Shephard, *J. Chem. Soc.*, **1909**, 95, 1943.
- [39] D. Goeckeritz, H. Brueckner, R. Pohloudek-Fabini, *Pharmazie*, **1967**, 3, 154-157.



## **Preface of Chapter 3**

The chapter 3, which is entitled “New Insights into Photochromic Properties of N-Salicylideneaniline Derivatives Using a CoCrystal Engineering Approach” has been published in *Crystal Growth and Design* and the text is presented as such.



## Chapter 3

# New Insights into Photochromic Properties of *N*-Salicylideneaniline Derivatives Using a CoCrystal Engineering Approach\*

*Gabriel M. Mercier*<sup>a</sup>, *Koen Robeyns*<sup>a</sup>, *Nikolay Tumanov*<sup>b</sup>, *Benoit Champagne*<sup>b</sup>, *Johan Wouters*<sup>b</sup>, *Tom Leyssens*<sup>a</sup>

<sup>a</sup> Institute of Condensed Matter and Nanosciences, Université catholique de Louvain, 1348 Louvain-la-Neuve, Belgium

<sup>b</sup> Unité de Chimie Physique Théorique et Structurale, Chemistry Department, Namur Institute of Structured Matter (NISM), University of Namur, 61 rue de Bruxelles, B-5000 Namur, Belgium

\* Published in *Crystal Growth & Design* **2019** 19 (10), 5544-5556  
DOI: 10.1021/acs.cgd.9b00363

## **Abstract**

In this contribution, we aim to modify the photochromic properties of anils using a crystal engineering approach. Previous work has shown cocrystallization to alter the photochromic behavior of anils. Here a full screening of 15 anil derivatives (including 8 newly described anils) with 21 coformers (carboxylic acids, amides and halogenated benzene derivatives) was performed, resulting in 89 new anil cocrystals. This large amount of results allows drawing statistically valid insights on the complex photochromic mechanism providing evidence of a continuous phenomenon instead of the classic binary photochromic/non-photochromic one. This is supported by the discovery of “weakly photochromic compounds” presented in this contribution. All the results allowed confirming that an enol-imine character is a requirement and that reducing the amount of short contacts involving the moieties of interest is an interesting way to fine-tune properties as this acts on both electronical and structural aspects. Following this “continuous hypothesis”, the role of the dihedral angle has been explored and shown to be related to the intensity of photochromism instead of being determinant for its occurrence. On top, in this contribution we present a novel way of interpreting DRS (Diffuse Reflectance Spectroscopy) data.

## Introduction

Photochromism, defined as a light induced reversible color change of a material [1] is a property of continuous interest as it serves for many applications such as: optical devices [2,3], intelligent screens [4], changing color lenses [5], secured inks for banknotes or confidential notes [6,7] and optical data storage [8,9].

Among photochromic materials *N*-Salicylideneaniline (anil) derivatives are among the most studied as they present this property at the solid-state, showing high solid-state stability [10] and easy synthesis [11,12].

Anil photochromism is attributed to a *cis-trans* isomerization mechanism as illustrated in Figure 1. At room temperature, most anils present an enol /*cis*-keto equilibrium usually in favor of the enol form. This equilibrium involves an internal proton transfer between the nitrogen of the azomethine bond and the oxygen of the ortho-phenolic moiety. A change in temperature shifts the equilibrium to the *cis*-keto form, associated with a change in color from white (enol) to yellow (*cis*-keto). Upon UV-*vis* irradiation, both enol and *cis*-keto form can undergo a transition to a *trans*-keto form [3,11-18]. As this latter absorbs at higher wavelengths, this “photochromic” transition is clearly visible with the solid usually presenting a color change from colorless/yellow to red. Even if many anils are photochromic in solution [19], only a limited number of them present this feature in the solid state.

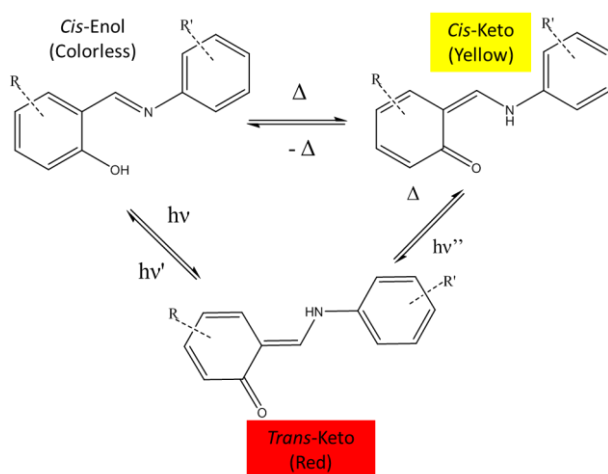


Figure 1: general scheme of the main thermo- and photochromic transitions in anils.

To understand why at the solid state some anils are photochromic and others not, early studies tried to link the photochromic characteristic to structural features, mainly focusing on the dihedral angle present between the aromatic moieties. Indeed, most of the photochromic anils reported show a dihedral angle  $\phi > 25^\circ$  [18,20-22] while planar anils usually tend to be thermochromic only [23]. However, recent findings disclosed this feature is no longer sufficient, with increasing counter-examples appearing in literature [19]. The full structural environment of an anil does nevertheless have an important impact on its photochromism as shown by alteration of the properties when inserting anils in environments such as a polymers [21], Metal-Organic Frameworks (MOFs) [24,25], zeolites [26] or through a cocrystallization approach [27-29]. All of these studies combined with a theoretical study [22] highlight the necessity of an open-packing structure to be a prerequisite for photochromism (presence of an interplanar distance of at least 3.3 Å between molecular planes) [14,30].

Even though an open-packing is a requirement, it is not a guarantee for photochromism. A full understanding of why some anils are photochromic and others are not remains an open question. Such an understanding can help guide future synthetic efforts for novel photochromic materials, and furthermore will allow transforming non-respondent anils into photochromically active ones by changing structural surroundings [28]. Cocrystallization might be the most promising approach to perform such studies, as it is commonly applied to modify and improve the chemical and physical properties of pharmaceutical compounds [31-33]. This approach has already been used in the context of Schiff bases (to which anils belong [15]) and specifically in the case of *N*-Salicylideneaniline derivatives through hydrogen bonding [27-29] which recently provided a successful way to reversibly switch properties through hydration/dehydration [34] or through ammoniation/deammoniation in case of salts [35]. Another recent approach used halogen bonding [36,37] as a tool to change photochromical properties.

In order to gain new insights into the link between photochromic activity and structural features, we performed a statistical study on a full set of anils as well as their cocrystals. By considering 15 different anils and coupling them to 21 coformers, a substantial dataset is obtained with a variety of different structural environments for a limited set of target compounds. This data underlines cocrystal screening efficiency for anils, and allows linking structural features to the photochromic characteristics. Furthermore, we were able to show that each non-photochromic anil could be 'switched on' using a cocrystallization approach, highlighting the fact that, in principle, all anils can become photochromic in the solid state when given the right structural surroundings. From this dataset we were able to place many hypotheses/results already present in literature in perspective such as the keto-enol equilibrium, dihedral angle, free space and short contacts confirming the importance of these last ones over the ortho-hydroxy moiety [19] but also with the moving moiety which is a new conclusion to the best of our knowledge.

### **Experimental Section**

Starting Materials and Synthesis of the different anils are described in the supporting information (section 10).

#### **Mechanochemical Cocrystal Screening.**

Liquid-assisted grinding (10  $\mu$ l of acetonitrile) was performed using an equimolar (+/- 10<sup>-3</sup> mol) mixture of starting materials. Samples were ground in a RETSCH Mixer Mill MM 400 for 90 min with a beating frequency of 30 Hz. The resulting powders were characterized using X-ray Powder Diffraction. Upon cocrystal identification, attempts were made to obtain a single crystal of suitable size and quality for X-RD single crystal measurement. As chemical reactions can occur during liquid-assisted grinding, <sup>1</sup>H-NMR was used to eliminate samples that led to degradation/reaction.

**Single Crystal Formation.** Solvent evaporation at room temperature starting from an under-saturated solution, yielded single crystals of suitable quality for: C-C16, D-C1, E, E-C1, E-C2, E-C4, E-C5, E-C6, E-C8, E-C8, E-C9, E-

C11, E-C12 (solvate), F-C4 (hydrate), F-C5, H, I-C10 (hydrate), L (hydrate), M, M-C15, N, N-C5 (hydrate), O-C13 from acetonitrile; for C-C20 from ethanol; for D from acetone; and for F-C9 from ethyl-acetate.

Saturated solutions were prepared by adding an excess of compound to acetonitrile. By combining equivalent supernatant volumes of target anil and coformer and leaving this combined solution to evaporate at room temperature single crystals were obtained for A-C20, a monohydrate of D (from the experiment coupling anil D and coformer C2), a dihydrate structure of E (from the experiment coupling anil E and coformer C13) for anil G (from the experiment coupling anil G and coformer C3) and for anil H (from the experiment coupling anil H and coformer C9).

#### **X-Ray Powder Diffraction (XRPD).**

X-ray diffraction measurements were performed on a Siemens D5000 diffractometer equipped with a Cu X-ray source operating at 40 kV and 40 mA and a secondary monochromator allowing to select the  $K\alpha$  radiation of Cu ( $\lambda=1.5418 \text{ \AA}$ ). A  $2\theta$  scanning range from  $2^\circ$  to  $50^\circ$  at a scan rate of  $0.6^\circ \text{ min}^{-1}$  was applied. Simulated patterns of the known starting compounds were calculated from their single crystal structures with Mercury 3.5.1 and plotted with WinPLOTR (version: September 2015). For each reported mixture the diffraction pattern (in blue) is superimposed onto simulated patterns of its components (in red for the corresponding anil and green for the co-former). All data are normalized to 100 for the highest peak. We assume formation of new phases when at least 2 new peaks appear and at least 2 reference peaks are missing.

#### **Single Crystal X-Ray Diffraction.**

Structures were integrated with the CrysAlisPro software [38] and the implemented multi-scan absorption correction procedure was applied. Each structure was solved by direct methods, SHELXT [39] and refined by full-matrix least squares on  $|F|^2$  using SHELXL-2014 or 2018 [40]. Non-hydrogen atoms were refined anisotropically and hydrogen atoms were either placed on calculated positions in riding mode with temperature factors fixed at 1.2 times  $U_{eq}$  of the parent atoms and 1.5 times  $U_{eq}$  for methyl groups, or located in the Fourier difference maps when involved in H-bonds.

### Diffuse Reflectance Spectroscopy Measurements.

DRS spectra were obtained with a Varian 5E spectrophotometer equipped with a “praying mantis” diffuse reflection accessory and were converted to absorption spectra using the Kubelka-Munk function [41,42] and using PTFE as a reference for baseline correction. Spectra were measured on pure solid and were normalized relatively to their highest peak. Signal assignment was supported by reported band range for *N*-Salicylideneaniline derivatives [43]. Prior to the DRS measurement, the purity of the new solid phase was checked through XRPD to ensure the cocrystal phase is the only phase present, and the measurement does not suffer interference from one of the parent compounds. DRS results show an important shift of the trans-keto band (CFR Table 2) which also inherently confirms the presence of a new phase.

A novel alternative way of looking at the DRS data is presented here. Photochromic profiles are obtained by plotting the ratio of the spectra after/before irradiation. According to Kubelka-Munk theory, the Kubelka-Munk function  $F(R) = k/s$  where  $R$  is the reflectance,  $k$  is the molar extinction coefficient from the UV-Vis measurements in solution and  $s$  a scattering coefficient depending on all physical parameters of the sample surface [41,44]. If one assumes each existing electronic state (noted  $\xi_i(T, \lambda)$  with  $\lambda$  the probe wavelength) to contribute to  $k$ , then  $k$  is dependent on the population  $N_i(T)$  of these states and thus one can write:  $k(\lambda) = \sum_i N_i(T) \cdot \xi_i(T, \lambda)$ . The ratio of consecutive solid state measurements  $m$  and  $n$  (with conservation of the sample surface throughout the experiment) would give for a given wavelength:  $F_m(\lambda)/F_n(\lambda) = \sum_i N_{im}(T) \cdot \xi_i(T, \lambda) / \sum_{in} N_{in}(T) \cdot \xi_i(T, \lambda)$  under the assumption that the scattering coefficient  $s$  does not change. For a given wavelength and temperature, this ratio changes upon irradiation, if a change in population of absorbing species occurs. If no population change occurs, or the species do not respond at a given wavelength, a fixed ratio is obtained. The ratio can therefore be directly related to population changes independently of experimental parameters such as surface, scattering coefficient or powder grain-size. Under the assumption that only a limited amount of absorbing species are present, non-photochromical compounds should present a perfectly linear profile (i.e. no evolution of state populations) equal to 1 (in case there is no experimental variation) while

photo-respondent compounds should present upward and/or downward peaks as the state-population changes. In the context of this work, a change in ratio was considered significant when larger than  $\geq 0.3$  (30% intensity variation occurring over less than 50 nm). This value was chosen as experimental variations between consecutive measurements on a single sample were 10% (ratio change = 0.1) in the worst case. Considering 3 times this value, any change in ratio should represent a true population change. The highest ratio change is noted  $I_{\max}$  (in case of downward peak the ratio is inverted to have a clear comparison with normal cases). We then introduced  $\Delta = F(R)_j - F(R)_i$ , the absorption intensity difference between irradiated and non-irradiated compound (from normalized Kubelka-Munk measurements) at the wavelength where the ratio is highest. We found that  $\Delta$  values below 0.25 were not visible anymore by the naked eye.

Light irradiations were carried out with a MAX-303 lamp (Xenon light source 300 W) at 360 nm (by the use of 20 nm bandpass filters) for 30 minutes. Kubelka-Munk spectra were averaged over three measurements (removing and replacing the sample from the device between each but without changing the surface).

Thermal fading was analyzed by monitoring the evolution of absorption at 550 nm after irradiation (absorption measured each second over 6000 sec in a dark environment).

### **Short Contacts Analysis.**

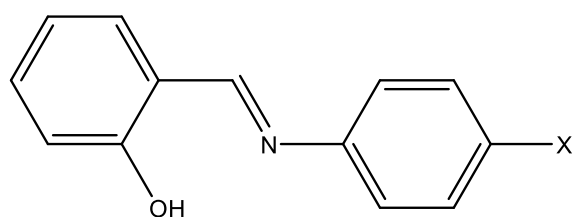
We measured the total amount of close contacts involving any atom of a moiety of interest (detailed in the text) within a defined distance  $D$ , allowing quantifying weak, medium and strong short contacts. Thus, we assigned a strong short contact when this contact is shorter than the sum of the Vander Waals radii of involved atoms (noted as  $\sum r_{vdw}$ , with values as defined in Mercury version 3.5.1) reduced by 0.05 Å ( $D < \sum r_{vdw} - 0.05$  Å). A medium short contact is considered for lengths comprised between  $\sum r_{vdw} - 0.05$  Å and  $\sum r_{vdw} + 0.05$  Å and a weak short contact for a length comprised between  $\sum r_{vdw} + 0.05$  Å and  $\sum r_{vdw} + 0.2$  Å. Hirshfeld surfaces and 2D molecular fingerprints were calculated and drawn using the  $D_{\text{norm}}$  function of CrystalExplorer 17.5 Software [45] and corresponding CIF files.

## Results

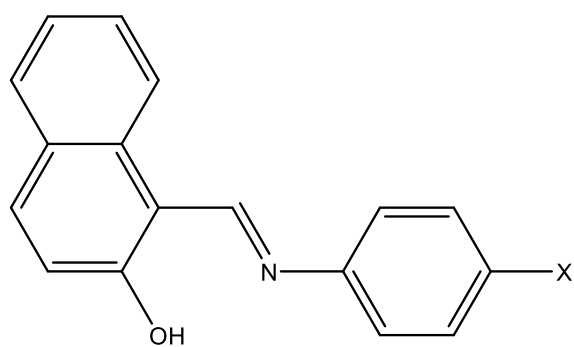
### Cocrystal screening

Scheme 1 shows the fifteen anil derivatives used (**A** to **O**) (see supporting information-section 10 for their synthesis) and Scheme 2 the selected 21 coformers (C1 to C21), among which carboxylic acids, amides and halogenated benzene derivatives. Table 1 shows the results of the full cocrystal screening between anils and coformers. For 33 combinations degradation of the anil occurred upon grinding.

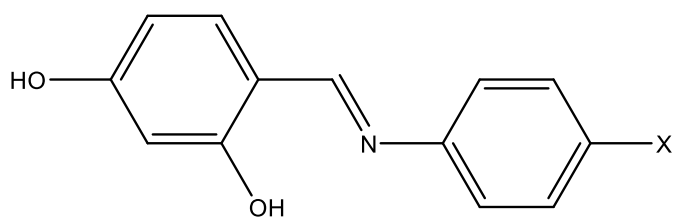
Table 1 shows a total of 95 cocrystals identified out of 315 possible combinations, 21 of which were structurally analyzed. This corresponds to a cocrystal formation success rate of +/- 30%. Even though such high rates are occasionally observed in literature [46] the generally accepted success rate is about 10 to 15% [44,47]. The high number observed here is likely due to the co-former selection, as we focused on co-formers already prove to cocrystallize with anils [28,29]. The efficiency of carboxylic acids as co-formers is apparent from Table 2 and is likely due to the possibility of forming hydrogen bonds between the carboxylic acid of the coformer and the anil –OH bond. It is also apparent from Table 1 that the second and third anil series (respectively with the naphthyl and para hydroxy group on the salicylidene moiety) have an enhanced tendency to form cocrystals. This can also be explained by intermolecular interactions such as  $\pi\cdots\pi$  interactions or hydrogen bonding with the –OH group.



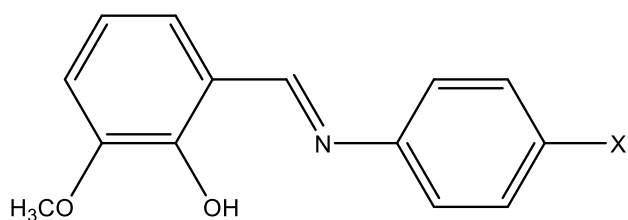
- A: X=H  
 B: X=F  
 C: X=COOH  
 D: X=CONH<sub>2</sub>



- E: X=H  
 F: X=F  
 G: X=COOH  
 H: X=CONH<sub>2</sub>

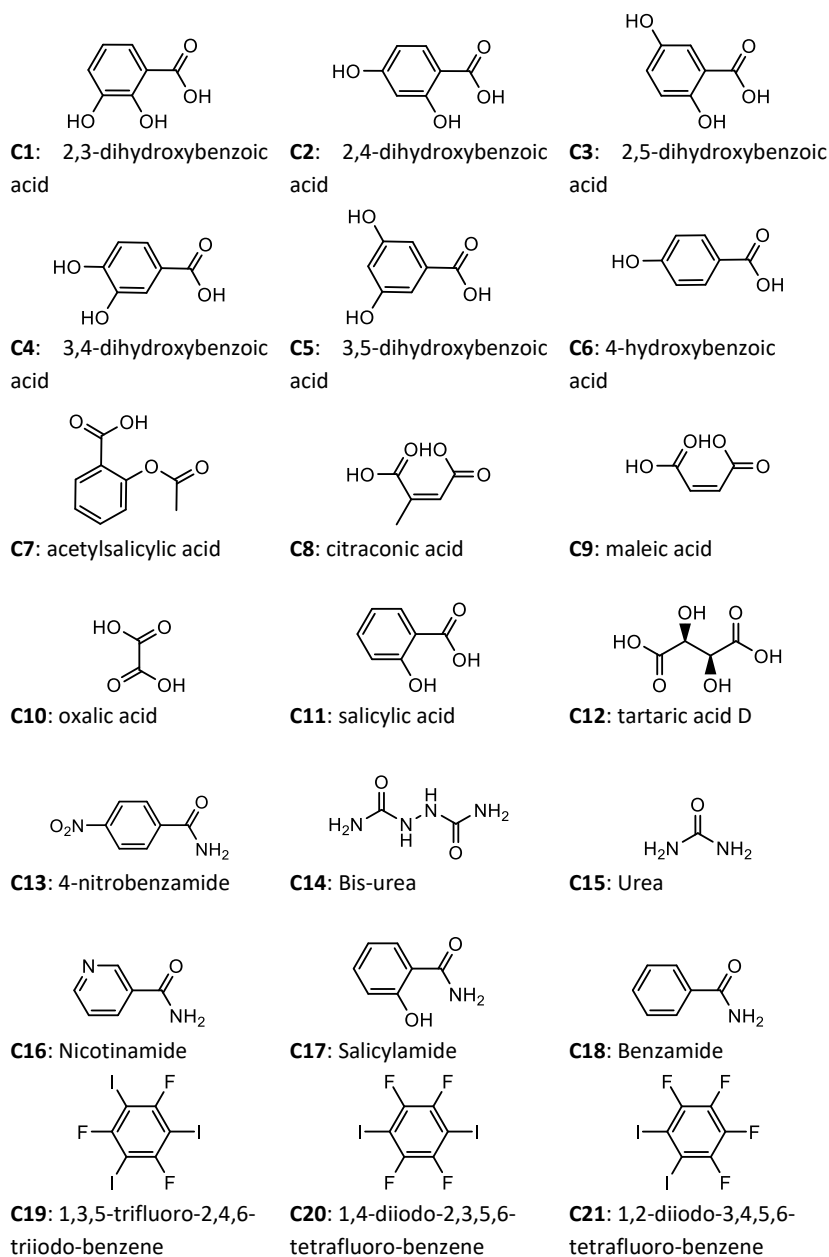


- I: X=H  
 J: X=F  
 K: X=COOH  
 L: X=CONH<sub>2</sub>



- M: X=H  
 N: X=F  
 O: X=COOH

Scheme 1: anils studied in this work.



Scheme 2: cofomers selected for the cocrystal screen.

Table 1: Cocystal screening results. Deg. = degradation. CC = cocystal formation and CC-SC = cocystal which is structurally characterized. Empty cell = no cocystal observed.

	A	B	C	D	E	F	G	H	I	J	K	L	M	N	O
C1				CC-SC	CC-SC	CC		CC		CC					
C2	Deg. <sup>a</sup>	CC <sup>a</sup>		CC	CC-SC		CC	CC							
C3					CC	Deg.	CC	CC			CC				
C4	Deg. <sup>a</sup>	CC <sup>a</sup>	CC		CC-SC	CC-SC		CC	Deg.	Deg.	CC		Deg.		
C5			CC	CC	CC-SC	CC-SC	CC				CC		CC	CC-SC	Deg.
C6					CC-SC	CC	CC	CC		CC	CC				Deg.
C7									CC	CC	Deg.				
C8	CC-SC <sup>a</sup>	Deg. <sup>a</sup>	CC	Deg.	CC-SC	CC	Deg.	Deg.	CC	CC	Deg.		Deg.	Deg.	Deg.
C9	Deg. <sup>a</sup>	CC <sup>a</sup>	CC	Deg.	CC-SC	CC-SC	Deg.	Deg.	CC	CC	CC	Deg.			CC
C10	Deg. <sup>a</sup>	CC <sup>a</sup>	CC	Deg.	CC	CC	Deg.	Deg.	CC-SC	CC	CC	Deg.	CC	CC	
C11				CC	CC-SC	CC			CC	CC					
C12				Deg.	CC-SC	CC		CC	CC			CC			
C13					CC		CC								CC-SC
C14								Deg.							
C15					CC						CC		CC-SC		CC
C16			CC-SC				CC	CC		Deg.	CC				CC
C17							CC								CC
C18															
C19					CC	CC		Deg.							
C20	CC-SC <sup>b</sup>		CC-SC	CC	CC			Deg.					CC		CC
C21					CC	CC	CC	Deg.						CC	

<sup>a</sup> Results from previous work [28]

<sup>b</sup> Result published by A. Carletta et al. [36]

## Photo- and non-photochromic behavior

All cocrystals as well as all parent anils were irradiated at 365 nm for 30 minutes and their solid-state absorption spectra were recorded. DRS strongly depends on experimental parameters such as surface planarity, grain-size, sample holder position, etc. [41], as illustrated in Figure 2 (left). An absolute variation up to 10% is not rare between two consecutive measurements, even when leaving the sample holder and sample in place. We thus decided to treat the data as mentioned above, coming to a signal that is less parameter dependent (Figure 2 - right).

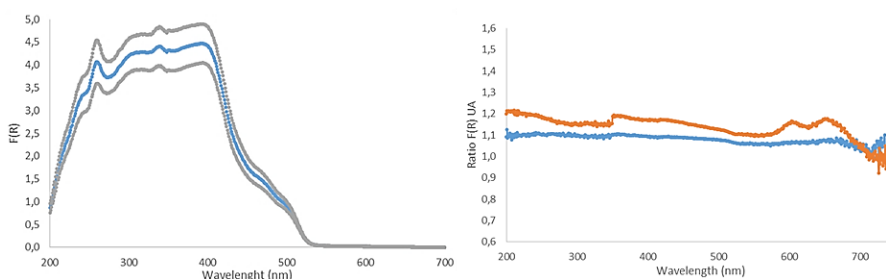


Figure 2 (left): Averaged DRS (Kulbelka-Munk) measurements of anil **B** (blue curve) over 8 measurements, with  $\pm 1$  standard deviation (grey curves). (Right): ratio of two consecutive measurements (blue curve) and ratio of 1<sup>st</sup> and 8<sup>th</sup> measurement (orange curve) for anil **B**.

As mentioned above, this relative signal shows upwards and downwards peaks when irradiation leads to population changes of different forms. This is illustrated in Figure 3, showing the DRS spectra for the **A-C20** (photochromic) and **C-C4** (non-photochromic) cocrystals, as well as the relative signal of the spectra before and after irradiation. The non-photochromic cocrystal show a flat line for all wavelengths, while a positive peak is observed when the cocrystal is photo-responsive, with a population increase of the *trans*-keto form as shown by the positive peak at around 560 nm. The value of the maximum ratio is further defined as  $I_{\max}$ .

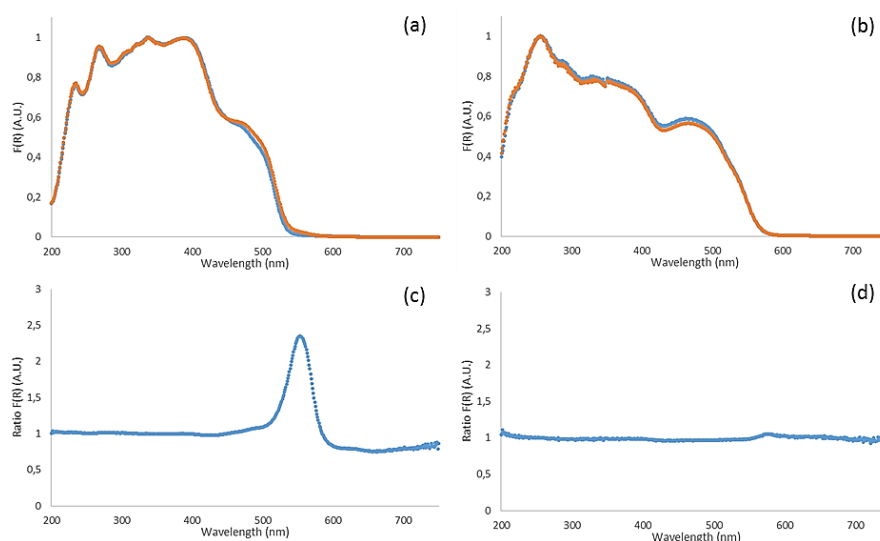


Figure 3: Normalized DRS spectra of cococrystals (a) **A-C20** and (b) **C-C4**. Spectra before (blue) and after (orange) irradiation at 360 nm. Relative ratio of both spectra for cococrystal **A-C20** (c) and **C-C4** (d).

This result is also confirmed visually (Figure 4), with cococrystal **A-C20** showing a weak but visible color change (from yellow to orange).

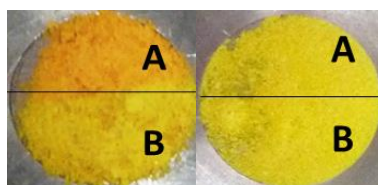


Figure 4: compounds **A-C20** (left) and **C-C4** (right). Top part (**A**) has been irradiated at 360 nm for 30 minutes while bottom part (**B**) was masked during the irradiation.

Analysis of the signal ratio (appearance of a peak at +/- 600 nm upon irradiation at 360 nm) allowed identifying 5 photochromic anils: **A**, **C**, **D**, **M** and **O**, with anil **A** and **C** already been reported as such [48,49]. Among the 95 cococrystals 20 were found photochromic: **A-C20**, **B-C4**, **B-C9**, **B-C10**, **B-C20**, **C-C8**, **C-C16**, **C-C20**, **C-C21**, **D-C2**, **D-C5**, **E-C15**, **H-C1**, **H-C16**, **I-C7**, **I-C12**, **J-C6**, **J-C7**, **M-C15** and **O-C15**. It is interesting to highlight that **B-C4**, **B-C9** and **B-C10** were previously reported as non-photochromic [28]. This is

understandable as the peak height is around 1.3 (the lower limit used in this work). Furthermore, calculating the absorption difference  $\Delta$  (as detailed in experimental part) we found a  $\Delta \approx 0.05\%$ , an extremely low value (not detectable by the naked eye) which explains they were reported non-photochromic. The data treatment presented in this paper can therefore help to identify borderline cases (Figure 5). The presence itself of borderline cases is new and shows photochromism to be a continuous phenomenon instead of a binary one, as the limit between photochromic and non-photochromic character is hard to find and has been established here based on experimental limitations (see experimental part) more than on an explicative model.

All the compounds presented here completely faded under visible light and some interesting cases were studied further (see Kinetic paragraphs below).

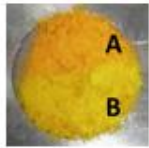
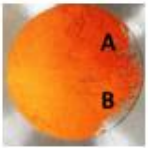
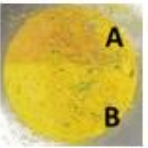
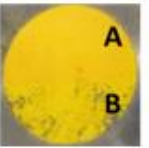
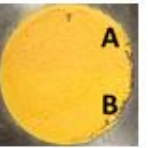
A-C20	M-C15	J-C7	C-C16	D-C5
				
$\Delta \approx 5\%$	$\Delta \approx 2.4\%$	$\Delta \approx 2\%$	$\Delta \approx 0.7\%$	$\Delta \approx 0.25\%$

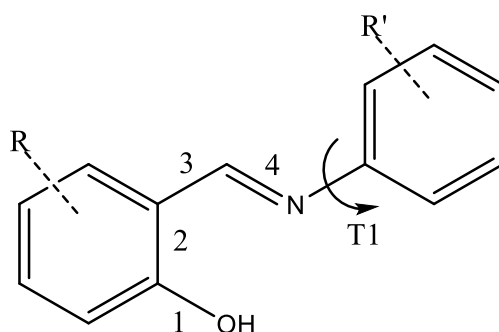
Figure 5: Comparison of not-irradiated (Bottom part - B) and irradiated (Top part - A) materials for different delta values/different cocrystals. As delta decreases it is harder to distinguish the color change.

Table 1 (combined with DRS-ratio analysis) also reveals that most of anils considered in this work lead to both photochromic as well as non-photochromic cocrystals. This also implies that for all parent compounds which are non-photochromic (**B, E, F, H** and **I**) cocrystallization can always be used as a tool to render them photochromic. Similarly, all photochromic anils (**C, D, M, O**) can be 'turned off' using this tool.

### Linking photochromism to structural characteristics

Among the 110 forms identified (95 cocrystals and 15 parent anils), 8 photochromic ones were structurally characterized (**A** [48], **C** [27], **D**, **M** [50], **A-C20** [36], **C-C16**, **C-C20** and **M-C15**). The structural data and ORTEP representations of the ones determined here can be found in the supporting information (section 9).

Table 2 reports the main structural features of the photochromic center (Scheme 3), the maximum ratio change  $I_{\max}$  and the intermolecular distances: distance between parallel planes (Figure 6) for structures presenting a “close-packing” feature.



Scheme 3: Reference diagram with the bond lengths of interest marked as 1 to 4 and the main dihedral angle T1 (between the two aromatic rings).

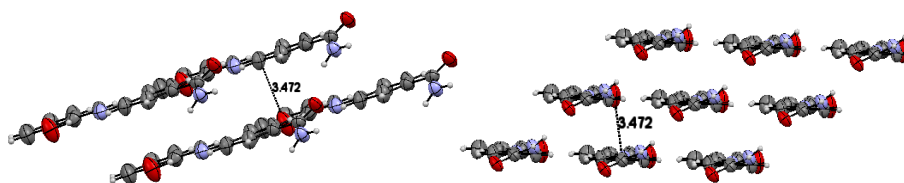


Figure 6: Interplanar distance illustrated in case of anil **D** along two different views.

Table 2: Main structural data of photochromic solids, as well as maximum ratio intensity (and its corresponding wavelength). Novel structures are highlighted in green.

Compound	Bond 1 (Å)	Bond 2 (Å)	Bond 3 (Å)	Bond 4 (Å)	T1 Angle (°)	$I_{\max}$ (A.U.) (λ nm)	Interplanar Distances (Å)
<b>A<sup>a</sup></b>	1.352	1.419	1.455	1.280	47(2)	45 (535 nm)	/
<b>C<sup>a</sup></b>	1.345	1.391	1.446	1.276	6.4(4)	9.3 (572 nm)	3.420
<b>C-C16</b>	1.359(8)	1.369(8)	1.435(8)	1.296(7)	12(2)	2.2 (560 nm)	3.424
<b>C-C20</b>	1.347(5)	1.406(6)	1.465(5)	1.283(5)	5.6(2)	1.6 (569 nm)	3.462
<b>D</b>	1.344(2)	1.384(3)	1.449(3)	1.268(2)	0.6(5)	1.6 (571 nm)	3.472
<b>M<sup>a</sup></b>	1.356(2)	1.406(2)	1.449(3)	1.284(2)	30(2)	3.1 (578 nm)	/
<b>M-C15<sup>b</sup></b>	1.347(4)	1.397(7)	1.445(9)	1.282(5)	26.4(2)	2.1 (587 nm)	/
<b>X<sub>1</sub><sup>a</sup></b>	1.350(3)	1.400(3)	1.444(3)	1.284(3)	30(3)	6 (550 nm)	3.597
<b>X<sub>2</sub><sup>a</sup></b>	1.350(2)	1.403(3)	1.446(3)	1.281(3)	39(2)	16 (555 nm)	3.275
<b>X<sub>3</sub><sup>a</sup></b>	1.346(2)	1.402(2)	1.446(2)	1.281(2)	30(3)	7 (575 nm)	3.533
<b>Average</b>	1.350	1.398	1.448	1.282	23	/	/
<b>Standard deviation</b>	0.005	0.014	0.008	0.007	16	/	/

<sup>a</sup> Compound **A**, **C** and **M** from respective refs [48], [27] and [50]. **X<sub>1</sub>**, **X<sub>2</sub>**, **X<sub>3</sub>** are taken from [29]

<sup>b</sup> Cocrystal **M-C15** presents two slightly different molecules in the asymmetric unit. The results presented here are the average values.

Table 2 shows photochromic centers to have rather similar bond lengths as reflected by the small standard deviations. Based on reference bond lengths [28] the photochromically active compounds can be considered of the Enol-Imine type confirming previous studies [19]. All compounds (except **A**) were measured at room temperature proving a weak thermochromic character (as the thermal equilibrium is displaced toward keto form with increasing temperature). Interestingly, the values of the dihedral angle vary between 0 and 40°, with a strong standard deviation. The largest dihedral angle found in literature for a photochromic anil is 90° [51] while we here present a cocrystal **C-C20** showing visible photochromism with a dihedral angle as low as 5.6°. In total, 4 photochromic compounds studied here presented a dihedral angle lower than 25° as shown in table 2. Also 2 non-photochromic compounds presented a high dihedral angle of about 35° as shown in table 3 which means in total 6 over 28 compounds do not obey

the “dihedral angle rule” in this contribution. Again, the standard deviation is thus very important compared to the average value for non-photochromic compounds. Another statistical study performed over a small dataset of 40 *N*-Salicylideneaniline derivatives still concludes to the importance of this rule despite the presence of counter-examples (6 over 40) [52]. Our results confirm the recent believe that the dihedral angle (between the two aromatic rings) is not fully representative of the photochromic character, and the ‘dihedral angle rule’ ( $\phi > 25^\circ$  is required for photochromism to occur) should therefore be revised [19,20].

Nevertheless, the value of the dihedral angle has a non-negligible impact on the photochromic process as it impacts the maximum ratio change observed upon irradiation. Figure 7 shows photochromic compounds with low dihedral angles (between  $0^\circ$  and  $25^\circ$ ) to show only weak photochromic behavior whereas a stronger effect is obtained for the higher angles. This can possibly be explained by a loss of rigidity of the molecule in the solid with higher dihedral angles, allowing an easier *cis/trans* isomerization [49]. The low ratio changes associated with the lower dihedral angle cases leads to visually difficult to observe color changes, and possibly explains why these anils could have been classified as non-photochromic. This would also explain how the dihedral angle rule came about. Thus, we propose a revision of this rule, with the dihedral angle relating to the intensity of the color change rather than to the photo- or non-photochromic character of the compound, leading to strong color changes for those photochromic compounds with  $\phi > 25^\circ$ .

Compounds **E-C2**, **E-C4**, **E-C6** and **O-C13** present two or more significantly different anil forms in the asymmetric unit meaning averaging the values of bond lengths makes little sense. Values are then shown for each different form and noted with a small letter (a to d). In case of **E-C6**, the second form is disordered and no accurate values can be extracted. Along with compounds presented in Table 3, MeCN solvate of **E-C12** and hydrates of **D**, **I-C10**<sup>4</sup>, **L** and **N-C5** were also found during the crystallization experiments but their simulated powder pattern did not match the initial powder pattern

---

<sup>4</sup> **I-C10** was observed as a cocrystal salt instead of pure cocrystal.

after grinding. They are thus discarded from discussion but their structures are displayed with the other CIF files in the supporting information. **F-C4** hydrate perfectly matched the initial powder pattern and thus is conserved for further analysis.

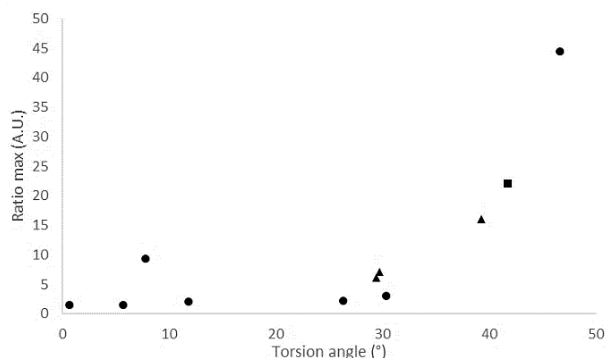


Figure 7: the maximum ratio change (arbitrary units) with respect to the absolute dihedral angle for 12 photochromic forms studied in this work (round dots) and those coming from literature (Ref. [29] - triangles and Ref. [3] - square).

Table 3, in turn, reports the data for 20 non-photochromic compounds. With exception of **B**, **N** and **O-C13**, all the compounds present an enhanced keto character. This seems to suggest that a more pronounced keto form leads to a reduced possibility of photochromism in accordance with previously reported results [19]. In other words, the enol-imine character can therefore be seen as a requirement for photochromism. However, as mentioned there are also some anils showing enol-character which are non-photochromic only, or which show both characteristics as e.g., anil **C** [49]. On the other hand, no photochromic anil was identified showing an enhanced keto-character. One could therefore conclude that a partial keto-character (bond 1 < 1.34 Å) excludes photochromism while an enol-imine character is a necessary condition (but not a guarantee) for photochromism.

Table 3: Structural data for non-photochromic solid forms – novel structures are highlighted in green.

Compound	Bond 1 (Å)	Bond 2 (Å)	Bond 3 (Å)	Bond 4 (Å)	Angle T1 (°)	Intermolecular distance (Å)
<b>B<sup>a</sup></b>	1.352	1.410	1.448	1.275	6.3(1)	3.435
<b>E</b>	1.332(2)	1.408(2)	1.427(2)	1.297(2)	35(1)	/
<b>D-C1</b>	1.336(2)	1.414(2)	1.436(2)	1.291(2)	5.9(8)	3.367
<b>E-C1<sup>b</sup></b>	1.286(2)	1.434(4)	1.390(2)	1.314(5)	11(1)	3.518
<b>E-C2a</b>	1.283(5)	1.434(5)	1.401(5)	1.300(5)	10.1(6)	3.431
<b>E-C2b</b>	1.287(5)	1.432(5)	1.397(5)	1.315(5)	11.4(2)	3.607
<b>E-C2c</b>	1.329(6)	1.447(6)	1.377(6)	1.345(5)	0.90(2)	3.410
<b>E-C2d</b>	1.285(5)	1.428(6)	1.401(5)	1.313(5)	4(2)	3.326
<b>E-C4<sup>b</sup></b>	1.294(11)	1.436(11)	1.404(10)	1.312(11)	9(5)	3.321
<b>E-C5a</b>	1.331(6)	1.416(6)	1.400(6)	1.304(5)	7.3(8)	3.342
<b>E-C5b</b>	1.296(6)	1.427(6)	1.408(6)	1.315(6)	6.90(8)	3.342
<b>E-C6a</b>	1.293(5)	1.441(6)	1.388(5)	1.329(5)	3.2(8)	3.477
<b>E-C6b</b>	1.284(11)	1.398(11)	1.392(9)	1.326(10)	7.6(7)	3.270
<b>E-C6c<sup>c</sup></b>	1.277(14)	1.402(14)	1.394(14)	1.325(15)	6(4)	3.270
<b>E-C9<sup>d</sup></b>	1.318(3)	1.412(3)	1.418(3)	1.302(3)	0.9(9)	3.495
<b>E-C11<sup>b,c</sup></b>	1.298(5)	1.44(3)	1.394(12)	1.316(12)	5(5)	3.477
<b>F<sup>e</sup></b>	1.322(2)	1.409(2)	1.423(2)	1.296(2)	21(1)	3.412
<b>F-C4</b>	1.289(2)	1.430(2)	1.398(2)	1.308(2)	10(1)	3.524
<b>F-C5<sup>b</sup></b>	1.287(2)	1.427(2)	1.394(5)	1.310(5)	12(3)	3.258
<b>F-C9</b>	1.276(2)	1.437(2)	1.392(2)	1.317(2)	18.0(8)	3.389
<b>G<sup>a</sup></b>	1.265	1.448	1.394	1.325	1	3.310
<b>H</b>	1.274(2)	1.438(3)	1.389(3)	1.315(2)	0.3(2)	3.440
<b>N</b>	1.342(2)	1.398(2)	1.441(3)	1.275(2)	12.4(6)	3.353
<b>O-C13a</b>	1.355(4)	1.397(5)	1.444(5)	1.284(5)	36(2)	3.516
<b>O-C13b</b>	1.364(4)	1.398(5)	1.447(5)	1.278(5)	38(1)	2.882
Averages	1.306	1.422	1.409	1.305	10.6	3.38
Standard deviations	0.027	0.015	0.020	0.015	10.2	0.14

<sup>a</sup> Structure from CSD: CAVQAR02 [53] and DIWMAY [54] for Anils **B** and **G** respectively.

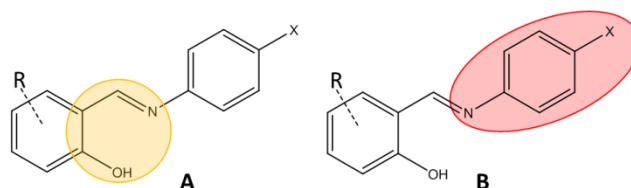
<sup>b</sup> Average values of extremely similar structures in crystal packing. Errors displayed are the highest value between bond lengths error and calculated standard deviation on the average.

<sup>c</sup> Structure is disordered so values are less accurate.

<sup>d</sup> E-C9 was observed as a cocrystal salt.

<sup>e</sup> Values used here are from a newly crystallized structure and not from MUDGAT [55] structure in CSD.

A further factor which is often mentioned in the context of photochromism is the presence of an open or close packing structure [11]. We therefore investigated whether an open packing is present in all photochromic anils (enol-imine character) and absent for the non-photochromic compounds. First of all, it should be noted that all photochromic compounds show an interplanar distance of at least 3.3 Å, the limit for open packing according to literature [11]. However, all non-photochromic studied here also present this feature. The difference between open and closed packing on its own does therefore not seem a determining factor. Recent studies, indeed show a combination of different structural factors such as free available space, packing index and dihedral angle is likely required if one would aim at predicting photochromism [56,57]. In future efforts, the open-packing feature could therefore still intervene when combined with other factors. To understand close-packing on a more fundamental level, short contacts were investigated. Short contacts are expected to block the movement of the anil and hence block the photochromic behavior. Through Hirshfeld surface analysis Wouters et al. already highlighted a link between the C···C  $\pi$ -stacking interactions and the presence of photochromism [29]. As this type of interaction is correlated with the overall packing, studying short-contacts might therefore be a valid approach to increase the understanding of the structure-property relationship. We therefore focused first on the total number of short contacts involving any of the atoms of two sub-units of the anil: the “photochromic center” and the “moving phenyl moiety” as shown in scheme 4. These subunits are present in all cases considered here and are expected to be the most important with respect to the photochromic process. Short contacts were divided into three categories in order to rationalize the results: strong ( $D < \sum r_{vdw} - 0.05 \text{ \AA}$ ), medium ( $\sum r_{vdw} - 0.05 \text{ \AA} < D < \sum r_{vdw} + 0.2 \text{ \AA}$ ) and weak ( $D > \sum r_{vdw} + 0.2 \text{ \AA}$ ). This analysis was performed on the 8 photochromic compounds and 20 non-photochromic compounds discussed here (see experimental section for detailed explanation and Supporting Information-section 13 for detailed results). A summary of this analysis is presented in Table 4 below.



Scheme 4: General anil skeleton with the 7 atoms of the “photochromic center” (A) circled in yellow and the 12 atoms of the “moving phenyl moiety” (B) circled in red.

Table 4: Average amount of strong, medium and weak short contacts for each moiety in function of the photochromic nature.

moiety	Nature of compounds	Strong	Medium	Weak	Total	Standard deviation
A	Photochromic	0.44	1.88	5.00	7.31	2.25
	Non-photo.	1.80	1.58	4.23	7.65	2.90
B	Photochromic	0.88	2.06	6.63	9.56	2.13
	Non-photo.	1.85	2.48	7.98	12.23	2.43

Table 4 shows some interesting overall features. The total cumulated average number of short contacts is significantly higher for the moving moiety of non-photochromic compounds (12.23 vs 9.56). One could therefore state that this moiety is in average more stabilized in non-photochromic compounds, impeding rotation around T1.

For the photochromic center there does not seem to be a major different in total amount of short contacts between the photochromic and non-photochromic compounds. However, there is a significant difference in strong (shorter) close contacts: non-photochromic compounds show a four-fold increase in strong interactions (1.80 vs. 0.44). In depth analysis revealed that for the photochromic compounds, only 2 (25% of photochromic compounds studied here) present a strong short contact involving the hydroxy group of the photochromic center while this feature was observed for 18 (90% of non-photochromic compounds studied here) of the non-photochromic compounds. From these we can draw two conclusions: 1) the moving moiety (B) is more stabilized (more involved in all type of short contacts) for non-photochromic compounds; 2) for the photochromic center (A) there is an important difference in amount of strong short contacts

between the photochromic and non-photochromic compounds meaning these strong short contacts might play a role in inactivating photochromism. As the majority of these strong short contacts are in fact hydrogen bonding interactions (with the –OH group) they are able to shift the keto-enol equilibrium toward the keto form [58], thus increasing the energy-barrier to reach the *trans*-keto state and rendering the anils non-photochromic [19]. To illustrate this, we decided to calculate Hirshfeld surfaces and 2D molecular fingerprints [59,60] for newly presented enol structures: **C**-C16, **C**-C20, **D**, **M** and **M**-C15 along with **C** as reference for photochromic compounds and **D**-C1, **N** and **O**-C13 along with **C** as reference for non-photochromic compounds (both **D**-C1 and **E** are close to the enol form with bond 1 > 1.33 Å). Calculated Hirshfeld surfaces with  $D_{\text{norm}}$  functions are presented in Figure 8 and corresponding fingerprints in Figure 9. As shown by Figure 8, most of photochromic compounds don't have strong short contacts involving the ortho-hydroxy moiety of the photochromic center with the exception of cocrystal **M**-C15 (f) which shows photochromism can still occur when strong short contacts are not able to displace the keto-enol equilibrium. In parallel, non-photochromic structures more likely present strong interaction involving the moving moiety as in the case of **E** (h) and **N** (i)

From the fingerprints (Figure 9) we can notice strong contributions to the O...H interactions in almost all cases. By comparison with Figure 8, we can assign this to the carboxylic/amide or methoxy moiety for photochromic compounds **C** (a), **C**-C16 (b), **C**-C20 (c) and **M** (e) while in case of the non-photochromic compound **E** (h) and **N** (i) the only possible contribution is due to ortho-phenolic moiety. In the case of photochromic compounds **D** (d), **M**-C15 (f) and non-photochromic cocrystal **D**-C1 (g) and **O**-C13 (j) both moieties contribute to the signal. The anil **D**/ cocrystal **D**-C1 presents an interesting comparison of the impact of short-contacts on photochromism as anil **D** (d) exhibits weak photochromism and a weak contribution of the ortho-hydroxy group on Hirshfeld surfaces while cocrystal **D**-C1 (g) shows a stronger contribution of this moiety with a complete removal of the photochromic behavior. Hirshfeld maps and fingerprints of other compounds (keto form) also exhibit strong short contacts involving the ortho-hydroxy moiety in most cases and are displayed in the supporting information, section 15. This result confirms previous studies on the impact of this moiety/short contacts in disabling photochromism [19] which means this can be used to fine-tune

photochromical properties of anils: to promote photochromism in these compounds it is beneficial to reduce the number of short contacts in particular with two moieties of interest. For instance, the addition of bulky groups on the anil might reduce the hydrogen bonds or  $\pi$ -stacking and T-axial interactions. This has already been successfully experimented (but in order to force a non-planar conformation - a completely different approach) by T. Kawato et al. [13]. They also performed the “Bulky-group substitution method” to increase the space available in order to allow the movement of the phenyl moiety [13] but which should also result in a global reduction of the amount of strong short-contacts and thus again show that engineering short-contacts might be a key to fine-tune photochromism.

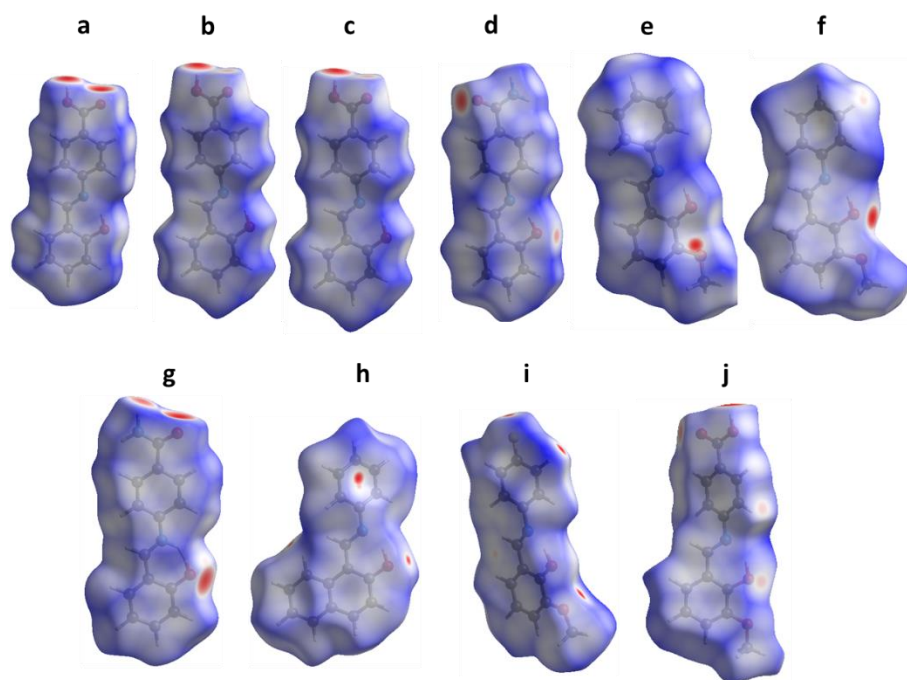


Figure 8: Mapped Hirshfeld surfaces with  $D_{\text{norm}}$  functions for the anil moiety of photochromic compounds **C** (a), **C-C16** (b), **C-C20** (c), **D** (d), **M** (e), **M-C15** (f) and non-photochromic enol compounds **D-C1** (g), **E** (h), **N** (i) and **O-C13** (j). Red spots show strong intermolecular contacts, white spots show weak intermolecular contacts and blue spots show no intermolecular contacts.

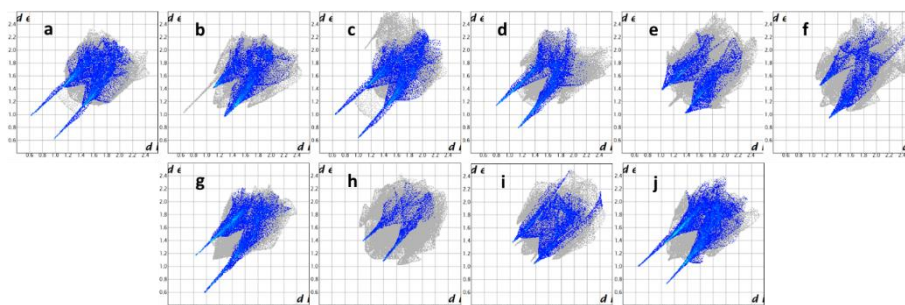


Figure 9: Fingerprints of calculated Hirshfeld surfaces for the anil moiety of photochromic compounds **C** (a), **C-C16** (b), **C-C20** (c), **D** (d), **M** (e), **M-C15** (f) and non-photochromic enol compounds **D-C1** (g), **E** (h), **N** (i) and **O-C13** (j). Highlighted area corresponds to O...H interactions.

### Kinetic measurements

In order to study further the impact of short-contacts, the thermal reversibility of photochromism of the cocrystals was studied focusing on two different photochromic systems, cocrystals **A-C20** and **C-C16**, as for these compounds the respective parent anils **A** and **C** have already been studied [49,61].

The kinetic measurements were done at 550 nm which is close to the maximum ratio change for both compounds (respectively 556 nm and 558 nm) and present an expected exponential decay over time after irradiation (disappearance of *trans*-keto band). The data was linearized and shows a two-stage first order kinetics for both cases, similar to reported behavior for anil **C** [13].

The corresponding rate constants  $k_1$  and  $k_2$  were calculated using the Malkin equation ( $\ln\left(\frac{Abs_{\infty}-Abs(t)}{Abs_{\infty}-Abs_0}\right) = -k.t$ ) and yield values of  $k_1 = 1.96 \times 10^{-4} \text{ s}^{-1}$  and  $k_2 = 1.17 \times 10^{-4} \text{ s}^{-1}$  for **A-C20** and for **C-C16**:  $k_1 = 3.58 \times 10^{-4} \text{ s}^{-1}$  and  $k_2 = 6.32 \times 10^{-4} \text{ s}^{-1}$ . These latest values are of the same order of magnitude than those reported for anil **C**:  $k_1 = 3.28 \times 10^{-4} \text{ s}^{-1}$  and  $k_2 = 7.04 \times 10^{-4} \text{ s}^{-1}$  [49]. For anil **A** we measured a value of  $k_1 = 3.57 \times 10^{-4} \text{ s}^{-1}$  at 20 °C while  $k_1 = 1.4 \times 10^{-3} \text{ s}^{-1}$  is

reported at 30 °C [61]). The usual reported range for  $k_1$  in anils varies between  $3 \times 10^{-2} \text{ s}^{-1}$  and  $1.8 \times 10^{-8} \text{ s}^{-1}$  [2].

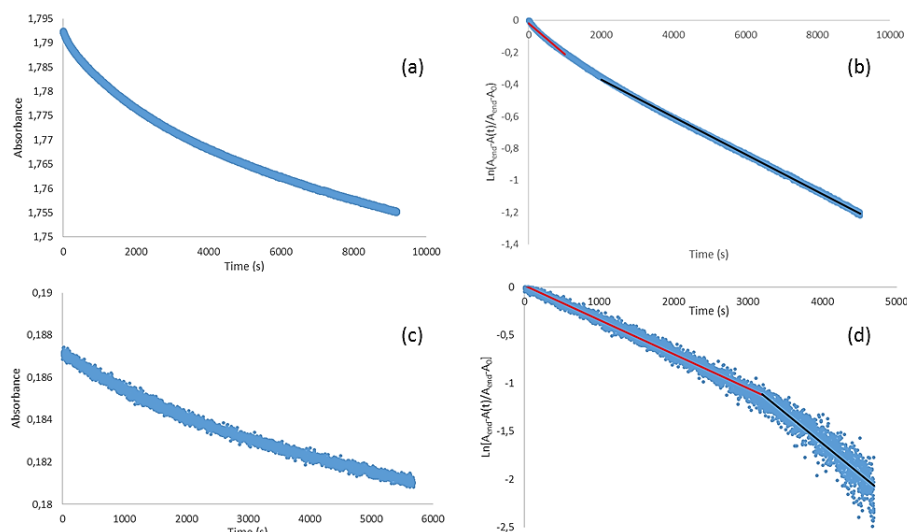


Figure 10: (a): Absorbance at 550 nm over time of **A-C20** after irradiation at 365 nm. (b): First order linearization. (c): Absorbance at 550 nm over time of **C-C16** after irradiation at 365 nm. (d): First order linearization.

Cocrystallization in the case of compound **C** therefore almost shows no effect on the relaxation process. For anil **A** the rate constant ( $k_1$ ) is about 2 times lower when **A** is inserted in the cocrystal. This can be correlated to the structure of these systems: both anil **C** and cocrystal **C-C16** have a similar interplanar distance (3.424 Å and 3.420 Å respectively for **C-C16** and **C**) and one intermolecular interaction ( $\text{O} \cdots \text{HC}$  in both cases) directly involving the moving moiety. For the system with anil **A**, there are significant differences between the structure of anil and the cocrystal: in case of anil **A** there is no face-to-face orientation and only one (average-medium) T-Axial interaction  $\text{CH} \cdots \pi$  while cocrystal **A-C20** presents an interplanar distance of 3.291 Å and two strong (short)  $\text{I} \cdots \pi$  interactions involving the moving moiety. These features show the moving moiety is more stabilized in the cocrystal possibly explaining the slower relaxation.

## Conclusion

Within this work 15 anils were screened with respect to 21 cocrystal formers, leading to 95 cocrystal systems. Carboxylic acids were found to be good cofomer candidates as a hydrogen bonding interaction with the anil–OH group can be expected. Furthermore, we showed that cocrystallization can be used to ‘switch on’ any non-photochromic anil.

We also introduced a novel approach to the data interpretation by looking at the ratio of consecutive DRS measurements. This led to a better classification of photochromic and non-photochromic solids, allowing identifying those “weakly photochromic compounds” that do not (or barely) show a visible change when looking with the naked eye. Our data furthermore consolidates the current believe that the ‘dihedral angle rule’ should be revised, as the dihedral angle is not decisive for the photochromic nature of a compound, but rather impacts the intensity of this effect. These results clearly suggest that photochromism is a continuous phenomenon and not a binary one.

Interestingly, all anils presenting a photochromic behavior at 360 nm showed a marked enol character at room temperature while non-photochromic (at 360 nm) compounds exhibited an enhanced keto-character. One can therefore conclude that a partial keto-character (bond 1 < 1.34 Å) excludes photochromism while enol-imine character is a necessary condition (but not a guarantee) for photochromism to occur at the working wavelength. Hydrogen bonding to the anil ortho–OH group can have a strong impact on the keto-enol character of a target compound and should be avoided as much as possible. Anils showing enol character but no photochromism show an important number of short contacts involving the moving moiety, and hence a likely reduced possibility of molecular movement (a requirement for photochromism). Overall, this analysis thus confirms that to promote photochromism, intermolecular interactions should be reduced as much as possible, in alignment with the bulky substitution approach.

### **Supporting Information.**

Structures described in this contribution have been deposited at the Cambridge Crystallographic Data Centre and allocated the deposition numbers CCDC 1903903 to 1903930. Supporting Information also contains XRPD, DRS spectra, <sup>1</sup>H-NMR Data, starting materials, thermal analysis (TGA/DSC), synthesis, structural chemical data and short contacts analysis of discussed compounds (PDF). This material is available free of charge via the Internet at:

<https://pubs.acs.org/doi/abs/10.1021/acs.cgd.9b00363>.

### **Corresponding Author.**

\* Email: tom.leysens@uclouvain.be.

### **Acknowledgments.**

The authors would like to thank the UCL for financial support (Gabriel Mercier is a UCL teaching assistant). This work was published thanks to funding of "Actions de Recherche Concertées (ARC)" de la Direction générale de l'Enseignement non obligatoire et de la Recherche scientifique – Direction de la Recherche scientifique – Communauté française de Belgique. The authors would also like to Thanks Ir. Séverine Schiltz for her contribution to data processing through VBA coding.

## References

- [1] G. H. Brown, Photochromism, Wiley-Interscience, New York **1971**.
- [2] K. Nakatani, J. A. Delaire, Reversible Photoswitching of Second-Order Nonlinear Optical Properties in an Organic Photochromic Crystal, *Chem. Mater.*, **1997**, 9, 2682-2684.
- [3] M. Sliwa, S. Létard, I. Malfant, M. Nierlich, P. G. Lacroix, T. Asahi, H. Masuhara, P. Yu, K. Nakatani, Design, Synthesis, Structural and Nonlinear Optical Properties of Photochromic Crystals: Toward Reversible Molecular Switches, *Chem. Mater.* **2005**, 17, 4727.
- [4] W. Zhu, Photochromic protective film and preparation method thereof Faming Zhuanli Shenqing, Patent **2015**, CN 105129225 A 20151209.
- [5] G. C. Yoo, Photochromic contact lens and manufacture method thereof, Repub. Korean Kongkae Taeho Kongbo, Patent **2018**, KR 2018137234 A 20181227.
- [6] M. Maurer, M. Huegin, T. Raimann, L. Feiler, B. Inderbitzin, A. Fuchs, Preparation of a photochromic ink, PCT Int. Appl., **2010**, WO 2010079098 A1 20100715.
- [7] D. Zhang, Photochromic anti-counterfeiting ink, Faming Zhuanli Shenqing, Patent **2016** CN 106147399 A 20161123.
- [8] B. L. Feringa, W. F. Jager and B. Delange, Organic materials for reversible optical data storage, *Tetrahedron* **1993**, 49, 8267-8310.

- [9] S. Kawata and Y. Kawata, Three-Dimensional Optical Data Storage Using Photochromic Materials, *Chem. Rev.* **2000**, 100, 1777-1788.
- [10] E. Hadjoudis, S. D. Chatziefthimiou, I. M. Mavridis, Anils: Photochromism by H-transfer, *Curr. Org. Chem.*, **2009**, 13, 269-286.
- [11] E. Hadjoudis, Molecular Engineering, Photochromic and Thermochromic Anils, **1995**, 5, 301.
- [12] B. Kaitner, M. Zbačnik, Solvent-free Mechanochemistry of Two Thermochromic Schiff Bases, *Acta Chim. Slov.*, **2012**, 59, 670.
- [13] K. Amimoto, T. Kawato, Photochromism of organic compounds in the crystal state, *J. Photoch. Photobiol.*, **2005**, 6, 207-226.
- [14] F. Robert, A. D. Naik, F. Hidara, B. Tinant, R. Robiette, J. Wouters, Y. Garcia, Engineering Solid-State Molecular Switches: *N*-Salicylidene *N*-Heterocycle Derivatives, *Eur. J. Org. Chem.*, **2010**, 621-637.
- [15] B. C. Jain, P. Mirchandani, B. H. Iyer, P. C. Guha, Schiff's bases of 4-nitro-4'-aminodiphenyl sulfone and their reduction products, *Sci. Culture*, **1946**, 11, 567-8.
- [16] M. D. Cohen, G. M. J. Schmidt, S. Flavian, Experiments on Photochromy and Thermochromy of Crystalline Anils of Xalicylaldehydes, *J. Chem. Soc.*, **1964**, June, 2041-2051.
- [17] W. F. Richey, R. S. Becker, Spectroscopy and mechanisms of the photo- and thermal reactions of photochromic anil, *J. Chem. Phys.*, **1968**, 49, 5, 2092-2101.

- [18] F. Milia, E. Hadjoudis, J. Seliger, Hydrogen Bond Studies In Thermochromic And Photochromic *N*-Salicylidene Anilines, *J. Mol. Struc.*, **1988**, 177, 191-197.
- [19] M. S. Rawat, S. Mal, P. Singh, Photochromism in Anils - A Review, *Open Chem.*, **2015**, 2, 7-19.
- [20] S. D. Chatziefthimiou, Y. G. Lazarou, E. Hadjoudis, T. Dziembowska, I. M. Mavridis, Keto Forms of Salicylaldehyde Schiff Bases: Structural and Theoretical Aspects, *J. Phys. Chem.*, **2006**, 110, 23701-23709.
- [21] E. Hadjoudis, V. Verganlakis, C. Trapalis, G. Kordas, Environmental Effect of Sol-Gel Encapsulation on Photochromic and Thermochromic Anils, *Mol. Eng.*, **1999**, 8, 459-469.
- [22] F. Robert, A. D. Naik, B. Tinant, R. Robiette, Y. Garcia, Insights into the Origin of Solid-State Photochromism and Thermochromism of *N*-Salicylideneanils: The Intriguing Case of Aminopyridines, *Chem. Eur. J.*, **2009**, 4327-4342.
- [23] E. Hadjoudis, Solid State Photochromism of Anils, *Mol. Cryst. Liq. Cryst.* **1994**, 246, 127-134.
- [24] T. Haneda, M. Kawano, T. Kojima, M. Fujita, Thermo-to-Photo-Switching of the Chromic Behavior of Salicylideneanilines by Inclusion in a Porous Coordination Network, *Angew. Chem. internat. Edit.*, **2007**, 46, 6643-6645.
- [25] F. Robert, A. D. Naik, B. Tinant, Y. Garcia, *N*-Salicylidene anil anions as thermo-sensitive components of organic-inorganic hybrid materials, *Inorg. Chim. Acta*, **2012**, 380, 104-113.

- [26] I. Casades, M. Álvaro, H. García, M. N. Pillai, Photochemistry of anils in NaY zeolite, *Eur. J. Org. Chem.*, **2002**, 2074-2079.
- [27] K. Johmoto, A. Sekine, H. Uekusa, Photochromism Control of Salicylideneaniline Derivatives by Acid–Base Co-Crystallization, *Cryst. Growth Des.*, **2012**, 12, 4779-4786.
- [28] G. M. Mercier, K. Robeyns, T. Leysens, Altering the Photochromic Properties of *N*-Salicylideneanilines Using a Co-Crystal Engineering Approach, *Cryst. Growth. Des.*, **2016**, 16, 3198-3205.
- [29] A. Carletta, B. Xavier, T. Leysens, B. Champagne, J. Wouters, Polymorphic and Isomorphic Cocrystals of a *N*-Salicylidene-3-aminopyridine with Dicarboxylic Acids: Tuning of Solid-State Photo and Thermochromism, *J. Phys. Chem. C*, **2016**, 120, 10001-10008.
- [30] E. Hadjoudis, I. M. Mavridis, Photochromism and thermochromism of Schiff bases in the solid state: structural aspects, *Chem. Soc. Rev.*, **2004**, 33, 579.
- [31] N. K. Duggirala, M. L. Perry, Ö. Almarsson, M. J. Zaworotko, Pharmaceutical Cocrystals: Along the Path to Improved Medicines., *Chem. Commun.*, **2016**, 52, 640–655.
- [32] N. Schultheiss, A. Newman, Pharmaceutical Cocrystals and Their Physicochemical Properties, *Cryst. Growth Des.*, **2009**, 9, 2950–2967.
- [33] A. Tilborg, B. Norberg, J. Wouters, Pharmaceutical Salts and Cocrystals Involving Amino Acids: A Brief Structural Overview of the State-of-Art, *Eur. J. Med. Chem.*, **2014**, 74, 411–426.

- [34] H. Sugiyama, K. Johmoto, A. Sekine, H. Uekusa, Reversible on/off switching of photochromic properties in *N*-salicylideneaniline co-crystals by heating and humidification, *CrystEngComm*, **2019**, 21, 3170-3175.
- [35] H. Sugiyama, K. Johmoto, A. Sekine, H. Uekusa, In-Situ Photochromism Switching with Crystal Jumping through the Deammoniation of *N*-Salicylideneaniline Ammonium Salt, *Cryst. Growth Des.*, **2019**, 19, 4324-4331.
- [36] A. Carletta, M. Zbačnik, M. Vitković, N. Tumanov, V. Stilinović, J. Wouters, D. Cinčić, Halogen-bonded cocrystals of *N*-salicylidene Schiff bases and iodoperfluorinated benzenes: hydroxyl oxygen as a halogen bond acceptor, *CrystEngComm.*, **2018**, 20 (36), 5332-5339.
- [37] A. Carletta, M. Zbačnik, M. Van Gysel, M. Vitković, N. Tumanov, V. Stilinović, J. Wouters, D. Cinčić, Playing with Isomerism: Cocrystallization of Isomeric *N*-Salicylideneaminopyridines with Perfluorinated Compounds as Halogen Bond Donors and Its Impact on Photochromism, *Cryst. Growth Des.*, **2018**, 18, 6833–6842.
- [38] CrysAlis PRO, Data Collection and Processing Software for Agilent X-ray Diffractometers User Manual, Agilent Technologies UK Ltd., Oxford, UK, **2013**.
- [39] G. M. Sheldrick, SHELXT - Integrated space-group and crystal-structure determination, *Acta Crystallogr., Sect. A: Found. Crystallogr.*, **2015**, 71, 3-8.
- [40] G. M. Sheldrick, Crystal structure refinement with SHELXL, *Acta Crystallogr., Sect. C: Found. Crystallogr.*, **2015**, 71, 3-8.

- [41] Methods of Soil Analysis. Part 5. Mineralogical Methods, Chapter 13: Diffuse Reflectance Spectroscopy, J. Torrent, V. Barron, SSSA Book Series, No. 5. USA., **2008**, 367-385.
- [42] Advances in Catalysis, Chapter 3: Ultraviolet–Visible–Near Infrared Spectroscopy in Catalysis: Theory, Experiment, Analysis, and Application Under Reaction Conditions, B. C. Gates, H. Knozinger, Eds., F. C. Jentoft, Assoc. Ed., Elsevier, **2009**; Vol.52.
- [43] T. Fujiwara, J. Harada, K. Ogawa, Solid-State Thermochromism Studied by Variable-Temperature Diffuse Reflectance Spectroscopy. A New Perspective on the Chromism of Salicylideneanilines, *J. Phys. Chem.*, **2004**, 108, 4035-4038.
- [44] G. Kortuem, W. Braun, G. Herzog, Principles and methods of diffuse reflection spectroscopy, *Angew. Chem. internat. Edit.*, **1963**, 2, 7, 333-404.
- [45] M. J. Turner, J. J. McKinnon, S. K. Wolff, D. J. Grimwood, P. R. Spackman, D. Jayatila and M. A. Spackman, *CrystalExplorer17*, University of Western Australia, **2017**, <http://hirshfeldsurface.net>.
- [46] K. Fucke, S. A. Myz, T. P. Shakhtshneider, E. V. Boldyreva, U. J. Griesser, How good are the crystallisation methods for co-crystals? A comparative study of piroxicam, *New J. Chem.*, **2012**, 36, 1969-1977.
- [47] M. Viertelhaus, R. Hilfiker, F. Blatter, M. Neuburger, Piracetam Co-Crystals with OH-Group Functionalized Carboxylic Acids, *Cryst. Growth. Des.*, **2009**, 9, 2220-2228.
- [48] R. Destro, A. Gavezzotti, M. Simoneta, [Crystal structure of] salicylideneaniline, *Acta Crys. B*, **1978**, 34, 2867.

- [49] M. Avadanei, V. Cozan, S. Shova, J. A. Paixao, Solid state photochromism and thermochromism of two related *N*-salicylidene anilines, *Chem. Phys.*, **2014**, 444, 43-51.
- [50] Y. Y. Yu, 6-Methoxy-2-[(*E*)-phenyliminomethyl]phenol, *Acta Cryst.*, **2011**, E67(4), o889.
- [51] M. Taneda, K. Amimoto, H. Koyama, T. Kawato, Photochromism of polymorphic 4,4'-methylenebis-(*N*-salicylidene-2,6-diisopropylaniline) crystals, *Org. Biomol. Chem.*, **2004**, 2, 499-504.
- [52] Multi-component crystals, Chapter 4: Control of photochromism in *N*-salicylideneaniline by crystal engineering, K. Johmoto, H. Uekusa, E. R. T. Tiekink (Eds.), J. Zukerman-Schpector (Eds.), De Gruyter, **2017**.
- [53] T.S. Chundawat, N. Sharma, P. Kumari, S. Bhagat, *Synlett*, **2016**, 27, 404-408.
- [54] M. Akkurt, S. O. Yildirim, A. M. Asiri, V. McKee, 4-[(2-Hydroxy-1-naphthyl)methylideneamino]benzoic acid, *Acta Cryst.*, **2008**, E64(4), o682.
- [55] H. Unver, D.M. Zengin, T. N. Durlu, *Anal. Sci.*, **2001**, 17, 1021-1022.
- [56] P.-L. Jacquemin, K. Robeyns, M. Devillers, Y. Garcia, Photochromism emergence in *N*-Salicylidene *p*-Aminobenzenesulfonate Diallylammonium Salts, *Chem. Eur. J.*, **2015**, 21, 6832-6845
- [57] H. Sugiyama, H. Uekusa, Relationship between crystal structures and photochromic properties of *N*-

salicylideneaminopyridine derivatives, *CrystEngComm*, **2018**, 20, 2144-2151.

[58] M. Zbacnik, B. Kaitner, Supramolecular Influence on Keto-Enol Tautomerism and Thermochromic Properties of *o*-Hydroxy Schiff Bases, *Croat. Chem. Acta*, **2016**, 89(1), 125-132.

[59] J. J. McKinnon, D. Jayatila, M. A. Spackman, Towards quantitative analysis of intermolecular interactions with Hirshfeld surfaces, *Chem. Commun.*, **2007**, 3814-3816.

[60] M. A. Spackman, D. Jayatila, Hirshfeld Surface Analysis, *CrystEngComm*, **2009**, 11, 19-32.

[61] H. Koyama, T. Kawato, H. Kanatomi, H. Matsushita and K. Yonetani, Utilization of crystal lattice cavities of host deoxycholic acid for achieving photochromism of guest salicylideneanilines in the crystal state, *J. Chem. Soc., Chem. Commun.*, **1994**, 579.

## Preface of Chapter 4

The chapter 4, which is entitled “Anils cross crystallization” presents some unpublished results. In this chapter, the notation  $\mathbf{X+Y}$  has been used to design two-component ( $\mathbf{X}$  and  $\mathbf{Y}$ ) systems for which no cocrystal structure could be obtained while the notation  $\mathbf{X/Y}$  has been used to design systems for which solid-solution structures could be obtained through SC-XRD.



## **Chapter 4**

### **Anils cross crystallization**



## Introduction

The previous chapters focused on the cocrystal screening of anils with small organic molecules of various kinds (such as carboxylic acids, amines, amides and benzene halides) and resulted in the establishment of an important data set of cocrystals among which many were found to be photochromic [1, 2]. However, this extensive search can never be exhaustive as millions of coformer candidates exist and the chosen selection criteria were mostly based on practical constraints such as availability, stability, cost and toxicity. However, besides these considerations, efforts were placed in choosing specific functionalities (as cited above) in order to permit the formation of known synthons as presented in the introduction of the present thesis.

Continuing the search for the “ideal” coformer, we noticed that almost all the successful cofomers had common features with selected anils: the presence of either a hydroxy group or an aromatic ring or both. In other words: anils cocrystallize quite well with compounds that are similar to themselves. This can be easily understood considering the presence of two aromatic rings in their structure which allows  $\pi$  interactions such as  $\pi\cdots\pi$  stacking, axial  $\pi\cdots\text{H}$  interactions [3], etc. We therefore picked up the idea to try and use anils as cofomers themselves, or in other words to couple anils together through cocrystallization. Such an approach should have many advantages: better cocrystal yield due to structural similarity, the combination of properties and the “patron effect” of one of the species which could dominate the structure and force the other species to crystallize in a different crystal form. As a result, photochromism might be strongly impacted.

This approach (called anils cross crystallization within this thesis) led to two different types of solid states and which need to be considered: true stoichiometric cocrystals and the solid-solutions. Stoichiometric cocrystals contain a fixed amount of both compounds present in the cocrystal, whereas for solid-solutions this ratio may vary [4]. The latter form due to the high similarities between parent anils. This was observed when the only difference between the two anils was the fluorine substitution of a hydrogen and corresponding results are treated in the Chapter 5 of the present thesis. However, cocrystal screening is provided in the current chapter and

therefore also includes those positive hits, which were shown later on to correspond to solid-solution.

In the context of this thesis, we decided to focus on solid-solutions, as they allow modulating the anil1-anil2 ratio freely. The part covering stoichiometric anil cocrystals presented in this chapter is therefore not fully completed. Nevertheless, the preliminary results obtained are presented here and may serve as a basis for future work in this field.

### **Materials and methods**

Materials, compounds, solvents and methodologies used within this work are mostly identical to those of chapter 3 and any variation is discussed in the text below.

## Results

All anils reported in Chapter 3 were used in the current chapter and are presented in Figure 1. The same methodology for cocrystal screening was applied with the exception that two different anils were ground together instead of an anil with another type of compound. An equimolar mixture of two compounds was prepared and ground through liquid assisted ball-milling (with acetonitrile). The resulting powder was analyzed by X-ray powder diffraction and the resulting diffractogram compared to simulated/experimental parent anils diffractograms. When a new phase was observed (appearance of new peaks), a routine NMR check was performed to identify unexpected reactions/degradations. At last, when a combination passed the previous tests, an ultimate check was performed in order to verify the new pattern was due to cocrystal appearance, and not due to a solid-state transition such as a new polymorph appearing. When a sample showed a new phase with no further reaction and no observed polymorphism, it was assumed to be a new cocrystal. Detailed analysis can be found in the Supporting Information (annexes of Ch.4). Also, a crystallization screening was performed in order to provide single crystals of suitable quality for SC-XRD and in-deep structural study (as well as ultimate proof of the cocrystal existence). Corresponding results are presented with the selected systems along with DSC analysis when performed.

### Screening results

Final results of the screening are presented in Table 1.

After removing polymorph/degradation occurrences, a total of 11 of the 105 anil combinations showed the presence of a new phase upon grinding, among which 3 were identified as solid-solutions (**A/B**, **E/F**, **M/N**) and are treated in Chapter 5. This corresponds to a positive rate of 10% which is in agreement with screening results presented in literature [5] but below the 30% found in previous research [1]. As a result, cocrystallizing anils together instead of using other selected cofomers does not improve the cocrystal yield.

Among the 11 newly identified anil phases, 3 are identified as solid-solutions (**A/B**; **E/F** and **M/N**) and are treated in chapter 5. Attempts to crystallize the 8 other systems failed and thus no in-deep structural study can be performed with the means used throughout this thesis. Other techniques

exist (such as synchrotron XRPD, as discussed in the introduction, which may allow to obtain compounds structures) but require other materials and devices and thus these systems are classified as perspectives of the current work.

Even though structural studies were not available, some preliminary studies were performed on a few systems in order to assess their interest for future work and the results are presented below.

#### **Photochromic studies**

Three systems (**A+M**, **E+N** and **G+H**) were studied through Diffuse Reflectance Spectroscopy and the results presented below. Other systems were not studied.

At first, the absorption spectra of the new phases were measured from 800 to 200 nm and compared to the average absorption spectrum of the two parent anils used. This further yield evidence of a new solid phase after grinding as the spectra strongly differ from those of the parent compounds. Following this confirmation, the photochromic intensity was measured through a previously established experimental protocol [1].

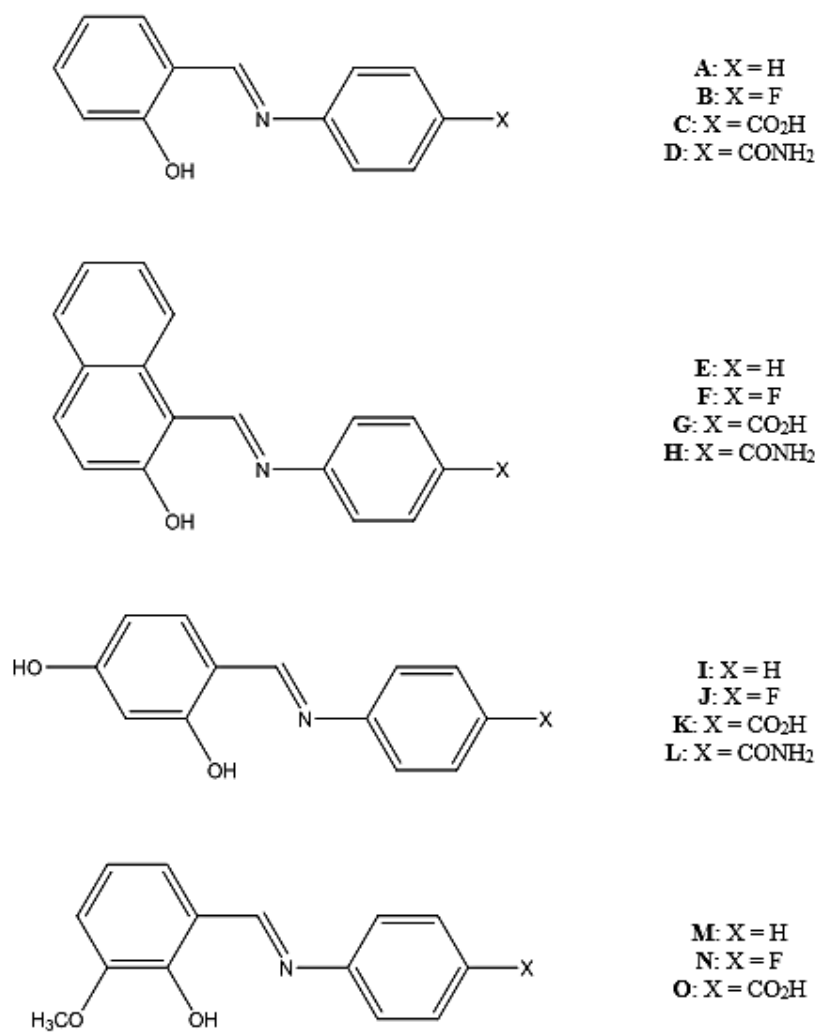


Figure 1: anils and their corresponding labels used within this work [1].

Table 1: Screening results after grinding. NP means New Phase identified (but no single crystal obtained) and NP: SS means New Phase: Solid-Solution identified (these cases are treated in chapter 5). Empty cell means no cocrystal phase has been identified. Symmetrical combinations are colored in grey to avoid double counting.

	A	B	C	D	E	F	G	H	I	J	K	L	M	N	O
A															
B		NP:SS													
C			NP												
D				NP											
E					NP:SS										
F						NP:SS									
G							NP								
H								NP							
I									NP						
J										NP					
K											NP				
L												NP			
M													NP		
N														NP:SS	

### System A+M

System **A+M** exhibits a strong difference in its absorption spectrum after grinding compared to the average of **A** and **M** spectra (equivalent to a physical mixture) as presented in Figure 2. In particular, a relative increase of the band at 500 nm is observed in the new phase meaning the keto-enol equilibrium is shifted towards the *cis*-keto form [6]. This sample exhibits strong photochromism with a large difference between absorption spectrum before and after irradiation at 365 nm as shown in Figure 3. Consequently, it exhibits a maximum ratio intensity of 6.2 centered at 575 nm (as shown in Figure 4) which represents a hypochromic and a 40 nm bathochromic shift compared to anil **A** alone (ratio intensity = 45.0 at 535 nm) but is similar to anil **M** photochromism (ratio intensity = 3.1 at 578 nm) [1]. As a result, we can make the hypothesis that the anil **M** structure dominates the new phase and the properties of the **A+M** cocrystal system. This is also coherent with the intense band at 500 nm observed in the ground sample and which is not present in **A** sample alone but is present in anil **M** alone. Getting a single crystal of the novel **A+M** phase is necessary to prove this hypothesis, however, all attempts failed so far. Single crystal tests were run using acetonitrile, ethyl acetate, methanol and ethanol/acetonitrile (20/80) as solvents through slow solvent evaporation. Dissolving **M** into the melt of anil **A** at 50°C was also tried but no crystal of suitable quality for SC-XRD could be produced. System **A+M** was also studied through DSC and the corresponding thermogram (presented in Figure 5) shows the presence of one unique thin peak at 35 °C associated to the melting of the sample which remains in the liquid phase up to 100 °C. The presence of a single and well-defined peak is also another element in the favor of a new cocrystal phase being formed.

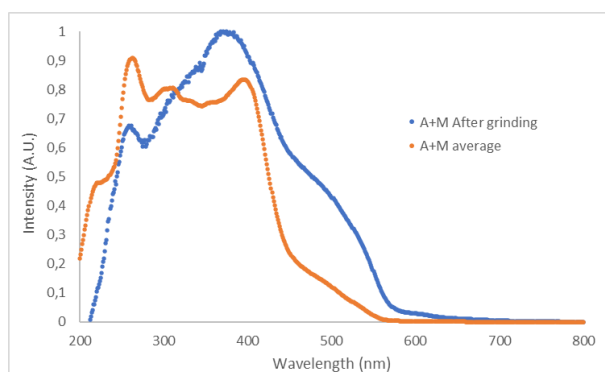


Figure 2: comparison between **A+M** spectrum after grinding (blue curve) and the average of **A** and **M** spectra before grinding (orange curve).

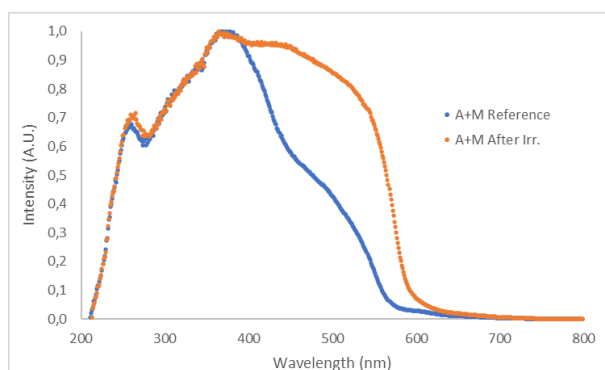


Figure 3: comparison between **A+M** spectrum before irradiation (blue curve) and after 5 min irradiation at 365 nm (orange curve).

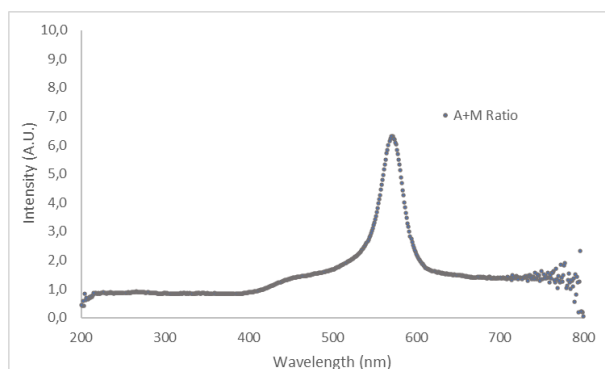


Figure 4: ratio between **A+M** absorption spectrum after irradiation divided by **A+M** absorption spectrum before irradiation.

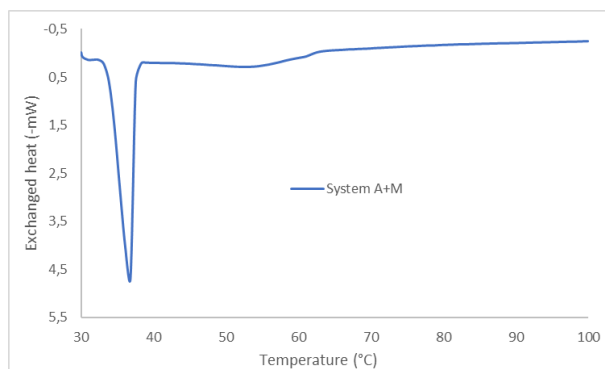


Figure 5: DSC thermogram of new **A+M** phase.

### System E+N

System **E+N** also exhibits a strong difference in its absorption spectrum after grinding compared to the average of **E** and **N** spectra before grinding (equivalent to a physical mixture) as presented in Figure 6. In particular, a slight relative decrease of the band at 500 nm is observed in the new phase meaning the keto-enol equilibrium is shifted towards the enol form [6]. This sample may seem to exhibit photochromism with a slight difference between the absorption spectrum before and after irradiation as shown in Figure 7. Consequently, the calculated maximum ratio intensity gives a value of 6.0 centered at 597 nm (as shown in Figure 8) which seems to represent a switch of the photochromic properties as both of the parent anils alone were found to be non-photochromic [1]. However, the quality of the spectra isn't high with some experimental noise present below 500 nm as shown on Figure 6 and 7. Thus, another analysis has been performed in order to compare system **E+N** with system **A+M** for which the DRS spectra after irradiation strongly differs visually and for which the ratio profile gives a peak of similar intensity to **E+N** system: replacing the ratio  $I_{after}/I_{before}$  by  $\frac{I_{after} - I_{before}}{I_{after} + I_{before}}$  gives the graphs presented in Figure 9 and 10. These new ratio profiles should give further hints about the accuracy of the ratio analysis. No major difference is observed between the shape of the curves within the two analyses. However, **E+N** ratios present some discontinuities in both analyses (which are magnified in the second ratio analysis performed) while no such feature is observed for **A+M** system. These discontinuities may indicate the presence of experimental artefacts. Thus, no conclusion can be drawn about a photochromic change in the case of **E+N** system based on the performed analyses.

As a result, this experiment should be performed again along with, for instance, pictures of the sample, in order to definitely conclude on this system. Still, we can clearly see from Figure 6 there is a new phase which strongly differs from parent anils.

In conclusion, this compound might be of interest for further studies, however the attempts to crystallize it all failed so far: tests were run using acetonitrile, ethyl acetate, methanol and ethanol/acetonitrile (20/80) as solvents through slow solvent evaporation and no crystal of suitable quality for SC-XRD could be produced.

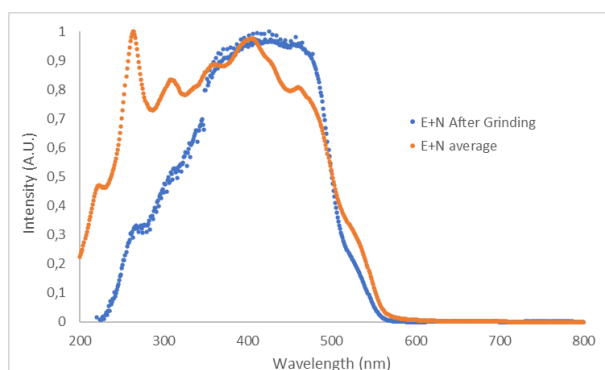


Figure 6: comparison between **E+N** spectrum after grinding (blue curve) and the average of **E** and **N** spectra before grinding (orange curve).

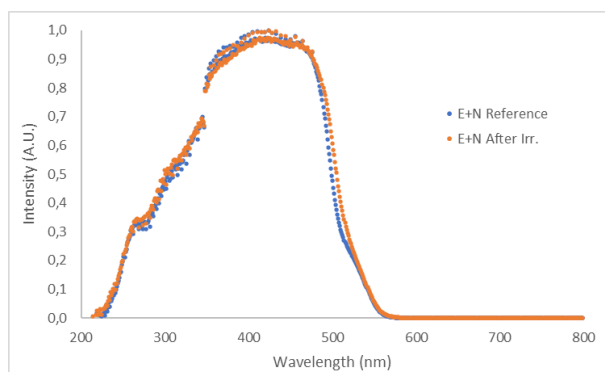


Figure 7: comparison between **E+N** spectrum before irradiation (blue curve) and after 5 min irradiation at 365 nm (orange curve).

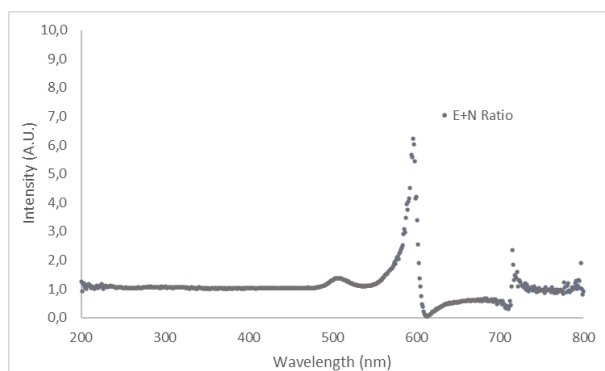


Figure 8: ratio between **E+N** absorption spectrum after irradiation divided by **E+N** absorption spectrum before irradiation.

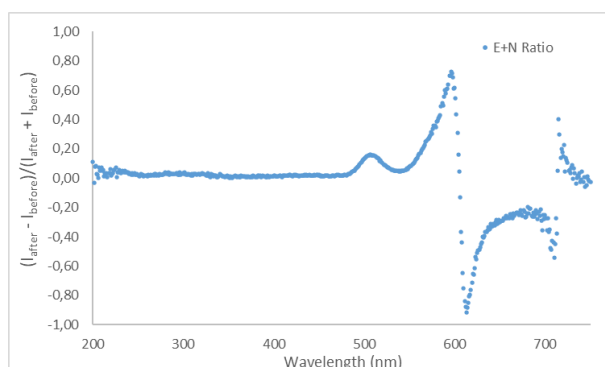


Figure 9: new ratio (corresponding to Figure 7) calculated with **E+N** absorption spectrum after irradiation ( $I_{\text{after}}$ ) minus **E+N** spectrum before irradiation ( $I_{\text{before}}$ ) divided by the sum of  $I_{\text{after}}$  and  $I_{\text{before}}$ .

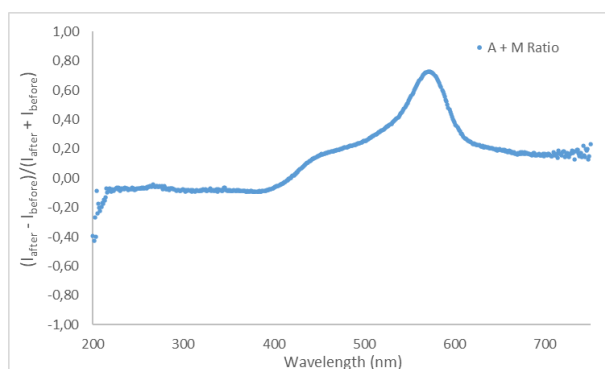


Figure 10: new ratio (corresponding to Figure 3) calculated with **A+M** absorption spectrum after irradiation ( $I_{\text{after}}$ ) minus **A+M** spectrum before irradiation ( $I_{\text{before}}$ ) divided by the sum of  $I_{\text{after}}$  and  $I_{\text{before}}$ .



### System G+H

System **G+H** does not exhibit a strong change in the area between 350 and 600 nm after grinding compared to the average of the references **G** and **H** (equivalent to a physical mixture) as presented in Figure 11, meaning the keto-enol equilibrium is not strongly impacted after the appearance of the new phase.

No change is observed in the photochromic properties as both parent anils were found to be non-photochromic in previous research [1] and no change was observed for the sample spectrum after irradiation as presented in Figure 12. This is confirmed by the ratio of the absorption spectra after and before irradiation which is almost perfectly linear for the whole studied wavelength range as shown in Figure 13.

Further attempts to crystallize this new phase also failed: tests were run using acetonitrile, ethyl acetate, methanol and ethanol/acetonitrile (20/80) as solvents through slow solvent evaporation but no crystal of suitable quality for SC-XRD could be produced.

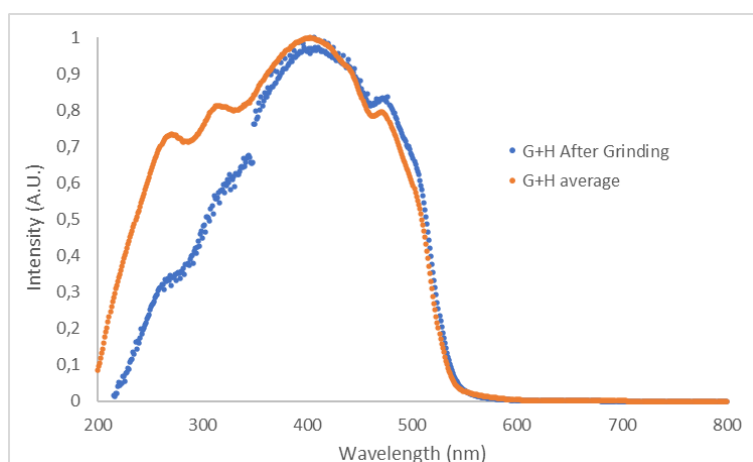


Figure 11: comparison between **G+H** spectrum after grinding (blue curve) and the average of **G** and **H** spectra before grinding (orange curve).

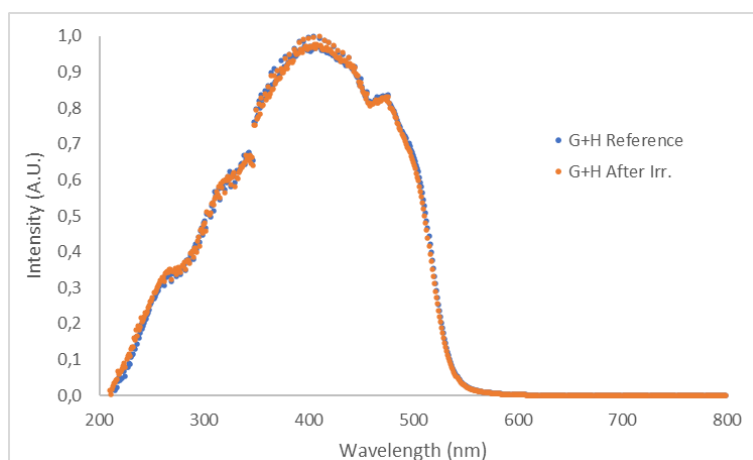


Figure 12: comparison between **G+H** spectrum before irradiation (blue curve) and after 5 min irradiation at 365 nm (orange curve).

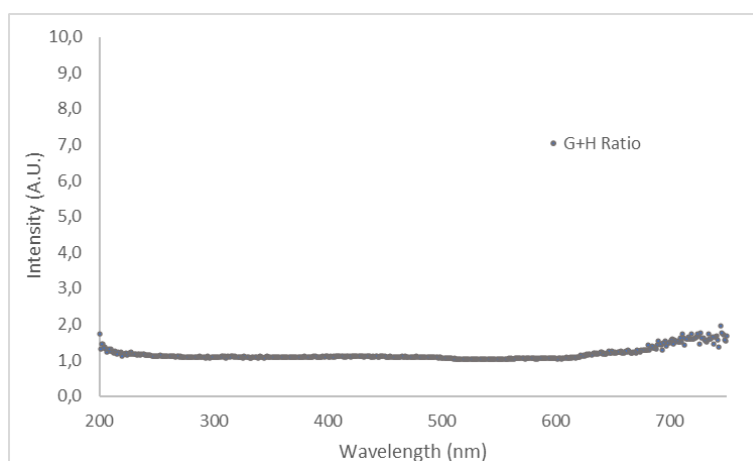


Figure 13: ratio between **G+H** absorption spectrum after irradiation divided by **G+H** absorption spectrum before irradiation.

## Conclusion

Through this preliminary work on anil cocrystals with other anils, cocrystal screening through ball-milling grinding allowed to identify 11 new phases out of the 105 possible combinations. Attempts to crystallize these systems failed but the differences in absorption spectrum of the samples after grinding compared to references evidence cocrystal formation. Three of the newly observed phases are identified as solid-solution (**A/B**; **E/F** and **M/N**) and among the 8 remaining systems (expected to be stoichiometric cocrystals), 3 were studied further with Diffuse Reflectance Spectroscopy (**A+M**, **E+N** and **G+H**) and showed interesting features for system **A+M** which seems to exhibit photochromism.

The results and analysis presented within this chapter are uncomplete but may serve as the basis for future work in the field.

## References

- [1] G. M. Mercier, K. Robeyns, N. Tumanov, J. Wouters, B. Champagne and T. Leyssens, "New Insights into Photochromic Properties of N-Salicylideneaniline," *Cryst. Growth Des.*, no. 19, pp. 5544-5566, 2019.
- [2] G. M. Mercier, K. Robeyns and T. Leyssens, "Altering the Photochromic Properties of N-Salicylideneanilines Using a Co-Crystal Engineering Approach," *Cryst. Growth Des.*, no. 16, pp. 3198-3205, 2016.
- [3] G. R. Desiraju, J. J. Vittal and A. Ramanan, *Crystal Engineering: A Textbook*, Singapore: World Scientific Publishing Co. Pte. Ltd., 2011.
- [4] A. D. McNaught and A. Wilkinson, *IUPAC. Compendium of Chemical Terminology*, Oxford: Blackwell Scientific Publications, 1997.
- [5] K. Fucke, S. A. Myz, T. P. Shakhtshneider, E. V. Boldyreva and U. J. Griesser, "How good are the crystallisation methods for cocrystals?," *New J. Chem.*, no. 36, pp. 1969-1977, 2012.
- [6] T. Fujiwara, J. Harada and K. Ogawa, "Solid-State Thermo-chromism Studied by Variable-Temperature Diffuse Reflectance Spectroscopy. A New Perspective on the Chromism of Salicylideneanilines.," *Journal of Physical Chemistry*, no. 108, pp. 4035-4038, 2004.



## Preface of Chapter 5

The chapter 5, which is entitled “*N*-Salicylideneaniline solid-solutions between structurally related anils: a complex multitude of phases and evidences of an organic four-phasic solid-solution” presents some unpublished results. This chapter is however structured as a publication and for this reason, the anil labels used in chapter 3 and 4 do not correspond to these of the present chapter.



## Chapter 5

***N*-Salicylideneaniline solid-solutions  
between structurally related anils: a  
complex multitude of phases and  
evidences of an organic four-phasic  
solid-solution**

### **Abstract**

In this contribution, four solid-solution systems of anils were studied in order to check photochromic property alteration through solid-solution formation. Among these 4 systems, one shows important changes of its photochromic properties, as well as the presence of multiple phases. These observations were confirmed by the crystallization of two types of solid-solutions, both of which differ from the parent anils. These results point to a four-phasic solid-solution binary diagram - an extremely rare occurrence in the case of organic molecules.

## Introduction

Anils or *N*-Salicylideneaniline derivatives form a family of well-known organic molecules most of which exhibit a reversible UV-Vis induced color-change at the solid state – a property known as photochromism. This feature has led to the use of anils in various applications such as photochromic glass lenses, secured inks for banknotes and official stamps, intelligent screens, new optical devices and for optical data storage.

Anils are typically characterized by two aromatic rings linked together by an azomethyn bridge and possessing an ortho-hydroxy group which can form an internal H-bond feature with the nitrogen atom of the azomethyn bridge. Due to this special feature, anils can undergo a keto-enol tautomerization. The keto form can furthermore undergo a cis-trans isomerization (Figure 1). Both transformations are reversible and can be induced either by heat, light or both depending on the nature of the molecule. The three thus obtained isomers often present a different absorption behavior leading to characteristic chromic properties: the ground state (*trans*-enol) is often found colorless; the *cis*-keto state yellow and the *trans*-keto form red.

One of the main interests of anils lie in the fact that these transitions not only occur in solution but also in the solid-state, which make them ideal candidates for applications as in this state, they are easy to handle, and resistant to fatigue [1] [2]. On the downside, at the solid state, most anils are limited to either a pronounced photo- or thermochromic behavior. Furthermore, photochromic transitions mostly occur at the surface of crystals and with a low conversion: around 5% conversion has been reported in the case of the anils [3].

In the past, a general empiric rule of thumb stated that photochromic anils showed a torsion angle of 30° and above, whereas non-photochromic anils (and thus thermochromic anils) were characterized by a torsion angle of 20° or less [4] [5]. Even though structural packing could potentially explain this observation [6], in the recent years an increasing amount of counter-examples were reported, including weakly photochromic anils [7], which incited a revision of this rule. In a previous contribution, we showed a direct relation between the intensity of the photochromic effect and the torsion

angle rather than a binary “photochromic/non-photochromic” cut-off due to the torsion angle. However, a large majority of anils remain non-photochromic at the solid-state while most of them exhibit photochromism in solution showing structural aspect are predominant factors for the photochromic behavior. To render anils responsive, efforts thus focused on engineering their molecular environment using tools such as: dispersion in polymers, inclusion into zeolites or, more recently, using a cocrystallization approach [7, 8, 9, 10, 11, 12]. In this paper, we continue on this latter approach focusing on a particular case of multi-component crystalline systems, mainly those that lead to a solid-solution.

A solid-solution can be defined as “Solid in which components are compatible and form a unique phase” according to the IUPAC definition [13]. This implies any composition of the components can exist in the same crystalline structure resulting in a constant evolution of the macroscopic properties which in turn allow fully controlling them [14]. The main interest of solid solutions lies in the fact that a continuous (albeit often minor) structural evolution is obtained according to the overall composition. As the photochromic property of anils is very sensitive to slight structural variations, even such slight variations can have a significant impact as shown in this contribution. Furthermore, the possibility of having a continuous composition evolution, allows a true fine-tuning of the photochromic property [14]. A similar approach was adopted by Cohen et al. who studied solid-solutions of photochromic *N*-Salicylidene-4-bromoaniline with non-photochromic *N*-Salicylidene-4-chloroaniline derivatives and found a photochromic solid-solution with 35% of the non-photochromic derivative [15]. A recent study performed by Uekusa et al. used this approach to combine non-photochromic planar anils with non-planar cofomers acting as a template. As a result, a solid solution exhibiting a high torsion angle (55°) and showing photochromism was obtained [2]. Both these studies focused on the on-off switch of the photochromic property. In previous work (chapter 3), we showed how weak photochromism can be detected [7]. Using such techniques allowed us to monitor how the maximal photochromic intensity changes over the varying molar ratios of a two-component system.

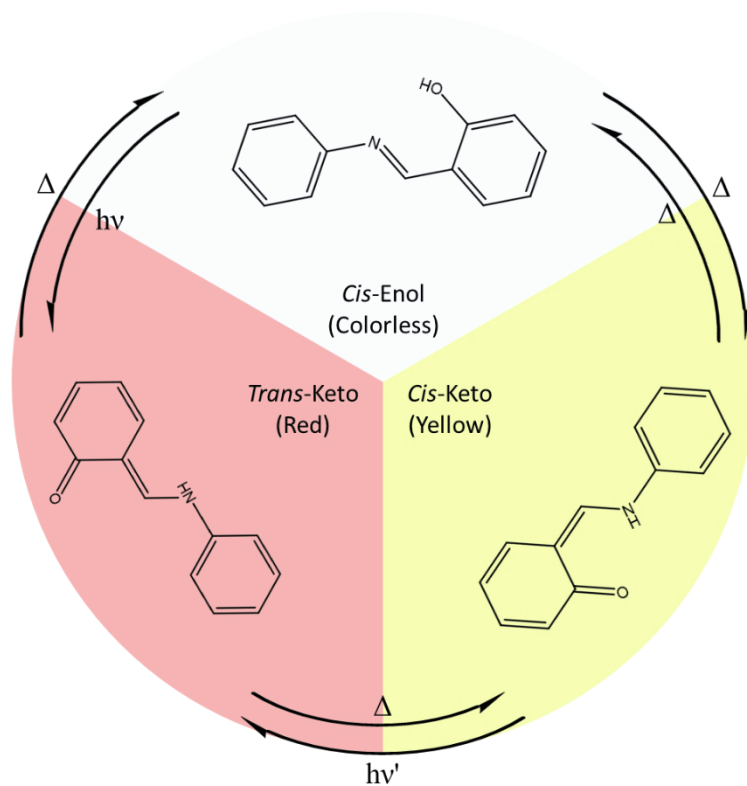


Figure 1: Generally accepted transition scheme between *N*-Salicylideneaniline isomers and corresponding chromic characteristic [6].

To evaluate the potential of solid-solutions in the scope of anil photochromism, 4 solid-solutions of well-known anils with their para-fluor-substituted equivalents (presented in Scheme 1) were successfully prepared using a mechanochemical approach and their optical properties evaluated through Diffuse Reflectance Spectroscopy (DRS). Among these 4 systems, one shows important changes in photochromic character and this case was studied in detail.

## Experimental Section

### Starting Materials and Synthesis

Following materials and solvent were purchased and used as such:

From Alfa Aesar: 4-aminobenzoic acid (10177463). From Accros Organic: 2,4-dihydroxybenzaldehyde (173640250); 4-fluoro-aniline (119290250); Ortho-vanilin (153071000). From Janssen Chimica: Acetic acid (14.893.52). From Sigma Aldrich: Salicylaldehyde (101669521); Salicylamide (101235208). From U.C.B. s.a.: Aniline (1163-4944). From TCI: hydroxy-1-naphtaldehyde (708-06-5). From VWR Chemicals: Acetonitrile (200-835-2); Ethanol (200-578-6); Ethyl acetate (205-500-4); Hexane (203-777-6); Methanol (20847.307).

Synthesis of the compounds were carried out following previously described method [7]:

Compound **A** (*N*-Salicylideneaniline) was prepared by hand grinding (ten minutes) of salicylaldehyde (0.1 mol) with aniline (0.1 mol) in presence of a catalytic amount of acetic acid (1 drop) in a 100 ml beaker and dried for 48 h at 45 °C and used as such (yield: 98%, purity: 99%). Compound **B** (4-fluoro-Salicylideneaniline) was prepared by hand grinding (5 minutes) of salicylaldehyde (0.1 mol) with 4-fluoro-aniline (0.1 mol) in a 100 ml beaker and dried for 48 h at 45°C and used as such (yield: 98%, purity: 99%). Compound **C** (3'-Methoxysalicylideneaniline) was prepared by dissolution of ortho-vanilin (0.1 mol) in 2 ml of acetonitrile at 50 °C after which benzamine (0.1 mol) and ethanol (5 mL) were added in a 100 ml beaker and the solution was stirred regularly with a spatula for 30 minutes. The solution was then left to evaporate overnight at 50 °C and led to a red gel. This gel was triturated with pure hexane and was left to evaporate leading to a red crystalline powder which was dried for 48 h at 50°C and used as such (yield: 98%, purity: 99%). Compound **D** (2-[[[4-Fluorophenyl]imino]methyl]-6-methoxyphenol) was prepared by dissolution of ortho-vanilin (0.1 mol) in 2 ml of acetonitrile at 50 °C in a 100 ml beaker. To this solution were added 4-fluoro-benzamine (0.1 mol) and ethanol (5 mL) and the solution was stirred regularly with a spatula for 30 minutes. The solution was left to evaporate overnight at 50 °C and led to a red gel. This gel was triturated with pure hexane and was left to evaporate at 50 °C leading to a dark-red crystalline powder which was dried for 48 h at 50°C and used as such (yield: 98%,

purity: 99%). Compound **E** (4-[(Phenylimino)methyl]-1,3-benzenediol) was prepared by addition of benzamine (10 mmol) to a mixture of 2,4-dihydroxy-benzaldehyde (10 mmol) and 10 ml of acetonitrile in a 100 ml beaker. The solution was kept at 60 °C overnight and led to a red gel. This gel was triturated with pure hexane and led to a yellow precipitate. The solution was left to evaporate and the yellow solid was dried for 48 h at 45°C and used as such (yield: 98%, purity: 99%). Compound **F** (4-[[4-Fluorophenyl]imino]methyl]-1,3-benzenediol) was prepared by addition of 4-fluoro-benzamine (10 mmol) to a mixture of 2,4-dihydroxy-benzaldehyde (10 mmol) and 10 ml of acetonitrile in a 100 ml beaker. The solution was kept at 60 °C overnight and led to a red gel. This gel was triturated with pure hexane and led to a yellow precipitate. The solution was left to evaporate and the yellow solid was dried for 48 h at 45°C and used as such (yield: 98%, purity: 99%). Compound **G** (2-Hydroxy-1-naphthalaniline) was prepared by dissolution of hydroxy-1-naphthaldehyde (10 mmol) in 5 ml of acetonitrile at 50 °C in a 100 ml beaker. Benzamine (10 mmol) was added to this solution and the solution was stirred regularly with a spatula. Precipitate started to appear after 10 minutes. The solution was then left to evaporate and the yellow solid was dried for 48 h at 45°C and used as such (yield: 98%, purity: 97%). Compound **H** (2-Hydroxy-1-naphthalidene-p-fluoroaniline) was prepared by dissolution of hydroxy-1-naphthaldehyde (10 mmol) in 5 ml of acetonitrile at 45 °C in a 100 ml beaker. To this solution were added 1 drop of pure acetic acid and 4-fluoro-benzamine (10 mmol) and the solution was stirred regularly with a spatula. Precipitate started to appear after 2 minutes. The solution was left to evaporate and the yellow solid obtained was dried for 48 h at 45°C and used as such (yield: 98%, purity: 97-99%).

### **Mechanochemical Solid-Solution Synthesis**

Solid-solution mixtures were prepared through liquid-assisted grinding using variable amounts of starting materials corresponding to the sample's labels used in the text (for a total mass of around 200 mg) and 10 µL of acetonitrile. Samples were ground in a RETSCH Mixer Mill MM 400 for 90 min at 30 Hz and dried in a desiccator at room temperature for at least 48h before use. The resulting powders were characterized using X-ray Powder Diffraction. Upon solid-solution identification, attempts were made to obtain a single crystal of suitable size and quality for X-RD single crystal measurement.

### Single Crystal Formation

Solvent slow evaporation at room temperature starting from an under-saturated solution yielded single crystals of suitable quality for: **A/B**: 50/50 from acetonitrile; **A/B**: 10/90; **A/B**: 05/95; **C/D**: 50/50; **C/D**: 75/25 and **G/H**: 50/50 from acetonitrile/ethanol: 20/80 mixture; **E/F**: 50/50 from methanol.

Solutions were prepared by adding around 10-20 mg of the corresponding ground powder to 1 mL of the corresponding solvent (see above) into a 1.5 mL vial. Crystals appeared after 1 to 3 weeks. Other attempts with pure ethanol, methanol or acetonitrile did not lead to crystal with sufficient quality for SC-XRD.

**X-Ray Powder Diffraction (XRPD).** X-ray diffraction measurements were performed on a Panalytical X'Pert PRO diffractometer (Bragg-Brentano geometry, X'Celerator detector) equipped with a Cu K $\alpha$  X-ray source (operating at 30 kV and 45 mA). A 2 $\theta$  scanning range from 4° to 40° with a 0.017° step size was applied. All data are normalized to 100 for the highest peak.

**Single Crystal X-Ray Diffraction.** Structures were integrated with the CrystallisPro software [16] and the implemented multi-scan absorption correction procedure was applied. Each structure was solved by direct methods, SHELXT [17] and refined by full-matrix least squares on  $|F|^2$  using SHELXL-2014 or 2018 [18]. Non-hydrogen atoms were refined anisotropically and hydrogen atoms were either placed on calculated positions in riding mode with temperature factors fixed at 1.2 times  $U_{eq}$  of the parent atoms and 1.5 times  $U_{eq}$  for methyl groups, or located in the Fourier difference maps when involved in H-bonds.

### Diffuse Reflectance Spectroscopy Measurements

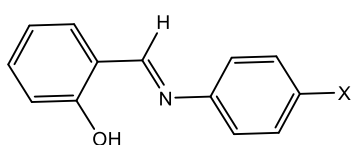
DRS spectra were obtained with a Varian 5E spectrophotometer equipped with a "praying mantis" diffuse reflection accessory and were converted to absorption spectra using the Kubelka-Munk function [19] [20] and using PTFE as a reference for baseline correction. Spectra were measured directly on sample powders and were normalized relatively to their highest peak. Kubelka-Munk spectra were averaged over three measurements (without changing the sample surface) and  $I_{max}$  values were calculated using the ratio method previously described [7]. Thermal fading was analyzed by monitoring the evolution of absorption at 550 nm after irradiation (absorption measured each second in a dark

environment). Irradiations were carried out with a MAX-303 lamp (Xenon light source 300 W) at 360 nm (by the use of 20 nm bandpass filters) for 5 minutes.

### Anils and systems studied:

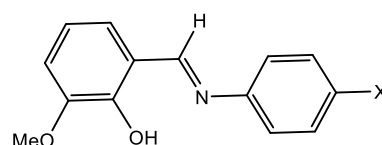
Scheme 1: List of anils used within this work

Solid-solution **A/B**



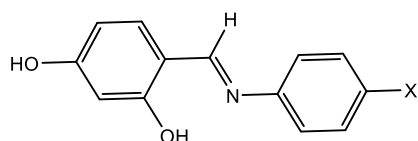
**A:** X = H  
**B:** X = F

Solid-solution **C/D**



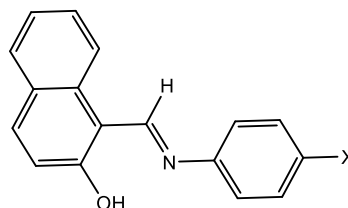
**C:** X = H  
**D:** X = F

Solid-solution **E/F**



**E:** X = H  
**F:** X = F

Solid-solution **G/H**



**G:** X = H  
**H:** X = F

## Results

### Solid-solution formation

Equimolar mixtures of the four above-cited systems were prepared through ball-milling and the resulting powders used to synthesize single crystals which could be characterized through SC-XRD. This highlights the ability of the anils to easily form solid solution with fluorinated derivatives. Furthermore, 3 others structures with different molar ratios were found for **A/B** system and 1 for **C/D** system, hence definitely proving the easiness these systems have to crystallize as solid-solutions with different ratios. Structures crystallized from equimolar mixtures for the 4 systems are presented in Figure 2.

Interestingly, **E/F** was successfully crystallized in a 48/52 ratio, whereas attempts to obtain single crystals of the parent compounds failed.

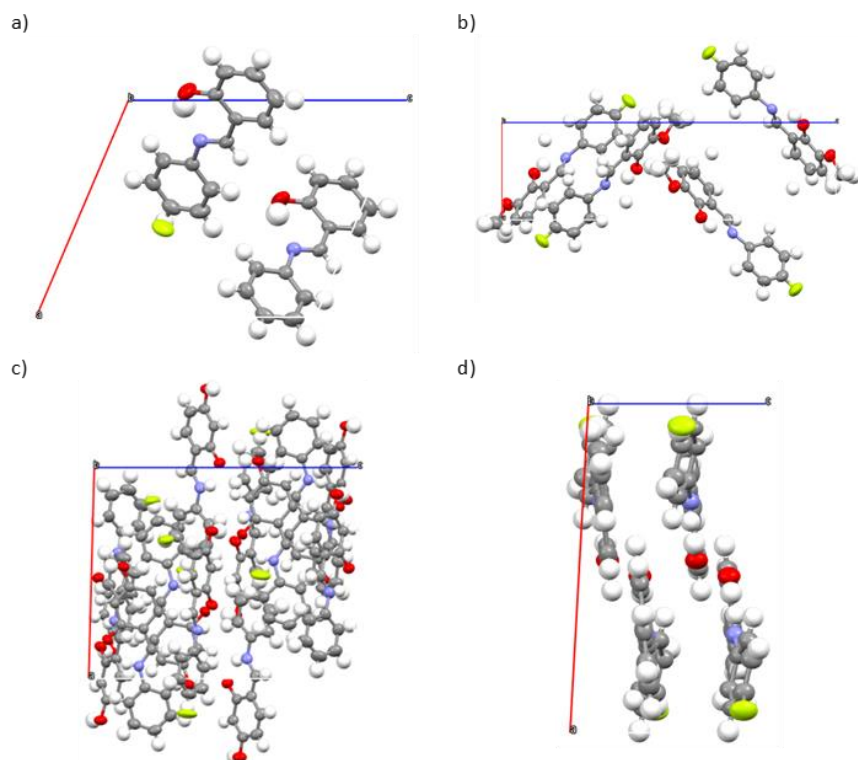


Figure 2: Crystal packing with thermal displacement ellipsoids drawn at the 50% probability level of solid-solutions a) **A/B**: 53/47 molar ratio; b) **C/D**: 68/32 molar ratio; c) **E/F**: 48/52 molar ratio and d) **G/H**: 53/47 molar ratio; all crystallized from an equimolar solution.

### Structural studies

As mentioned above, 4 different **A/B** solid-solution structures were obtained for the **A/B** system through crystallization (after ball-milling) and SC-XRD and correspond to 2 new phases as discussed below. Relevant structural parameters are reported in Table 1 below, along with these of parent anils **A** and **B** polymorphs used in this work and allowed to identify two different solid-solution phases which both differ from all anil **A** polymorphs and **B** structures: the sample prepared from a **A/B**: 80/20 molar ratio (yellow column; labeled **A/B-I** in the text) and the

family of 3 structures prepared from **A/B**: 50/50 to 05/95 molar ratios (green columns; labeled **A/B-II** in the text). As the molar ratios presented in Table 1 came from refinement of the structures after crystallization and SC-XRD, they slightly differ from the initial molar ratios specified in the sample names.

The  $\beta$  angle of the two new phases differs from all polymorphs of **A** and **B**, as well as the a, b and c unit cell parameters (while they are very similar within the 3 green columns), hence proving the existence of at least 4 phases in this system - a feature which has never been reported for organic solid-solution to the best of our knowledge. To further study this system and establish its binary diagram, XRPD and DSC measurements have been performed through the whole molar ratio domain (from 100% **A** to 100% **B**) and results are presented in the following section. Along with crystalline parameters given in Table 1 for the different phases, the corresponding molecular geometries of the new structures are given in Table 2.

Table 2 shows the new solid-solution phases are flat with a torsion angle (T1 as presented in Figure 3) below  $10^\circ$  and that interplanar distances are all around 3.4 Å, which is similar to what is found in anil **B** structure. Interestingly, the **A/B-I** phase strongly differs from anil **A** structure but is similar to **A/B-II** structure containing 47% of **B** with an enhanced keto-character of bond 1. Within the **A/B-II** phase, there is an evolution of this particular bond length from 1.336 Å with 47% **B** to 1.355 Å with 92% of **B**, this last value being close to what is found in anil **B** alone. As a result, there is a sharp transition from anil **A** to solid-solution **A/B-I** followed by a smooth transition towards **A/B-II** solid-solution and further anil **B** structure.

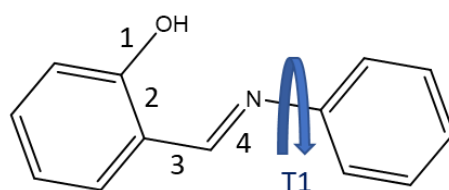


Figure 3: bonds of interest – labelled from 1 to 4, and the main torsion angle T1

Table 1: relevant structural parameters of parent anils **A** (4 polymorphs reported) and **B** and the 4 newly identified solid-solution structures. Newly identified structures are highlighted (yellow for phase **A/B-I** and green for phase **A/B-II**).

Sample name	SALCAN	SALCAN01	SALCAN02	Anil A (SALCAN04)	Solid Solution A/B: 80/20	Solid Solution A/B: 50/50	Solid Solution A/B: 10/90	Solid Solution A/B: 05/95	Anil B (CAVQAR02)
Phase name	/	/	/	A	A/B-I	A/B-II	A/B-II	A/B-II	B
Empirical formula	C <sub>13</sub> H <sub>11</sub> NO	C <sub>13</sub> H <sub>11</sub> NO	C <sub>13</sub> H <sub>11</sub> NO	C <sub>13</sub> H <sub>11</sub> NO	0.83(C <sub>13</sub> H <sub>11</sub> NO) <sub>1</sub> <sup>1</sup> 0.17(C <sub>13</sub> H <sub>10</sub> FNO)	0.53(C <sub>13</sub> H <sub>11</sub> NO) <sub>1</sub> <sup>1</sup> 0.47(C <sub>13</sub> H <sub>10</sub> FNO)	0.09(C <sub>13</sub> H <sub>11</sub> NO) <sub>1</sub> <sup>1</sup> 0.91(C <sub>13</sub> H <sub>10</sub> FNO)	0.08(C <sub>13</sub> H <sub>11</sub> NO) <sub>1</sub> <sup>1</sup> 0.92(C <sub>13</sub> H <sub>10</sub> FNO)	C <sub>13</sub> H <sub>10</sub> FNO
M [g/mol]	197.22	197.22	197.22	197.22	200.28	205.68	213.53	213.79	215.22
T [K]	283-303	283-303	283-303	283-303	283-303	293(2)	295(2)	295(2)	283-303
Wavelength [Å]	/	/	/	/	0.71073	0.71073	1.54184	1.54184	/
Crystal system	Orthorhombic	Orthorhombic	Orthorhombic	Triclinic	Monoclinic	Monoclinic	Monoclinic	Monoclinic	Monoclinic
Space group	Fd2d	P2 <sub>1</sub> 2 <sub>1</sub> 2 <sub>1</sub>	Pbc2 <sub>1</sub>	P1	P2 <sub>1</sub> /c	Pn	Pn	Pn	P2 <sub>1</sub> /c
a [Å]	27.968(16)	6.0750(11)	5.7918(6)	5.9183	17.994(3)	10.0734(13)	10.1254(6)	10.1272(3)	12.8323
b [Å]	5.941(2)	11.6306(15)	13.6449(15)	7.1869	4.6428(4)	4.6722(4)	4.6521(2)	4.65409(11)	5.791
c [Å]	12.882(3)	14.484(2)	13.6449(15)	14.295	12.184(2)	11.9195(15)	11.9793(8)	11.9724(4)	14.8234
α [°]	90	90	90	85.13	90	90	90	90	90
β [°]	90	90	90	78.03	100.001(16)	113.022(15)	113.781(8)	113.823(4)	107.817
γ [°]	90	90	90	65.80	90	90	90	90	90
V [Å <sup>3</sup> ]	2140.45	1023.38	1078.34	542.535	1002.42	516.31(12)	516.36(6)	516.21(3)	1048.72
Z	8	2	4	2	4	2	2	2	2

<sup>1</sup> Values of molar ratios were obtained through XRD refinement and present an uncertainty of around 0.05

Table 2: Geometrical molecular parameters of new phases and pure parent anils.

Compound	Bond 1 (Å)	Bond 2 (Å)	Bond 3 (Å)	Bond 4 (Å)	T1 Angle (°)	Interplanar Distances (Å)
<b>A</b> <sup>a</sup>	1.352	1.419	1.455	1.280	47	/
<b>A/B-I</b> (83/17) <sup>b</sup>	1.330	1.395	1.434	1.254	5.1	3.493
<b>A/B-II</b> (53/47) <sup>b</sup>	1.336	1.399	1.452	1.270	0.3	3.424
<b>A/B-II</b> (08/92) <sup>b</sup>	1.355	1.402	1.442	1.279	0.3	3.448
<b>B</b> <sup>a</sup>	1.352	1.410	1.448	1.275	6.3	3.435

<sup>a</sup> Compound **A** and **B** values from respective references [21] and [22].

<sup>b</sup> Molar ratio of **A** and **B** anils from Table 1.

<sup>c</sup> **A/B-I** structure is a disordered structure and the given values have less precision but are still provided here as they were similar to the values of other structures.

### XRPD results

Prior to further XRPD analysis, the XRPD patterns of the two new solid-solution structures (**A/B-I** and **A/B-II**) were simulated and compared in order to identify specific peaks of each compound. The patterns are quite similar as presented in Figure 4, but a few differences can be found: the first peak appears at  $2\theta = 9.97^\circ$  for the **A/B-I** structure and at  $2\theta = 9.75^\circ$  for the **A/B-II** structure. Also the patterns differ between  $19^\circ$  and  $22^\circ$  and **A/B-II** exhibits a typical peak at  $2\theta = 22.35^\circ$ . All the 4 phases observed in the **A/B** system present a peak at around  $15^\circ$  which slightly differs:  $15.2^\circ$  for anil **A**,  $14.75^\circ$  for **A/B-I**,  $14.7^\circ$  for **A/B-II**, and  $14.5^\circ$  for anil **B**. This might allow to monitor transformation based on this area only, however in the case of **A/B-I** and **A/B-II**, the difference is within the experimental uncertainty and the transition between these two phases cannot be monitored unless high precision XRPD is performed.

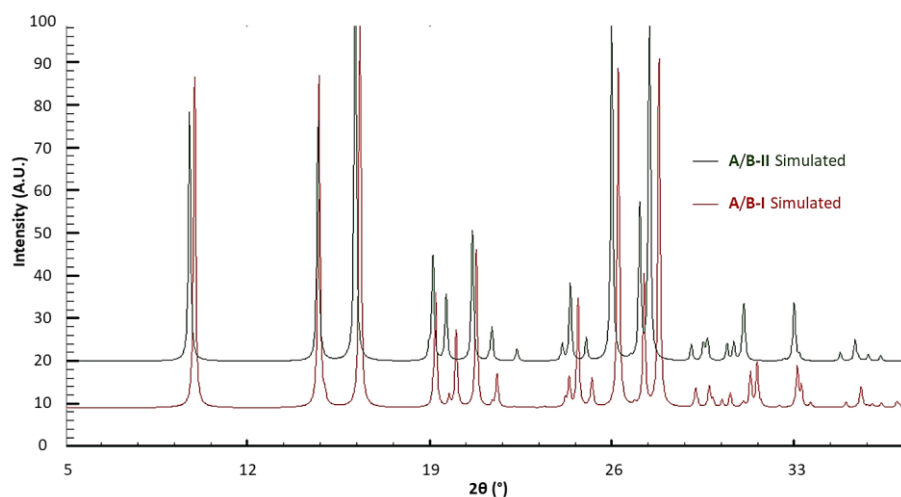


Figure 4: XRPD patterns of **A/B-I** (red) and **A/B-II** (black) simulated from crystal structure.

Mixtures with varying molar amount of **B** (from pure anil **A** to pure anil **B**) were prepared through ball-milling and XRPD results are presented in Figure 5. Pattern 1 (blue - 0% **B**) shows pure anil **A** while pattern 2 (turquoise - 13% **B**) exhibits peaks from both anil **A** and a new phase. This new phase matches to pattern 3 (black - 17% **B**) which is simulated from solid-solution **A/B-I** crystal. Pattern 4 (green - 35% **B**) is an intermediate between pattern 3 and 5 and thus corresponds to a mixture of **A/B-I** and **A/B-II**. Pattern 5 (violet - 47% **B**) is simulated from **A/B-II** crystal. Pattern 6 (orange - 83% **B**) corresponds to a superposition of **A/B-II** pattern and pure anil **B** pattern (with a typical peak at 7.3°) and finally pattern 7 (red - 100% **B**), which corresponds to the simulated pattern of **B** (CAVQAR02).

It would be interesting to use Vegard's law using these XRPD analysis as this law stipulates that crystal lattice parameters do evolve linearly with molar composition in a solid-solution [23]. As crystal lattice parameters can be deduced from XRPD (using Rietveld refinement), plotting their evolution along with varying **B** molar ratio might allow to deduce the limit composition for phase transitions (as parameters should behave differently in the different phases but linearly within the same phase) [24]. However this would require more XRPD measurements and of high quality in order to draw a precise figure and is thus left as a perspective of the current work.

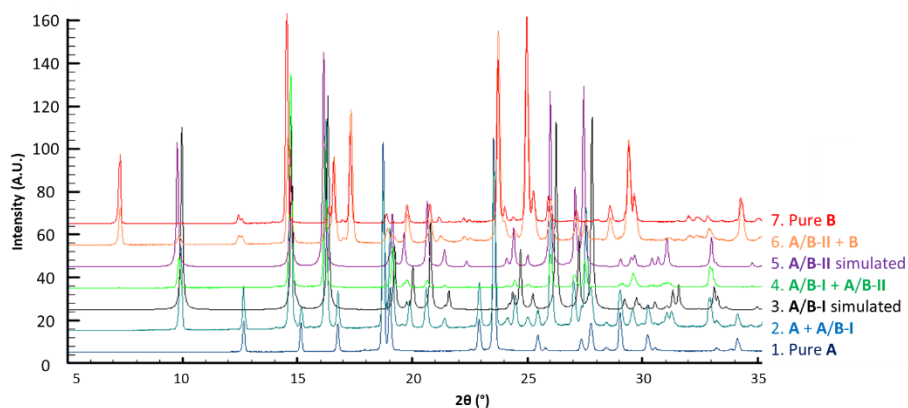


Figure 5: X-ray powder diffraction pattern of parent anils **A** and **B** and **A/B** mixtures.

### Thermal analysis

Differential Scanning Calorimetry measurements were performed on eighteen samples in order to have a precise view of the melting points evolutions. Single melting endotherms are observed for 0, 26, 63 and 100% **B** respectively (thermograms 1, 9, 14 and 18 on Figure 6) and with all other thermograms characterized by a eutectic melt followed by a liquidus.

For mixtures containing 0.2% to 23% **B** (thermograms 2-8) with a eutectic peak at 44.6 °C for 13.1% **B** (thermogram 7). The second transition is expected to start around 35% **B** as the peak of pattern 10 (orange – 35.07% **B**) is not very well defined meaning a new eutectic peak is appearing, even though the corresponding XRPD pattern matched pure **A/B-I** structure pattern (meaning the other product is only present as traces or amorphous phase). The second transition thus occurs from 35% **B** and is perfectly visible on thermograms 11-13 (orange - 43.42 to 58.44% **B**) with and eutectic peak at 51 °C and a liquidus peak at different temperatures. The third and last transition is visible on thermograms 15-17 (red – 70.03 to 93.37% **B**) with and eutectic peak at around 61 °C and again a liquidus peak at different temperatures.

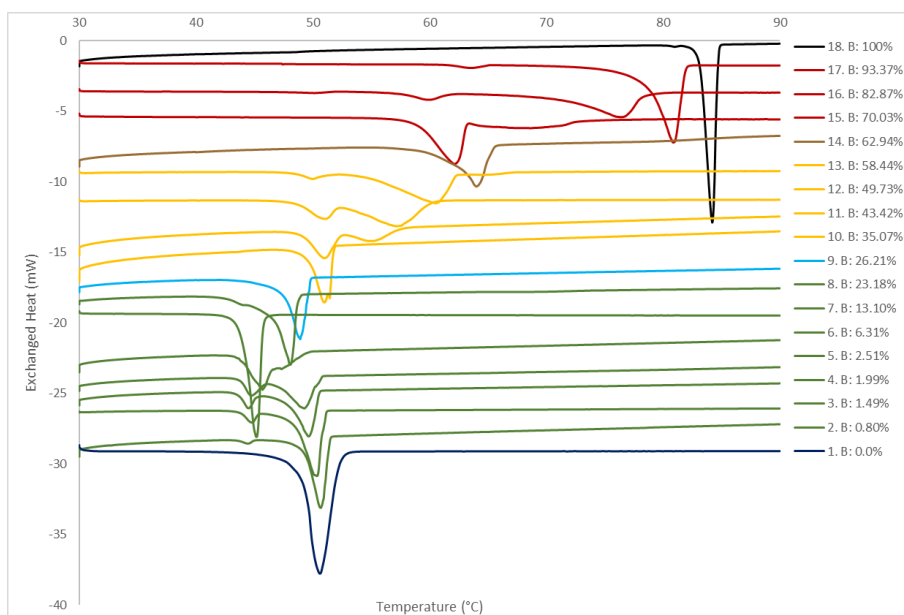


Figure 6: DSC patterns for various **A/B** powders with molar content of **B** varying from 0 to 100%.

Based on these results, we can plot the eutectic (first peak) and liquidus (second peak) temperatures when two peaks are observed and the single melting endotherm temperature when only one peak is encountered, as a function of the **B** molar ratio in the system and the results are displayed in Figure 7.

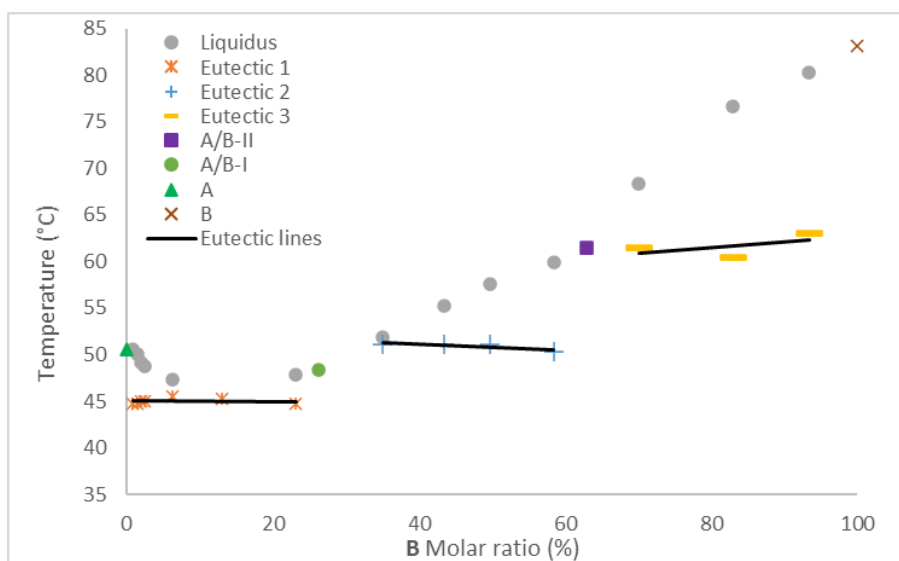


Figure 7: eutectic and liquidus points temperature with varying molar amount of **B** in the **A/B** system and corresponding pure phases.

### Photochromic properties of **A/B** system

Among the 4 systems discussed in the solid-solution formation section, **A/B** was the only one exhibiting an observable change in photochromic property while comparing the solid-solution to parents anils. Anil **A** is strongly photochromic [25] and **B** is not [26]. To evaluate the evolution of the photochromic property, different samples were prepared through ball-milling with varying ratios of **A** and **B** and their maximum photochromic intensity change measured through Diffuse Reflectance Spectroscopy (according to our previously reported method [7] which can be found in chapter 3).

Even though a complete disappearance of photochromism in the system could be expected over increasing **B** molar ratio, it didn't occur in a constant and regular way – a typical feature for regular solid-solution [13] hence showing at least one new phase does appear. This is in agreement with the structural analysis showing multiple phases appearing. Among them, only the **A**-phase is photochromic and this feature disappears quickly over increasing **B** molar ratio as presented in Figure 8 and is also in accordance with visual observations of the powders after irradiation as presented in Figure 9.

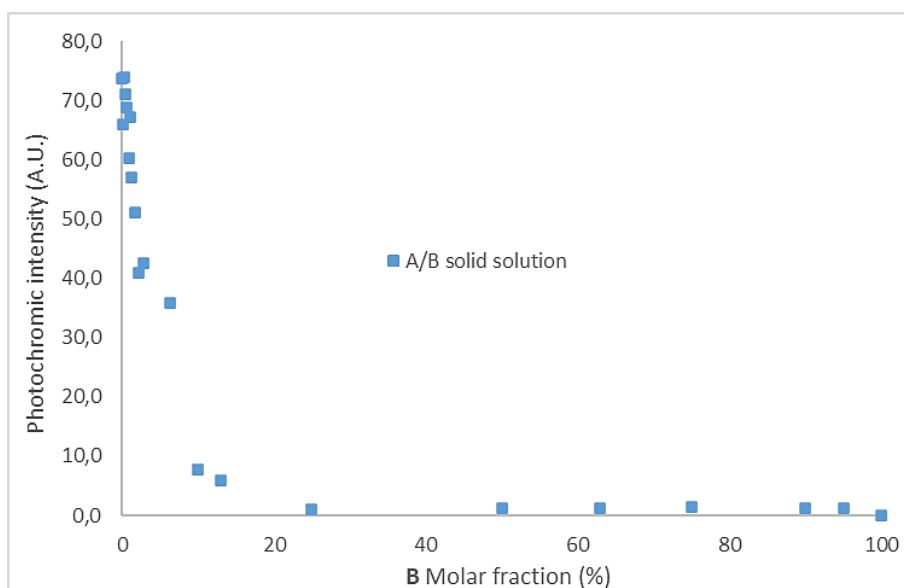


Figure 8: Evolution of the maximum photochromic intensity with varying molar ratio of anil **B** in the system.

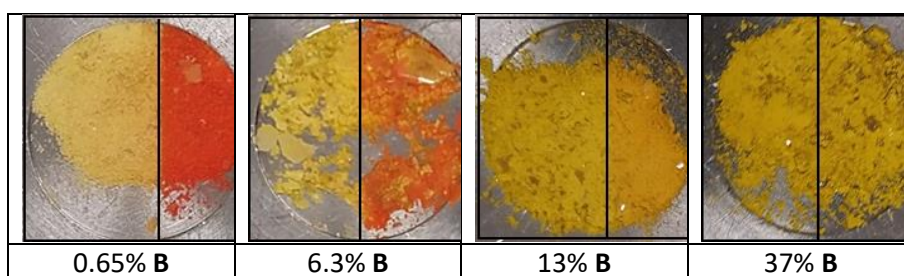


Figure 9: Observed color changes in **A/B** solid solution with varying amount of **B** (expressed in molar percentage). The right part of each sample was irradiated for 5 min at 365 nm while left part was masked.

Kinetical decay of photochromism was studied through DRS measurements which were performed on 5 different **A/B** solid-solutions with **B** amount comprised between 0% (pure **A** – already reported value [27]) and 13% (the identified transition point). Powders were irradiated 5 min at 365 nm and the Kubelka-munk function measured at 550 nm over time and were linearized using the Malkin equation [11]. The kinetic is expected to be a bi-exponential one [11] but  $k_2$  parameters were not calculated. Obtained  $k_1$  parameters are given in Table 3 and plotted as a function of **A** molar content

with corresponding tendency curve as presented in Figure 10. Original graphs and  $k_1$  analysis can be found in the supporting information section Ch5.2.

Figure 10 shows a  $k_1$  increase of almost one order of magnitude through increase of **B** molar fraction in the solid solution from  $3.5 \times 10^{-4} \text{ s}^{-1}$  for pure **A** to  $27.6 \times 10^{-4} \text{ s}^{-1}$  with 13% of **B**. Thus, the addition of **B** to the structure leads to a much faster depletion of the color after irradiation (faster thermal-back reaction) and this could be due to a decreased stability of the *trans*-keto form. This hypothesis explains why no photochromism is observed above 13% **B**.

Table 3: kinetical parameter ( $k_1$ ) for studied solid solutions.

<b>B</b> Molar fraction (%)	$k_1$ ( $\cdot 10^{-4} \text{ s}^{-1}$ )
0	3.5
0.5	7.3
2.0	6.1
2.5	9.0
10.0	26.2
13.1	27.6

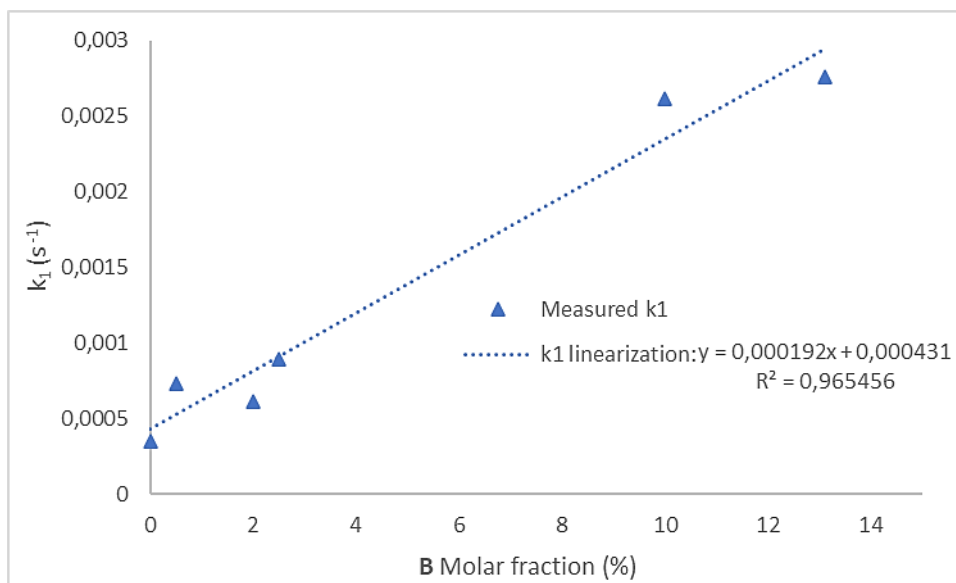


Figure 10: evolution of kinetical parameter  $k_1$  ( $\text{s}^{-1}$ ) over **A** molar fraction in the **A/B** solid-solution.

## Discussion

XRPD measurements over different powder compositions revealed the existence of two intermediate solid-solution phases which were successfully crystallized and analysed through SC-XRD. XRPD patterns allowed to observe transitions between pure parent anils **A** and **B** phases and the solid-solution **A/B-I** and **A/B-II** phases (with intermediate patterns corresponding to superposition of phases) and these results were also confirmed with DSC measurements (Figure 6) which revealed 3 different eutectic areas which in turn separate 4 different phases. All these results put together provide evidence for the existence of a four-phasic solid-solution binary diagram for this system - a feature never reported in literature for organic molecules to the best of our knowledge.

The existence of two intermediate solid-solution phases is responsible for the strange evolution of photochromic properties. Pure solid-solutions were not photo-responsive (this is proven by the absence of photochromic response after irradiation for samples with more than 20% **B** molar content, as shown on Figure 8 and 9), the disappearance of photochromism occurs quickly within mixture of pure **A** (strongly photochromic) and pure **A/B-I** (non-photochromic) with an inflexion point in the photochromic evolution pattern (Figure 8) at 13% **B** molar composition which in turn corresponded to the eutectic point between **A** and **A/B-I** on DSC patterns. Thus, as long as phase **A** is present in the environment there is a visible photochromic response. The three other phases are not photo-responsive.

To complete the binary diagram of Figure 7, the limits of many areas can be determined through the realization of Tammann's plot (plot of eutectics enthalpy vs molar content) [28]. As many eutectic peaks were not completely separated from liquidus peak, a mathematical correction was applied to approximate total peaks enthalpy :  $\Delta H_{eutectic}^{corrected} = \left( \frac{\Delta H_{eutectic}^{measured}}{\Delta H_{eutectic}^{measured} + \Delta H_{liquidus}^{measured}} \right) \cdot \Delta H_{total}^{measured}$  with  $\Delta H_{eutectic}^{measured}$  the measured enthalpy of the eutectic peak (A on Figure 11);  $\Delta H_{liquidus}^{measured}$  the measured enthalpy of the liquidus peak (B on Figure 11) and  $\Delta H_{total}^{measured}$  the total measured enthalpy (A+B+C as presented in Figure 11).

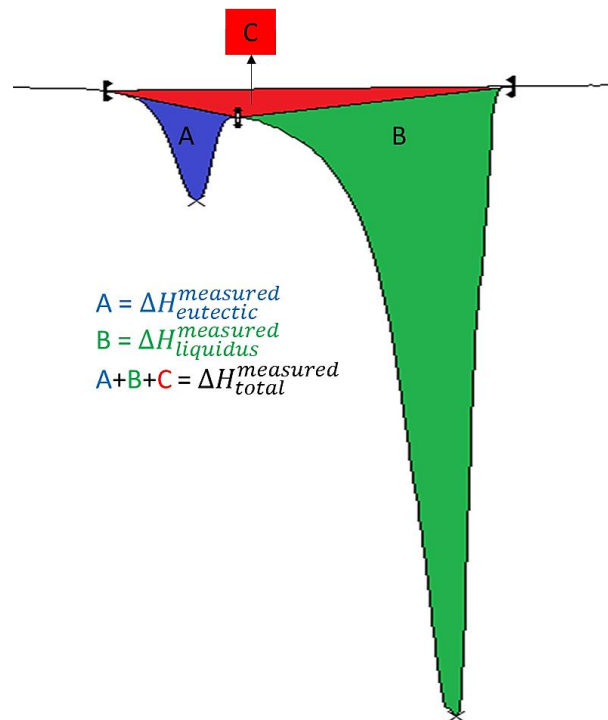


Figure 11: Example of close eutectic and liquidus peaks and corresponding areas (integrals) used in the calculations.

Using the  $\Delta H_{\text{eutectic}}^{\text{corrected}}$  calculated from DSC patterns allowed to draw Tammann's plot for the **A** side (transition **A**  $\rightarrow$  **A+A/B-I**) eutectic limit and for the eutectic limit for transition **A/B-I** + **A/B-II**  $\rightarrow$  **A/B-II** with accuracy (respectively 0,4% and 62,7% **B** molar composition for the eutectic limits) and corresponding graphs are presented below (Figure 12; limits are calculated for  $\gamma = 0$ ).

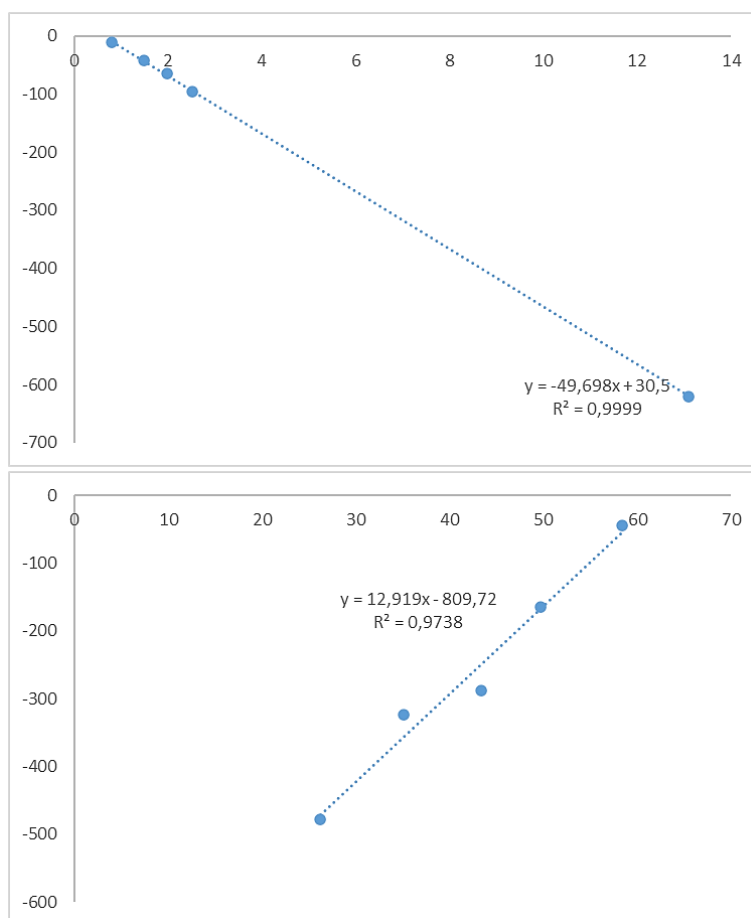


Figure 12: (top) Tammann's plot for transition  $A \rightarrow A+A/B-I$ ; (bottom) Tammann's plot for transition  $A/B-I + A/B-II \rightarrow A/B-II$ .

Transitions  $A+A/B-I \rightarrow A/B-I$  and  $B+A/B-II \rightarrow B$  could also be evaluated but with less data and thus a decreased accuracy and give respectively 23,3% and 94,5% **B** molar composition for the eutectic limits. All these values are in agreement with DSC and XRPD measurements. However there weren't enough data to properly evaluate  $A/B-I \rightarrow A/B-I + A/B-II$  and  $A/B-II \rightarrow A/B-II + B$  eutectic limits.

Based on eutectic and liquidus temperatures from DSC measurements along with calculated Tammann's limits, we propose the following binary diagram for the **A/B** system (Figure 13).

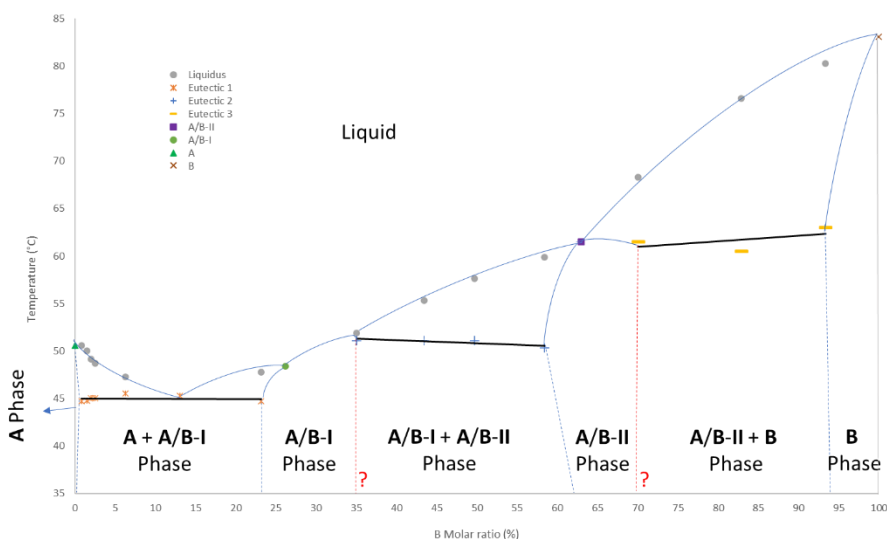


Figure 13: proposed binary diagram of the **A/B** system with calculated Tammann limits (blue dashed lines) and unknown limits (red dashed lines).

### Conclusion

To evaluate the impact solid-solutions can have over photochromic properties of *N*-Salicylideneaniline derivatives, 4 systems composed by an anil and one of its fluorinated derivatives were prepared and a total of 8 new solid-solution structures were obtained through SC-XRD. The **A/B** system exhibited a dramatic change in its photochromism with the 50/50 molar ratio powder sample being non-photochromic while parent anil **A** is strongly photochromic. Further studies of this system revealed two different intermediates solid-solution phases which also structurally differs from parent anils **A** and **B** phases, hence providing evidences for a four-phasic solid-solution binary diagram – an extremely rare pattern for organic molecules. Based on DSC, XRPD and Tammann's plots, an approximative binary diagram could be draw and is proposed for this system.

As a dramatic change in photochromic property was observed with varying **B** molar ratio within anil **A** phase, this system deserves further studies in order to assess exactly which parameters affects this evolution – especially from the structural point of view, which is left as a perspective of the current work.

## References

- [1] E. Hadjoudis, S. D. Chatziefthimiou and I. M. Mavridis, "Anils: Photochromism by H-transfer," *Molecular Engineering*, no. 5, pp. 301-337, 1995.
- [2] K. Johmoto and H. Uekusa, "Control of photochromism by manipulation of molecular conformation," in *Multi-Component Crystals: Synthesis, Concepts, Function*, E. R. T. Tiekink and J. Zukerman-Schpector, Eds., De Gruyter, 2018, pp. 103-11.
- [3] M. Sliwa, S. Létard, I. Malfant, M. Nierlich, P. G. Lacroix, T. Asahi, H. Masuhara, P. Yu and K. Nakatani, "Design, Synthesis, Structural and Nonlinear Optical Properties of Photochromic Crystals: Toward Reversible Molecular Switches," *Chem. Mater.*, vol. 17, pp. 4727-4735, 2005.
- [4] M. D. Cohen and G. M. J. Schmidt, "Photochromy and Thermochromy of Anils," *The Journal of Physical Chemistry*, no. 66, pp. 2442-2446, 1962.
- [5] S. D. Chatziefthimiou, Y. G. Lazarou, E. Hadjoudis, T. Dziembowska and I. M. Mavridis, "Keto Forms of Salicylaldehyde Schiff Bases: Structural and Theoretical Aspects," *J. Phys. Chem. B*, no. 110, pp. 23701-23709, 2006.
- [6] F. Robert, A. D. Naik, F. Hidara, B. Tinant, R. Robiette, J. Wouters and Y. Garcia, "Engineering Solid-State Molecular Switches: N-Salicylidene N-Heterocycle Derivatives," *Eur. J. Org. Chem.*, pp. 621-637, 2010.
- [7] G. M. Mercier, K. Robeyns, N. Tumanov, J. Wouters, B. Champagne and T. Leyssens, "New Insights into Photochromic Properties of N-Salicylideneaniline," *Cryst. Growth Des.*, no. 19, pp. 5544-5566, 2019.
- [8] I. Casades, M. Álvaro, H. García and M. N. Pillai, "Photochemistry of anils in NaY zeolite," *Eur. J. Org. Chem*, no. 13, pp. 2074-2079, 2002.
- [9] T. Haneda, M. Kawano, T. Kojima and M. Fujita, "Thermo-to-Photo-Switching of the Chromic Behavior of Salicylideneanilines by Inclusion

- in a Porous Coordination Network," *Angew. Chem., Int. Ed.*, no. 46, p. 6643–6645, 2007.
- [10] E. Hadjoudis, V. Verganelakis, C. Trapalis and G. Kordas, "Environmental Effect of Sol-Gel Encapsulation on Photochromic and Thermochromic Anils," *Molecular Engineering*, no. 8, p. 59–469, 1999.
- [11] K. Johmoto, A. Sekine and H. Uekusa, "Photochromism Control of Salicylideneaniline Derivatives by Acid–Base Co-Crystallization," *Cryst. Growth Des.*, no. 12, p. 4779–4786, 2012.
- [12] G. M. Mercier, K. Robeyns and T. Leyssens, "Altering the Photochromic Properties of N-Salicylideneanilines Using a Co-Crystal Engineering Approach," *Cryst. Growth Des.*, no. 16, pp. 3198–3205, 2016.
- [13] A. D. McNaught and A. Wilkinson, IUPAC. Compendium of Chemical Terminology, Oxford: Blackwell Scientific Publications, 1997.
- [14] M. Lusi, "Engineering Crystal Properties through Solid Solutions," *Cryst. Growth and D.*, no. 18, pp. 3704–3712, 2018.
- [15] M. D. Cohen, "Topochemistry. Part XXVIII. The system: 4-chloro-N-salicylideneaniline—4-bromo-N-salicylideneaniline," *Journal of Chemical Society B: Physical Organic*, pp. 373–376, 1968.
- [16] "CrysAllys PRO Data Collection and Processing Software for Agilent X-ray Diffractometers User Manual," Agilent Technologies UK, Ltd., Oxford, 2013.
- [17] G. M. Sheldrick, "SHELXT - Integrated space-group and crystal-structure determination," *Acta Crystallogr., Sect. A: Found. Adv.*, no. 71, pp. 3–8, 2015.
- [18] G. M. Sheldrick, "Crystal structure refinement with SHELXL," *Acta Crystallogr., Sect. C: Struct. Chem.*, no. 71, pp. 3–8, 2015.
- [19] J. P. Blitz, "Diffuse Reflectance Spectroscopy," in *Modern Techniques in Applied Molecular Spectroscopy*, John Wiley & sons, Inc., 1998, pp. 185–219.

- [20] J. Torrent and V. Barron, "Diffuse reflectance Spectroscopy," in *Method of Soil Analysis. Part 5. Mineralogical Methods.*, 2008, pp. 367-385.
- [21] R. Destro, A. Gavezzotti and M. Simoneta, "[Crystal structure of] salicylideneaniline," *Acta Crys. B*, vol. 34, p. 2867, 1978.
- [22] T. S. Chundawat, N. Sharma, P. Kumari and S. Bhagat, "Microwave-assisted nickel-catalyzed one-pot synthesis of 2, 4, 5-trisubstituted imidazoles," *Synlett*, vol. 27, pp. 404-408, 2016.
- [23] L. Vegard, "Die Konstitution der Mischkristalle und die Raumfüllung der Atome," *Zeitschrift für Physik*, vol. 5, pp. 17-26, 1921.
- [24] Y. Nakamura, N. Shibayama, A. Hori, T. Matsushita, H. Segawa and T. Kondo, "Crystal Systems and Lattice Parameters of  $\text{CH}_3\text{NH}_3\text{Pb}(\text{I}_{1-x}\text{Br}_x)_3$  Determined Using Single Crystals: Validity of Vegard's Law," *Inorg. Chem.*, vol. 59, pp. 6709-6716, 2020.
- [25] E. Hadjoudis, "Photochromic and Thermochromic Anils," *Molecular Engineering*, no. 5, pp. 301-337, 1995.
- [26] J. Burgess, J. Fawcett, D. R. Russell, S. R. Gilani and V. Palma, "Four N-(2-hydroxybenzylidene)aniline derivatives," *Acta Crystallogr., Sect. C: Cryst. Struct. Commun.*, no. 55, pp. 1707-1710, 1999.
- [27] H. Koyama, T. Kawato, H. Kanatomi, H. Matsushita and K. Yonetani, "Utilization of crystal lattice cavities of host deoxycholic acid for achieving photochromism of guest salicylidene anilines in the crystal state," *J. Chem. Soc., Chem. Commun.*, no. 5, pp. 579-580, 1994.
- [28] A. Mbodji, G. Gbabode, M. Sanselme, Y. Cartigny, N. Couvrat, M. Leeman, V. Dupray, R. M. Kellogg and G. Coquerel, "Evidence of Conglomerate with Partial Solid Solutions in Ethylammonium Chlodyphos," *Cryst. Growth Des.*, no. 20, pp. 2562-2569, 2020.

## **Chapter 6**

### **Conclusion and perspectives**



## Conclusion

The general aim of the present thesis was to achieve a fine-tuning of photochromic properties of *N*-Salicylideneaniline derivatives through a cocrystal engineering approach. In order to do so, a step-by-step plan was designed: the first step (chapter 2) consisted in an exploration of potential cofomers for cocrystallization with anils in order to prove that the photochromic properties of anils can be altered through this process. The second step (chapter 3) consisted in an exhaustive search of cocrystals of various anils with selected cofomers with the purpose to establish an important data set of structures to provide statistical information for future researches. The last step (chapter 4 and 5) consisted in the design of ideal systems (i.e., systems with improved photochromism and/or with tunable properties) based on the knowledge gathered within the previous steps.

In the first step, we aimed to answer the question: “can cocrystallization alter photochromism?”. The answer is “yes” as we here reported for the first time a cocrystal (not a salt or solvate for instance) with modified photochromic properties. In order to do so, two well-known anils (*N*-Salicylideneaniline and 4-fluoro *N*-Salicylideneaniline respectively called **A** and **B** in all chapters) were ground with eighteen different carboxylic acids (specified in chapter 2) and resulted in the identification of 6 new phases among which one could be crystallized and provided a new cocrystal structure. This cocrystal resulted from the combination of anil **A** and citraconic acid (labelled C10) through liquid-assisted ball-milling grinding and presented new and unexpected properties: an inverted photochromism could be observed compared to parent anil **A** alone. The yellow-brown coloration of the sample disappeared after irradiation at 365 nm and it turned white, instead of the classical red-appearing coloration. This change of color could be reproduced at least 5 times before the compound color completely faded away (probably due to degradation in contact with air humidity).

These results were published in *Crystal Growth and Design* and the conclusions of this first chapter is that anils can easily co-crystallize with small carboxylic acid molecules and that the photochromism can be completely altered/modified through this process. One of the reasons advanced to explain such a change is the involvement of the ortho-hydroxy moiety in the supra-molecular bonding with one of the carboxylic moieties of the citraconic

acid. As this ortho-hydroxy moiety plays a central role in the keto-enol equilibrium, any supramolecular bonding involving this moiety is expected to alter the process. These conclusions were drawn in regards to a statistical analysis performed on the CCSD over structures presenting an enol-imine or a conjugated ketone in order to assess the average bond length involved in the photochromic process. Using this analysis, we were able to show the equilibrium was shifted towards the keto form in cocrystal **A-C10** and that a zwitterionic representation of the structure is the most accurate as shown in Figure 1.

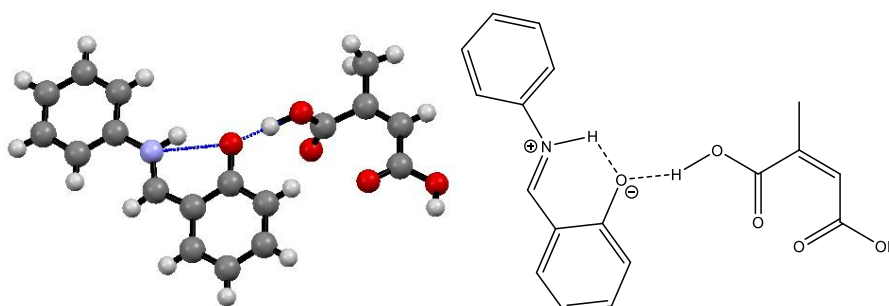


Figure 1: (Left) Ortep representation of **A-C10** cocrystal structure, (right) molecular scheme showing the zwitterionic character of the anil.

In a second step, we aimed to study further the role intermolecular interactions in the photochromic process. In order to do so, a large cocrystal screening of anils **A** and **B** and 13 of their derivatives with 21 different cofomers (carboxylic acids, amides and benzene halides) was performed and resulted in the identification of 95 cocrystals over the 315 possible combinations. This gives a cocrystal yield of around 30% which is much higher than the usual 10% rate reported and shows the efficiency of the selected cofomers.

Among these 95 cocrystals, 21 were successfully crystallized and structurally analyzed. The amount of data collected allowed us to determine statistically valid insights: the main conclusions are that photochromic structures are very close to the average enol-imine bond lengths and that the “moving moiety” (the phenolic moiety which is expected to move through the photochromic process) is in average involved in more supramolecular interactions in non-photochromic structures. Also, we observed that the

involvement of the ortho-hydroxy moiety in strong supramolecular interactions tends to switch off photochromism - in agreement with other already reported studies in literature.

As a result, it is now recommended to reduce the total amount of short contacts involving these specific moieties (the moving moiety and the ortho-hydroxy moiety) in order to improve photochromism. Thus, precise crystal structure prediction is now a requirement to pursue on this way and is left as a perspective of this work.

Along with these observations, a fundamental discovery – the existence of weakly photochromic compounds - was made and published in *Crystal Growth and Design* along with above cited results. This discovery is due to a new approach performed in the data treatment of DRS spectra and the definition of the “photochromic profile” which correspond to the ratio of the absorption spectra of a sample before and after irradiation. This profile (or ratio) is directly dependent of the state’s populations and any change of these populations (through irradiation for instance) generates an intense peak in the photochromic profile. Without such treatment, changes could be overlooked (when occurring for weakly absorbing states or when different states have similar absorbing properties).

The discovery of weakly photochromic compounds allowed us to shift the paradigm of the classical binary photochromic/non-photochromic approach and consider instead photochromism as a continuous property. This is in agreement with experimental observations of the photochromic intensity (the maximum measured ratio on the photochromic profile) versus the torsion angle: there seems to be a correlation between the two as an increasing torsion angle corresponds to an increasing photochromic intensity as shown in Figure 2 (which also includes other examples found in literature) instead of being only responsible for the occurrence of the property. Our conclusion is now that structures with low dihedral angles tends to exhibit weaker photochromism.

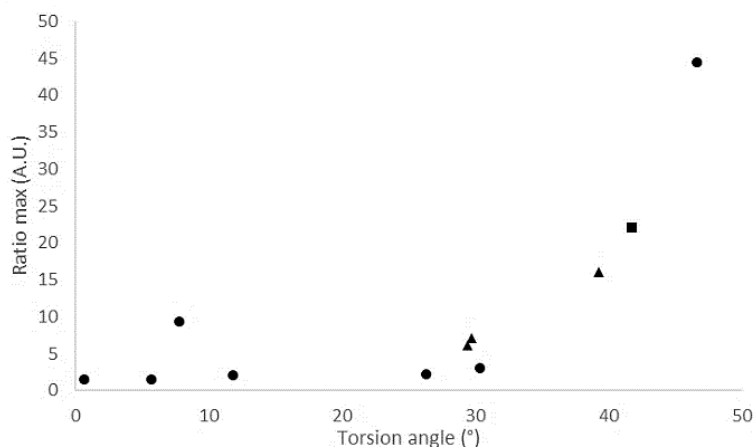


Figure 2: Photochromic intensity versus the torsion angle for anils studied within this thesis (circle marks) and other examples found in literature (triangles and square marks).

The last step of the present thesis focused on designing “ideal systems” of anil cocrystals. It has been noticed that all used coformers were able to hydrogen and/or halogen bond and most of them also had delocalized electrons or an aromatic ring. All these features are already present in most of the selected anils in chapter 3. As a result, the next logical step was to use anil derivatives as coformer for other anils as they all crystallize easily as demonstrated in previous chapters. The resulting screening allowed to identify 11 combinations resulting in a new phase, 3 of which were identified as solid-solutions.

Among the other 8 expected stoichiometric cocrystal systems, one (**E+N**) exhibited detectable photochromism while both constituent anils alone are non-photochromic.

Due to time limitation, we did not focus on these systems but rather put efforts on the solid-solution systems, as a last part of this thesis, as they allow theoretically to achieve fine-tuning of the properties over a wide composition range. Depending on the nature of the systems, properties may reach a maximum for a specific molar ratio when using solid-solutions. Furthermore, as photochromism is highly dependent of structural aspects, even slight structural changes may produce a very large difference in photochromic properties. Going along with one of the main conclusions of

that chapter, which is the easiness to produce solid-solutions using the hydrogen-fluorine replacement in the case of the anils, this incited us to move forward on this path. This easiness was demonstrated as all systems tried were successfully crystallized, and especially for system **I/J**, which produced solid-solution crystals suitable for SC-XRD while all attempts to crystallize parent anils alone failed.

A more profound investigation of the **A/B** system showed a complicated solid-state landscape, exhibiting a four-phasic solid-solution, a never reported before feature for organic molecules. This was ultimately proven with the SC-XRD measurements of two different solid-solution structures which also both differ from the parent anils. Based on DSC, XRPD and SC-XRD analysis, the binary diagram of this system could be drawn and is presented in Figure 3. However, this system presents a drawback as it revealed to be sensitive to air humidity and thus is not stable over time.

Among the four observed phases, only one (the **A**-phase) revealed to be photochromic, and the measured photochromic intensity quickly goes down to reach a minimum at the first eutectic point (at 13% **B** molar ratio). Also, the thermal back-reaction shows a linear correlation of the kinetic  $k_1$  parameter with increasing **B** molar ratio – meaning the thermal-back reaction is faster and from this, we can conclude the *trans*-keto form state of **A** is less stabilized with increasing molar amount of **B**. Nevertheless, this is the first time a variety of different photochromic intensities and  $k_1$  parameters could be obtained for the same system, thus achieving a major step towards the fine-tuning of properties.

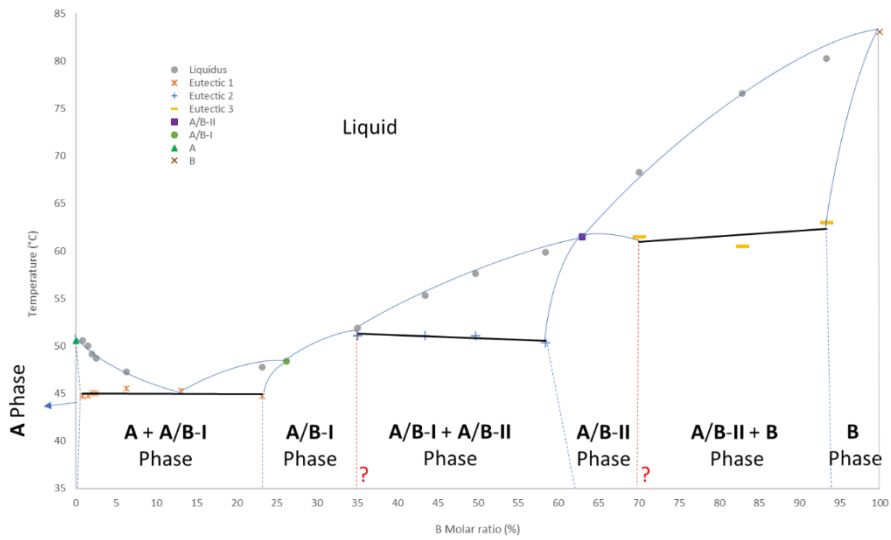


Figure 3: proposed binary diagram for the **A/B** system from experimental and calculated results. Question marks shows limits for which no exact results could be obtained.

## Perspectives

The current work leaves various paths to explore to come to the “ideal photochromic system” using anils. First of all, despite many advances, the cofomer selection is still not optimized and many trials still have to be performed to find cofomers allowing not only to cocrystallize but also to switch on photochromism or to improve it. The second and third chapter show carboxylic acid functional groups to lead to many cocrystals but they do not improve photochromism (no switch-on observed within this thesis) and more often switch it off or change it completely (like anil **A** – citraconic acid cocrystal). On the other hand, amide and benzene halide derivatives allowed to find photochromic cocrystals with improved properties but with a lesser cocrystal yield. As a result, findings should continue towards this type of cofomer in order to find cocrystals with enhanced photochromic properties.

The dataset of cocrystals presented within this thesis still remains small with “only” 106 newly identified cocrystals and a total of 34 structures (including parent anils alone) could be studied through SC-XRD. However, it would require hundreds of structures in order to have highly significant statistics and tendencies about the roles of bond lengths, short contacts or the torsion angle. For this last, the largest study published by Uekusa et al. in order to prove the empirical “torsion angle rule” (stipulating a dihedral angle higher than 30° leads to photochromism in anils) only focused over 40 anils structures which is still a quite small dataset – especially considering many counter-examples to this rule were found within this thesis but also by other groups and published in literature. In this work we found a link between the value of this angle and the intensity of photochromism rather than its occurrence. Hence, having data over hundreds of structures would allow a better understanding of this link and may open new pathways for improving photochromic properties of anils. Thus, using the synthesis and methods elaborated and generated within this thesis, one may consider to perform a drastically increased cocrystal screening, adding a few new anils but also many new cofomers such as amines and alcohols and exploring other amides and more benzene halides (especially because these last allowed to find cocrystals with improved properties).

To tackle this lack of exhaustive studies and perform a large statistical analysis, efforts should also be done to improve the crystallization yield of cocrystals in order to grow more single crystals suitable for SC-XRD analysis.

Within this thesis, only about 30% of the identified cocrystals could be properly crystallized. However, only the following experimental methods were tried in order to get crystals: solvent slow evaporation, cooling of supersaturated solutions, vapor slow diffusion, melting and cooling of solids. Meanwhile, no detailed studies of crystallization conditions were performed such as ternary diagrams. This might require time and efforts but improving the crystallization yield is a necessity to move forwards within this field as studying anil properties in various solid environment is the central part of all these researches. Another option is to perform high precision XRPD (using synchrotron radiation) which may allow to obtain crystalline structure directly from the powder. However, this would require high purity sample and costly experimental set-ups, with no guarantee to obtain the desired structures. At last, theoretical approaches and studies may also help to link properties with structure and would allow to directly find which structural parameters are relevant in order to fine-tune photochromic properties of anils.

From the conclusions of chapter 3, the aim is now to reduce the strength/ number of intermolecular interactions involving some specific moieties of the anils. Such an approach is now limited by the ability to predict the final crystalline structure in order to select best coformers and to design systems with desired properties. Many progresses have been made in that field and the recent developments of A.I. using deep-learning in order to predict crystals or protein structures shows it's maybe just a matter of a few years before we achieve the design of ideal systems towards specific industrial applications.

Interestingly, the results of last chapter show anils easily form solid-solutions with their corresponding fluorinated derivatives. In this thesis, only 4 different anils with only one of their fluorinated derivatives were explored while hundreds of possibilities exist for each anil: anil usually have around 10 hydrogen atoms meaning there exist at least 10 mono-fluorinated derivatives, 45 bi-fluorinated derivatives, 120 tri-fluorinated derivatives etc., the total number of possible solid-solutions structures already reaching 1022 in that case!

Even though solid-solution properties should be the exact average of its constituent properties in the ideal case, in most cases there are slight variations as the replacement of one by another may cause slight stabilization or destabilization of the structure. This allows to find either increased or decreased properties and thus, there are many potential solid-

solution structures with improved properties for each anil: a naïve approach would be to consider half of the possible solid-solution structures will have improved properties and thus there could already be as much as 500 possible different structures with enhanced properties compared to the parent anils. Furthermore, while the variations of properties are usually expected to be small within the solid-solution range, in the case of anil photochromism the impact might be much stronger as this property is highly sensitive to structural parameters. For instance, the dramatic photochromic change observed for anil **A** phase in chapter 5 should be studied along the structural changes provoked by the increase of anil **B** molar ratio within the structure by combining SC-XRD or XRPD with DRS measurements. This experiment might give further indications about critical structural parameters in the case of anil photochromism.

After the research carried within this thesis, there is also a chapter which remains completely open for study: the impact on temperature over the photochromic process. Very few studies can be found in literature about this as it requires to precisely control the temperature while using techniques such as DRS, SC-XRD and XRPD. These experiments are all feasible with appropriate experimental set-up and could give additional relevant information over the mechanism and process involved in photochromism.

Similarly, there is also the possibility to combine UV irradiation with SC-XRD and XRPD in order to study any structural changes due to the photochromic process. Furthermore, it would be extremely interesting to perform UV irradiation while recording DRS spectra at controlled temperature. Such measurement would allow to directly observe the photochromism without any experimental modifications of the surface sample or its position within the device, allowing extremely precise measurements and a clear classification of photochromic behavior for borderline cases.

Combining properties of different anils (such as combining thermochromism and photochromism or combining different wavelengths of activation for photochromism etc.) could be a very interesting continuation of the current works, leading to potentially more complex applications. Some preliminary researches have been performed in chapter 4 but they were stopped due to the lack of crystallization results. As a result, exploring other crystallization methods for the 8 identified cocrystal systems might lead to new structures and the possibility to explore deeper these

property combinations. Also, performing the ternary diagram for the most interesting systems might allow to find the best methods/parameters to crystallize these systems of interests.

All the above cited perspectives for future works are related to fundamental research, especially because it is the global context of this thesis. The next step is to use this newly acquired knowledge in order to perform new industrial applications. Many of them have already be cited in the Introduction such as secured inks, photochromic glasses etc. but many other options can be evaluated such as photochromic and/or thermochromic tiles to perform a more efficient heating/insulation of houses and building with changing weather conditions: the roof could turn black if the temperature is low in order to absorb more energy from the sun and thus use less energy to heat during winter. As this process is reversible, the roof would turn clear/white during summer in order to avoid overheating and the use of air conditioning.

Such industrials applications would require extremely stable compounds in order to resists to external conditions such has rain, snow, etc. Another option would be to study the photochromic properties of anils included in a matrix such has polymers, which could offer sufficient protection over weather changes and external conditions. Also, we could expect a better resistance to fatigue etc. Hence, having photochromic compounds included into polymers could open the doors to many other industrial applications such as screens for electronic devices for instance. As some anils have already been reported to be photochromic while included in such matrix, there is a clear room for research, improvement and industrial applications in such areas.

## **Supporting information**



The present section covers some relevant supporting information of chapters 4 and 5. As chapter 2 and 3 correspond to publications, their respective supporting information is already available online and can be downloaded free of charge via the internet at:

<https://pubs.acs.org/doi/10.1021/acs.cgd.6b00108> for chapter 2;

<https://pubs.acs.org/doi/abs/10.1021/acs.cgd.9b00363> for chapter 3.

**Supporting information for chapter 4 contains:**

Ch4.1.	XRPD patterns of ground anil mixtures and comparison with anil references	p.195
Ch4.2.	Cross-crystallization screening results	p.207
Ch4.3.	Screening polymorph/degradation check	p.208
Ch4.4.	E+J NMR check	p.216

**Supporting information for chapter 5 contains:**

Ch5.1.	Table 1: complementary structural information for new solid-solutions structures	p.217
Ch5.2.	Kinetical studies of A/B system	p.218

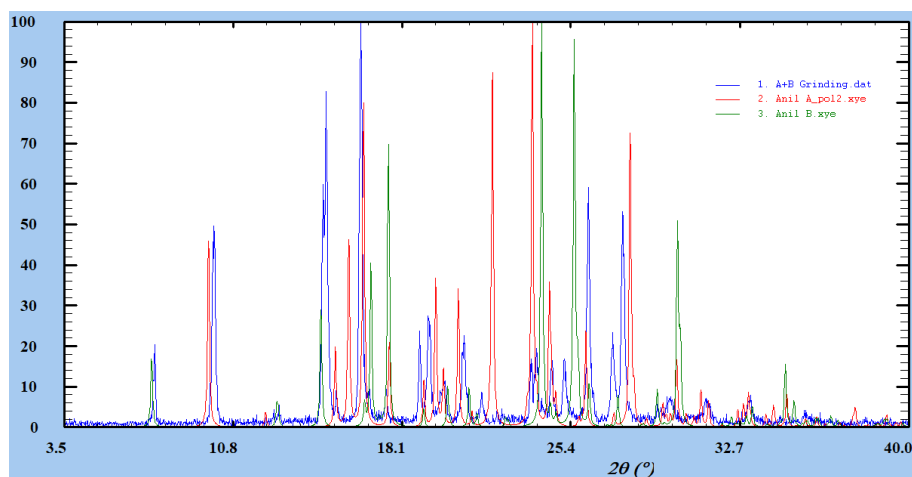


## Chapter 4 Supporting Information

### Ch4.1. XRPD patterns of ground anil mixtures and comparison with anil references

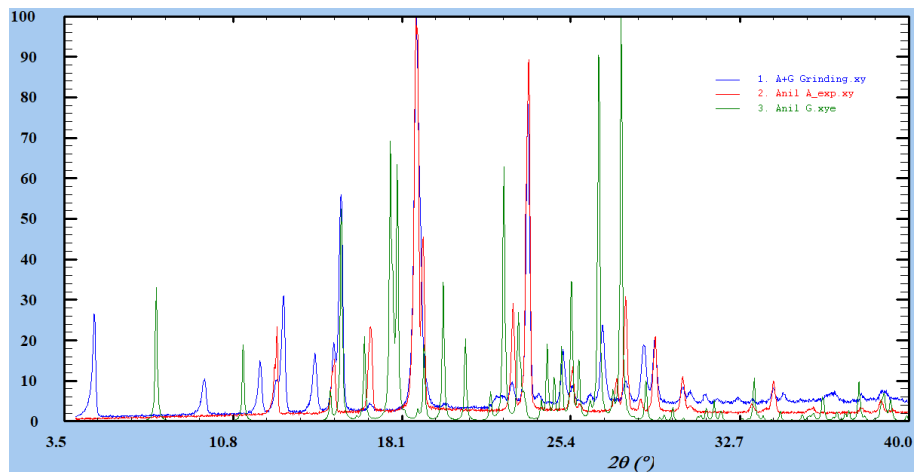
All data are normalized with highest peak = 100 (arbitrary units). Each ground sample is presented in blue while parents anil patterns are presented in red and green. Results are shown only when a new phase has been detected.

#### 1) Sample A+B:



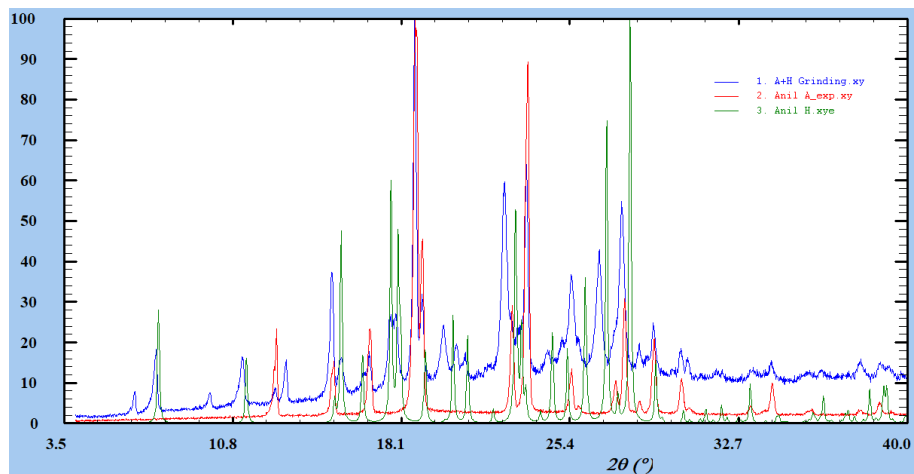
Shown with polymorph of anil **A** which is the closest to the ground sample (best match). Most of the peaks are slightly moved either to left or right: expected solid-solution.

## 2) Sample A+G:



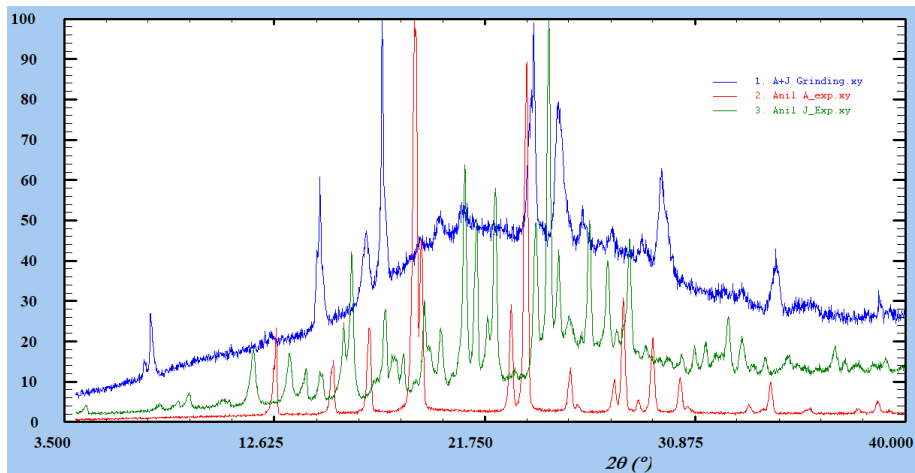
Compared with experimental anil **A** pattern. Many new peaks. Perfect match with reference **A** and no match with reference **G**. New phase expected – possible polymorph/degradation product of **G**.

## 3) Sample A+H:



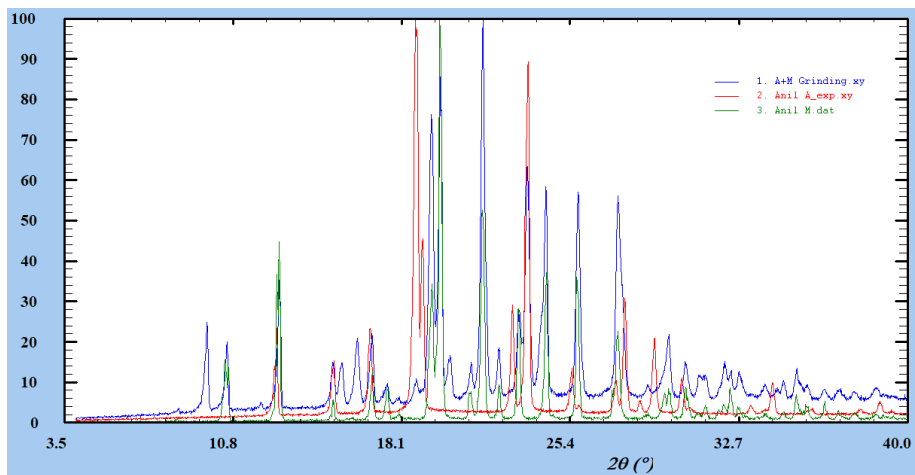
Compared with experimental anil **A** pattern. Many new peaks. Perfect match with reference **A** and no match with reference **H**. New phase expected – possible polymorph/degradation product of **H**.

#### 4) Sample A+J:



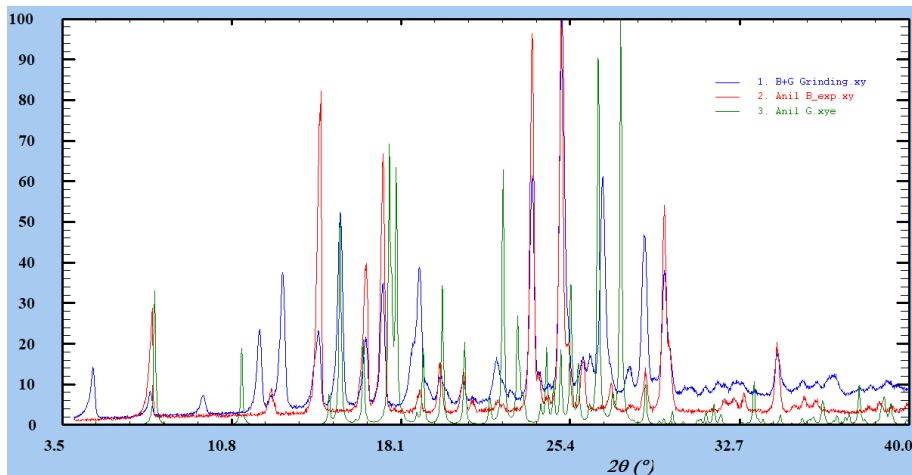
Compared with experimental anil **A** and **J** patterns. Partly amorphous material. Many new peaks and no match with references: new phase expected.

#### 5) Sample A+M:



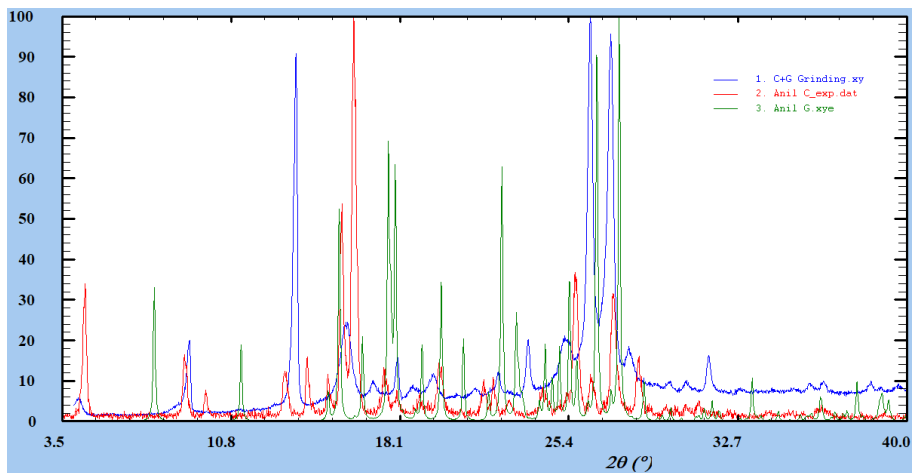
Compared with experimental anil **A** and **M** patterns. Many new peaks, good match with **M** reference patterns, partial match with **A** reference: possible new phase or polymorph of **A**.

### 6) Sample B+G:



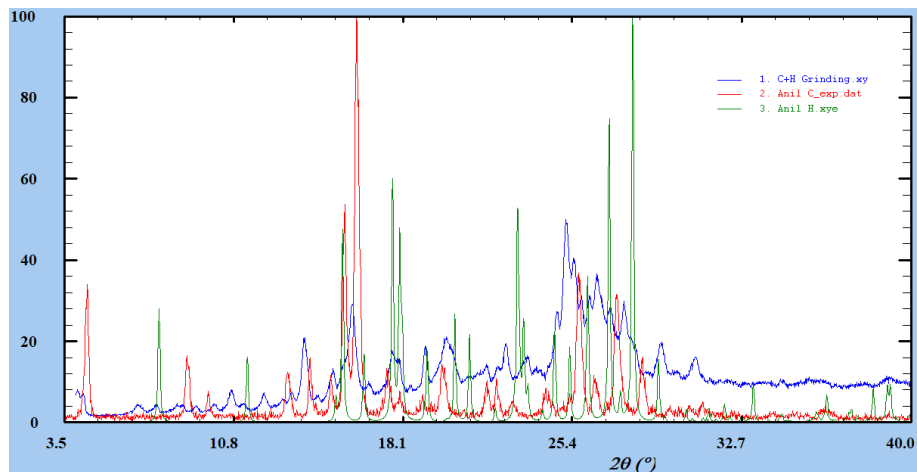
Compared with experimental anil **B** and simulated anil **G** patterns. Excellent match with **B** reference pattern, no match with **G** reference pattern: new phase expected – possible polymorph/degradation product of **G**.

### 7) Sample C+G:



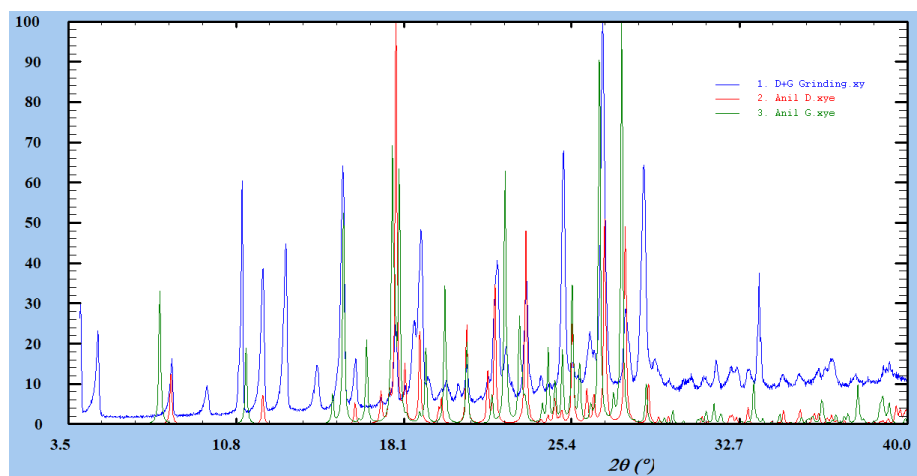
Compared with experimental anil **C** and simulated anil **G** patterns. No match with both reference patterns: new phase expected.

### 8) Sample C+H:



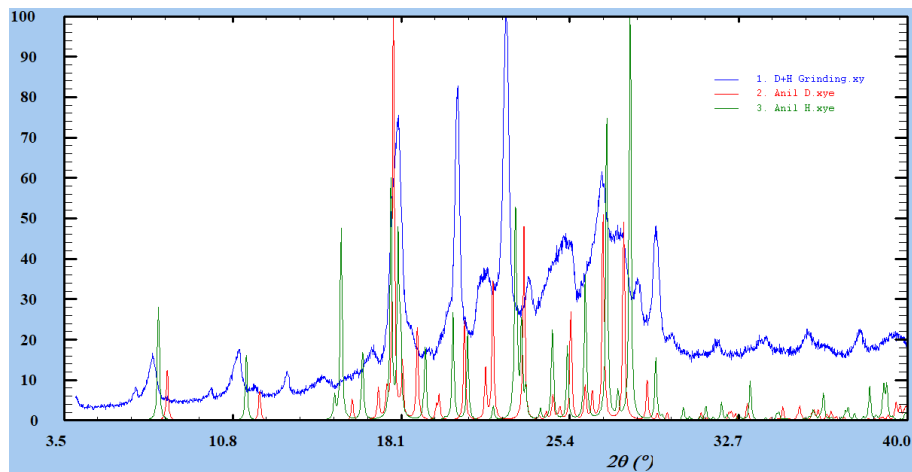
Compared with experimental anil **C** and simulated anil **H** patterns. No match with both reference patterns: new phase expected.

### 9) Sample D+G:



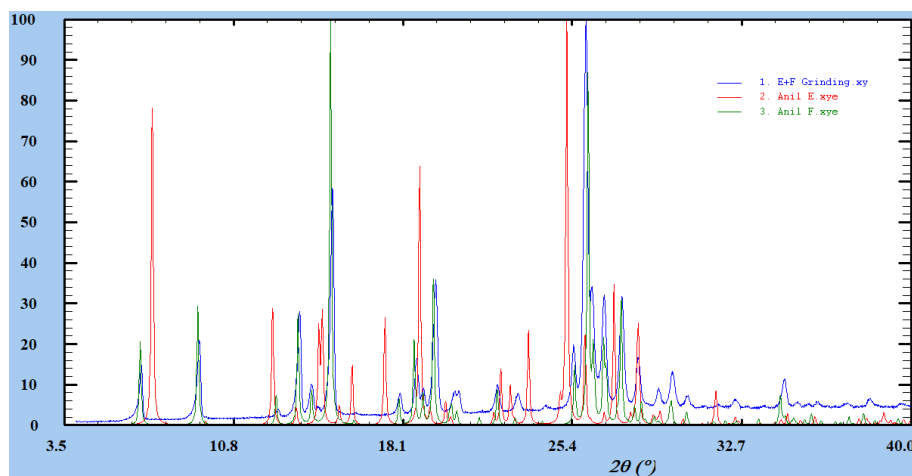
Compared with simulated anil **D** and **G** patterns. Excellent match with **D** reference pattern, no match with **G** reference pattern: new phase expected – possible polymorph/degradation product of **G**.

### 10) Sample D+H:



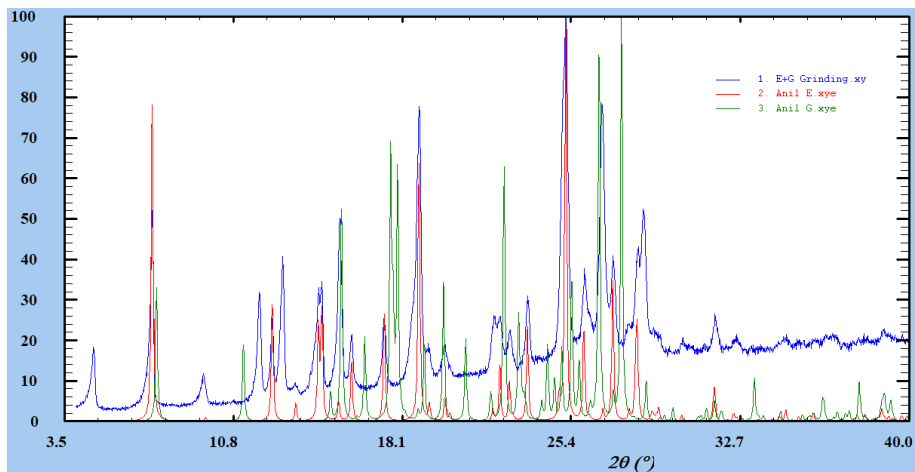
Compared with simulated anil **D** and **F** patterns. No match with both reference patterns: new phase expected.

### 11) Sample E+F:



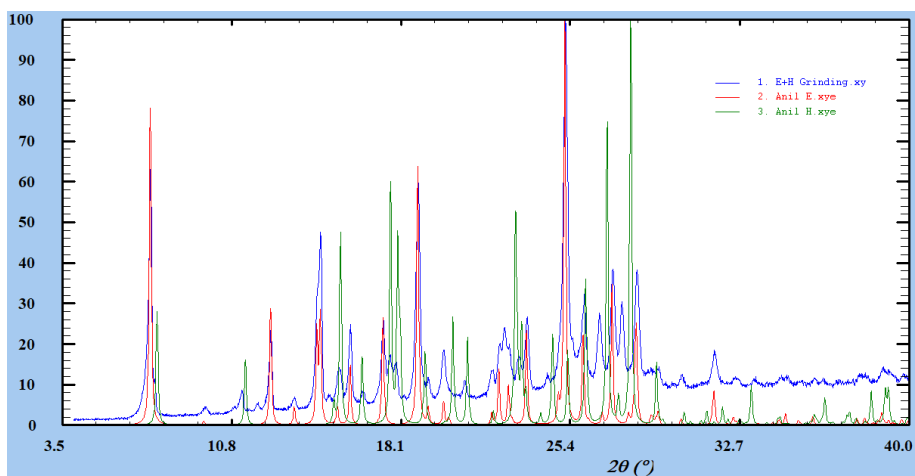
Compared with simulated anil **E** and **F** patterns. No match with **E**, Good match with **F** reference patterns but many peaks are slightly displaced either towards left ( $25.43^\circ$ ,  $25.95^\circ$ ) or right ( $13.60^\circ$ ,  $15.50^\circ$ ,  $17.94^\circ$ ,  $19.47^\circ$ , ...) while others shows no displacement ( $14.15^\circ$ ,  $22,17^\circ$ ,...). Expected new phase (a solid-solution close to **F** structure).

### 12) Sample E+G:



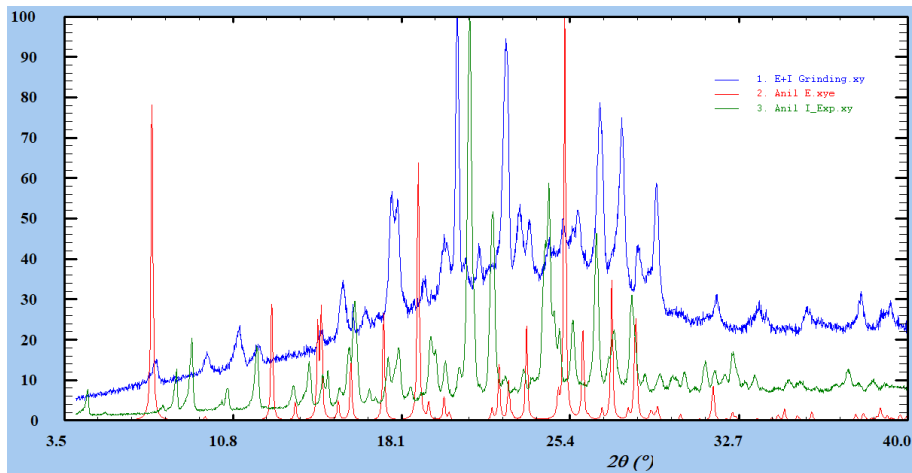
Compared with simulated anil **E** and **G** patterns. Excellent match with **E** reference pattern, no match with **G** reference pattern: new phase expected – possible polymorph/degradation product of **G**. Similar case to samples 6, 19 and 42.

### 13) Sample E+H:



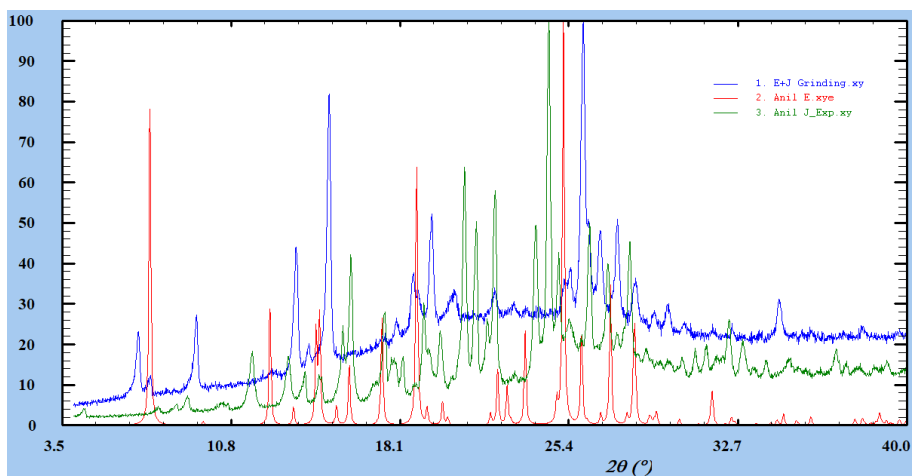
Compared with simulated anil **E** and **H** patterns. Excellent match with **E** reference pattern, no match with **G** reference pattern: new phase expected + anil **E**.

#### 14) Sample E+I:



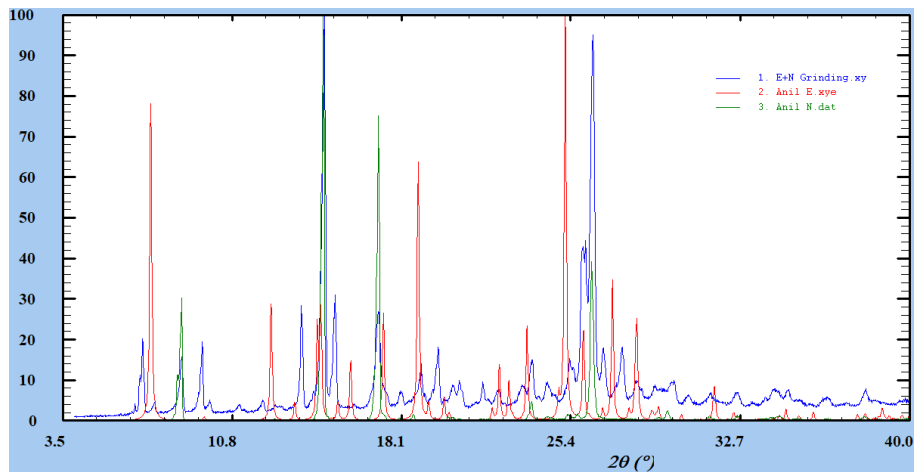
Compared with simulated anil E and experimental anil I patterns. No match with both references: new phase expected.

#### 15) Sample E+J:



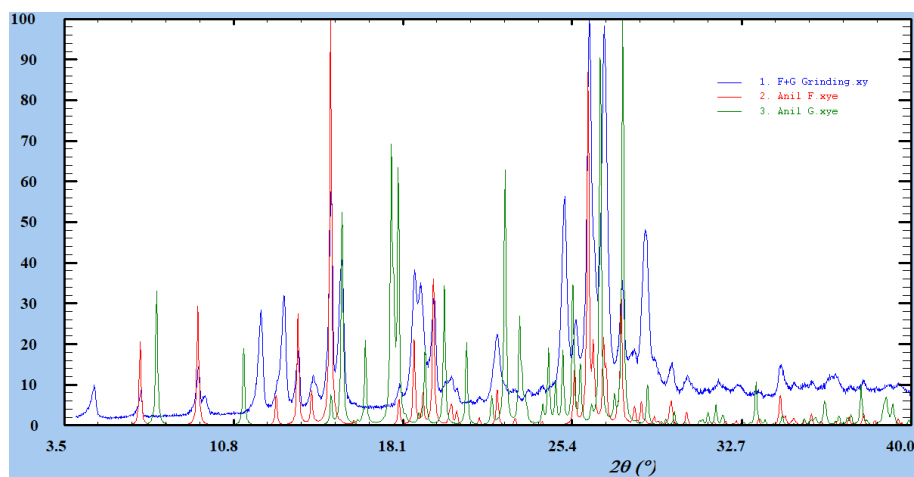
Compared with simulated anil E and experimental anil J patterns. No match with both references: new phase expected.

### 16) Sample E+N:



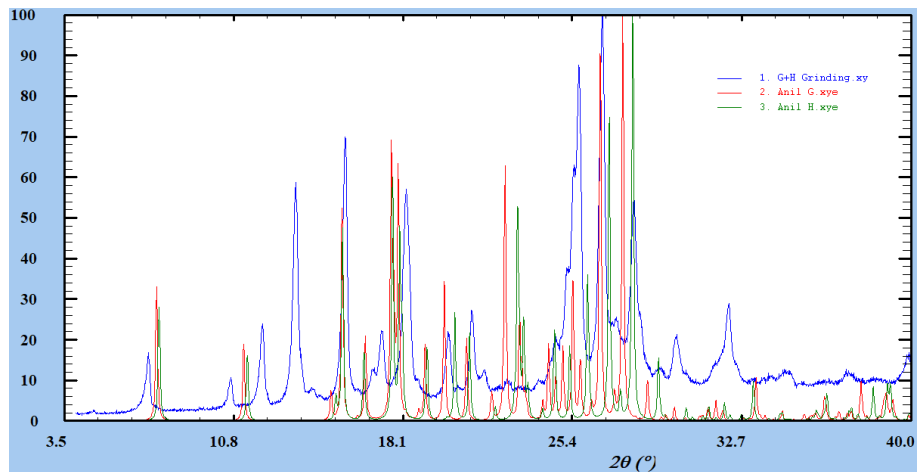
Compared with simulated anil **E** and experimental anil **N** patterns. Good match with reference **N**, no match with anil **E**, many new peaks: new phase expected.

### 17) Sample F+G:



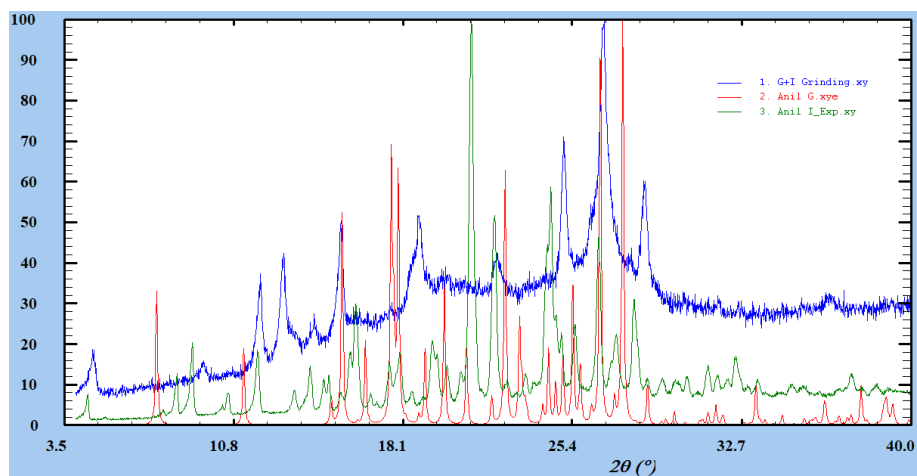
Compared with simulated anil **F** and **G** patterns. Excellent match with **F** reference pattern, no match with **G** reference pattern: new phase expected – possible polymorph/degradation product of **G**. Similar case to samples 6, 19, 42 and 52.

### 18) Sample G+H:



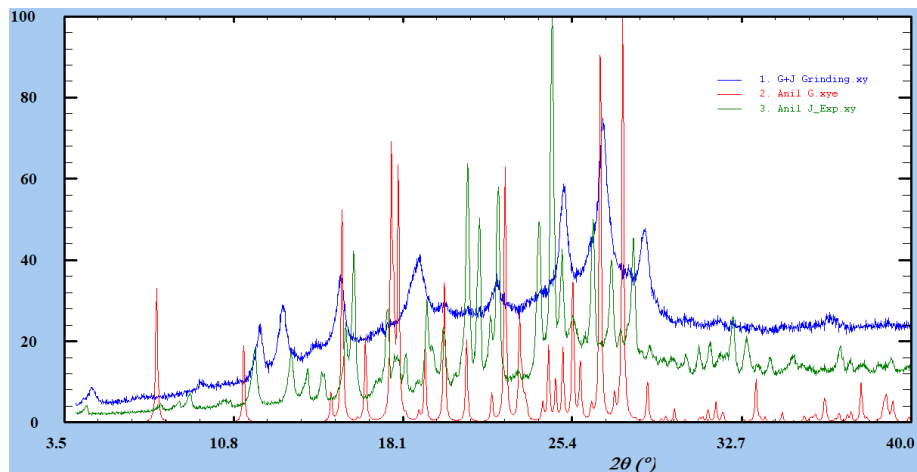
Compared with simulated anil **G** and **H** patterns. No match with both references: new phase expected.

### 19) Sample G+I:



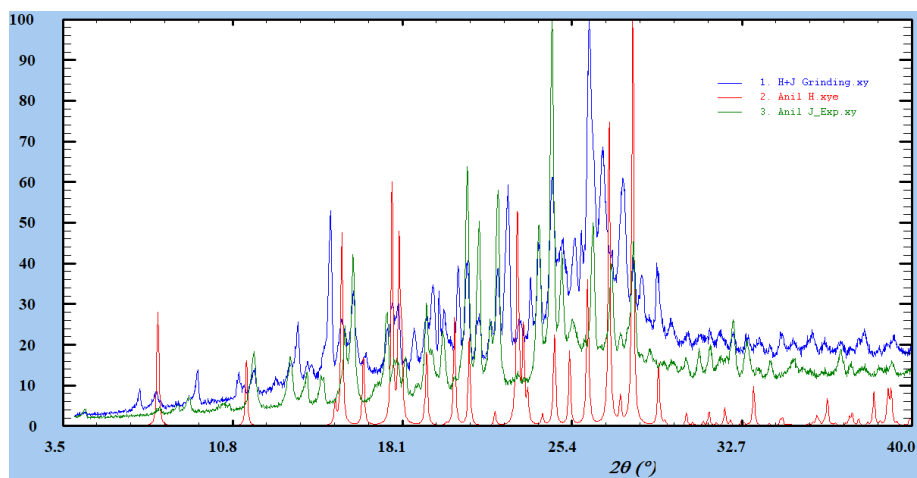
Compared with simulated anil **G** and experimental anil **I** patterns. No match with both references: new phase expected.

## 20) Sample G+J:



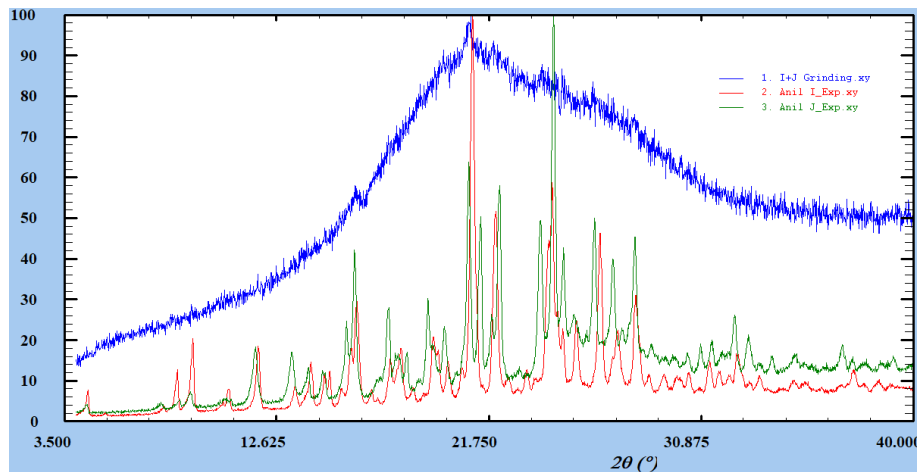
Compared with simulated anil **G** and experimental anil **J** patterns. No match with both references: new phase expected.

## 21) Sample H+J:



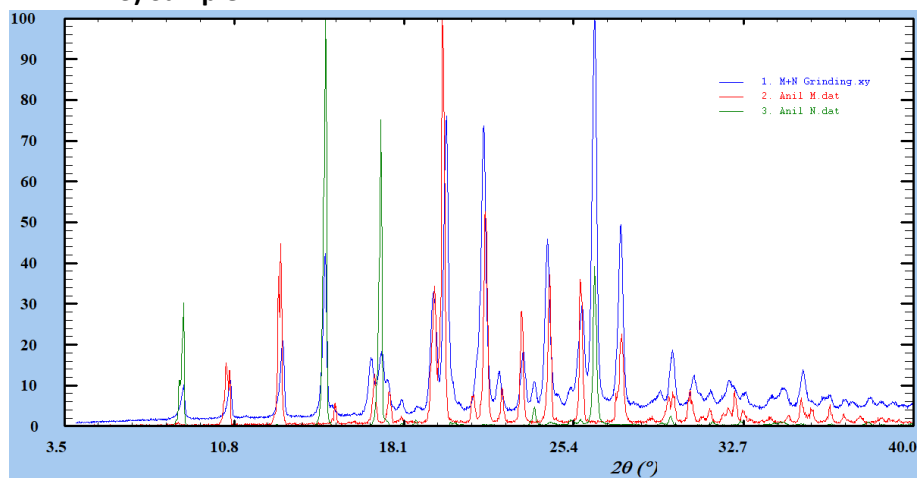
Compared with simulated anil **H** and experimental anil **J** patterns. Good match with both references but a few new peaks: possible new phase + mixture of 2 parent anils.

## 22) Sample I+J:



Compared with experimental anil **I** and **J** patterns. Complete amorphization of the sample: no conclusion possible.

## 23) Sample M+N:



Compared with experimental anil **M** and **N** patterns. Good match with both references with some peaks slightly shifted either to left or right for both references: Solid-solution expected.

## Ch4.2. Cross-crystallization screening results

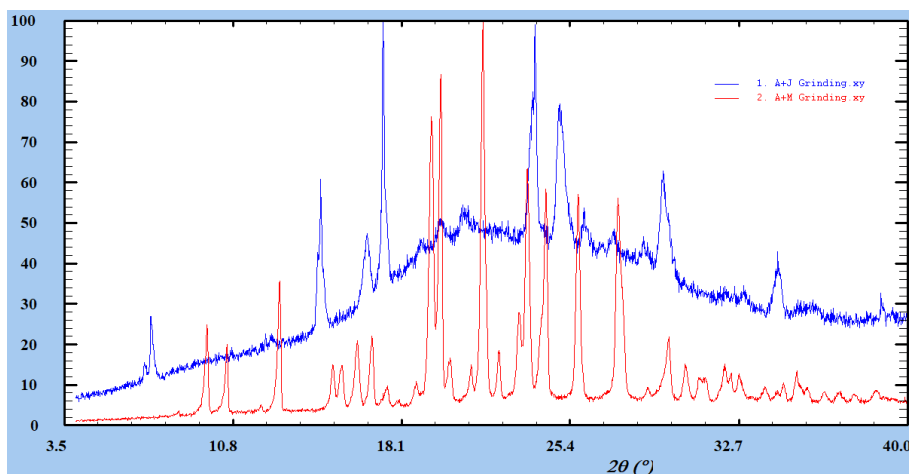
Summary of results after first analyze: NP means “New Phase”, NP: SS means “New Phase Solid-Solution”, Amorph. means the sample was partly or totally amorphous and no conclusion can be drawn so far.

	B	C	D	E	F	G	H	I	J	K	L	M	N	O
A	NP: SS					NP	NP	Amorph.	NP			NP		
B						NP		Amorph.						
C			NP			NP	NP							
D						NP	NP	Amorph.	Amorph.					
E					NP: SS	NP	NP	NP	NP				NP	
F						NP		Amorph.	Amorph.					
G							NP	NP	NP	NP	NP	NP	NP	NP
H									NP					
I									Amorph.	Amorph.		Amorph.	Amorph.	
J														
K														
L														
M													NP: SS	
N														
O														

### Ch4.3. Screening polymorph/degradation check

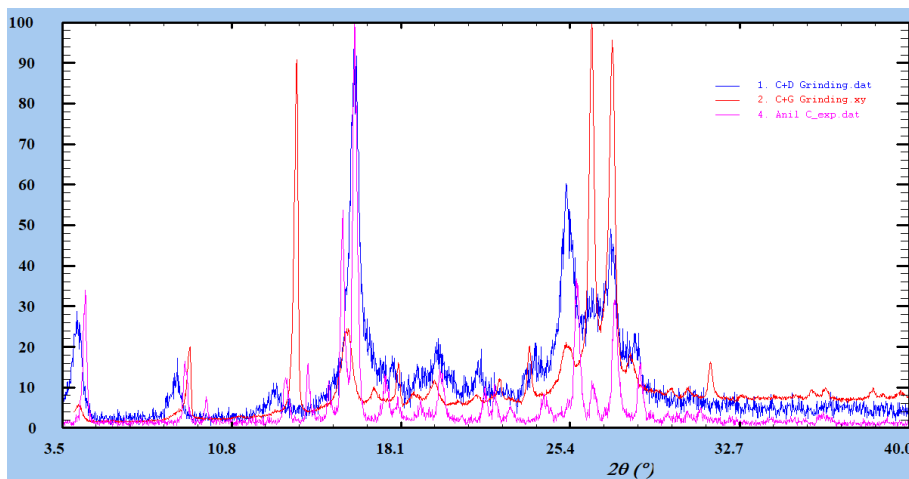
Each time an anil had more than one identified new phase after cross-screening, a two-by-two comparison of the results has been performed in order to identify polymorph transformation or degradation reaction.

#### 1) Sample A+J and A+M:



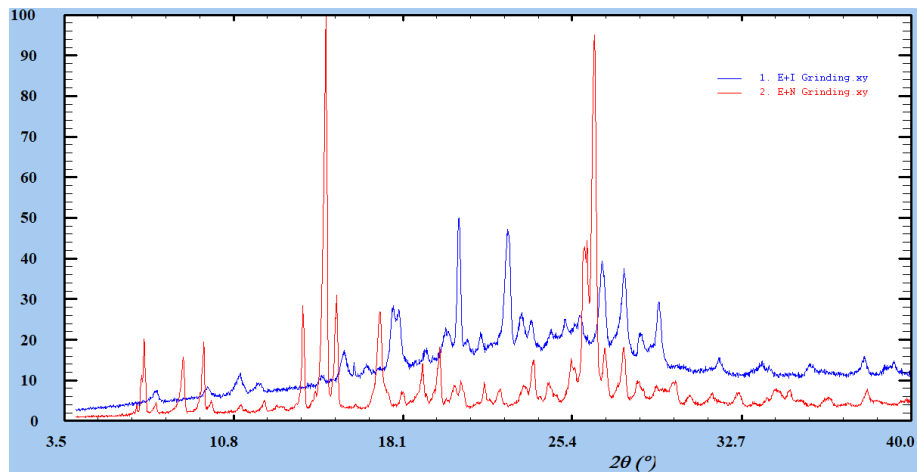
No correspondence between the two samples: new phase confirmed in both cases.

#### 2) Sample C+D and C+G:



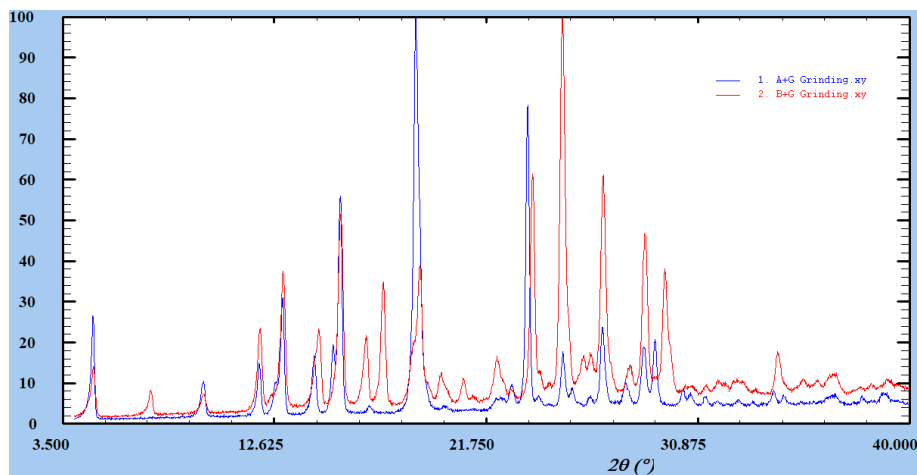
Unexplained new peaks in C+G are not present in C+D and vice-versa: new phase confirmed in both cases.

### 3) Sample E+I and E+N:



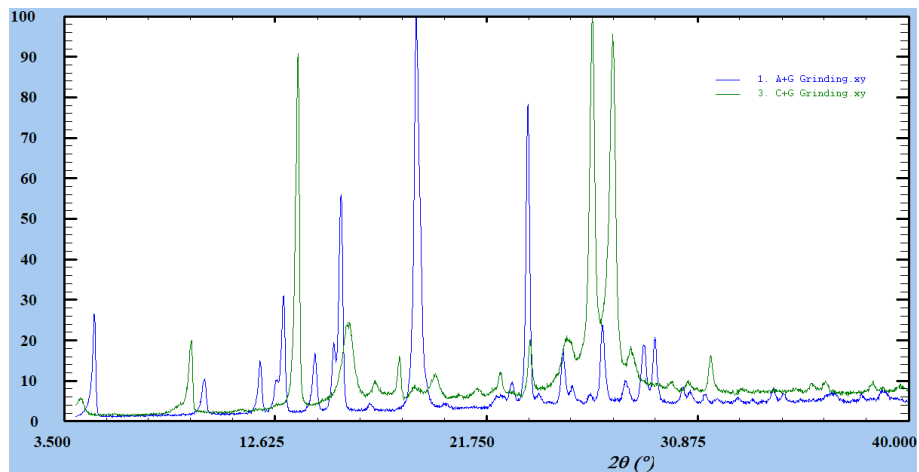
Unexplained new peaks in **E+I** are not present in **E+N** and vice-versa: new phase confirmed in both cases.

### 4) Samples A+G vs B+G:



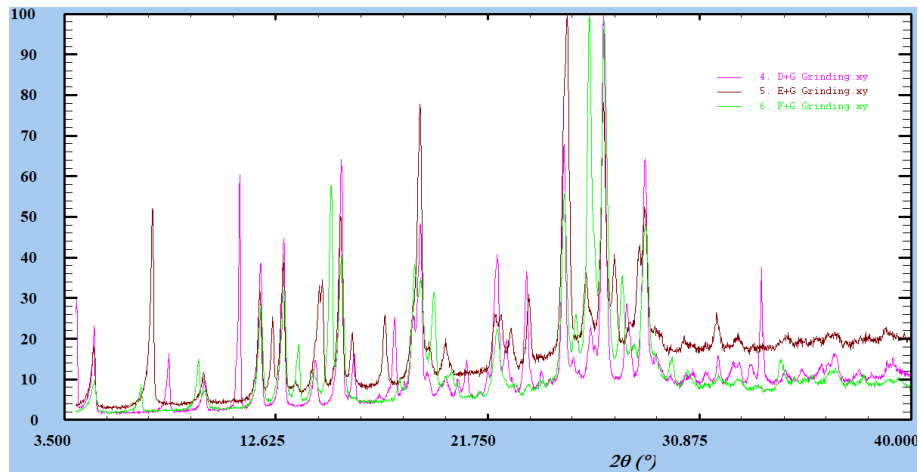
Peaks at 4.8°, 9.5°, 12.0° and 13.0° which were unexplained in **A+G** and **B+G** do match perfectly: no cocrystal but either polymorph or degradation product of **G**.

### 5) Samples A+G vs C+G:



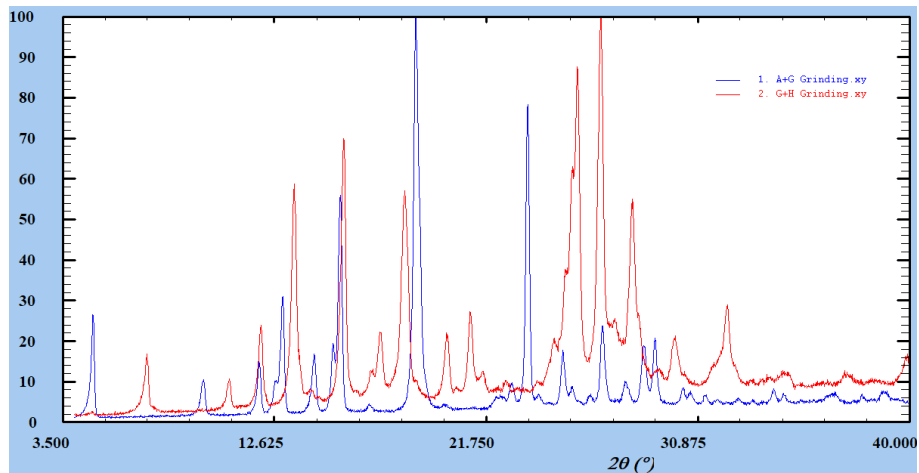
Peaks at 4.8°, 9.5°, 12.0° and 13.0° which are characteristic of the impurity (polymorph or degradation product of **G**) are not present in **C+G**: new phase confirmed.

### 6) Samples D+G, E+G, F+G:



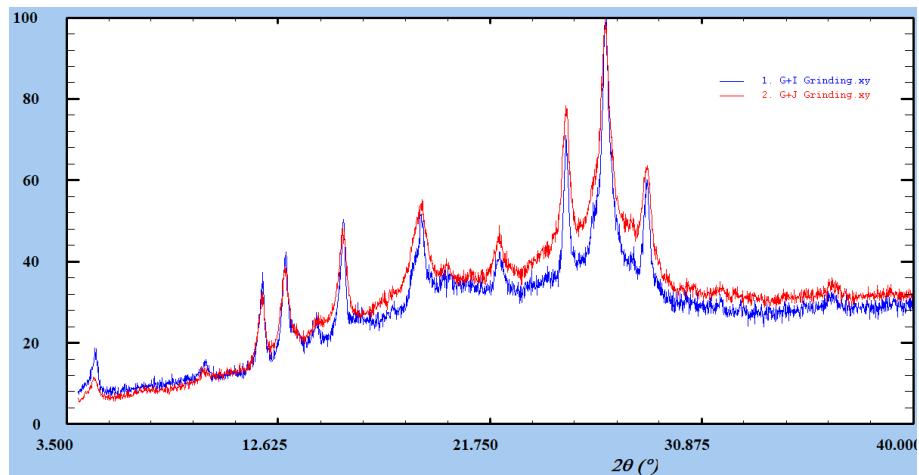
Peaks at 4.8°, 9.5°, 12.0° and 13.0° which were unexplained in **D+G**, **E+G**, **F+G** are also present here and do match perfectly: no cocrystal but either polymorph or degradation product of **G**.

### 7) Samples A+G vs G+H:



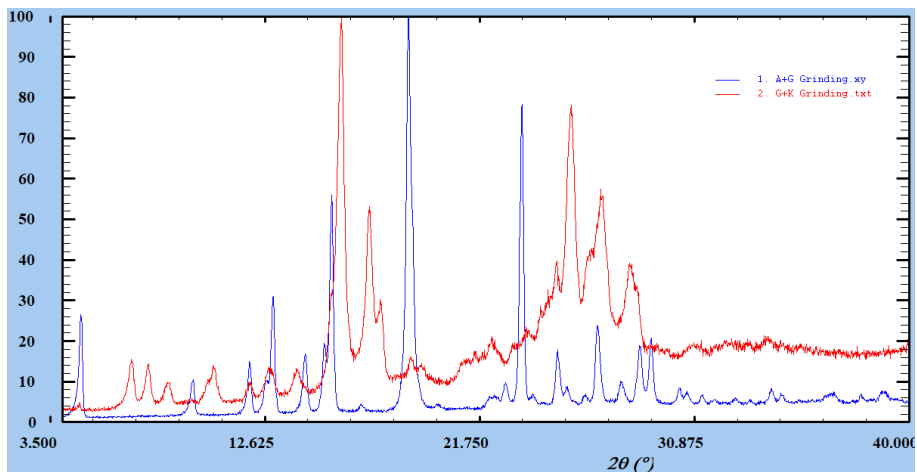
Peaks at 4.8°, 9.5°, 12.0° and 13.0° which are characteristic of the impurity (polymorph or degradation product of **G**) are not present in **G+H**: new phase confirmed.

### 8) Samples G+I vs G+J:



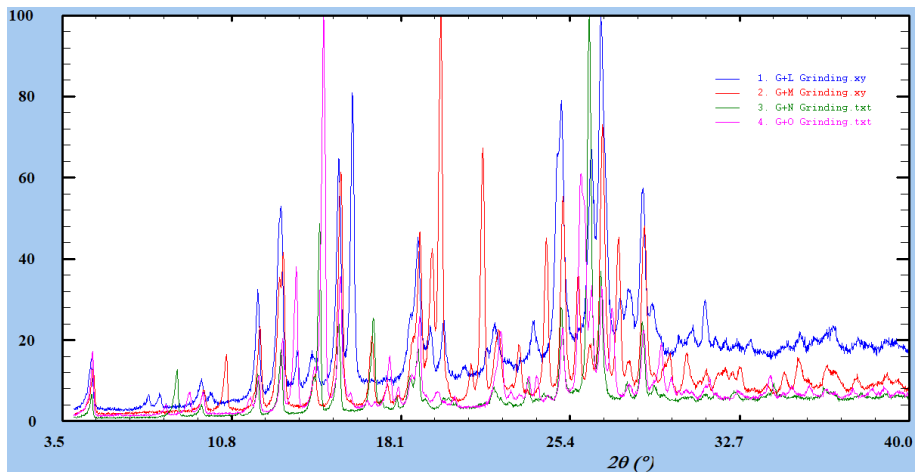
Peaks at 4.8°, 9.5°, 12.0° and 13.0° which were unexplained in **G+I**, **G+J**, are also present here and do match perfectly (the whole patterns match perfectly): no cocrystal but either polymorph or degradation product of **G** and amorphization of anils **I** and **J**.

### 9) Samples A+G vs G+K:



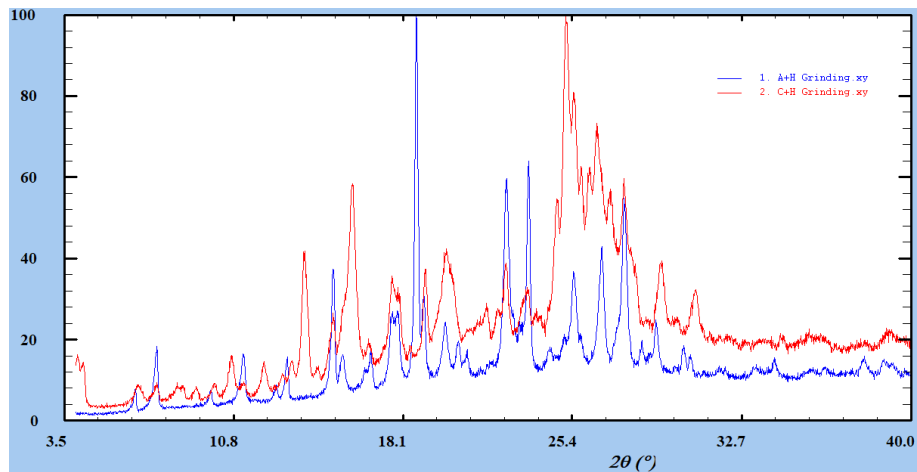
Peaks at 4.8°, 9.5°, 12.0° and 13.0° which are characteristic of the impurity (polymorph or degradation product of **G**) are not present in **G+K**: new phase confirmed.

### 10) Samples G+L, G+M, G+N, G+O:



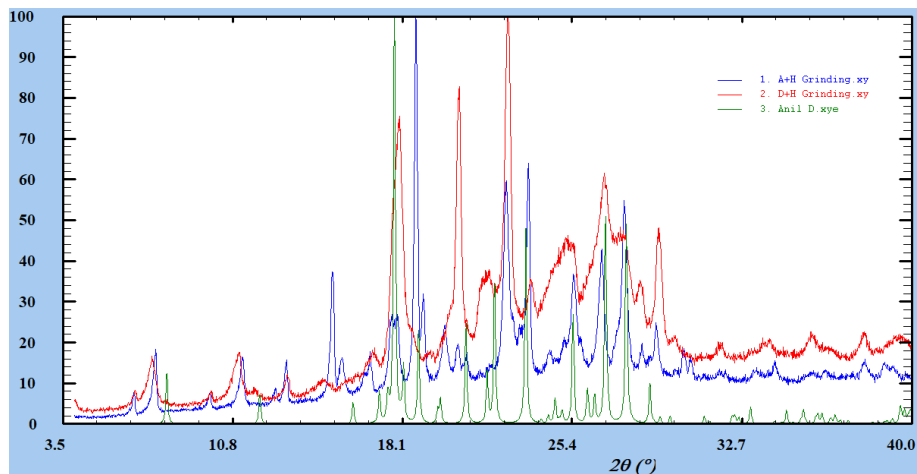
Peaks at 4.8°, 9.5°, 12.0° and 13.0° which were unexplained in **G+L**, **G+M**, **G+N** and **G+O** are also present here and do match perfectly: no cocrystal but either polymorph or degradation product of **G**.

### 11) Samples A+H, C+H:



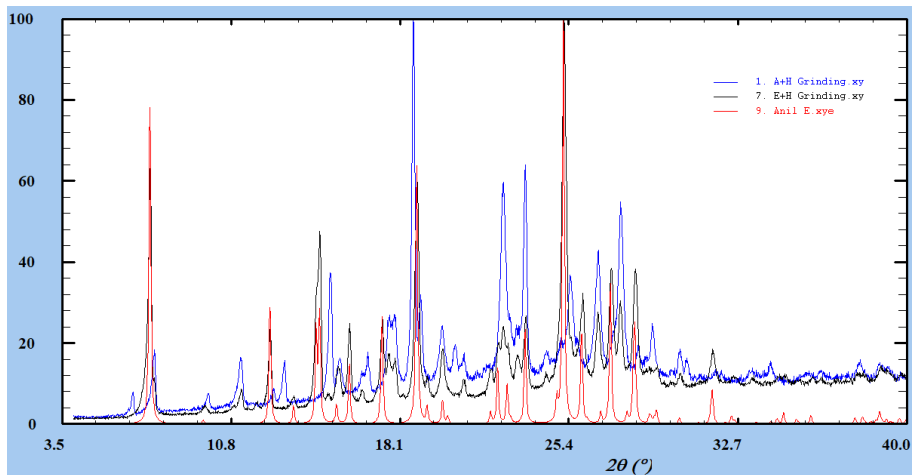
Peaks at  $6.5^{\circ}$ ,  $7.5^{\circ}$ ,  $9.8^{\circ}$ ,  $11.2^{\circ}$  and  $13.1^{\circ}$  which were unexplained in **A+H**, are also present in **C+H**: no cocrystal but either polymorph or degradation product of **H**.

### 12) Sample D+H:



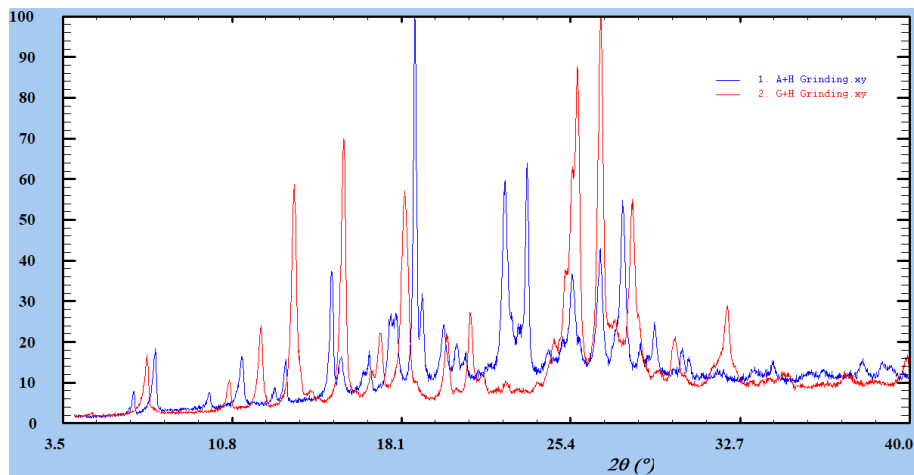
Peaks at  $6.5^{\circ}$ ,  $7.5^{\circ}$ ,  $9.8^{\circ}$ ,  $11.2^{\circ}$  and  $13.1^{\circ}$  which were unexplained in **D+H**, are also present in **A+H**: no cocrystal but either polymorph or degradation product of **H**.

### 13) Sample E+H:



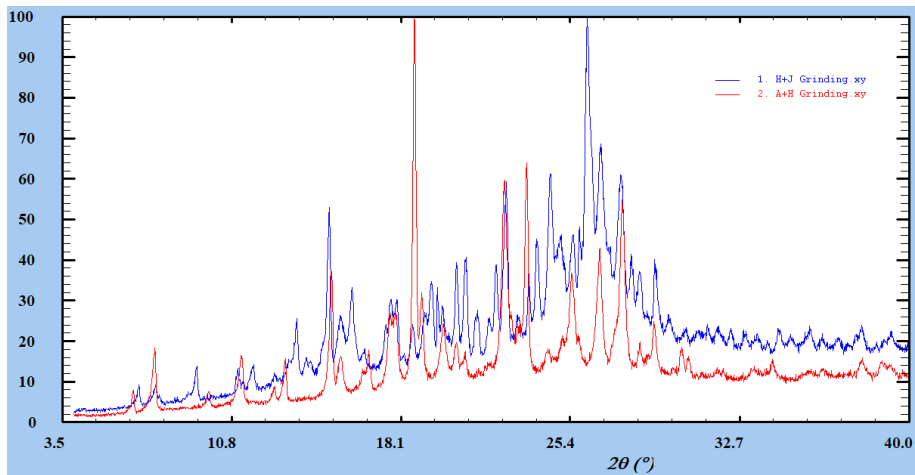
Unexplained **E+H** peaks (11.25°, 15.0°, 16.5°, 17.6°, 17.8°, 20.8°, etc.) are also present in **A+H**: no cocrystal but either polymorph or degradation product of **H**.

### 14) Sample G+H:



No match between **A+H** and **G+H** and characteristic peaks of the impurity (6.5°, 7.5°, 9.8°, 11.2° and 13.1°) are not present. New phase is confirmed.

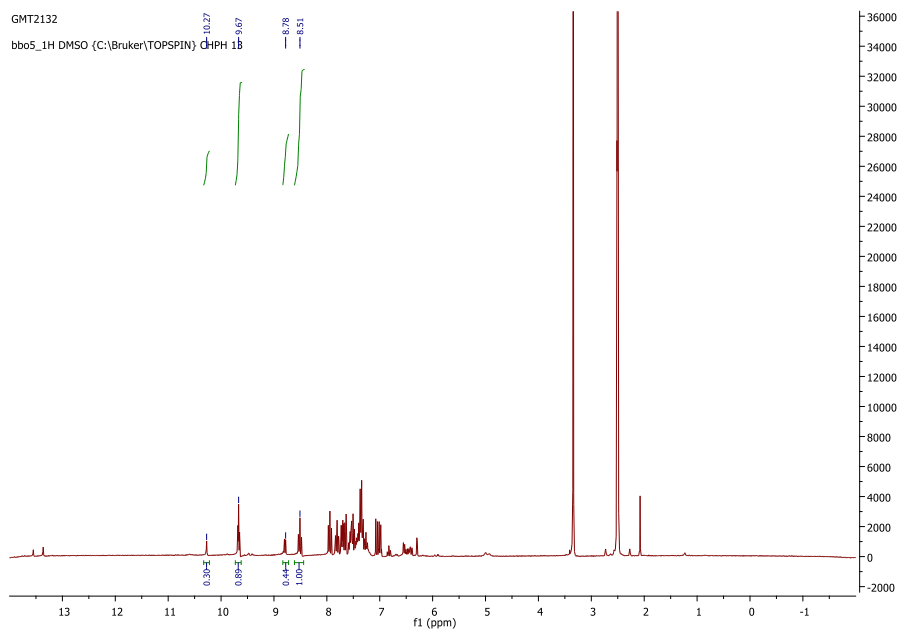
### 15) Sample H+J:



Peaks at  $6.5^\circ$ ,  $7.5^\circ$ ,  $11.2^\circ$  and  $13.1^\circ$  which were unexplained in **H+J**, are also present in **A+H** along with other common peaks: no cocrystal but either polymorph or degradation product of **H**.

#### Ch4.4. E+J NMR check

Among the remaining cocrystal candidates, E+J Showed unexpected peak in H-NMR analysis at 10.27 and 8.78 ppm. These peaks indicate further reaction/degradation occurred and thus the new observed phase for this sample is discarded.



Chapter 5 Supporting Information: Ch5.1. Table 1: complementary structural information for new solid-solutions structures

Sample name	Solid Solution A/B: 50/50	Solid Solution A/B: 10/90	Solid Solution A/B: 05/95	Solid Solution C/D: 75/25	Solid Solution C/D: 50/50	Solid Solution E/F: 50/50	Solid Solution G/H: 50/50
Empirical formula*	0.53(C <sub>3</sub> H <sub>3</sub> NO) <sub>1</sub> 0.47(C <sub>3</sub> H <sub>3</sub> FNO) <sub>1</sub>	0.09(C <sub>3</sub> H <sub>3</sub> NO) <sub>1</sub> 0.91(C <sub>3</sub> H <sub>3</sub> FNO) <sub>1</sub>	0.08(C <sub>3</sub> H <sub>3</sub> NO) <sub>1</sub> 0.92(C <sub>3</sub> H <sub>3</sub> FNO) <sub>1</sub>	0.81(C <sub>3</sub> H <sub>3</sub> NO) <sub>1</sub> 0.19(C <sub>3</sub> H <sub>3</sub> FNO) <sub>1</sub>	0.68(C <sub>3</sub> H <sub>3</sub> NO) <sub>1</sub> 0.32(C <sub>3</sub> H <sub>3</sub> FNO) <sub>1</sub>	0.48(C <sub>3</sub> H <sub>3</sub> NO) <sub>1</sub> 0.52(C <sub>3</sub> H <sub>3</sub> FNO) <sub>1</sub>	0.53(C <sub>3</sub> H <sub>3</sub> NO) <sub>1</sub> 0.47(C <sub>3</sub> H <sub>3</sub> FNO) <sub>1</sub>
M [g/mol]	205.68	213.53	213.79	230.70	233.02	222.59	255.66
T [K]	293(2)	295(2)	295(2)	295(2)	295(2)	295(2)	295(2)
Wavelength [Å]	0.71073	1.54184	1.54184	0.71073	0.71073	0.71073	1.54184
Crystal system	Monoclinic	Monoclinic	Monoclinic	Orthorhombic	Orthorhombic	Monoclinic	Monoclinic
Space group	Pn	Pn	Pn	P212121	P212121	P21/n	P21/c
a [Å]	10.0734(13)	10.1254(6)	10.1272(3)	6.1370(3)	6.1693(2)	13.2649(3)	12.9996(2)
b [Å]	4.6722(4)	4.6521(2)	4.65409(11)	9.1783(4)	9.1491(3)	14.8079(4)	13.9001(2)
c [Å]	11.9195(15)	11.9793(8)	11.9724(4)	21.1606(10)	21.1615(6)	16.6390(5)	7.02103(10)
α [°]	90	90	90	90	90	90	90
β [°]	113.022(15)	113.781(8)	113.823(4)	90	90	91.504(2)	93.1830(14)
γ [°]	90	90	90	90	90	90	90
V [Å <sup>3</sup> ]	516.31(12)	516.36(6)	516.21(3)	1194.92(10)	1194.42(7)	3267.20(15)	1266.71(3)
Z	2	2	2	4	4	4	4
ρ <sub>calc</sub> [Mg m <sup>-3</sup> ]	1.384	1.373	1.375	1.286	1.296	1.358	1.341
μ [mm <sup>-1</sup> ]	0.10	0.82	0.82	0.088	0.090	0.098	0.709
F(000)	224	222	223	486	490	1394	535
Crystal size [mm]	N.D.	0.18 x 0.15 x 0.03	0.31 x 0.23 x 0.03	0.53 x 0.35 x 0.14	0.65 x 0.31 x 0.27	0.61 x 0.30 x 0.20	0.60 x 0.33 x 0.13
Theta range for data collection [°]	3.387 to 26.365	4.85 to 67.112	4.84 to 66.772	2.935 to 29.250	2.434 to 29.586	3.067 to 30.255	3.134 to 66.866
Reflections collected	2144	4098	8578	10520	9127	10344	12387
Independent reflections	1554	1576	1847	2521	3088		2261
Completeness to θ <sub>max</sub> [%]							
Max. and min. transmission							
Data / restraints / parameters	1554 / 2 / 146	1576 / 2 / 151	1847 / 2 / 151	2521 / 0 / 166	3088 / 0 / 166	10344 / 0 / 470	2261 / 0 / 187
Goodness-of-fit on F <sub>o</sub>	1.048	1.0125	1.099	1.035	1.020	0.988	1.026
Final R indices [I > 2σ(I)]	R <sub>1</sub> = 0.0465, wR <sub>2</sub> = 0.1091	R <sub>1</sub> = 0.0336, wR <sub>2</sub> = 0.0800	R <sub>1</sub> = 0.0296, wR <sub>2</sub> = 0.0801	R <sub>1</sub> = 0.0351, wR <sub>2</sub> = 0.0856	R <sub>1</sub> = 0.0351, wR <sub>2</sub> = 0.0830	R <sub>1</sub> = 0.0487, wR <sub>2</sub> = 0.1379	R <sub>1</sub> = 0.0374, wR <sub>2</sub> = 0.1023
R indices (all data)	R <sub>1</sub> = 0.0512, wR <sub>2</sub> = 0.1185	R <sub>1</sub> = 0.0432, wR <sub>2</sub> = 0.0969	R <sub>1</sub> = 0.0319, wR <sub>2</sub> = 0.0833	R <sub>1</sub> = 0.0435, wR <sub>2</sub> = 0.0927	R <sub>1</sub> = 0.0462, wR <sub>2</sub> = 0.0887	R <sub>1</sub> = 0.0892, wR <sub>2</sub> = 0.1496	R <sub>1</sub> = 0.0402, wR <sub>2</sub> = 0.1056
Largest diff. Peak/hole [e Å <sup>-3</sup> ]	0.20 and -0.13	0.13 and -0.10	0.13 and -0.11	0.089 and -0.123	0.089 and -0.128	0.264 and -0.239	0.159 and -0.138

\*Molar compositions were calculated through XRD refinement and thus present an uncertainty of about 0.05. Also, crystals composition (after crystallization) may differ from initial powder composition (after grinding).

## Ch5.2. Kinetical studies of A/B system

The kinetic measurements (blue curves) of a few **A/B** mixtures were done at 550 nm after 5 minutes irradiation at 365 nm of the powders. Results show an expected exponential decay over time after irradiation (disappearance of *trans*-keto band). The kinetical curves were linearized using the Malkin equation:  $\ln(M) = -k_1 \cdot t$ , with  $M = \frac{Abs_{\infty} - Abs(t)}{Abs_{\infty} - Abs_0}$  and results for  $k_1$  parameter (orange curves) are displayed for each sample.  $k_2$  parameters were not calculated.

